NNT : 2017SACLS259

Thèse de doctorat
de l'Université Paris-Saclay
préparée à l'Université Paris-Sud et au
Commissariat à l'énergie atomique et
aux énergies alternatives

École doctorale n°576
Particules, Hadrons, Énergie, Noyau,
Instrumentation, Imagerie, Cosmos et Simulation
(PHENIICS)
Spécialité de doctorat: Physique des particules
par

Francesco Gizzarelli

Mesure du rapport des sections efficaces d'interaction des neutrinos sur les noyaux d'oxygène et de carbone, à partir des données du détecteur proche ND280 de l'expérience T2K

Thèse présentée et soutenue à Saclay, le 27 Septembre 2017.

Composition du jury :

Alain Blondel,	Université de Genève,	Président du jury
Jan Sobczyk,	Institut de physique theorique de l'université de Vratislavie,	Rapporteur
Alessandra Tonazzo,	Laboratoire AstroParticule et Cosmologie, Paris,	Rapporteur
François Mauger,	Université de Caen Normandie,	Examinateur
Andrea Giuliani,	Centre de Sciences Nucléaires et de Sciences de la Matière, Orsay,	Examinateur
Sara Bolognesi,	Institut de recherche sur les lois fondamentales de l'Univers, CEA Saclay,	Co-encadrante de thèse
Marco Zito,	Institut de recherche sur les lois fondamentales de l'Univers, CEA Saclay,	Directeur de thèse

Contents

List of Figures

List of Tables

A Tonino, all'Abruzzo "forte e gentile",

a quel 6 Aprile 2009 perché il sisma m'ha scosso.

Résumé

Le Modèle Standard (MS) de la physique des particules décrit les interactions des particules sub-atomiques à travers les interactions fortes, faibles et électromagnétiques. Toutefois, il est clair que cette théorie ne constitue pas une description complète de la Nature. Parmi les preuves irréfutables se trouvent :

- Le MS ne décrit pas l'interaction gravitationnelle, l'une des forces les plus influentes dans l'Univers.
- Il ne fournit pas de candidat viable pour la matière noire.
- Il n'explique pas l'asymétrie matière-antimatière observée dans l'Univers.
- Dans le MS, les neutrinos sont de masse nulle, en opposition avec les données expérimentales des oscillations des neutrinos.

Postulé par Wolfgang Pauli au debut du XXème siècle pour expliquer le spectre continue en énergie des électrons produit par l'émission bêta (désintégration-β), le neutrino a été observé expérimentalement pour la première fois il y a 50 ans, il a depuis trouvé sa place dans le cadre du MS qui s'est construit dans les années 70 et qui a ètait prouvé avec des résultats très précis. Cependant, le neutrino est également la première sonde d'une physique allant au delà de la physique proposée par ce modèle. En effet, les neutrinos sont décrits comme des particules de masse nulle, mais le fait expérimental qu'ils changent de saveur au cours de leur propagation (oscillation des neutrinos) implique qu'ils ont une masse non nulle ce qui n'est pas prévu par la théorie. Le phénomène d'oscillation , correspondant à une probabilité que possède le neutrino de changer de saveur lorsqu'il se propage dans le vide ou la matière, il a été prouvé expérimentalement en 1998 par l'expérience Super-Kamiokande (SK) avec les neutrinos créés par l'interaction de rayons cosmiques dans l'atmosphère de la Terre et en suite en 2001 par l'expérience Observatoire de Neutrinos de Sudbury (SNO) utilisant les neutrinos provenant du centre du soleil.
Il est aujourd'hui le sujet d'investigation de nombreuses expériences dans le monde, à la fois étudié avec les neutrinos solaires ou atmosphériques ou encore avec des neutrinos fabriqués par des sources artificielles auprès de réacteurs nucléaires ou d'accélérateurs de particules. Le Chapitre 1 de ce manuscrit résume l'histoire de la découverte du

neutrino, la théorie et les premières observations des oscillations, ainsi que l'état actuel des expériences d'oscillation.
Le travail de cette thèse se concentre sur l'expérience T2K (Tokai-vers-Kamiokande), une expérience à longue ligne de base, située au Japon et qui inclut un complexe de deux détecteurs proches et un détecteur lointain. Son objectif principal est la mesure des paramètres gouvernant le phénomène d'oscillation ainsi que l'étude des propriétés d'interaction des neutrinos avec la matière.
Afin de mesurer les changements de saveur du neutrino, T2K utilise un faisceau intense de neutrinos muoniques (ν_μ), produits auprès du complexe de l'accélérateur de protons de J-PARC. Les protons sont accélerè jusqu'à une energie de 30 GeV, ceux-ci interagissent avec une cible en graphite de 90 cm de long produisant des mésons principalement des pions et des kaons. Les mésons chargés sont alors sélectionné par charge et focalisé de manière à produire essentiellement un faisceau de (anti)neutrinos muoniques ν_μ ($\overline{\nu}_\mu$) avec une énergie piquant environ à 650 MeV. T2K est, en outre, la première expérience à employer la technique dite hors axe, qui permet de produire un spectre en énergie des neutrinos plus étroit par rapport à l'axe traditionnel et d'augmenter aussi significativement la sensibilité de la mesure aux paramètres d'oscillation. En effet le faisceau peut être centré selon la région d'énergie intéressante correspondant au maximum de la probabilité d'oscillation.
Le faisceau de neutrinos est dirigé vers les détecteurs et observé à deux distances différentes par deux détecteurs qui se trouvent hors axe, à un angle de 2.5° : un détecteur proche (ND280), situé à 280 m de la source de neutrinos afin de le caractériser alors que la probabilité d'oscillation est encore négligeable, et un détecteur lointain (Super-Kamiokande) qui mesure l'amplitude des oscillations après une propagation des neutrinos traversant la Terre á une distance de 295 km. Le détecteur proche est donc utilisé pour mesurer le taux d'interactions de neutrinos avant qu'ils n'aient le temps d'osciller ainsi que les différents bruits de fond liés à la mesure d'apparition des neutrinos électroniques dans le détecteur lointain. Il permet ainsi de contraindre les sections efficaces et le flux à Super-Kamiokande pour l'analyse d'oscillation.
T2K a pu observer pour la première fois en 2013 l'oscillation $\nu_\mu \rightarrow \nu_e$ (l'apparition de neutrinos de saveur électronique dans son détecteur lointain utilisant un faisceau principalement composé de neutrinos muoniques) et ainsi mesurer le dernier angle de mélange θ_{13}, inconnu à cette époque. La mesure d'une valeur non nulle de θ_{13} ouvre le champ à l'évidence de la violation de la symétrie de Charge-Parité (δ_{CP}), non encore observée dans le secteur leptonique. Cela est devenu l'objectif principal de l'expérience. De plus, T2K a également été conçue pour mesurer précisément les paramètres d'oscillations θ_{23} et Δm^2_{23} grâce à la disparition des neutrinos muoniques $\nu_\mu \rightarrow \nu_\mu$, ainsi que pour rechercher d'éventuels neutrinos stériles. T2K et ses principaux résultats sur la détermination des paramètres d'oscillations sont détaillés dans le Chapitre 2.
Afin de rendre cette mesures possibles à l'avenir, une amélioration de la compréhension compréhension du détecteur, des modèles et des sections efficaces d'interaction des

neutrinos est nécessaire et vient s'ajouter à la liste des objectifs de T2K. Cette thèse se concentre donc sur ces deux objectifs :

1. réduire l'erreur systématique liées au détecteur à travers un'étude de l'alignement des modules Micromegas de les Chambres à Projections Temporelles (TPC) du détecteur proche ND280;

2. approfondir nos connaissances sur l'interaction des neutrinos avec la matière à travers la mesure du rapport des sections efficaces des neutrinos sur les noyaux de carbone et d'oxygène pour l'interaction quasi élastique de courant chargé (CCQE). Celui-ci est le processus dominant à l'énergie de T2K.

Le Chapitre 3 décrit les TPCs du détecteur proche ND280, elles permettent l'identification des particules chargées produit par l'interaction de neutrinos dans le détecteur et la mesure de leur impulsion. En effet, le détecteur proche est plongé dans un champ magnétique d'une valeur nominale de 0.2 T qui courbe la trajectoire des particules chargées proportionnellement à leur impulsion. Toutefois, les défauts d'alignement entre différents modules Micromegas (MM) qui instrumentent chaque plan de lecture des TPCs peuvent constituer une source d'erreur sur la mesure de cette courbure et doivent donc être estimés et pris en compte pour réduire l'incertitude sur la valeur de l'impulsion des particules. Le groupe CEA, dans lequel je suis impliqué, est responsable de la maintenance et de l'opération des TPCs, donc une partie de mon travail a consisté en l'étude des TPCs et en particulier de l'alignement des modules MicroMegas installés sur les plans de lecture.
La méthode utilisée pour déterminer l'orientation et la position relative des modules MM est décrite dans le Chapitre 4. Celle-ci est basée sur la comparaison des segments appartenant à la même projection de trace et traversant deux modules adjacents. L'algorithme de reconstruction a été modifié de telle facon que chaque segment est considéré comme une trace particulière, dont les paramètres sont déterminés en effectuant une reconstruction indépendante dans chaque module. La différence relative (résidu) d'orientation ($\Delta\phi$) et de décalage (Δy) de la projection de la trace sur le plan YZ est calculée, pour une paire de modules, à la coordonnée z qui est fixée dans le plan médian entre les deux colonnes de détecteurs MM. Ainsi, les constantes de corrections des défauts d'alignements associés aux rotations ($\delta\phi$) et aux décalages relatives (δy et δz) entre les deux modules dans le plan YZ définissent complètement les distributions des résidus $\Delta\phi$ et Δy. Pour déterminer les défauts d'alignements des modules MM, les données des traces cosmiques sont prises sans champ magnétique ($|\vec{B}| = 0$). Cette configuration permet d'utiliser une trajectoire paramétrée par des lignes droites, découplant les effets de désalignement dûs aux inhomogénéités du champ magnétique dans le détecteur. De plus, ni les corrections de champ $\vec{B}$ ni $\vec{E}$ sont appliquées dans le processus de reconstruction de la trace afin de ne pas introduire un potentiel biais dans la procédure d'alignement MM dû aux corrections externes.
La procedure d'alignement des MM utilise un ajustement aux residus $\Delta\phi$ et Δy des trace pour la détermination des constantes de corrections $\delta\phi$, δy, δz. Cette méthode

est éprouvée avec des géométries MM bien connues générées par des simulations Monte-Carlo dans le détecteur afin de tester sa fiabilité. L'étude présentée dans ce chapitre a comme but l'amélioration des résultats obtenus avec la mesure optique de la position des modules qui a été effectuée avant l'installation de l'életronique des MM, pendant la construction des TPC et qui sont actuellement utilisés dans la reconstruction des événements pour tenir compte des défauts d'alignement des modules MM. La mesure optique donne une precision d'environ 0.5 mrad pour les rotations et de 100 μm pour les décalages en y et z, en revanche la méthode utilisée dans cette étude porte un'amélioration dans la reconstruction de traces après la correction des défauts d'alignement observés qui arrive à 0.07 mrad pour les rotations et de 20 μm et 50 μm pour les décalage en y et z. De plus, cette mèthode offre la possibilité de suivre dans le temps l'évolution éventuelle des défauts d'alignement de MM, notamment pendant les périodes de prise de données. Enfin, l'impact des nouvelles corrections d'alignement sur la mesure de l'impulsion par rapport aux constantes de corrections optiques actuellement est quantifiée.

La deuxième partie de cette thèse se focalise sur une mesure de la section efficace des neutrinos muoniques interagissant par courants chargés quasi-élastique (CCQE). Les interactions CCQE ont été choisis car elles correspondent au signal utilisé par l'analyse d'oscillation à T2K et à la majeure partie de la statistique du spectre en énergie de neutrinos. Ce manuscrit décrit la mesure du rapport des sections efficaces d'interaction des neutrinos sur les noyaux de carbone et d'oxygène. En effet, cette mesure contribue à la réduction des incertitudes pour l'analyse d'oscillation, liés à l'utilisation d'une différente cible pour le détecteur proche et le détecteur lointain. Les neutrinos sont étudiés grâce à l'observation de l'état final de leur interaction avec la matière. Ainsi, les modèles d'interactions doivent être parfaitement bien compris, afin d'en déduire les propriétés des neutrinos correctement. En effet, les expériences d'oscillation présentes et futures approchent d'une phase où notre connaissance des interactions des neutrinos devient un facteur limitant pour la détermination des paramètres d'oscillations (par exemple les réux-interaction de l'état final FSI, ou la correlation entre nucléons 2p2h). Le Chapitre 5 présente les différents types d'interaction pour les neutrinos à l'énergie de T2K et les différents modèles théoriques qui les décrivent.

Les mesures des interactions CCQE sur des cibles nucléaires relativement lourdes (comme le carbone et l'oxygène) ne sont pas en accord avec les prévisions des chambres à bulles sur les cibles d'hydrogène et de deutérium. De plus, l'état final mesuré ne correspond pas à la véritable interaction des neutrinos en raison de la physique (FSI ou 2p2h) et des effets expérimentaux (la reconstruction). Par exemple, en raison de FSI, un événement produisant un muon et un pion chargé peut imiter un événement CCQE si le pion est absorbé avant de sortir du noyau. En plus, une interaction CCQE est caractérisée par la présence d'un muon et d'un seul proton dans l'état final, mais la reconstitution des nucléons (protons ou neutrons) est un défi expérimental. Le proton a souvent une impulsion très faible et, s'il sort du noyau, il peut s'échapper sans être détecté. Ensuite, les interactions multi-nucléon produisent dans l'état final plus d'un nucléon qui

souvent ne sont pas détectés, imitant ainsi un événement CCQE. Pour ces raisons là, une définition de l'interaction correspondant à ce qui est effectivement observé dans ND280 est nécessaire afin d'éviter une mesure dépendante du modèle. Le signal considéré est constitué d'interactions de Courants Chargés avec Zéro Pions (CC0π) où un muon, un nombre quelconque de nucléons et aucun pions sont détectés dans l'état final. Le Chapitre 6 détaille la sélection d'événements CC0π, la stratégie permettant la détermination du rapport, ainsi que les incertitudes sur la sélection liées au détecteur et théoriques. La sélection des événements CC0π est basée sur l'observation de ètat final avec d'une trace compatible avec un muon de charge négative et pas des pions.
Le but de l'analyse est la mesure du rapport de section efficace CC0π sur les noyaux d'oxygène et de carbone afin de réduire l'incertitude totale sur l'analyse d'oscillation due à l'extrapolation du taux d'interaction du détecteur proche ND280 au détecteur lointain SK. Puisque SK est un détecteur de Cherenkov à eau, ND280 doit contraindre précisément les taux d'interaction des neutrinos sur l'oxygène. Les sections efficaces de neutrinos dépendent du noyau par les effets nucléaires (FSI, 2p2h) qui pour l'instant ne sont pas bien décrits par la théorie. Par conséquent, les taux d'interaction doivent être mesurés sur l'oxygène au niveau du détecteur proche.
Dans le détecteur proche ND280, des cibles d'eau sont présentes dans le sous-détecteurs FGD2 et P*O*D. Ce dernier se compose de sacs d'eau qui peuvent être remplis avec de l'eau ou être vides. Par conséquent, l'extraction de la section efficace en oxygène peut être réalisée en utilisant une méthode basée sur une soustraction statistique des événements. Cette méthode n'identifie pas les interactions de l'eau individuellement, mais les infère en prenant des données avec et sans eau dans le détecteur. Puisque le FGD2 est constitué d'un module d'eau non-instrumenté et de barres de scintillateur en plastique, une méthode alternative consiste à trouver la position du vertex d'interaction dans le matériau actif afin de contraindre les interactions d'eau. Cette analyse utilise une combinaison de ces deux méthodes: la détermination du vertex d'interaction et la soustraction de la composante d'oxygène en comparant les interactions dans les scintillateur. Cependant, la mesure de la section dans l'eau avec la soustraction statistique est également possible dans FGD2 en comparant le taux d'interaction entre les FGD. En effet, étant donné que le FGD1 est entièrement constitué de scintillateurs en plastique (à base de carbone), il peut être utilisé pour modéliser avec précision le taux hors eau dans FGD2 (carbone + eau). Toutefois, ici le FGD1 sera utilisé comme échantillon de contrôle pour contraindre l'erreur systématique du à la migration des vertexes.
Les résultats de la mesure sont montrés dans le Chapitre 7 et présentés comme une section efficace différentielle en fonction de la cinematique (angle et impulsion) du muon ainsi que en fonction de l'énergie du neutrino. L'analyse présentée dans cette thèse utilise les données prises pendant le RunII-IV comprenant 5.80×10^{20} interactions de protons avec la cible. La rapport de section efficace CC0π sur les noyaux d'oxygène et de carbone totale au détecteur proche obtenue est de :

$$R_{O/C} = \frac{\sigma_O}{\sigma_C} = 0.930 \pm 0.048 \text{ (stat.)} \pm 0.045\text{(syst.)} \quad (1)$$

Introduction

The Standard Model (SM) of particle physics describes the interactions of subatomic particles through the strong, weak and electromagnetic interactions. However, it is known that this theory is not a complete description of Nature. Some of the compelling evidences of its incompleteness are:

- SM does not describe gravitational interactions, one of the largest driving forces of the universe;
- it cannot provide a valid dark matter candidate;
- it cannot explain many astrophysical and cosmological phenomena which indicate that there is more matter in the universe than we can see;
- it does not allow neutrinos to have a mass, in clear contrast with the experimental evidence of neutrino oscillations.

Neutrinos are indeed described as massless particles in the SM, but the observation that they can change their flavor along their propagation path (neutrino oscillation) proves that they actually have a mass. Chapter 1 of this thesis summarizes the history of neutrino discovery, the theory and the first observations of oscillations, as well as the current state of art of oscillation experiments.
The work of this thesis has been performed in the Tokai to Kamioka (T2K) experiment: a long baseline experiment located in Japan. The T2K experiment and its main results in the determination of the oscillation parameters are presented in Chapter 2. Using the data collected so far, T2K has been able to observe for the first time the $\nu_\mu \rightarrow \nu_e$ appearance and to give first results on the Charge-Parity symmetry in neutrino oscillations. T2K provides also precise measurements of the oscillation parameters θ_{23}, Δm^2_{23}. The precise measurement of the oscillation parameters requires a good understanding of the detector and of the neutrino interaction model. This thesis is thus focused on both these aspects: the reduction of the detector uncertainties and the improvement of our knowledge of neutrino interactions with matter.
The CEA Saclay group where I performed this thesis, is in charge of the maintenance and operation of the Time Projection Chambers (TPCs) of the T2K near detector (ND280) which are used to identify and measure the kinematics of the charged particles produced in neutrino interactions, as described in Chapter 3. Part of my work was

focused on the study of the TPC and in particular on the alignment of the MicroMegas modules which instrument their readout planes. Misalignments between modules may cause a bias on the momentum measurement of the particles crossing the TPC. An alignment procedure using cosmic muons is presented in Chapter 4.
Neutrinos are studied through the observation of the final state of their interactions with matter. Therefore, the interaction models need to be well understood to infer the neutrino properties correctly. Current and next future oscillation experiments are approaching the phase of precise measurements of the mixing parameters where the knowledge of neutrino uncertainties will play an important role. Chapter 5 highlights the dominant neutrino interactions at the T2K energy and the theoretical models developed so far to describe them. The charged current quasi-elastic (CCQE) interaction is the most relevant process at T2K. This manuscript describes the measurement of the CCQE cross-section ratio between oxygen and carbon nuclei, that can contribute to reduce the uncertainties on the oscillation analysis arising from the different target between the near and far detector. Chapter 6 presents the selection of the CCQE sample, the strategy to extract the ratio measurement, as well as the detector and theory systematic uncertainties associated to the selection. Finally the results are shown in Chapter 7.

Chapter 1

Neutrino Oscillations

Neutrinos are one of the most abundant particles in the Universe: they are produced in a wide range of natural and artificial reactions such as nuclear fusion in the core of the stars or fission in nuclear reactors. Described by the Standard Model (SM) of particle physics as massless neutral particles, they interact only via the weak force which lead them to be very elusive and difficult to detect. Since their discovery, in 1956, many experiments have contributed to improve our knowledge of their properties. Oscillation experiments like the Sudbury Neutrino Observatory and Super-Kamiokande proved the existence of neutrino oscillations: a phenomenon in which neutrinos change their leptonic flavor when they propagate in vacuum or through the matter. This phenomenon proves that neutrinos have mass. Indeed neutrino flavor eigenstates are a superposition (mixture) of the mass eigenstates. In this Chapter after a brief history of their discovery, the theory of neutrinos and the first observations of neutrinos oscillations will be discussed as well as the status of the current and future oscillation experiments.

1.1 History of neutrinos discovery

The existence of a new weakly interacting particle was first postulated by Wolfgang Pauli in 1930 [1] in his famous letter *"Dear radioactive ladies and gentlemen"* in order to explain the continuous spectrum in nuclear β-decay. Initially this process, by which certain nuclear elements turn into different ones, was described by the emission of a single particle (electron) by the nucleus

$$(A, Z) \rightarrow (A, Z + 1) + e^{-}. \tag{1.1}$$

According to this theory the outgoing particle should have a monochromatic spectrum corresponding to the energy difference between the initial and final nuclear energy levels. However experimental results obtained by James Chadwick in 1914 [2] showed that the energy spectrum of the emitted electron was continuous rather than discrete, in contradiction to the law of conservation of energy. Initially Pauli called this undetectable neutral, light particle *neutron* and proposed it as nuclear constituent of the

atom. Although he first suggested the existence of this new particle, he never published the idea. The heavy neutron, as we know it today, was discovered in 1932 by Chadwick himself [3]. Two years later Enrico Fermi, based on Pauli's assumption, built the first full theory of β-decay [4]. This theory described the β-decay as:

$$n \rightarrow p + e^- + \nu \tag{1.2}$$

where ν is a new particle named *neutrino*, to distinguish it from the heavier neutron. After two decades, in 1956 a team lead by Cowan and Reines made the first experimental direct observation of the neutrino [5]. They designed an experiment at the Savannah River Plant to detect the inverse β-decay caused by anti-neutrinos produced by the reactor

$$\bar{\nu}_e + p \rightarrow e^+ + n. \tag{1.3}$$

The detector consisted of two water tanks doped with a cadmium chloride ($CdCl_2$) sandwiched between three liquid scintillator detectors. The water in the tanks acted as target for anti-neutrino interactions with protons, the neutrons in the final state were captured by the Cadmium emitting a gamma ray, while the positrons were detected in the scintillator layers using the photon pairs produced when they annihilate with electrons in the material.
A new neutrino flavor was discovered slightly afterwards, in 1962, at Brookhaven National Laboratory by Lederman [6]. Lederman's experiment was the first accelerator neutrino experiment exploiting a 15 GeV proton beam hitting a Beryllium (Be) target to produce a neutrino beam through the decay in flight of pions $\pi^{\pm}$ via the reaction:

$$\pi^{-(+)} \rightarrow \mu^{-(+)} + \nu_\mu(\overline{\nu}_\mu) \tag{1.4}$$

If the neutrinos associated with muons in pion decays were identical to the neutrinos produced in β-decays, they would have produced electrons when interacting with the detector. However, these neutrinos were found to produce only muons, proving the existence of a second flavor. In 1975 at Stanford a third lepton the tau (τ), similar to e, μ but heavier, was observed using a positron-electron ($e^+ - e^-$) collider [7]. As a consequence, the existence of a third neutrino flavor ν_τ has been suggested. It was experimentally observed only in 2001 by the DONUT experiment at Fermilab [8].
According to the SM, that will be briefly described in the next Sec. 1.2, the conservation of the lepton flavor implies that each neutrino is coupled with the corresponding charged lepton, forming with it an electroweak doublet.

1.2 The Standard Model Neutrino

The Standard Model of particle physics (SM) is a relativistic quantum field theory, based on the gauge symmetry $SU(3)_C \otimes SU(2)_L \otimes U(1)_Y$ that describes three of the four fundamental interactions:

- $SU(3)_C$ is the color symmetry group, describing the strong interactions;
- $SU(2)_L \otimes U(1)_Y$ is the group associated to the electroweak interactions (including the electromagnetic and weak interactions).

The SM does not include the fourth fundamental force, the gravitational interaction. According to their properties, particles are split into two main categories: interacting particles (fermions) which constitute the matter and mediators of the forces (bosons) which mediate those interactions. The SM, describes the electromagnetic, weak and strong interactions through the exchange of spin-1 gauge fields:

Gluons (g) are the eight color charged mediators of the strong interaction, one for each generator of $SU(3)_C$. They are massless and electrically neutral.

Photon (γ) is the mediator of the electromagnetic interaction, it is massless and carries no electrical charge.

$\mathbf{W}^{\pm}$ and $\mathbf{Z}^0$ are the three massive gauge bosons responsible for the weak interaction. They get mass through the mechanism of spontaneous symmetry breaking [9, 10].

The matter content instead consists of half-integer spin (1/2) fields which can be further sorted into two categories:

Quarks (q) exist in six flavors organized in three generations or families. Each family consists of a *Up* component of weak isospin $I = +1/2$ and a electric charge $Q = 2e/3$ and a *Down* component with $I = -1/2$ and $Q = -e/3$, where e is the electron charge. Moreover quarks are color-charged. Up quarks are up (u), charm (c) and top (t) quarks, while Down quarks are down (d), strange (s) and bottom (b)

$$\begin{pmatrix} u \\ d \end{pmatrix}, \begin{pmatrix} c \\ s \end{pmatrix}, \begin{pmatrix} t \\ b \end{pmatrix}. \tag{1.5}$$

Leptons (ℓ) are six and also organized in three generations of different flavors. Each generation consists of one neutrino ($\nu_e,\ \nu_\mu,\ \nu_\tau$) paired with the corresponding charged lepton ($Q = e$). As quarks, leptons have isospin $I = \pm 1/2$

$$\begin{pmatrix} \nu_e \\ e \end{pmatrix}, \begin{pmatrix} \nu_\mu \\ \mu \end{pmatrix}, \begin{pmatrix} \nu_\tau \\ \tau \end{pmatrix}. \tag{1.6}$$

All these particles are described as massless in the SM of particles contrary to experimental evidence of massive bosons and leptons. Higgs [9], Brout and Englert [10] in 1964 provided a model, today known as Higgs-Brout-Englert mechanism, to solve the mass problem for fermions and bosons and preserve the gauge invariance of the theory.

This model introduces a new boson responsible for the spontaneous symmetry breaking:

Higgs boson (H^0) is a massive complex scalar field in form of isospin doublet. It is a neutral and colorless particle and gives mass to all SM particles.

A summary of the main properties (generation, mass, quantum numbers) of all SM particles is shown in Fig. 1.1. The numbers in the green, red and orange boxes next to the particle symbols indicate the corresponding charges under the gauge group: electric charge, color and isospin respectively.

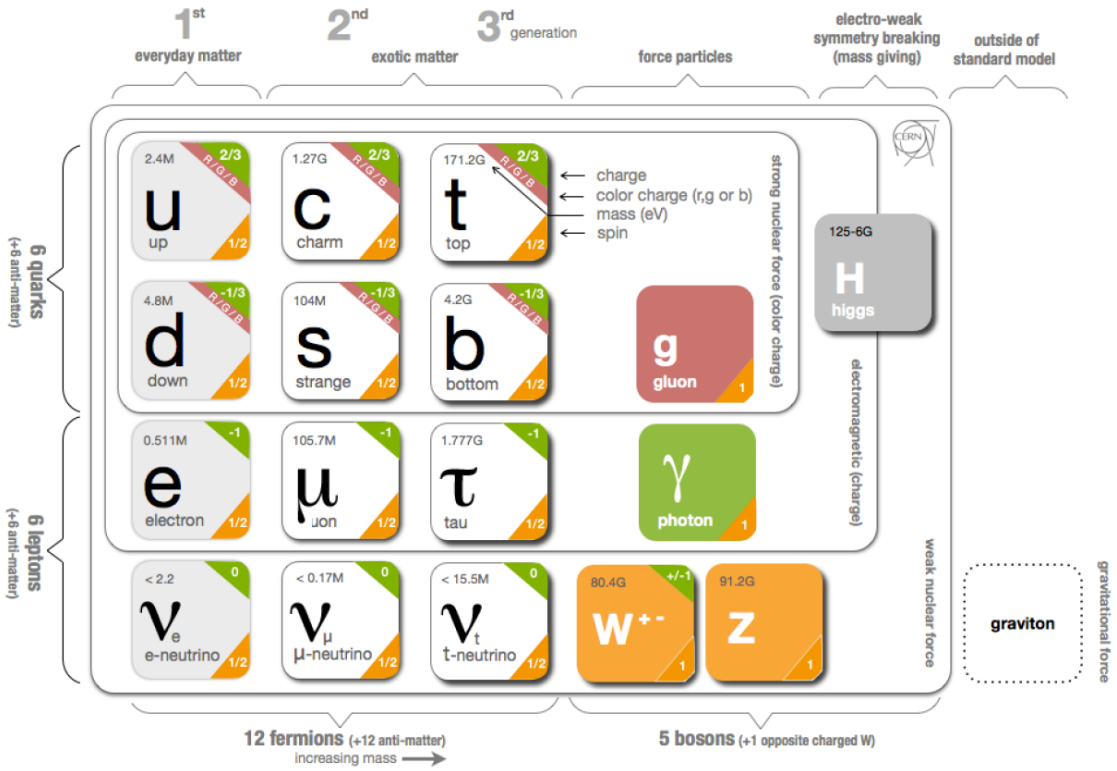

Figure 1.1: An overview of the Standard Model with the main particles and interaction mediators properties. Figure from [11].

The electroweak theory proposed by Weinberg [12] and Salam [13], was developed with the purpose to describe the QED and weak interactions as different manifestations of the same force. The $SU(2)_L \otimes U(1)_Y$ group, which describes a chiral theory, has four generators $\vec{\tau} = \frac{1}{2}\vec{\sigma}$, where $\vec{\sigma}$ are the Pauli's matrices, plus a hypercharge generator Y. Elementary particles are arranged in isospin doublets for left-handed fields and isospin singlets for right-handed fields. The field of the fermion ψ can be indeed described in

term of chiral projector P_L and P_R for negative (left) and positive (right) chirality as:

$$\psi = \psi_L + \psi_R = P_L\psi + P_R\psi = \frac{1-\gamma_5}{2}\psi + \frac{1+\gamma_5}{2}\psi. \tag{1.7}$$

In the SM with massless neutrinos, the neutrino is the only left-handed field which does not have a corresponding right-handed isospin singlet, since such singlet would not carry any charge and would not undergo any interaction. For this reason, the SM neutrinos in the lepton doublets are also called active neutrinos. They are electrically neutral and colorless fermions, hence they do not interact neither electromagnetically nor strongly but can interact only via the weak interaction. As shown in Fig. 1.2 two type of weak interactions exist: charged current (CC) and neutral current (NC) interactions. In a CC process, a ν_α ($\overline{\nu}_\alpha$) is coupled with the associated lepton $\alpha^{-(+)}$ by exchanging a $W^{-(+)}$ boson. In a NC process, the outgoing lepton is also a (anti-)neutrino.

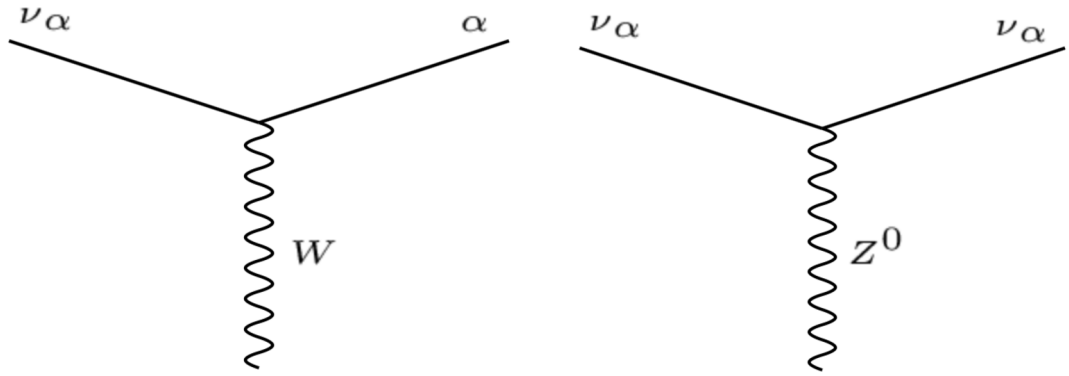

Figure 1.2: Charged Current (CC) and Neutral Current (NC) neutrino interactions on the left and on the right respectively.

As shown in Fig. 1.1 there are three families ($\nu_e,\ \nu_\mu,\ \nu_\tau$) of weakly interacting neutrinos (left-handed), their number was experimentally measured by the LEP experiments at CERN measuring the width of the decay $Z^0 \to \nu_\alpha\bar{\nu}_\alpha$. The measurement found that the number of light active neutrinos is $N_\nu = 2.984 \pm 0.008$ [14]. If more light neutrinos exist, they must not have any gauge interaction within the SM, being therefore singlets of the complete SM gauge group. Whether such neutrinos, known as sterile neutrinos, exist or not is one of the open questions in neutrino physics.
Since the left-handed and right-handed components of the fermion fields change in a different way under local transformations of the gauge group, a mass term of the form:

$$\mathcal{L} = m\bar{\psi}\psi = m(\bar{\psi}_L\psi_R + \bar{\psi}_R\psi_L) \tag{1.8}$$

is forbidden by gauge symmetry. The mass of fermions is provided, as a result of the Higgs mechanism, coupling right-handed singlets with left-handed doublets through

Yukawa couplings of the fermion fields with the Higgs doublet. This term must be invariant under $SU(2)_L \otimes U(1)_Y$:

$$\begin{aligned}\mathcal{L}_{Yukawa} &= \mathcal{L}_{quarks} + \mathcal{L}_{leptons} = \Lambda_{ij}\bar{\psi}_{Li}\phi\psi_{Rj} + h.c. \\ &= \Lambda^d_{ij}\bar{Q}_{Li}\phi d_{Rj} + \Lambda^u_{ij}\bar{Q}_{Li}\tilde{\phi}u_{Rj} + \Lambda^l_{ij}\bar{L}_L i\phi l_{Rj} + h.c.,\end{aligned} \tag{1.9}$$

where ψ is the fermion field, ϕ is the scalar Higgs doublet and $\tilde{\phi} = i\tau_2\phi^*$ is a given direction, Λ is a complex matrix of Yukawa couplings and L_L, Q_L, l_R, q_R are the leptonic and quark doublets and singlets respectively. After spontaneous symmetry breaking, the Yukawa coupling leads to a mass term of the form:

$$m_l\bar{l}_L l_R + m_q q_L \bar{q}_R, \tag{1.10}$$

the fermion mass then is given by:

$$m^f_{ij} = \Lambda^f_{ij}\frac{v}{\sqrt{2}}, \tag{1.11}$$

where v is the vacuum expectation value of the Higgs field. The masses of charged leptons and quarks are not predicted by the SM theory, therefore they must be determined by experimental measurements. Since in the neutrino case the right-handed singlets are not predicted, a mass term from the Yukawa interactions cannot be introduced for them within this theory. In the SM they are postulated to be Weyl fermions. In Hermann Weyl's theory [15], neutrinos are left-handed particles while their anti-particles, the anti-neutrinos, are right-handed. Therefore, neutrinos in the SM are purely left-handed and massless particles, anti-neutrinos are distinct from neutrinos and right-handed. Experimental results are in clear discrepancy with the hypothesis of massless neutrinos. Even though, experiments have given only an upper limit of neutrino masses so far and no direct measurements exist yet, the observation of the phenomenon of neutrino oscillations, by different experiments, is a proof that neutrinos must have non-zero masses. Hence, the SM as it is has to be extended, in order to include neutrino masses.

1.3 Theory of neutrino oscillations

Neutrino oscillations were postulated for the first time in 1950 by Bruno Pontecorvo [16] in analogy with neutral meson oscillation $K^0 \rightarrow \bar{K}^0$. Initially, just one family of active neutrino (ν_e) was known so he suggested oscillations between neutrino and anti-neutrino. Only in 1962 Maki, Nakagawa and Sakata [17] built a model describing mixing between neutrinos of different flavors. The essential principle of neutrino oscillations assumes that the neutrino flavor eigenstates are not identical to the their mass eigenstates. This implies massive neutrinos that can change their flavor during propagation. Therefore in neutrino oscillations the flavor eigenstate $|\nu_\alpha>$ is defined as

a superposition of the mass eigenstates $|\nu_i>$ through a unitary mixing matrix $\mathcal{U}$:

$$|\nu_\alpha >= \sum_{k=1}^{3} U^*_{\alpha,k} |\nu_k >, \tag{1.12}$$

where $\alpha = e, \mu, \tau$ while $k = 1, 2, 3$ in a three neutrino mixing scenario. The matrix $\mathcal{U}$ is also known as the Pontecorvo-Maki-Nakagawa-Sakata (PMNS) mixing matrix. In a three neutrino mixing scenario it can be parametrized in terms of three mixing angle $(\theta_{12}, \theta_{23}, \theta_{13})$ and a CP-violation phase δ_{CP}. Using a terse notation in which $c_{ij} = \cos\theta_{ij}$ and $s_{ij} = \sin\theta_{ij}$ the PMNS matrix is:

$$\begin{aligned} \mathcal{U}_{PMNS} &= \begin{pmatrix} U_{e1} & U_{e2} & U_{e3} \\ U_{\mu 1} & U_{\mu 2} & U_{\mu 3} \\ U_{\tau 1} & U_{\tau 2} & U_{\tau 3} \end{pmatrix} \\ &= \begin{pmatrix} 1 & 0 & 0 \\ 0 & c_{23} & s_{23} \\ 0 & -s_{23} & c_{23} \end{pmatrix} \begin{pmatrix} c_{13} & 0 & s_{13}e^{-i\delta_{CP}} \\ 0 & 1 & 0 \\ -s_{13}e^{+i\delta_{CP}} & 0 & c_{13} \end{pmatrix} \begin{pmatrix} c_{12} & s_{12} & 0 \\ -s_{12} & c_{12} & 0 \\ 0 & 0 & 1 \end{pmatrix}. \end{aligned} \tag{1.13}$$

The δ_{CP} phase, also called Dirac phase, has an impact on oscillations leading to a leptonic CP-violation if found to be non-zero. From the Schroedinger equation for time evolution, if a neutrino of a given flavor ν_α is a superposition of its mass eigenstates, its evolution with time can be expressed as:

$$|\nu_\alpha(t) >= \sum_{k=i}^{3} U^*_{\alpha k}\ e^{-iE_k t} |\nu_k >, \tag{1.14}$$

where $E_k = \sqrt{p^2 + m_k^2}$ is the neutrino relativistic energy. Similarly, mass eigenstates can be described, by inverting Eq. 1.12, as a superposition of flavor eigenstates:

$$|\nu_k >= \sum_{\alpha} U_{\alpha k} |\nu_\alpha > . \tag{1.15}$$

Substituting Eq. 1.15 into 1.14 it is clear that the time evolved state $|\nu_\alpha(t) >$ can be expressed in terms of all flavor eigenstates:

$$|\nu_\alpha(t) >= \sum_{\beta} \sum_{k=i}^{3} U^*_{\alpha k}\ e^{-iE_k t} U_{\beta k} |\nu_\beta > . \tag{1.16}$$

Therefore the probability of a transition to a flavor β for a neutrino created with flavor α and detected at time t after propagation with flavor β ($P(\nu_\alpha \to \nu_\beta)$), is given by:

$$P(\nu_\alpha \to \nu_\beta) = | < \nu_\beta | \nu_\alpha(t) > |^2 = \sum_{k,j} U^*_{\alpha k} U_{\beta k} U_{\alpha j} U^*_{\beta j}\ e^{-i(E_k - E_j)t}. \tag{1.17}$$

If the detected flavor is equal to the flavor at the production, $\beta = \alpha$, the transition probability is commonly called survival probability ($P(\nu_\alpha \to \nu_\alpha)$). The ultrarelativistic approximation $E \approx p$ leads to:

$$E_k = E + \frac{m_k^2}{2E}, \tag{1.18}$$

in the same limit the distance L at which the neutrinos travel will be approximated as $t \approx L$ and Eq. 1.17 can be rewritten as:

$$P(\nu_\alpha \to \nu_\beta) = \sum_{k,j} U^*_{\alpha k} U_{\beta k} U_{\alpha j} U^*_{\beta j} \; e^{-i\frac{\Delta {m^2}_{kj} L}{2E}}, \tag{1.19}$$

where Δm^2_{kj} is the mass squared difference of the neutrino mass eigenstates. Flavor transformation is essentially a quantum mechanical phenomenon requiring the existence of non-zero and distinct neutrino masses and a non trivial mixing matrix $\mathcal{U}$. It is determined by the phase:

$$\phi_{kj} = -\frac{\Delta m^2_{kj} L}{2E}. \tag{1.20}$$

This phase depends on a physical constant Δm^2_{kj} but also on the parameter L/E, the source-detector distance over the neutrino energy. The latter parameter can be therefore tuned, in an oscillation experiment, to maximize/minimize the transition probability. The amplitude of the oscillation instead, is determined by the elements of the mixing matrix $\mathcal{U}$ in Eq. 1.19 which are constants of nature. In a more general case it is also possible to write Eq. 1.19 using the properties of complex exponential and the unitary of the mixing matrix. In this case the vacuum oscillation probability for a neutrino α being detected as β is given by:

$$\begin{aligned} P(\overset{(-)}{\nu}_\alpha \to \overset{(-)}{\nu}_\beta) = \delta_{\alpha\beta} &- 4 \sum_{k>j} Re(U^*_{\alpha k} U_{\beta k} U_{\alpha j} U^*_{\beta j}) \sin^2\left(\frac{\Delta m^2_{kj} L}{4E}\right) \\ &\pm 2 \sum_{k>j} Im(U^*_{\alpha k} U_{\beta k} U_{\alpha j} U^*_{\beta j}) \sin^2\left(\frac{\Delta m^2_{kj} L}{2E}\right), \end{aligned} \tag{1.21}$$

the $\pm$ sign distinguish neutrino (+) from anti-neutrino (-) oscillations. The imaginary part corresponds to the CP-violating term. Indeed, for anti-neutrinos the complex conjugate ($\mathcal{U}^*$) of the mixing matrix is used. Neutrino and anti-neutrino then, follow the same physical process if and only if the mixing matrix is real $\mathcal{U} = \mathrm{U}*$ leading to a conservation of the CP symmetry ($\delta_{CP} = 0, \pi$). In the most general case, neutrino oscillations from flavor μ to e are described by the formula:

$$\begin{aligned} P(\nu_\mu \to \nu_e) = {} & 4\, c^2_{13}\, s^2_{13}\, s^2_{23} \sin\phi_{31} + 8\, c^2_{13}\, s_{12}\, s_{13}\, s_{23}(c_{12}\, c_{23} \sin\delta - s_{12}\, s_{13}\, s_{23}) \cos\phi_{32} \sin\phi_{31} \sin\phi_{21} \\ & - 8\, c^2_{13}\, c_{12}\, c_{23}\, s_{12}\, s_{13}\, s_{23} \sin\delta \sin\phi_{32} \text{`} \sin\phi_{31} \sin\phi_{21} \\ & + 4\, s^2_{12}\, c^2_{13}(c^2_{12}\, c^2_{23} + s^2_{12}\, s^2_{23}\, s^2_{13} - 2\, c_{12}\, c_{23}\, s_{12}\, s_{23}\, s_{13} \cos\delta) \sin^2\phi_{21}. \end{aligned} \tag{1.22}$$

As example it is useful to study the case of two neutrinos. In this case just one mixing angle θ and no complex phase exists, the mixing matrix $\mathcal{U}$ and the probability of changing flavor can be written as:

$$\mathcal{U} = \begin{pmatrix} \cos\theta & \sin\theta \\ -\sin\theta & \cos\theta \end{pmatrix} \tag{1.23}$$

$$\begin{aligned} P(\nu_\alpha \to \nu_\beta) &= \left| U_{\alpha 1} U_{\beta 1}\, e^{-i\frac{m_1^2 L}{2E}} + U_{\alpha 2} U_{\beta 2}\, e^{-i\frac{m_2^2 L}{2E}} \right|^2 \\ &= \left| -\cos\theta\, \sin\theta\, e^{-i\frac{m_1^2 L}{2E}} + \cos\theta\, \sin\theta\, e^{-i\frac{m_2^2 L}{2E}} \right|^2 \\ &= 2\cos^2\theta\, \sin^2\theta - \cos^2\theta\, \sin^2\theta\, e^{-i\frac{(m_1^2 - m_2^2)L}{2E}} + \cos^2\theta\, \sin^2\theta\, e^{-i\frac{(m_1^2 - m_2^2)L}{2E}} \\ &= \frac{1}{2}\sin^2 2\theta \left(1 - \cos\left(\frac{(m_1^2 - m_2^2)L}{2E} \right) \right) \\ &= \sin^2 2\theta\, \sin^2\left(\frac{\Delta m_{21}^2 L}{4E} \right) \\ &= \sin^2 2\theta\, \sin^2\left(\frac{1.27 \Delta m_{21}^2 [\mathrm{eV}^2] L[\mathrm{km}]}{4E[\mathrm{GeV}]} \right) \end{aligned} \tag{1.24}$$

while the survival probability is:

$$\begin{aligned} P(\nu_\alpha \to \nu_\alpha) &= 1 - P(\nu_\alpha \to \nu_\beta) \\ &= 1 - \sin^2 2\theta\, \sin^2\left(\frac{1.27 \Delta m_{21}^2 [\mathrm{eV}^2] L[\mathrm{km}]}{4E[\mathrm{GeV}]} \right). \end{aligned} \tag{1.25}$$

Equations 1.24 and 1.25 show that, including only the two families ($\alpha = \mu$ and $\beta = e$), a pure source ν_μ with a given energy E at a certain distance L will be composed of a mixture of ν_μ and ν_e because of neutrino oscillations. Moreover the amount of the mixing, for fixed L and beam energy E, is given by two parameters: the mass squared difference between the two neutrinos Δm^2 and the mixing angle θ.

1.3.1 Massive Neutrinos

The compelling experimental evidence for neutrino oscillations imply that neutrinos are massive. However, neutrino oscillation experiments cannot probe the absolute values of the neutrino masses, since they are only sensitive to the mass squared difference between them. Actually, the three neutrino mixing can be factorized in two neutrino mixing approximation under the assumption that the differences in mass between the two neutrino pairs differ by orders of magnitude. Experimental results confirm this assumption $|\Delta m_{32}^2| \approx |\Delta m_{31}^2| \gg |\Delta m_{21}^2|$, in this case it is usual, for historical reason,

to talk about *atmospheric* and *solar* neutrinos. A description of the two experimental cases will be give in Sec. 1.4.2 and 1.4.1 respectively.
Although experimentally the ν_e survival probability through matter shows a positive mass-splitting Δm^2_{21}, on the other hand currently the ν_μ survival probability in vacuum determines only the magnitude of Δm^2_{32} but not its sign. The difficulty in determining the sign is essentially caused by the uncertainties on Δm^2_{32} and Δm^2_{31} being larger than the size of Δm^2_{21}, and therefore the sign has a negligible effect on the oscillation probabilities compared to current experimental uncertainties. Therefore the mass ordering or hierarchy in neutrino masses is still unknown. According to the sign of $\Delta m^2_{32} = m^2_3 - m^2_2$ there are two possibilities:

$$\begin{aligned} \text{Normal Hierarchy} &: m_3 > m_2 > m_1 \ (\Delta m^2_{32} > 0) \\ \text{Inverted Hierarchy} &: m_2 > m_1 > m_3 \ (\Delta m^2_{32} < 0) \end{aligned} \tag{1.26}$$

Figure 1.3 illustrates the normal (left) and the inverted (right) hierarchies.

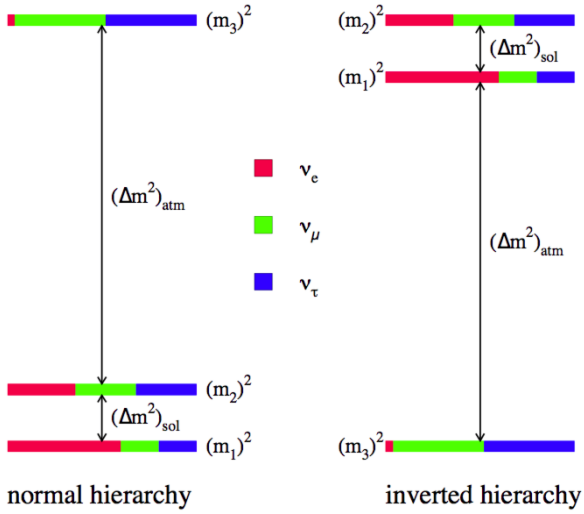

Figure 1.3: Drawing of the normal and inverted neutrino mass hierarchies, showing the fractions of flavor eigenstates content in each mass eigenstates. Figure from [18].

1.3.2 Matter effects

For the calculations in Sec. 1.3, neutrinos are propagating in vacuum, however when they travel through a medium the coherent forward scattering from electrons in matter can significantly modify their propagation. Indeed the different types of neutrinos react differently to the potential due to the matter density: while neutral current (Fig. 1.2) interactions can occur for all the neutrino flavors, electron neutrinos can also undergo charge current interactions with the electrons in the medium. As a result, the probability for changing flavor in matter can be rather different than the one in vacuum.

Wolfestein [19] first and Mikhaev-Smirnov [20] further, studied neutrino oscillations in matter by modeling the coherent forward scattering with the electrons with a potential term, for this reason this phenomenon is called MSW effect. The potential felt by ν_e is defined as:

$$V_W = \pm\sqrt{2}E_\nu G_F n_e, \tag{1.27}$$

where n_e is the local electron density, G_F the Fermi constant and the sign is opposite for neutrinos (+) and antineutrinos (−). Since V_W changes sign for antiparticles, matter effects can lead to different oscillation probabilities for neutrino and anti-neutrino for instance $P(\nu_\mu \to \nu_e) \neq P(\bar{\nu}_\mu \to \bar{\nu}_e)$ even if the mixing matrix $\mathcal{U}$ is real (no CP violation). Therefore care must be taken when comparing measurements with neutrinos and anti-neutrinos, these differences must not be misinterpreted as a CP violating signal but reflect the fact that Universe is composed of matter. Moreover this difference leads also the effective mass-splittings in matter ($\Delta\tilde{m}_{ij}$) to be slightly different from the vacuum mass-splittings (Δm^2_{ij}), hence experiments in which matter effect is not negligible allow measurements of the signs of Δm^2.
For instance given the two neutrino case (Eq. 1.23), the effective mixing angle ($\tilde{\theta}$) and mass splitting ($\Delta\tilde{m}^2$) in matter can be parametrized as:

$$\sin 2\tilde{\theta} = \frac{\Delta m^2}{\Delta\tilde{m}^2}\sin^2 2\theta \tag{1.28}$$

$$\Delta\tilde{m}^2 = \sqrt{(\Delta m^2\ \cos 2\theta\ - V_W)^2 + (\Delta m^2\ \sin\theta)^2}. \tag{1.29}$$

Then the mass eigenstates in matter do not coincide with the mass eigenstates. If $E \gg \Delta m^2 \cos 2\theta / V_W$ (*"adiabatic condition"*), matter effects dominate and vacuum oscillations are suppressed. However the maximal probability will depend on the sign of the mass splitting and is produced at the neutrino energy $E = \Delta m^2 \cos 2\theta / V_W$. Thus, in order to study the mass hierarchy, experiments with significant matter effects are necessary.
In the case of a source of muon neutrinos propagating through the Earth, the MSW effect results in a change of the oscillation probability from ν_μ to ν_e by adding a term to Eq. 1.22:

$$\begin{aligned} T_{matter} = &-8\frac{aL}{4E}\ c^2_{13}\ s^2_{13}\ s^2_{23}(1-2s^2_{13})\cos\phi_{32}\ \sin\phi_{31} \\ &+8\frac{a}{\Delta m^2_{31}}\ c^2_{13}\ s^2_{13}\ s^2_{23}(1-2s^2_{13})\sin\phi_{31}, \end{aligned} \tag{1.30}$$

where $a[\mathrm{eV}^2] = 7.56 \times 10^{-5} \times \rho[\mathrm{g/cm}^3] \times E_\nu[\mathrm{GeV}]$ is a function of the matter density and of the neutrino energy.

1.4 First observations of neutrino oscillations

During the second half of the twentieth century, as neutrinos from various sources continued to be studied, inconsistency emerged between the SM theoretical prediction

and the experimentally observed number of neutrinos. Various experiments have been performed to understand the neutrino physics which was plagued by: *The Solar Neutrino Problem* and *The Atmospheric Neutrino Anomaly*. Such effects were ultimately explained by the theory of neutrino oscillation.

1.4.1 Solar Neutrinos

Solar neutrinos are created in the core of the Sun via nuclear fusion reactions. Their study provides valuable information about the reactions that occur in the Sun and about its structure. In the 60's the Standard Solar Model (SSM) was used to predict the neutrino flux from all nuclear fusion processes in the Sun. Figure 1.4 shows nuclear reactions and neutrino energy spectrum predicted by the SSM. However, solar neutrino experiments observed significantly lower ν_e fluxes than expected.

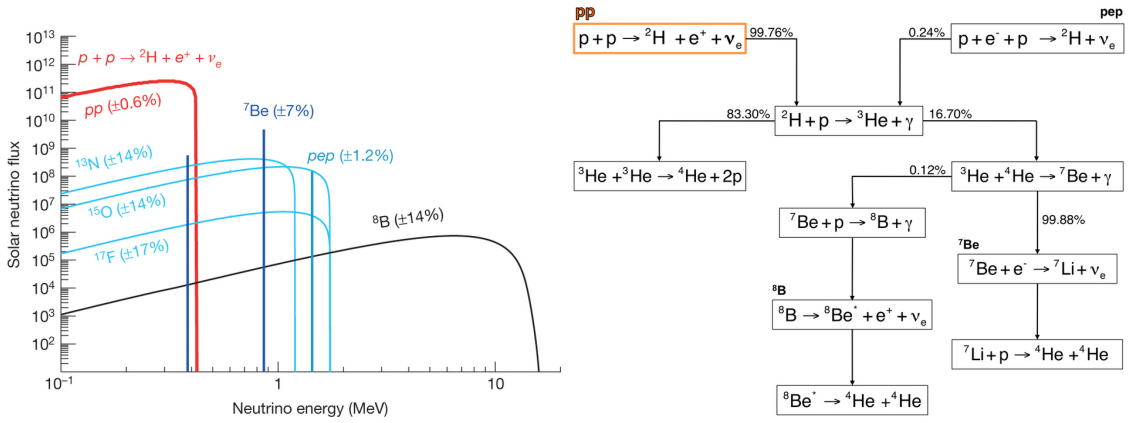

Figure 1.4: Neutrino energy spectrum (left) according to nuclear reactions (right) as predicted by the SSM. Figures from [21].

This motivated, in 1965-1967, the Homestake experiment: the first solar neutrino deep underground experiment [22]. It consisted of a steel tank containing 615 tons of tetrachloroethylene (C_2Cl_4) placed at 1478 m below the Earth surface in the Homestake Gold Mine in Lead, South Dakota. The experiment aimed at detecting ν_e coming from the Sun via inverse β-decay of ^{37}Cl turning into ^{37}Ar. In their early results, published in 1968 [23], Homestake observed a flux significantly smaller than expected, about 1/3 with respect to the prediction of the SSM. This was taken, at the time, to be indicative of an inaccuracy of the solar model. The experiment continue to run until 1994 measuring the flux of solar neutrinos with energies down to 0.814 MeV. Since then, many experiments were designed to detect, with different techniques and sensitivity to different neutrino energy regions: Gallex [24], GNO [25], Sage [26] and Borexino [27]. All those experiments observed the same deficit as measured by Homestake. Also other experiments exploiting elastic scattering (ES) $\nu_e + e^- \rightarrow \nu_e + e^-$, such as Kamiokande-II [28] and Super-Kamiokande [29], observed a deficit in the ν_e flux.

Another experiment aimed to prove this hypothesis was the Sudbury Neutrino Observatory (SNO). Placed 2 km underground in Creighton mine in Ontario, SNO used 1000 tons of ultra-pure heavy water (D_2O) able to detect not only CC interactions from ν_e, but also NC interactions on the deuterium nuclei by tagging the outgoing neutron. This means that SNO thanks to NC interactions was sensitive to all neutrino flavors. Furthermore SNO analyses, like Kamiokande-II, exploit also electron elastic scattering interactions which had higher energy thresholds for the reconstructed electrons, ranging from 5 MeV to 6 MeV, in order to distinguish signal from background. In 2002 SNO measured solar neutrino flux from both CC and NC interactions [30]:

$$\begin{aligned} \phi_{CC} = \phi_e &= 1.76 \pm 0.05\ (stat) \pm 0.09\ (syst) \times 10^6\ \frac{\nu}{\mathrm{cm^2 s}} \\ \phi_{NC} = \phi_e + \phi_\mu + \phi_\tau &= 5.09^{+0.44}_{-0.43}\ (stat)^{+0.46}_{-0.43}\ (syst) \times 10^6\ \frac{\nu}{\mathrm{cm^2 s}} \end{aligned} \tag{1.31}$$

Hence SNO was able to determine the electron and non-electron neutrino components of the solar flux proving the validity of the SSM and giving the direct evidence for neutrino oscillation phenomenon: ν_e coming from the sun arrive on Earth in a mixture of ν_e, ν_μ and ν_τ.

1.4.2 Atmospheric Neutrinos

In the early 1980s, searching for proton decay became an area of experimental interest. Forbidden by conservation of baryon number in the SM, this decay is predicted by the Grand Unified Theory (GUT) which allows the proton to decay with a very long half lifetime ($> 10^{31}$ years) [31]. Hence proton decay measurements imply large detector containing large numbers of protons heavily shielded from external background sources. Although installing the detector underground effectively reduces the background of cosmic ray muons, the atmospheric neutrinos produced by cosmic ray interacting in the atmosphere cannot be shielded. A precise knowledge of the atmospheric neutrinos background was therefore very important for proton decay measurements. Theoretical models of cosmic ray (muons) flux were studied at the time as well as the atmospheric neutrino production processes. Cosmic rays interacting with the high atmosphere produce a huge number of secondary particles, mainly pions. Those pions decay in flight via the reaction $\pi^+ \to \mu^+ + \nu_\mu$ ($\pi^- \to \mu^- + \bar{\nu}_\mu$), the produced muons again decay following the reaction $\mu^+ \to e^+ + \bar{\nu}_e + \nu_\mu$ ($\mu^- \to e^- + \nu_e + \bar{\nu}_\mu$). The typical spectrum of these neutrinos extends from hundreds of MeV up to several GeV. At lower energies, both pion and muon decays would occur in the atmosphere, leading to a ratio of $R = \frac{\nu_\mu + \bar{\nu}_\mu}{\nu_e + \bar{\nu}_e} \approx 2$. Instead as energies increase, the muon would be less and less likely to decay before reaching the Earth, resulting in fewer $\nu_e(\bar{\nu}_e)$ increasing then this ratio. Since atmospheric neutrinos can be generated in each point of the atmosphere they require a detector with good ability to measure the direction of interacting neutrinos. Indeed neutrinos can travel various distances before reaching the detector and this gives different oscillation probabilities.

Two of the proton decay experiments at the time, both water Cherenkov detectors, looked into the atmospheric neutrino background in more detail. The Irvine-Michigan-Brookhaven (IMB) experiment located in the Fairport salt mine in the United States, and the Kamioka Nucleon Decay Experiment (Kamiokande) in Japan (the predecessor of both Kamiokande-II and Super-Kamiokande). Both detectors were able to distinguish ν_μ interactions (μ-like events) from ν_e interactions (e-like events) with a technique that will be discussed in Sec. 2.7 in the context of Super-Kamiokande and T2K . They could therefore make measurements of the ratio μ-like over e-like ($R_{obs.}$) to make a comparison with the theory prediction (R_{theory}). Ultimately, the difference was quite large, IMB measured [32]

$$R_{obs}/R_{theory} = 0.54 \pm 0.05(stat.) \pm 0.11(syst.),$$

whereas Kamiokande-II measured [33]

$$R_{obs}/R_{theory} = 0.60 \pm 0.07(stat.) \pm 0.05(syst.).$$

This Atmospheric Neutrino Anomaly was clarified by Super-Kamiokande in 1998 [34]. If the atmospheric neutrinos are separated into two samples, up-going and down-going, it is possible to measure neutrino oscillations over different baselines in the same detector. Down-going neutrinos have a baseline from the production site of around $20 - 500$ km, whereas up-going neutrinos (traveling through the Earth) have a baseline from production of between 500 km and 12000 km. Assuming that cosmic rays are isotropic and that there is no ν_μ disappearance, equal fluxes are expected for the up-going and down-going neutrinos. However, the results from Super-Kamiokande showed an up-going flux (high L/E) of around half of the down-going flux, proving that the number of observed ν_μ depends on the distance between the neutrino production point in the atmosphere and the detector. Figure 1.5 shows the number of observed events as a function of the cosine of the angle between the neutrino direction and the zenith angle compared with the non-oscillated flux prediction (dashed red line). This was the first model-independent evidence for neutrino oscillations. Moreover Super-Kamiokande results provided also a strong evidence of the existence of neutrino oscillations with a different Δm^2 from the solar neutrinos.

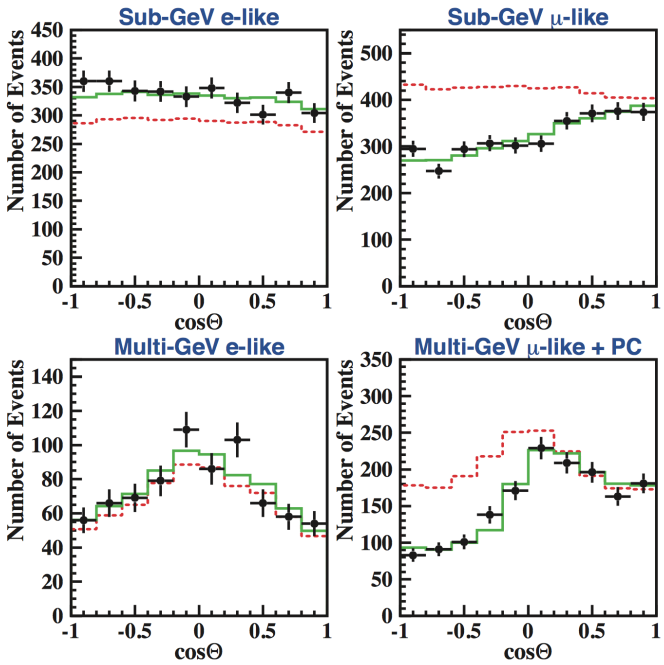

Figure 1.5: Zenith angle distributions for e-like and μ-like events with visible energy $<$ 1.33 GeV (sub-GeV) and $>$ 1.33 GeV (multi-GeV). The dashed histograms show the non-oscillated flux prediction while the solid histograms show the oscillations best fit. Figure from [35].

1.5 KamLAND and reactor Neutrinos

Nuclear reactors are a high intensity source of electron anti-neutrinos ($\bar{\nu}_e$). They are produced via β-decays of four isotopes ^{235}U, ^{238}U, ^{239}Pu and ^{241}Pu which are used to produce electric power from nuclear fission chain. Each fission chain produces about 200 MeV releasing six $\bar{\nu}_e$, thus the nuclear reactor provides about 2×10^{20} $\bar{\nu}_e$/s for each $\mathrm{GW_{th}}$.
The anti-neutrino flux is isotropic and decreases rapidly with the distance, anti-neutrinos have a typical energy of few MeV therefore only $\bar{\nu}_e$ disappearance can be investigated, since the energy is not sufficient to produce detectable muons or taus.
The Kamioka Liquid Anti-Neutrino Detector (KamLAND) was the first experiment designed to study the oscillation of $\bar{\nu}_e$ produced in nuclear reactors at very long distances [37, 38, 39]. It consisted of 1 kton of ultra-pure liquid scintillator detector located in the Kamioka mine in Japan. It was surrounded by 53 nuclear power reactors with an average baseline of 180 km between the production and the detection points. KamLAND collected data between 2002-2004 providing a strong evidence for $\bar{\nu}_e$ disappearance as a function of the L/E ratio, as shown in Fig. 1.7. The ratio between the expected (assuming no oscillations) and observed number of events after background and geo-neutrino

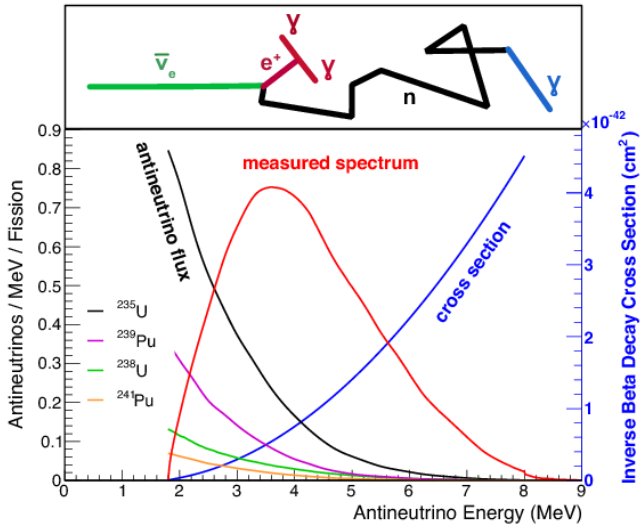

Figure 1.6: The observable $\bar{\nu}_e$ energy spectrum of the anti-neutrino flux from reactor. The contributions of four fission isotopes to the anti-neutrino flux are shown for a typical pressurized water reactor. The steps involved in the detection are schematically illustrated on the top of the plot. Figure from [36].

(neutrinos from natural radioactivity of the Earth) subtraction was:

$$\frac{N_{obs.} - N_{bkg}}{N_{No\ osc.}} = 0.611 \pm 0.085(stat.) \pm 0.041(syst.), \tag{1.32}$$

which shows a clear evidence of an event deficit due to neutrino oscillations. A three-neutrinos oscillation fit to KamLAND and global solar neutrino data, including constrains on θ_{13} from reactor and accelerator experiments (see Sec. 1.6), gives the best measurement of the solar sector parameters: mixing $\sin^2 2\theta_{12} = 0.023 \pm 0.002$ and mass splitting $\Delta m^2_{21} = 7.53 \pm 0.18 \cdot 10^{-5}$ eV [40].
Although reactor experiments are sensitive only to the $\bar{\nu}_e$ disappearance channel, many other experiments have provided more precise measurements of neutrino oscillation parameters. The study of oscillations from nuclear reactor neutrinos can provide also the cleanest measurement of the θ_{13} mixing angle. The oscillation probability $P(\bar{\nu}_e \to \bar{\nu}_e)$ for $\frac{\Delta m^2_{21} L}{E} \ll 1$ is a function only of θ_{13} and is independent from other oscillation parameters. It is described by the formula:

$$P(\bar{\nu}_e \to \bar{\nu}_e) \approx 1 - \sin^2 2\theta_{13} \sin^2 \left(\frac{1.27 \Delta m^2_{31} L}{E} \right). \tag{1.33}$$

Contemporary to KamLAND and SNO, the CHOOZ collaboration [41] produced the most stringent limit on the neutrino mixing angle θ_{13} at that time. Based in Chooz (France), it exploited anti-neutrinos provided by two pressurized water reactors with

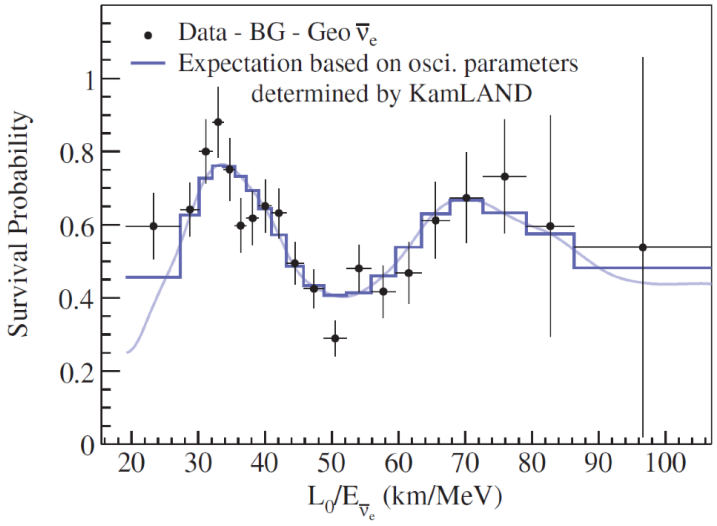

Figure 1.7: Ratio of the number of $\bar{\nu}_e$ observed at KamLAND (background and geo-neutrino contributions subtracted) as a function of L_0/E_ν, compared to the expectation in the case of no oscillations. The $L_0 = 180$ km is the effective baseline taken from a flux-weighted average across all reactors. Figure from [39].

an average energy of approximately 3 MeV. The detector was placed at a distance of roughly 1 km from the reactors. It searched for the disappearance of $\bar{\nu}_e$ at a L/E ratio similar to that in the atmospheric neutrino measurements. The upper limits measured was $\theta_{13} < 10°$ for a mass squared difference $\Delta m^2_{31} \sim 3 \cdot 10^{-3}$ eV^2. The CHOOZ experiment was later upgraded to Double-CHOOZ by adding a second detector close to the reactors in order to reduce the total uncertainty, constrain the flux and measure θ_{13}.

Recently, in addition to Double-CHOOZ, other two reactor experiments are able to measure the mixing angle θ_{13}: RENO in South Korea and Daya Bay in China. The RENO (Reactor Experiment for Neutrino Oscillations) experiment detects $\bar{\nu}_e$ from the 6 reactors of the Yonggwang nuclear power plant. It consists of two detectors: a near detector placed at 290 m of distance from the reactor which constrains the flux expected and the far detector, located at 1.4 km. Similar to RENO, Daya Bay consists of a near and a far detector complex placed around several nuclear reactors of two power plants. In 2012 both collaborations published the evidence at 5σ of non-zero θ_{13}. Figure 1.8 shows the experimental setup of the three experiments. The latest results from the three collaborations [42, 43, 44] are:

$$\begin{aligned} &\sin^2 2\theta_{13}|_{Daya\ Bay} = 0.084 \pm 0.005, \\ &\sin^2 2\theta_{13}|_{RENO} = 0.082 \pm 0.009(stat.) \pm 0.006(syst.) \\ &\sin^2 2\theta_{13}|_{Double-CHOOZ} = 0.090^{+0.032}_{-0.029}. \end{aligned} \tag{1.34}$$

However, since reactor experiments are not sensitive to any other oscillation parameters except θ_{13} an oscillation measurement in the appearance channel is needed to confirm reactor result. It is achievable with the so called *"accelerator experiments"*.

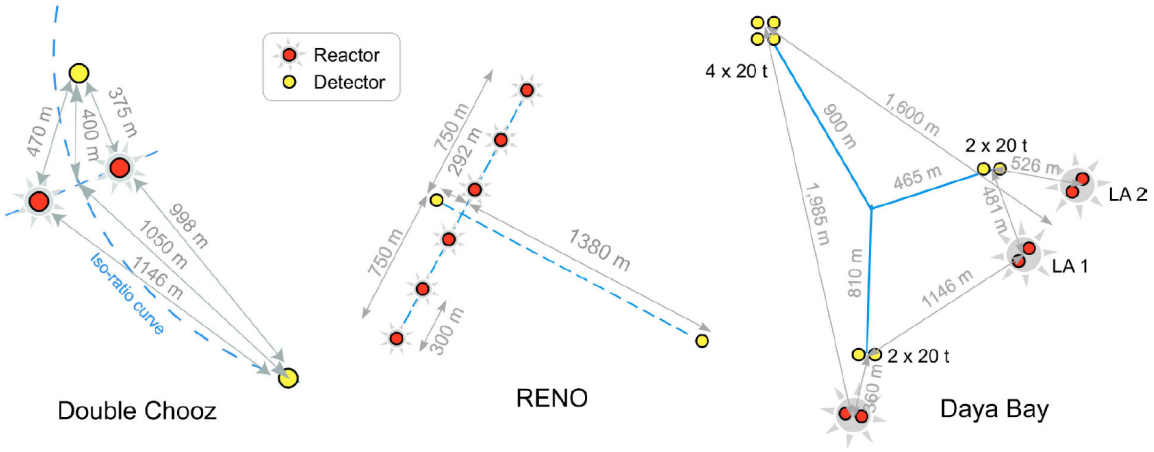

Figure 1.8: Experimental setup of Double-CHOOZ, RENO and Daya Bay experiments.

1.6 Accelerator Neutrinos

In order to access a wide range of measurements of the oscillation parameters, several experiments use accelerator complexes to produce neutrino beams. In this way it is possible to carefully choose the baseline of the experiment (the distance between the source and the detector L) and the neutrino energy spectrum (E) to maximize/minimize the oscillation probability $P(\nu_\alpha \rightarrow \nu_\beta)$. A muon neutrino beam can be generated with high purity by the decay of pions and kaons initially produced by a proton beam impinging a target. The pions and kaons decay in flight mainly producing ν_μ (or $\bar{\nu}_\mu$, according with the charge of the selected particles). Accelerator experiments can be classified by the value of the L, which determine the sensitivity with oscillations with different Δm^2, according to their baseline:

- Short Baseline (SBL) experiments: $L < 1$ km
- Long Baseline (LBL) experiments: $L > 10^2$ km.

1.6.1 Long-Baseline experiments

Long-baseline neutrino-beam experiments can perform precision measurements of muon neutrino disappearance and can study electron neutrino appearance in the ν_μ beam.

The baseline and beam energy are normally chosen such that the far detector lies at the first oscillation maximum according to:

$$\frac{L[\text{km}]}{E[GeV]} = \frac{\pi}{2}\frac{1}{1.27\Delta m^2[\text{eV}^2]}. \tag{1.35}$$

For instance for $\Delta m^2_{32} \approx 2.5 \times 10^{-3}$ eV^2, the appropriate ratio is approximately $L/E \approx 500$ km/GeV.
K2K (KEK to Kamioka), the predecessor of T2K, was the first long-baseline (LBL) neutrino accelerator experiment. Based in Japan, it used a neutrino beam produced at KEK in Tsukuba with a peak energy of ~ 1 GeV directed at Super-Kamiokande with a baseline of 250 km. Running between 1999 and 2004, K2K observed ν_μ disappearance with 4.2σ significance and constrained the atmospheric parameters Δm^2_{32} and $\sin^2 2\theta_{23}$. The two flavor fit results indicated a 90% confidence region of 1.9×10^{-3} eV^2 $< |\Delta m^2_{32}| < 3.5 \times 10^{-3}$ eV^2 and a mixing of $0.85 < \sin^2 2\theta_{23} < 1$ [45].
MINOS (Main Injector Neutrino Oscillation Search) was the LBL experiment predecessor of NOνA. Since 2005 it ran between the Neutrino Main Injector (NuMI) accelerator at Fermilab, and a far detector in the Soudan mine in northern Minnesota with a baseline of 735 km. As K2K, it constrained the atmospheric parameters through ν_μ disappearance and searched for electron neutrino appearance, which would be an indication of non-zero θ_{13}. Moreover MINOS had the possibility to run also in anti-neutrino mode measuring the same parameters by looking at the $\bar{\nu}_\mu$ disappearance. Good agreement was found between the oscillation parameters measured in ν_μ ($|\Delta m^2_{32}| = 2.41^{+0.09}_{-0.10} \times 10^{-3}$ eV^2 and $\sin^2 2\theta_{23} = 0.950^{+0.035}_{-0.036}$) and $\bar{\nu}_\mu$ ($|\Delta m^2_{32}| = 2.50^{+0.23}_{-0.25} \times 10^{-3}$ eV^2 and $\sin^2 2\theta_{23} = 0.97^{+0.03}_{-0.08}$ beams [46]. Starting from 2013 MINOS continued to run for additional 3 years with the medium energy configuration of the new NuMI beam designed for NOνA under the name MINOS+. It was more focused on the study of high energy neutrinos and search of new neutrino physics (Sterile Neutrinos and Non-Standard Interactions) as well as precise measurement of $\sin^2 2\theta_{23}$ and Δm^2_{32}.
The current generation of LBL experiments consists of T2K, Japan, and NOνA, United States. Since T2K will be described in details in the next Chapter, only NOνA will be briefly introduced here. Both use an off-axis technique (see Sec. 2.1) to create a narrow beam around the neutrino peak energy. With a baseline of 810 km and an off-axis angle of 14 mrad, NOνA has a peak beam energy of 2 GeV that leads to a value of $L/E \approx 405$ km/GeV at the flux peak (491 km/GeV for T2K with $L = 295$ km and an energy peak of 0.6 GeV at 44 mrad off-axis angle). As MINOS it uses the NuMI accelerator complex at Fermilab. The 222 ton near detector is housed in Fermilab while the 14 kton far detector is based in a site next to the Ash river in Minnesota. The near and far detectors are functionally identical, both use a carbon based liquid scintillator contained in plastic bars to track final state particles. NOνA was designed to precisely measure θ_{23} and Δm^2_{32} thanks to the ν_μ and $\overline{\nu}_\mu$ disappearance channel as well as to measure θ_{13} and constrain δ_{CP} by comparing the ν_e and $\overline{\nu}_e$ appearance channels. More-

over, due to the very long baseline that increases the size of matter effects, it is also sensitive to the mass hierarchy.

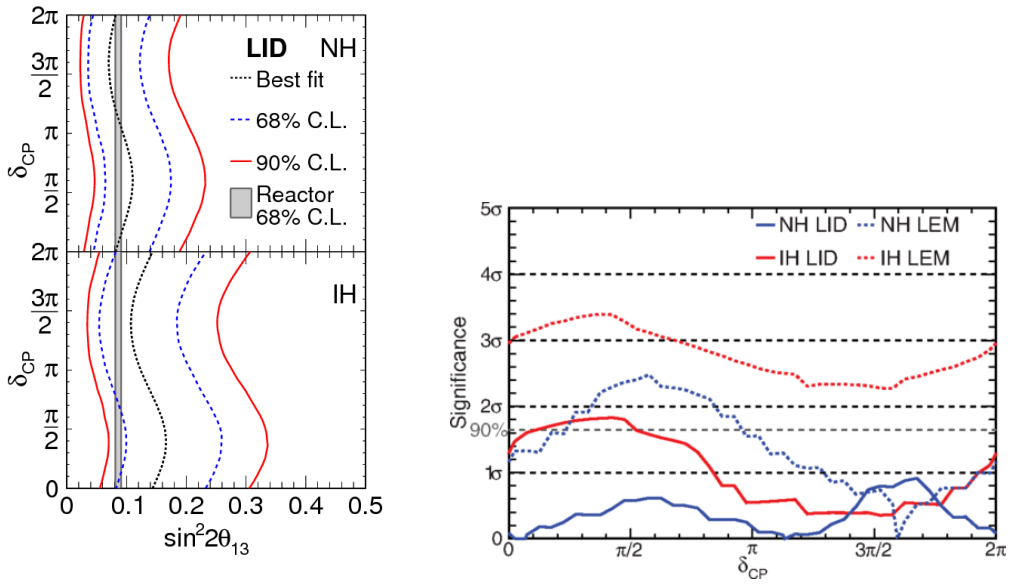

Figure 1.9: NOνA latest results. **Left:** dependency of δ_{CP} on the measurement of the mixing angle θ_{13} for the primary selection. Top (bottom) plot shows the mass ordering normal (NH) or inverted (IH). Contours show the 68% (90%) confidence regions, while the shaded regions are the θ_{13} value measured by reactor experiments. **Right:** Significance of the difference between the selected and the predicted number of events as a function of δ_{CP} and the hierarchy. The primary (secondary) selection technique is shown with solid (dotted) lines. Figures from [47].

Figure 1.9 shows, on the left, the allowed regions in the $\sin^2 2\theta_{13} - \delta_{CP}$ plane measured by NOνA. Shaded region shows $\sin^2 2\theta_{13}$ measured from reactors without any dependence from the value of δ_{CP}. Combining NOνA results with the reactor measurement, it is possible to constrain the value of the CP-violating phase. NOνA disfavored at 90% C.L. under NH hypothesis $0.25 < \delta_{CP} < 0.95$ ($0.1 < \delta_{CP} < 0.5$ for IH) [47], The precise measurement of the atmospheric parameters in the ν_μ disappearance channel is shown in Fig. 2.3, where NOνA [48] results are compared with accelerator results from MINOS [46] and T2K. The best fit, assuming NH, gives a value of $\Delta m^2_{32} = 2.67 \pm 0.11 \times 10^{-3}$ eV^2 and two statistically degenerate values at the 68% *C.L.* for $\sin^2\theta_{23} = 0.404^{+0.030}_{-0.022}$ or $\sin^2\theta_{23} = 0.624^{+0.022}_{-0.030}$. The IH fit gives $\Delta m^2_{32} = -2.72 \pm 0.11 \times 10^{-3}$ eV^2 and $\sin^2\theta_{23} = 0.398^{+0.030}_{-0.022}$ or $\sin^2\theta_{23} = 0.618^{+0.022}_{-0.030}$. T2K results will be discussed in Chapter 2.

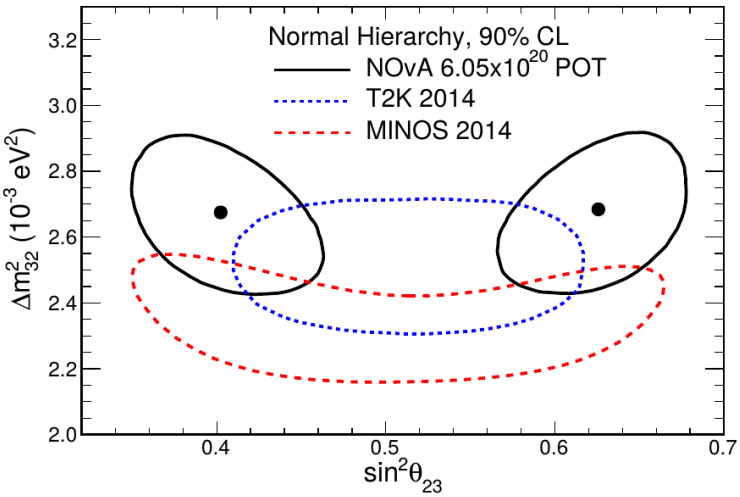

Figure 1.10: Best fit (black dots) and 90% confidence regions (solid black curves) of $\sin^2\theta_{23}$ and $|\Delta m^2_{32}|$ assuming NH. The dashed curves show the comparison with T2K, MINOS. Figure from [48].

1.7 The current knowledge of neutrino oscillation parameters

As previously illustrated, in a three active neutrinos scenario, oscillations can be described using six parameters: three mixing angles θ_{12}, θ_{13}, θ_{23}, two mass squared differences Δm^2_{21}, Δm^2_{32} and one complex phase δ_{CP}. Currently a large number of measurements of these parameters exists thanks to atmospheric, solar, reactor and accelerator neutrino experiments. The atmospheric (sector 23) and solar (sector 12) parameters have been precisely measured by the Super-Kamiokande, SNO, KamLAND, K2K, MINOS, T2K and NOνA experiments whereas reactor experiments have placed extremely tight constrains on the mixing angle θ_{13}. The current world-best results, as determined by the 2016 Particle Data Group [49], are summarized in Table 1.1. The value of $\Delta m^2 = m^2_3 - (m^2_2 + m^2_1)/2$ is used to define the neutrino hierarchy, thus Δm^2 greater (lower) than 0 corresponds to the normal (inverted) hierarchy.
Still unknown are the sign of the larger mass splitting Δm^2_{32}, the octant of the maximal mixing angle θ_{23} and the value of the CP violating phase δ_{CP}. In the next Section a quick overview about the future of the long-baseline neutrino accelerator experiments and their sensitivity to the unknown parameters is given.

Parameter	Normal (NH)	Inverted (IH)
$\sin^2\theta_{12}$	$0.297^{+0.019}_{-0.016}$	same
$\sin^2\theta_{23}$	$0.437^{+0.060}_{-0.019}$	$0.569^{+0.023}_{-0.062}$
$\sin^2\theta_{13}$	$0.0214^{+0.0011}_{-0.0010}$	$0.0218^{+0.0010}_{-0.0011}$
Δm^2_{21} $[10^{-5}$ eV$^2]$	$7.37^{+0.20}_{-0.15}$	same
Δm^2 $[10^{-3}$ eV$^2]$	$2.50^{+0.05}_{-0.04}$	$2.46^{+0.05}_{-0.04}$
δ_{CP}/π	$1.35^{+0.21}_{-0.14}$	$1.32^{+0.22}_{-0.16}$

Table 1.1: Best fit value within 1σ range of the neutrino oscillation parameters for both normal and inverted hierarchy.

1.8 Future long-baseline neutrino accelerator experiments

In the last two decades much has been learnt about neutrino oscillations, however in the future a new generation of LBL experiments is needed to measure the unknown parameters. For this reason a number of experiments has been proposed to be able to determine the mass hierarchy and observe CP-violation as well as to constrain more and more precisely the other parameters. The most promising projects are: Hyper-Kamiokande and DUNE.

Hyper-Kamiokande (Hyper-K) [50] is basically a larger version of Super-Kamiokande, it consists of 260 kton water Cherenkov detector placed in a hall beside to the current Super-Kamiokande site. Moreover, as part of the T2HK project an upgrade of the J-PARC neutrino beam power up to 1.3 MW is planned and the construction of a new near detector complex is envisaged. The same baseline and off-axis angle of T2K would be used, providing very high-statistics measurements at the first oscillation maximum.

DUNE (Deep Underground Neutrino Experiment) is a proposed neutrino oscillation experiment which would be based in the USA [51]. DUNE will utilize a wide-band neutrino beam provided at Fermilab, over an extremely long baseline ($\sim$ 1300 km), which would allow measurements also at the second oscillation maximum avoiding degeneracies between mass ordering and δ_{CP} measurements. The strength of the matter effects depends on the baseline length, being very small at T2K and T2HK ($\sim$ 300 km) and sizeable at NOνA ($\sim$ 800 km) and in DUNE ($\sim$ 1300 km). It is designed using several large-scale ($\sim$ 10 kton) Liquid Argon Time Projection Chambers as far detectors. Various projects, such as WA105 [52] and Proto-DUNE [53] at CERN, are prototyping such technology working on the R&D.

Chapter 2

The T2K experiment

The T2K (Tokai-to-Kamioka) experiment is a long baseline (LBL) neutrino oscillation experiment based in Japan [54]. It uses an high purity $\nu_\mu(\bar{\nu}_\mu)$ (anti-)neutrino beam produced at J-PARC (Japan Proton Accelerator Research Complex) in Tokai-mura (Ibaraki prefecture) to study the electron (anti-)neutrinos appearance and the muon (anti-)neutrinos disappearance. Neutrinos from the beam are detected first in a near detector complex, placed at 280 m from the production point and, afterwards a travel of 295 km through the Earth, to the Super-Kamiokande (SK) water Cherenkov far detector in mount Kamioka (Gifu prefecture). Oscillation parameters are evaluated by comparing the neutrino interaction rates observed at the near and far detectors.

Figure 2.1: The map of Japan shows a schematic view of the T2K experiment. The neutrino beam produced at J-PARC travels 295 km to the far detector SK.

The main physics goals of T2K, highlighted in the original proposal [55, 56], were:

1. discovery of electron neutrinos appearance, $\nu_\mu \to \nu_e$ oscillation channel, probing the non-zero value of the mixing angle $\theta_{13} \neq 0$;

2. precision measurements of the muon neutrino disappearance parameters ($\nu_\mu \rightarrow \nu_\mu$) down to $\delta(\Delta m^2_{23}) \sim 10^{-4}$ eV^2 and $\delta(\sin^2 2\theta_{23})$ at 1% level;

3. the search for sterile neutrinos components in the ν_μ disappearance channel.

T2K started its first neutrino physics run in January 2010 giving the first hint on $\theta_{13} \neq 0$ thanks to a direct evidence of electron neutrino appearance [57]. The non-zero value of θ_{13} was then constrained by the $\overline{\nu}_e$ disappearance in reactor experiments [58, 59, 60] in 2012. Finally in 2013 the T2K collaboration observed electron neutrino appearance ($\nu_\mu \rightarrow \nu_e$) with a significance of 7.3σ [61] with just 6.63×10^{20} of accumulated Protons on Target (POTs) which corresponds to $\sim 8\%$ of the total approved data.
Thanks to the relatively large value of $\theta_{13} \sim 9^\circ$, the primary goal of the collaboration has been achieved with such limited statistics. The T2K collaboration has therefore updated the physics program for the following years:

1. observation of anti-electron neutrino appearance in the $\overline{\nu}_\mu \rightarrow \overline{\nu}_e$ channel;

2. measurement of the CP violation phase (δ_{CP});

3. precision measurements of the ν_μ disappearance parameters Δm^2_{23} and $\sin^2 2\theta_{23}$ even beyond the initial planned precision;

4. determination of the θ_{23} octant and contribution to the determination of the mass hierarchy.

To achieve these new goals T2K started to run in 2014 with an antineutrino beam. The J-PARC accelerator complex, described in detail in Sec. 2.2.1, allows to produce either a neutrino (ν_μ) or an antineutrino ($\overline{\nu}_\mu$) beam just inverting the polarity of the current in the focusing horns. A summary of the beam power and of the total accumulated POTs collected so far are shown in Fig. 2.2. Red and violet points represent the neutrino and antineutrino beam data respectively, split by the main T2K Run periods.
The combination of ν_μ disappearance and ν_e appearance analyses in the neutrino and antineutrino modes is sensitive to possible CP violation in the leptonic sector. In the following a summary of the T2K latest oscillation results is given, for the first time they include a multi-ring sample at Super-Kamiokande (see Sec. 2.7) in which a pion decay is tagged together with the electron neutrino candidate [62]. Both the ν_e ($\overline{\nu}_e$) appearance and ν_μ ($\overline{\nu}_\mu$) disappearance channels are fitted simultaneously based on the reconstructed neutrino energy distribution. Oscillation parameters are estimated by comparing predictions and observations at the far detector.

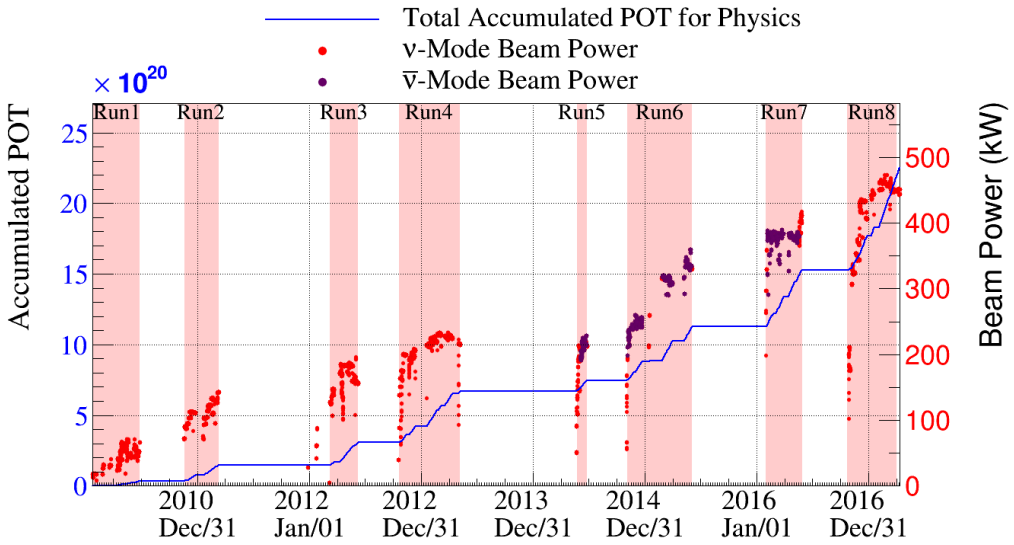

Figure 2.2: Number of accumulated protons on target and proton beam intensity at T2K. The red dots show the accumulated POTs during the neutrino mode runs while blue dots are the POTs in the antineutrino runs. The two long breaks in the data taking are related to the damages to the facilities due to Great Tohoku earthquake in 2011 and to an accident in the hadron hall in 2013.

Disappearance channel

The precise measurement of the *"23-sector"* parameters is performed in the ν_μ disappearance channel. The T2K two-dimensional contour in $\sin^2\theta_{23} - \Delta m^2_{32}$ is shown in Fig. 2.3 on the left in the different mass hierarchy scenarios. The best T2K fitted value is shown by a star and are:

$$\begin{aligned} \Delta m^2_{32} &= 2.545^{+0.081}_{-0.084} \times 10^{-3} \text{ eV (NH)} \\ &= 2.510^{+0.081}_{-0.083} \times 10^{-3} \text{ eV (IH)} \\ \sin^2\theta_{23} &= 0.55^{+0.05}_{-0.09} \text{ (NH)} \\ &= 0.55^{+0.05}_{-0.08} \text{ (IH)} \end{aligned} \tag{2.1}$$

Figure 2.3 shows also the world-leading contours comparison between accelerator results from T2K, MINOS [46] and NOνA [48] and the atmospheric results from SK [63] and IceCube [64] assuming the normal hierarchy only.

Appearance channel

While the reactor based measurement of $\sin^2\theta_{13}$ is independent form other oscillation parameters, in T2K and other accelerators the measurement is highly correlated to δ_{CP}. Although, currently, there is no measurements of the CP phase, T2K can give some hints

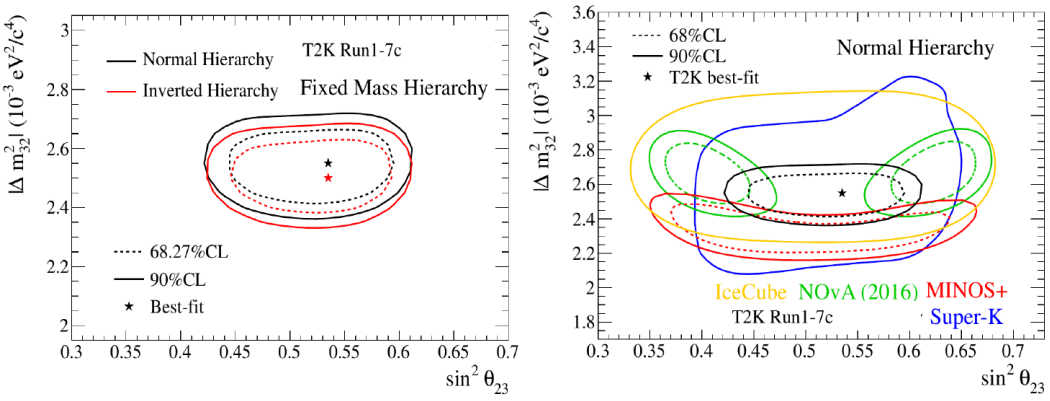

Figure 2.3: **Left:** the 68% (90%) confidence regions for the $\sin^2\theta_{23} - |\Delta m^2_{32}|$ plane. Both normal (black line) and inverted (red line) hierarchies are shown. **Right:** comparison between world-leading measurement from T2K, NOνA, MINOS+, SK and IceCube. Figure from [62].

on its value. A combined fit to both muon (anti-)neutrino disappearance and electron (anti-)neutrino appearance, using a Gaussian constraint from reactor measurement (the "reactor constraint"), gives a 68% and 90% credible intervals for the δ_{CP} as shown in Fig. 2.4. The confidence regions in the $\sin^2\theta_{13} - \delta_{CP}$ plane is shown as a function of the mass hierarchy without applying the reactor constraint. The best fit results for $\sin^2\theta_{13}$ (shown by the star) are in good agreement with the reactor measurement giving a δ_{CP} close to the maximal CP violation ($-\pi/2$). For NH the best-fit is $\delta_{CP} = -1.791$, while it is $\delta_{CP} = -1.414$ under IH. Therefore T2K excludes CP conservation at 90% C.L. ($\delta_{CP} = 0, \pi$) allowing at 90% C.L.:

$$\begin{aligned} \delta_{CP} &\in [-2.95, -0.44] \text{ (NH)} \\ \delta_{CP} &\in [-1.47, -1.27] \text{ (IH)} \end{aligned} \tag{2.2}$$

2.1 The off-axis method

T2K is the first experiment that uses an off-axis beam, originally introduced in Ref. [65]. The main idea is to produce a neutrino beam, via two bodies decay of charged pions, which is not in the exact direction of the detectors but is slightly misaligned (by few degrees) with respect to them. The off-axis technique has the advantage to produce a narrower neutrino energy spectrum with respect to the traditional on-axis one. Moreover the beam, according with the chosen off-axis angle, can be centered at the interesting energy region corresponding to the maximum of oscillation probability. In order to better understand the mechanism, let consider the ideal case where a pure π^+ beam is produced by impinging a proton beam against a graphite target [66]. The pions decay following the reaction $\pi^+ \to \mu^+ + \nu_\mu$. According to the two body decays

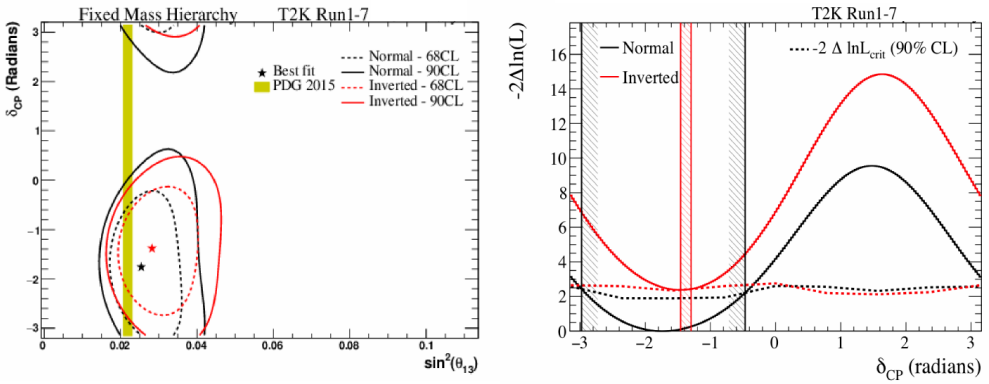

Figure 2.4: **Left:** The 68%, solid line, (90% dashed line) $-2\Delta\ln\mathcal{L}$ confidence regions in the $\sin^2\theta_{13}-\delta_{CP}$ plane. Both normal (black solid line) and inverted (black dashed line) hierarchies are shown. The shaded region represents the reactor measurement for θ_{13}, constraint which is not applied. **Right:** Measured $-2\Delta\ln\mathcal{L}$ distributions as a function of δ_{CP} and mass hierarchy. Figures from [62].

kinematics, in the pion rest frame the neutrino has the maximal energy:

$$E^{*,max}_{\nu_\mu} = \frac{m^2_\pi - m^2_\mu}{2m_\pi} = 29.8 \text{ MeV}, \tag{2.3}$$

where "*" indicates quantities in the pion rest frame. In this frame, the neutrino 4-momentum for $|\vec{P}_{\nu_\mu}| \gg m_{\nu_\mu}$ will be:

$$P^\alpha_{\nu_\mu} = (E^*_{\nu_\mu}, E^*_{\nu_\mu}\sin\theta^*, 0, E^*_{\nu_\mu} cos\theta^*), \tag{2.4}$$

where E_{ν_μ} is the neutrino energy, θ is the angle of the neutrino direction with respect to the pion and $\alpha = 0, 1, 2, 3$ is the 4-vector component index. Using a Lorentz transformation with a boost of $\gamma = E_\pi/m2_\pi$, to move from the pion to the laboratory frame, the neutrino 4-vector is then:

$$P^\alpha_{\nu_\mu} = (\gamma E^*_{\nu_\mu}(1+\cos\theta^*), E^*_{\nu_\mu}\sin\theta^*, 0, \gamma E^*_{\nu_\mu}(\beta+\cos\theta^*)), \tag{2.5}$$

$\beta = v_\pi/c$ and v_π is the magnitude of the pion velocity in the laboratory frame. Since a pion is a spin zero particle the decay is isotropic in its rest frame. Considering then the 4-vector components $\alpha = 1$ and $\alpha = 3$ of Eq. 2.4 and 2.5, a relation between angles in the two frames can be found. For high energy pions ($\beta \sim 1$):

$$\tan\theta \sim \frac{E^*_{\nu_\mu}\sin\theta^*}{\gamma E^*_{\nu_\mu}(1+\cos\theta^*)} \sim \frac{E^*_{\nu_\mu}\sin\theta^*}{E_{\nu_\mu}}, \tag{2.6}$$

being $\sin\theta^* < 1$, this relation suggests that there is a maximum value for the angle for which the neutrino of a given energy E_{ν_μ} can be emitted in the laboratory frame. The

maximum angle, for the pion case, can be computed thanks to the result of Eq. 2.3:

$$\tan\theta_{max} \sim \frac{E^{*,max}_{\nu_\mu}}{E_{\nu_\mu}} \sim \frac{29.8 \text{ MeV}}{E_{\nu_\mu}}. \tag{2.7}$$

This means that given the angle $\theta \neq 0$ there is a maximum energy at which the neutrino from the pion 2-body decay can be emitted. Figure 2.5 shows the expected neutrino energy as a function of the parent pions energy for different off-axis angles. For instance an off-axis angle of $\theta = 2.5°$ (~ 43 mrad) would lead to a maximum neutrino energy of $E_{\nu_\mu} \sim 682$ MeV.

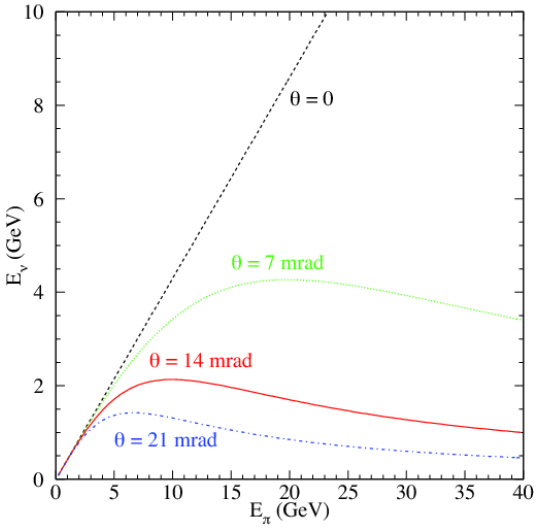

Figure 2.5: Expected neutrino energy as a function of the parent pions energy for different value of the off-axis angle. The distributions are calculated with 2-body decay kinematics for different angles. Figure from [65].

2.2 J-PARC accelerator complex

Accelerator neutrinos are produced via the decay of pions and kaons generated from the collision of a high intensity proton beam on a graphite target. A system of magnetic horns then focuses and selects in charge those mesons towards a decay tunnel where they decay in flight producing neutrinos and antineutrinos. The beam purity of neutrinos or antineutrinos will depend on the charge of the focused mesons. The J-PARC accelerator complex for proton fast-extraction consists of three accelerator phases: the linear accelerator (LINAC), the rapid cycling synchrotron (RCS) and the main ring synchrotron (MR). At the beginning a H^- beam is accelerated up to 400 MeV [54] by the 300 m long LINAC and converted in a proton beam H^+ by charge-stripping foils at the RCS injection. The beam is further accelerated in the RCS up to 3 GeV with a

25 Hz cycle and injected into the MR where protons are then accelerated up to 30 GeV in eight bunches (six before June 2010). The proton beam is finally fast-extracted in a single turn using five kicker magnets at spill cycle of 0.5 Hz which direct the eight bunches down to the graphite target in the neutrino beamline (NU). At the designed power each spill contains approximately 3×10^{14} protons and has a width of 5.6 μs, a time structure which allows to reject the out of time backgrounds due to cosmic rays at the near and far detectors. The parameters for MR protons fast-extraction are listed in Tab. 2.1. In the MR there are two extraction points which provide the proton beam to the hadron facilities via slow-extraction and to the neutrino facility (T2K) via fast-extraction [54]. Figure 2.6 shows a view of the J-PARC accelerator complex where each accelerator stage is highlighted in different colors.

Circumference	1567 m
Beam Power	$\sim$ 750 kW
Beam kinematic energy	30 GeV
Beam intensity	$\sim 3 \times 10^{14}$ protons/spill
Number of kicker magnets	5
Spill cycle	$\sim$ 0.5 Hz
Number of bunches	8/spill
RF frequency	$1.67 - 1.72$ MHz
Spill width	5.6 μs
Bunch width	58 ns

Table 2.1: List of the main design parameters of the MR accelerator for the proton fast extraction at J-PARC.

2.2.1 The neutrino beamline

Once the eight proton bunches of a single beam spill are extracted from the MR they are directed to the T2K neutrino beamline where the neutrino beam is produced. The beam line includes two sequential lines:

1. the primary beamline where protons are bended to point towards the far detector;
2. the secondary beamline where the proton beam hits the target to produce hadrons which are focused or rejected, according to the desired charge, by magnetic horns. Focused mesons decay then into neutrinos in a decay volume (tunnel). Finally, at the end of the line, a beam dump stops all the other particles which are not neutrinos (mostly muons).

An overview of the beamline is shown in Fig. 2.7.

The primary beamline

As shown in Fig. 2.7 the primary beamline is divided in three parts: the preparation (54 m), the arc (47 m) and the final focusing (37 m) sections.

Figure 2.6: Areal view of the J-PARC accelerator complex with the three accelerator facilities. The (anti-)neutrino beam is highlighted in light blue while the location of the near detector complex (ND280) is in purple.

1. In the preparation section a series of 11 conducting magnets (4 steerings, 2 dipoles, 5 quadrupoles) tunes the proton beam for the transportation in the arc section.
2. In the arc section the beam is bent by 80.7° using 14 doublets of superconducting magnets (dipoles and quadrupoles). The doublets configuration allows to reduce the number of magnets and maximizes the acceptance of the primary beam.
3. In the final focusing section 10 separate conducting magnets (4 steerings, 2 dipoles, 4 quadrupoles) adjust and focus the protons into the target station.

Before hitting the target a series of beam quality monitors has been installed to monitor the intensity, position center, profile and losses of the proton beam. In particular, the current transformers (CTs) consist of 50-turn toroidal coils which measure, along the beam pipe, the induced current generated as each bunch passes through the coil. The induced current is then converted into the number of protons in the spill to determine the protons on target (POTs) delivered.

The secondary beamline

The secondary beamline is separated from the primary beamline by a titanium-alloy beam window. As shown in Fig. 2.8 the secondary beamline contains the target station, a decay volume 96 m long and a beam dump at the end.
The target station is placed 12 m underground. It includes the baffle collimator, the target, the horns and an optical transition radiation (OTR) monitor. The target station is housed within an aluminum vessel of 1500 m^3 filled with helium gas (1 atm) to contain

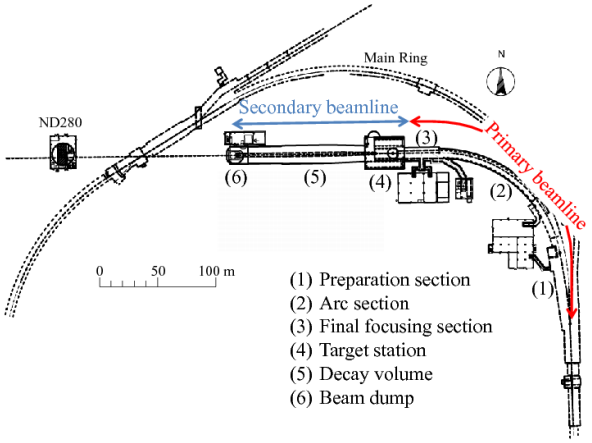

Figure 2.7: Overview of the T2K primary and secondary beamline from above. Figure from [67].

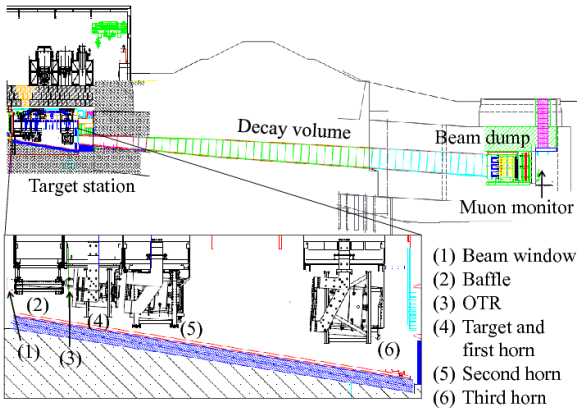

Figure 2.8: Side view of the secondary beamline. The beam enters from the left. Figure from [67].

radiation and avoid the air activation. Shielding is also ensured by iron blocks placed around the station. The OTR is a thin titanium foil used to measure the beam profile just before impinging on the target. The T2K target is a graphite rod of 2.6 cm in diameter, 91.4 cm long which corresponds to two interaction length for a density $\rho = 1.8$ g/cm^3. The rod is surrounded by a graphite tube 2 mm thick sealed to a 0.3 mm titanium case and placed within the first magnetic horn. The graphite was chosen as target because of its good resistance to thermal stress and high melting temperature. More dense material would be strongly damaged by the intensity of the beam after few spills. Gaseous helium, flowing within the coaxial pipes, is used as cooling system. At the designed beam power of 750 kW the center of the target is expected to reach 700° C. Mesons of a given charge are collected and focused (or deflected) in the toroidal magnetic field of the 3 magnetic horns. In each horn a pulsed current of ±250 kA is

used to select in charge the particles exiting the target: positive to produce a neutrino beam, negative for an antineutrino beam. The horns dimensions are listed on Tab. 2.2.

	Horn1	Horn2	Horn3
Inner diameter	5.4 cm	8 cm	14 cm
Inner conductor thickness	3 mm	3 mm	3 mm
Outside	0.4 m	1 m	1.4 m
Length	1.5 m	2 m	2.5 m

Table 2.2: The horns dimensions. The graphite target is placed inside the first horn.

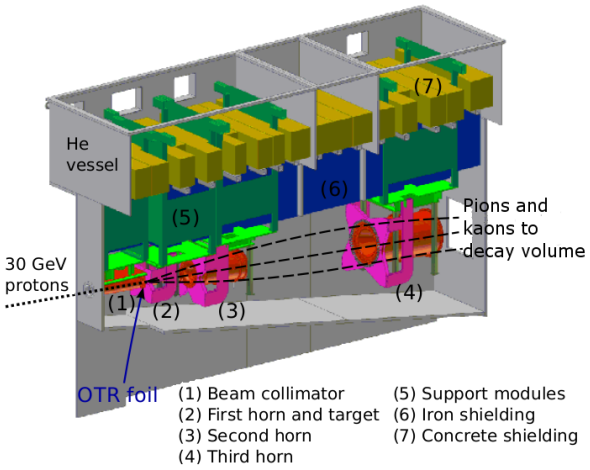

Figure 2.9: Design of the T2K target station. Figure from [54].

The decay volume is a tunnel 96 m long filled with helium, in order to minimize the pion absorption and prevent the production of tritium and other unwanted nuclei. The walls are made of iron plates equipped with a water cooling circuit to avoid heat load from secondary particles. Moreover the decay volume is surrounded by 6 m of concrete to shield the radiation. The (anti-)neutrino beam is produced by the secondary particles, mainly pions, that decay in flight into the tunnel according to the reaction:

$$\pi^{+(-)} \rightarrow \mu^{+(-)} + \nu_\mu(\overline{\nu}_\mu) \tag{2.8}$$

the muon in turn can also decay in flight as follows:

$$\mu^{+(-)} \rightarrow e^{+(-)} + \nu_e(\overline{\nu}_e) + \overline{\nu}_\mu(\nu_\mu). \tag{2.9}$$

For this reason to produce an high purity muon (anti-)neutrino beam the length of the tunnel has been chosen to fulfill two requirements: it has to be long enough to have as many muon (anti-)neutrinos as possible from pions decay (Eq. 2.8) but also short

enough to avoid the muon decay (Eq. 2.9). Its vertical dimension gradually increases so that the neutrino beam off-axis angle can be tuned, according to the oscillation analysis results, between 2° and 3°. As shown in Fig. 2.2, for RunI-IV and RunVIII T2K chose to run in neutrino mode focusing positive hadrons and deflecting negative hadrons which lead to the production mainly of ν_μ, while for RunV-VII, reversing the horn current, positive hadrons are deflected while negative hadrons are focused which lead to the production mainly of $\overline{\nu}_\mu$.
At the end of the tunnel, contained in a helium vessel, a beam dump is placed in order to stop all the undesired particles. It sits 109 m far from the center of the target along the neutrino beam direction for an off-axis angle of 2.5°. Its core has a size of $3.174 \times 1.94 \times 4.69$ m^3 and is made of 75 tons of graphite (1.7 g/cm^3). Fifteen iron plates are placed outside the vessel to shield from radiation while two additional plates are inside the downstream end of the graphite core, reaching a total iron thickness of 2.40 m. This system allows to stop all the hadrons as well as muons below 5 GeV, any muons or any other particle passing through the beam dump into the downstream muon pit are monitored to characterize the neutrino beam. Since the muons are typically produced in association with neutrinos, the measurement of their rate can be used to monitor the neutrino beam. For this reason just after the beam dump, 118 m from the target, sits the muon monitor (MUMOM) [68, 69]. Consisting of two types of detector arrays (ionization chambers and silicon PIN photodiodes), it covers a 1.5×1.5 m^2 area and measures the neutrino beam direction with a precision of 0.25 mrad which corresponds to a 3 cm precision on the muon profile center. Moreover it can be also used to monitor spill-by-spill the position of the proton beam and the efficiency of the horn focusing system. Finally any remaining muon stops in the $\sim$ 180 m of sand between the dump and the near detector complex.

2.3 The neutrino flux

In the T2K beamline design, the neutrino beam direction towards the far detector forms an angle that can be adjusted from a minimum of 2° to a maximum angle of 3°. The baseline and off-axis angle were precisely measured by a GPS survey [54]: the measured distance from the graphite target to the center of Super-Kamiokande is 295335.2 ± 0.7 m while the angle is $2.504 \pm 0.004°$. Figure 2.10 (left) shows the neutrino energy spectrum for different values of the off-axis angle. This off-axis technique, described in Sec. 2.1, leads to a narrow band energy spectrum thanks to the reduction of the dependency of the neutrino energy on the energy of the parent pion. The off-axis angle is then corrected to tune the peak of the neutrino energy spectrum to the energy at which the oscillation probabilities for electron neutrino appearance $P(\nu_\mu \rightarrow \nu_e)$ and muon neutrino disappearance $P(\nu_\mu \rightarrow \nu_\mu)$ are maximum and minimum respectively. For the T2K baseline of 295 km, considering a mass squared difference $\Delta m^2_{32} = 2.4 \cdot 10^{-3}$ eV^2, the maximum of the oscillation probability is found at 600 MeV which corresponds to

an off-axis angle of 2.5° currently used in T2K, as shown in Fig. 2.10. The right side of Fig. 2.10 presents the predicted neutrino beam composition when T2K runs in neutrino mode. Most of the charged pions decay through Eq. 2.8 producing an high purity ν_μ beam ($\sim$ 93%) with backgrounds from $\overline{\nu}_\mu$ (5.6%) and ν_e (1.1%). The first are mainly produced by forward going π^- (Eq. 2.8) which escape the horn deflection, the latter are mainly produced by μ^+ (Eq. 2.9) and kaon decays.

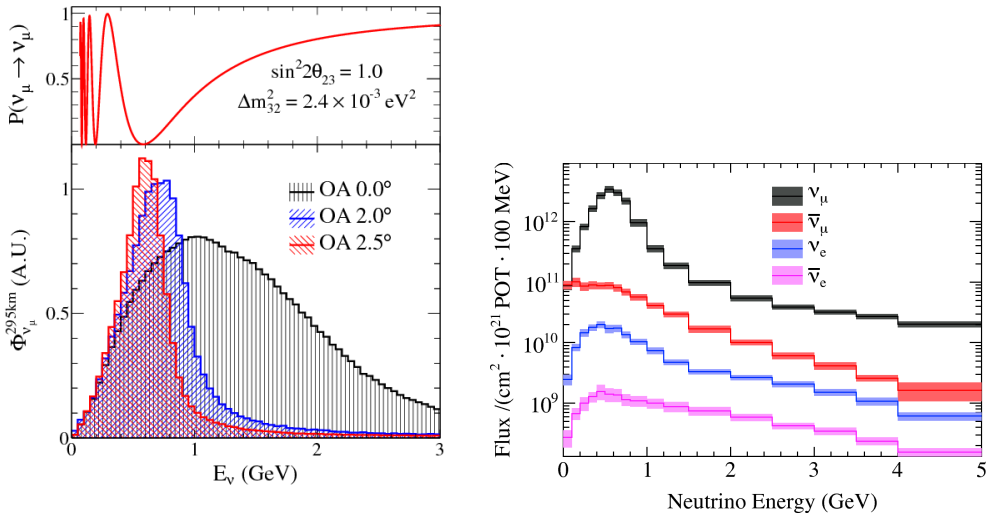

Figure 2.10: Expected T2K fluxes for different off-axis angles, compared to the muon neutrino survival probability at 295 km (left). Neutrino type composition of the flux in T2K (right). Figure from [67].

2.3.1 Flux simulation

The flux prediction is an essential part of the success of all the accelerator based neutrino oscillation experiments since it is used to propagate the observed spectra at the near detector to the one expected at the far detector. In order to accurately predict the neutrino flux, a good knowledge of the production cross-section and kinematics of hadron produced from proton-carbon interactions is necessary. T2K exploits a neutrino beam Monte Carlo (MC) simulation, developed by the collaboration, called JNUBEAM. JNUBEAM is a GEANT3 [70] based MC simulation of the baffle, target, horn magnets, helium vessel, decay volume, beam dump, and muon monitor. The geometry of these components is simulated accordingly to the final mechanical drawings of the constructed beamline (Fig. 2.7).

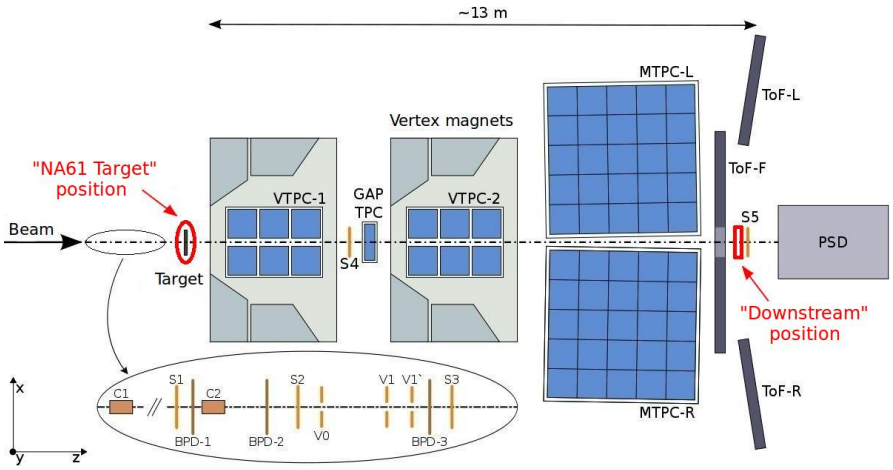

Figure 2.11: Schematic view of the NA61/SHINE experiment. Figure from [71].

The simulation starts after the proton fast-extraction, at the junction between the primary and secondary beamline, with the primary proton beam upstream of the baffle and ends with the decay of hadrons or muons that produce the neutrino beam. FLUKA [72, 73] is used to simulate the hadronic interactions inside the target while interactions outside the target are simulated by GCALOR [74] interfaced with GEANT. The neutrino flux prediction is then tuned using external hadron production data from an auxiliary experiment, NA61/SHINE at CERN SPS [75, 76]. It exploits a T2K replica target which allows to provide informations about the proton beam interactions in a graphite target in order to measure hadron cross-sections and kinematics. The NA61/SHINE experiment, shown in Fig. 2.11, includes four large TPCs (two operating in a magnetic field and two installed downstream the magnets) symmetrically placed with respect to the beam direction and a set of Time of Flight arrays in the downstream end. The primary interaction of the proton beam impinging on the graphite target leads to the production of about 60% of the flux at the peak energy while re-interactions in the target account for 30%. The remaining 10% is due to re-interactions in the beamline material [77]. Thanks to this sophisticated strategy to accurately tune the neutrino flux at T2K (beam monitoring + MC simulation + external data tuning) the total uncertainty on the flux at the peak energy (without near detector constraint) is now estimated to be $\sim$ 8%. Moreover, this allows also to precisely measure at the near detector the neutrino interaction cross-sections in order to predict the neutrino rate at the far detector. Figure 2.12 show the T2K flux prediction for neutrino (left) and antineutrino (right) mode after the external data tuning.

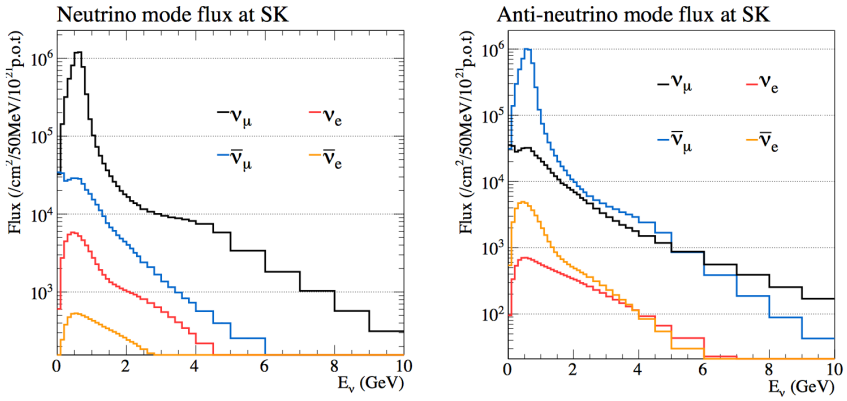

Figure 2.12: Tuned neutrino flux prediction at the far detector in neutrino mode (left) and antineutrino mode (right) normalized to 10^{21} POT.

2.4 The near detector complex

In a long-baseline accelerator neutrinos experiment both near and far detectors are necessary. Figure 2.13 details the T2K experimental setup. The near detector precisely

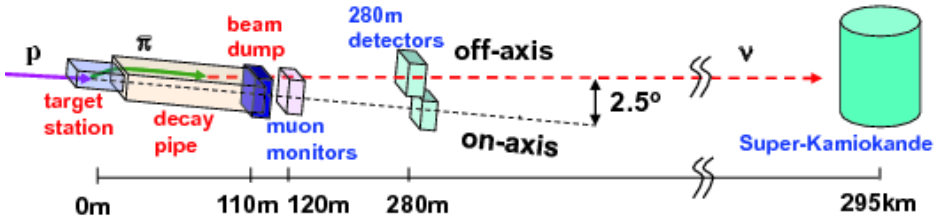

Figure 2.13: A schematic view of the T2K neutrino beamline and detectors. Beamline components are indicated by the words in red while the detectors are in blue. The dashed red line is the imaginary line which connects the average pion decay point with the far detector.

measures the characteristics of the neutrino beam (energy spectrum and flavor composition) before the oscillation and the neutrino interaction rates (cross-sections) in order to predict the neutrino interactions at the far detector (Super-Kamiokande, see Sec. 2.7) which measures the neutrino flux after the oscillation. The near detector complex of the T2K experiment has been installed at a distance of 280 m from the graphite target and it is composed of two detectors:

- the on-axis detector INGRID (Sec. 2.5) especially used to measure the beam direction and profile
- the off-axis detector ND280 (Sec. 2.6): a fully magnetized compact detector which measures the neutrino energy spectrum, flavor content and interaction cross-sections.

The near detectors are accommodated in the Neutrino Hall facility at J-PARC in a pit of 17.5 m in diameter and a depth of 37 m. A view of the pit is shown in Fig. 2.14 on the left. Both ND280 and INGRID use the same coordinate system where the z-axis is the direction of the nominal neutrino beam while x and y are the horizontal and vertical axes respectively. In the next two sections a detailed description of the near detectors is given.

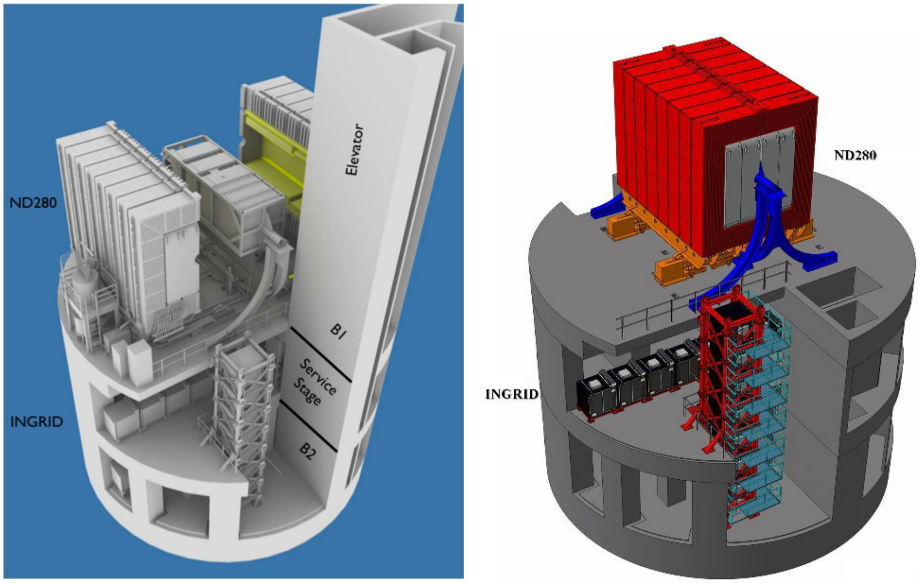

Figure 2.14: Detailed view of the near detector complex pit composition on the left while the near detectors installed in the Neutrino Hall are colored and highlighted on the right.

2.5 The on-axis near detector: INGRID

Interactive Neutrino GRID (INGRID) is the on-axis T2K detector installed 280 m downstream from the target. The main purpose is to monitor the neutrino beam profile, center and intensity by detecting the particles produced by neutrino interactions. INGRID consists of $7 + 7$ modules arranged in two identical segments along the horizontal an vertical directions to form a "*cross*" configuration, as shown in Fig. 2.15, plus two additional off-diagonal modules located outside the main cross which check the axial symmetry of the beam [54, 67]. The center of the cross is the neutrino beam center defined at 0° with respect to the direction of the primary beam (see Sec. 2.2.1). The cross structure samples the neutrino interaction distribution in a transverse area of 10×10 m^2 providing a beam center resolution of ~ 0.4 mrad.
Each module has a sandwich structure of 11 tracking scintillator planes interleaved with 9 iron planes for a total target mass of 7.1 tons par module. It is surrounded by veto scintillator planes to reject interactions from outside, as shown in Fig. 2.16

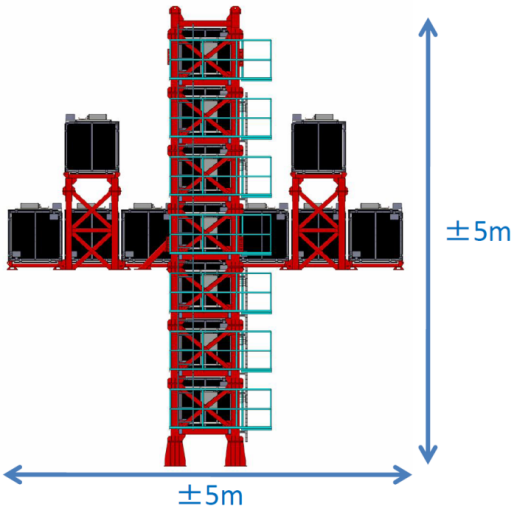

Figure 2.15: The INGRID on-axis near detector, the center of the cross corresponds to the neutrino beam center. Figure from [54]

Number of pixels	667
Active area	1.3×1.3 mm^2
Pixel size	$0.5 \times 0.5 \mu$m^2
Operational voltage	68-71 V
Gain	$\sim 10^6$
Photon detection efficiency at 525 nm	26-30%
Dark rate above 0.5 p.e. at 25 $^\circ C$	≤ 1.35 MHz

Table 2.3: Main specifications of the T2K MPPCs.

(left and center). The scintillator planes consist of scintillator bars of a dimension $1.0 \times 5.0 \times 120.3$ cm^3 and are composed of 24 horizontal bars glued to 24 vertical bars to enable 3D reconstruction of the particle path. Each bar is instrumented with Wave-Length-Shifting (WLS) fibers which collect the scintillation light produced by charged particles crossing the bar and bring the light to a photodetector. The signal is then amplified thanks to the use of Multi-Pixel Photon Counters (MPPCs) [78] attached at the end of the WLS fiber, a semiconductor photodiodes of small size (1.3×1.3 mm^2 active area) operating in Geiger mode [79] with an high gain ($\sim 10^6$) and a large number of pixel (667). The main specifications of MPPCs are summarized in Table 2.3. The same technology (WLS + MPPC) is used in ND280 as well because it has the advantage to properly work in a magnetic field and fits into a limited space inside the magnet.
An additional module has been installed in front of the central module where the vertical and horizontal INGRID segments cross. The extra module consists just of 34 scintillator planes and is surrounded, as the standard module, by veto planes. A side view of the extra module is shown in Fig. 2.16 (right). Thanks to the absence of iron plates and to the smaller section of the scintillator bars, low energetic particles, like

protons, produced in neutrino interactions can be detected. For this reason it is called Proton Module (PM). A typical neutrino event in the INGRID module + PM is shown in Fig. 2.17. Recently, thanks to the PM, the on-axis detector has been used to measure the neutrino interaction cross-section on carbon [80].

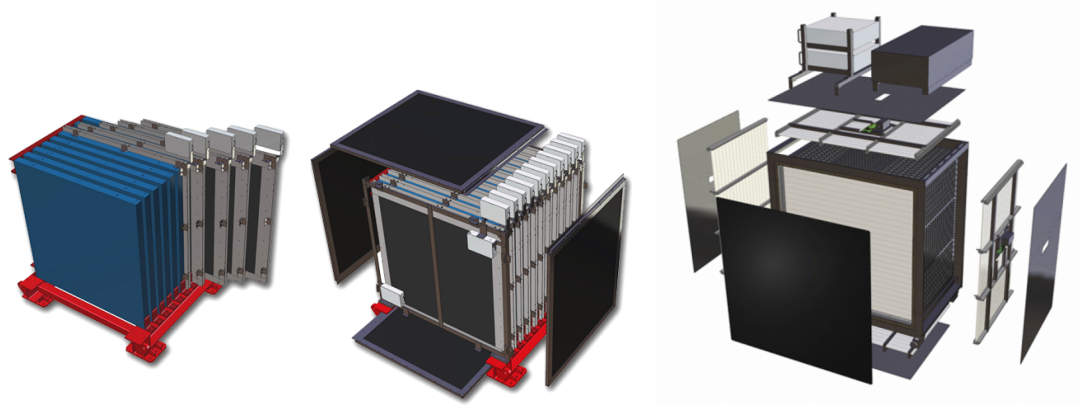

Figure 2.16: A standard INGRID module (first two modules on the left). On the left the inner structure: the tracking scintillator planes (blue) and iron plates (gray), on the center the veto planes are shown. Similarly the third image shows the Proton Module with the finer scintillator planes (white) and the veto planes (black). Figures from [54].

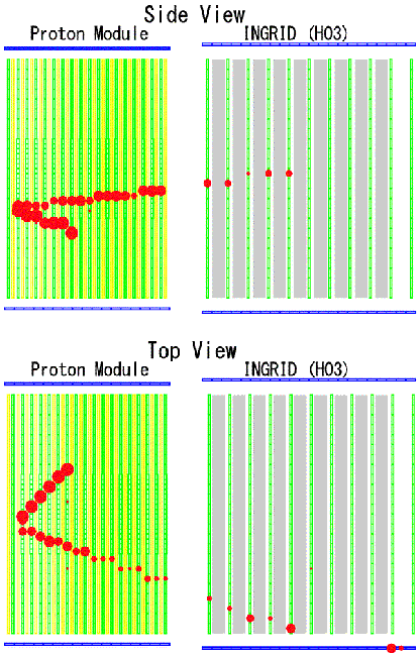

Figure 2.17: Event displays of events in the on-axis detector which take place in the PM and crosses an INGRID module. The tracks are shown as full red circles. Figure from [54].

2.6 The off-axis near detector: ND280

The off-axis Near Detector (ND280) is placed at 280 meters from the target with an angle of 2.5° with respect the neutrino beam center. It is located along the imaginary line that connects the average pion decay point with the far detector Super-Kamiokande, as shown in Fig. 2.13.
ND280 is a multi-purpose detector designed to measure the energy spectrum and the flavor composition (ν_e) of the un-oscillated beam and the neutrino interaction cross-sections on various targets in order to predict the neutrino interaction rate at the far detector. To this aim, ND280 has the capability to reconstruct and identify the particles produced in the final state of (anti-)neutrino interactions. As shown in Fig. 2.18, the ND280 elements are contained in the inner volume of the refurbished UA1/NOMAD magnet. At the upstream end lies a π^0 detector followed by a tracker system which tags and detects charged particles. Both are surrounded by an electromagnetic calorimeter for detecting electrons and photons while the return yoke of the magnet is instrumented with muon detectors. A ND280 event display is shown in Fig. 2.19.

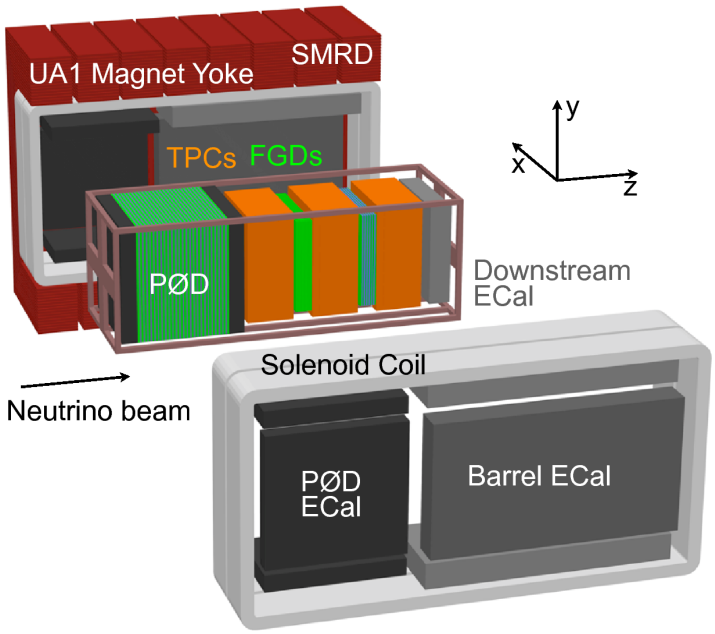

Figure 2.18: An exploded view of the ND280 near detector. Figure from [54].

2.6.1 The UA1/NOMAD magnet

ND280 uses the old UA1/NOMAD magnet [81, 82] which was refurbished and donated by CERN to J-PARC in 2008. The magnet creates a dipole magnetic field of 0.2 T horizontally oriented in the $+x$-axis direction, perpendicular to the neutrino beam direction. It consists of two symmetric halves composed by water-cooled aluminum coils

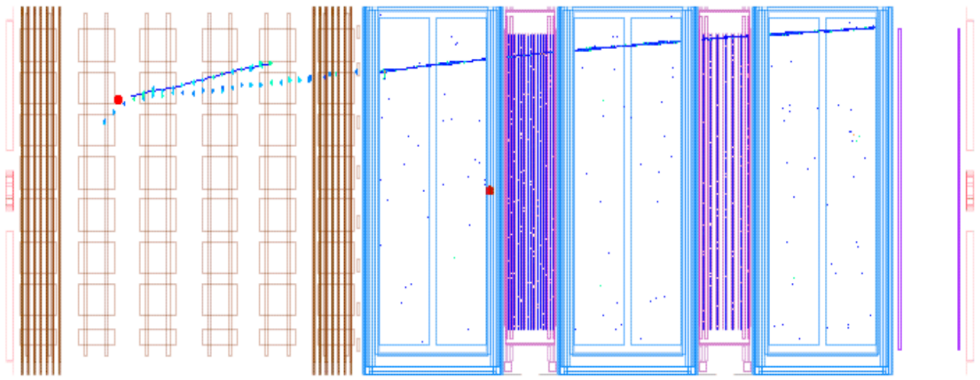

Figure 2.19: Event display of a neutrino interaction in the ND280 detector.

which generate the magnetic field and by the flux return yoke. Each half is made of 8 C-shaped flux return yokes of low-carbon steel plates. The size of the magnet inner volume is $7.0 \times 3.5 \times 3.6$ m^3 while the external dimensions are $7.6 \times 5.6 \times 6.1$ m^3 for a total weight of the yoke of 850 tons. The coils are made of aluminum bars with a 5.45 cm square section with a hole of 23 mm diameter for the water cooling. They are connected hydraulically in parallel and electrically in series and operate at a current of 3 kA.

2.6.2 The side muon range detector

The side muon range detector (SMRD) detects muons emitted at high angle with respect to the beam direction and measures their momentum. It is also used to trigger cosmic ray muons that enter the detector and to identify muons from neutrino interactions in the surrounding cavity walls and in the iron of the magnet. The SMRD instruments the 1.7 cm air gaps between the 4.8 cm thick iron plates of the UA1 magnet flux return yokes with 440 scintillator modules. WLS fibers, inserted in an S-shaped groove as shown in Fig. 2.20, are embedded into each module and read by a MPPC placed at the end of each fiber. The MPPCs are then connected to a miniature printed circuit board which leads the MPPC signal to the Trip-T front-end boards (TFBs) mounted on the vertical section of the magnet yokes.

2.6.3 The Pi-Zero detector

The π^0 detector (PØD) lies at the most upstream end of the basket (see Fig. 2.18). It was originally designed to measure the rate of neutral current π^0 production, a possible source of background in the ν_e appearance analysis at the far detector, but it can also be used to perform cross-sections measurements for various interaction channels. As shown in Fig. 2.21 the PØD can be divided in four sections, called Super-PØDules: the

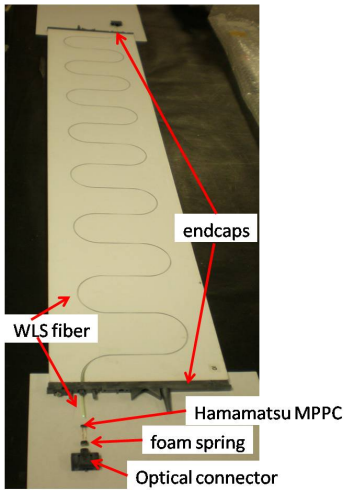

Figure 2.20: View of SMRD scintillator counter components prior to assembly. Figure from [54].

upstream and central water targets are sandwiched in the region between the upstream and central ECals placed at the upstream and downstream ends. The PØD dimensions are $2103 \times 2239 \times 2400$ mm^3 along the x, y and z axes. Each Super-PØDule is composed by polystyrene scintillator bars arranged in x (134 bars 2.2 m long) and y (126 bars 2.34 m long) directions called PØDules. Each scintillator bar has a triangular section and is read by a WLS fiber placed in a central hole and connected to a MPPC at one end and to an aluminum mirror at the other. The two ECals consist of 7 PØDules alternated with 0.4 mm lead layers to contain the electromagnetic shower from photon conversion and to act as veto to reject neutrino interactions originated outside the PØD. The two water target regions are made of 13 PØDules interleaved with 28 mm thick water bag followed by 1.5 mm of brass sheet. Since the far detector consists of water, the PØD is instrumented with passive water layers in order to measure the interaction rate on water. Water bags can be filled or emptied, in this way a subtraction method can be used for the determination of the neutrino water cross-section. The total water target mass is 1902 ± 16 kg, monitored with a precision of 5 mm in depth by pressure sensors.

2.6.4 The tracker system

The tracker system provides identification and momentum measurement of charged particles produced by neutrino interactions. It is installed downstream of the PØD and consists of three Time Projection Chambers (TPCs) interleaved with two Fine Grained Detectors (FGDs).

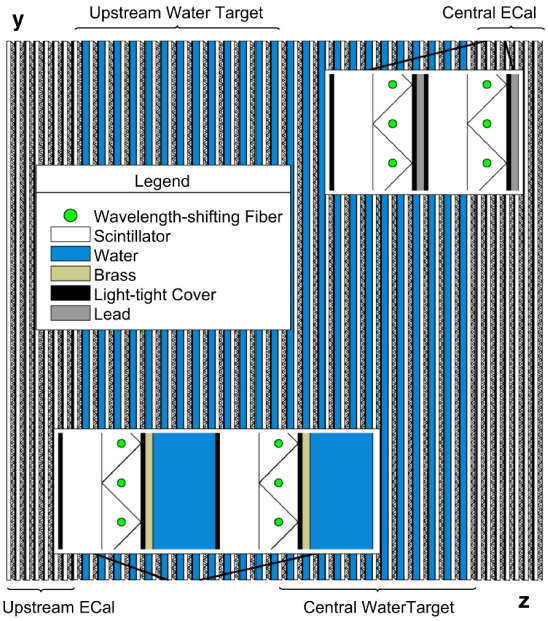

Figure 2.21: A schematic view of the Pi-Zero detector. The blue PØD-ules can be filled with water or drained. The beam runs from the left to the right. Figure from [54].

The Time Projection Chamber

The three TPCs are gaseous detectors which provide good position resolution for a 3D tracking of the charged particles by measuring the ionization produced in the gas volume. Moreover together with the magnetic field in which they are placed, they perform also a precise momentum measurement of the charged particles. Finally the energy loss (Eq. 2.10) is used to identify the particle type (μ, p, π, e). A detailed description of the TPC and its working principles will be given in the next chapter.

The Fine Grained Detector

The two FGDs [83] are interleaved with the three TPCs and provide ~ 2 tons of target material for neutrino interactions. Each FGD has outer dimensions of $2300 \times 2400 \times 365$ mm^3, thin enough to allow most of the penetrating particles produced in neutrino interactions (especially muons) to pass through the TPCs where their momenta and flavor can be determined. They consist of polystyrene scintillator bars alternately oriented perpendicular to the beam in the x and y directions allowing the tracking of charged particles coming from the neutrino interaction vertex. Scintillator bars are 1864.3 mm long with a section of 9.61×9.61 mm^2. They are arranged in both x and y layers including 192 bars each. A pair of orthogonal layers builds an "*XY-module*" of a dimensions $186.4 \times 186.4 \times 2.02$ cm (not including electronics). The left side of Fig.

2.22 shows a front view of the module. Each scintillator bar has a hole in the center where a WLS fiber of 1 mm diameter is placed, as shown on the right side of Fig. 2.22. One end is connected to a MPPC while the other is coated with aluminum to form a mirror.

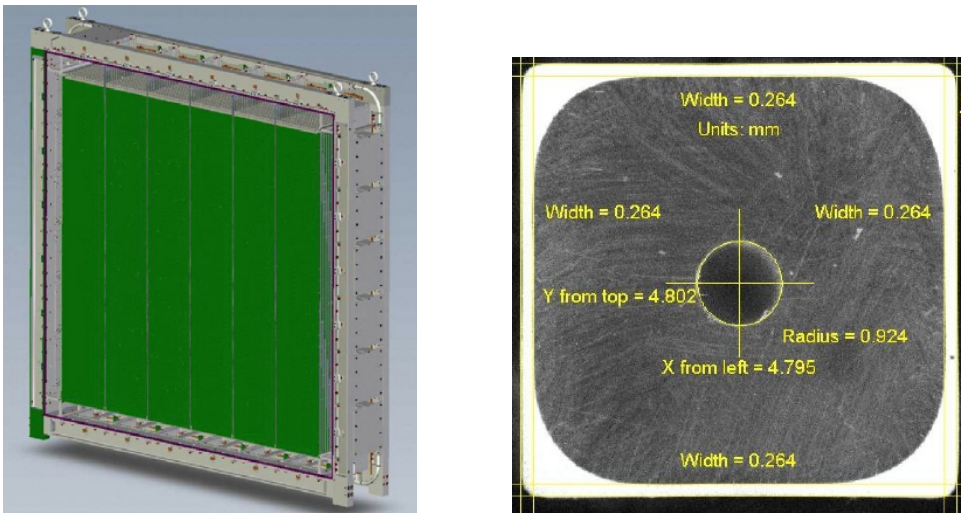

Figure 2.22: **Left:** front view of an FGD with the front cover removed. In green the XY-supermodule. **Right:** Section of a polystyrene scintillator bar. Figures from [54].

The most upstream FGD (FGD1) is placed downstream the first TPC. It consists of 30 layers of scintillator bars (15 XY-modules) providing a C_8H_8 target to neutrino interactions. The downstream FGD (FGD2) instead, has been installed between the second and the third TPCs. It is made of 14 scintillator layers (7 XY-modules) interleaved with six water modules: 25.4 mm thick and 1809 mm wide. The water modules consist of polycarbonate panels filled with water. Polycarbonate was chosen due to the rigidity, lightweight and waterproof capability of the material. The panels are divided into long cells by internal walls that provide rigidity and strength and also help to maintain the shape of the panel and avoid deformations when filled with water. Cells are vertically oriented inside the detector. Figure 2.23 shows a schematic view of the internal wall structure of a panel. Water continuously flows inside the long cells at sub-atmospheric pressure which avoids, in case of a leak, water spilling towards the electronics. The water modules serve as target for neutrino interactions on oxygen and do not contain a readout system, thus the events happening in water are identified as excess in the neighbour scintillator layers which can be directly compared to neutrino interactions in the carbon based scintillator bars. This enables the measurement of neutrino-oxygen interactions for a better modelling of interactions at Super-Kamiokande which is a water Cherenkov detector. Finally, in order to minimize the inactive mass inside the FGD, each XY and water module is surrounded by light structure, called dark box, in which the electronics is located. Since the FGD detector acts like target for neutrino cross-section analysis described in Chapter 6 an overview of its performances will be given in

the following.

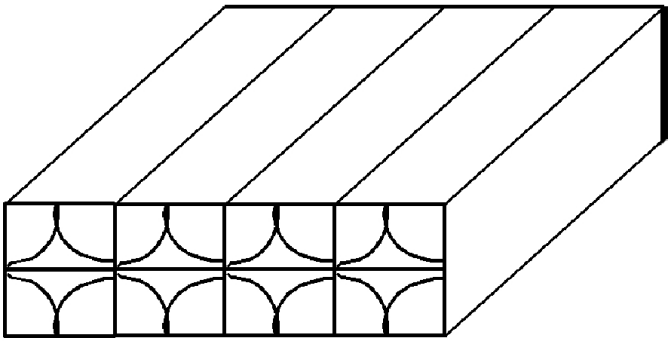

Figure 2.23: Section of a polycarbonate water module panel, showing the internal wall structure. Figures from [54].

2.6.4.1 The FGD performances

The primary ionization

When a relativistic charged particle passes through matter, it interacts with the atoms and loses energy mainly through collisions on the electrons. This energy loss is the results of a transfer of energy, via the exchange of low-energy virtual photons, from the charged particle to the surrounding matter. Depending on the scale of the energy transfer and of the ionization potential, these photons can either "*excite*" the atoms with the emission of a photon from the atom de-excitation, if the energy is below the ionization potential, or "*ionize*" the atoms with the subsequent emission of an electron, if the energy is above the ionization potential. Consequently the photons or electrons, issued from the primary ionization, may excite or ionize other atoms producing secondary photons or electrons, usually created close to the primary interaction point. At the end of these processes a certain number of photons or electrons have been produced along the particle trajectory. The average energy loss of a charged particle traversing the matter over a given distance can be quantified by the Bethe-Bloch formula [49]:

$$-\frac{dE}{dx} = 4\pi N_A r_e^2 m_e c^2 z^2 \frac{Z}{A}\frac{1}{\beta^2}\left[\frac{1}{2}\ln\frac{2m_e c^2\beta^2\gamma^2 T_{max}}{I^2} - \beta^2 - \frac{\delta}{2}\right] \tag{2.10}$$

where r_e and $m_e c^2$ are the electron radius and mass, z is the charge of the incident particle in unit of e (the electron charge) while Z and A are the atomic and mass number and I is the mean excitation potential of the absorber material. The term T_{max} is the maximum kinetic energy that can be transferred to a free electron and δ is a correction which takes into account density effects. Therefore Eq. (2.10) relates the energy loss along the trajectory (dE/dx) of a charged particle of given speed β and charge z to the composition Z, A, I of the crossing medium.

In FGD the detection of ionizing radiation is achieved using plastic scintillator bars coupled with wavelength shifter fibers which collect the scintillation light and transport it to photodiode light sensors (MPPCs). The plastic scintillator has been chosen because of its efficiency to convert the kinetic energy of charged particles into a detectable light (the light yield is proportional to the deposited energy) and because of the capability to generate fast signals. Moreover it allows to build large volumes with a relatively inexpensive price.

Signal extraction

Charged particles from a neutrino interaction in the FGD usually deposit their charge in approximately 60 bars [83]. Scintillation light from atom de-excitation, is collected by WLS fibers and propagates down to the fibers towards the MPPCs. Photons arriving on the MPPC pixels induce a Geiger avalanche in order to increase the amplitude of the charge signal above the electrical noise. The charge signal Q_i from a single pixel is directly proportional to the capacitance C_i of the pixel and to the applied voltage V_i. The total collected charge Q is proportional to the number of pixels that underwent Geiger discharge which in turn is proportional to the number of incident photons. It results in a characteristic pulse waveform which is sent to the electronic system where it is digitized and measured in ADC ready to be analyzed for the reconstruction process. The charge signal due to a single hit is shown in Fig. 2.24 on the left. The pulse height (PH) of such signal is proportional to the number of trapped photons in the fiber and represents the energy deposited by the particle in the scintillator bar. However, individual pixel of the MPPC can generate a signal when there is no incident photon, this is called "*dark noise*". Figure 2.24 on the right shows the PH spectrum obtained from a cosmic muon interacting in the scintillator bars, the dark noise dominates the PH spectrum at low ADC counts, it can be suppressed in the track reconstruction a threshold.
When charged particles lose energy in the plastic scintillator bar, the light yield L follows Birks' formula [84]:

$$\frac{dL}{dx} = S\frac{dE/dx}{1 + k_B\frac{dE}{dx}} \tag{2.11}$$

where S is the scintillation efficiency and k_B is Birks' constant which depends on the material, for a plastic scitillator it has been measured to be $k_B = 0.0208 \pm 0.0003(stat.) \pm 0.0023(syst.)$ cm/MeV [85]. A set of calibration corrections are also applied to the MPPC response in order to account for the temperature dependence and the attenuation of the number of photons during their propagation along the fiber [83].

Particle identification

Equation 2.10 implies that the energy loss along the particle path in the detector is a characteristic of the particle itself, thus knowing its energy loss is possible to identify

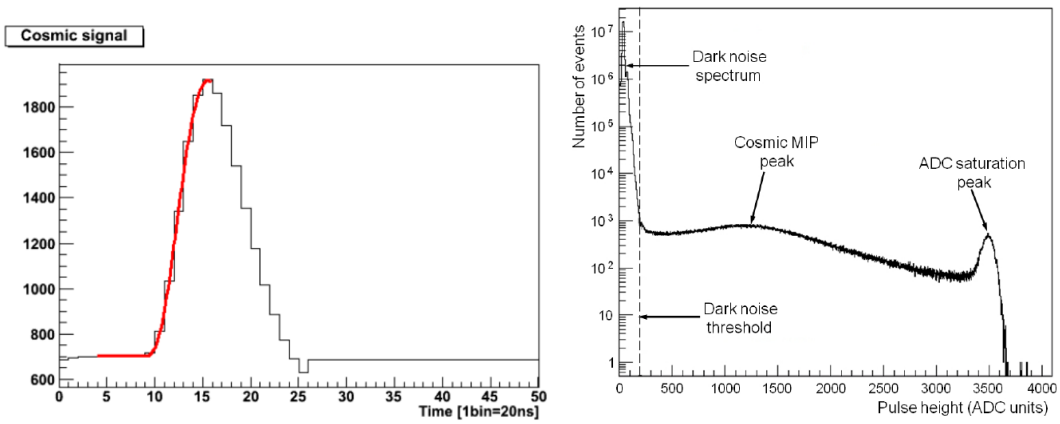

Figure 2.24: **Left:** example of waveform. The red line shows the fit. **Right:** MPPC pulse height distribution for cosmic muon event, with dark noise threshold displayed. Figure from [83].

it. In the FGD the particle identification (PID) is performed only for reconstructed tracks which are fully contained (stopping particles) in the detector volume. They do not enter the TPC. Typically, fully contained reconstructed tracks are due to low momentum particles (mainly pions and protons) created in association with the charged lepton of the neutrino CC interactions (see Fig. 1.2). Therefore, in order to tag the full final state of a neutrino interaction, a PID in the FGD is needed in addition to the TPC one. Since both FGDs and TPCs use the same method and the main PID in ND280 exploits the TPC detector, only the results in FGD are shown here. The particle identification method will be described in detail in Sec. 3.5.3. Figure 2.25 shows the reconstructed energy per path length for different particle hypothesis for both FGDs. The discrimination of protons from muons and pions is very accurate especially in FGD1 which is fully active, however this method does not distinguish between pions and muons because their energy loss is identical.

Michel electron tagging

When a fully contained track does not leave enough hits in the FGD to be reconstructed, the decay electron of the stopping particle can be used to tag the particle. This electron is commonly called "*Michel electron*". This method uses the FGD time separation between two consecutive hits to sort the hits in different clusters starting from the first hit. The maximum time difference between the hits is fixed at 100 ns, if it is less then the two hits are put together in a cluster otherwise the later hit is put in the next cluster. The timing determination in FGD will be described in the next section.
The main purpose of the time binning is to tag Michel electrons and to separate neutrino interactions in different bunches. Since the muon lifetime ($\approx 2.19\ \mu$s) is much

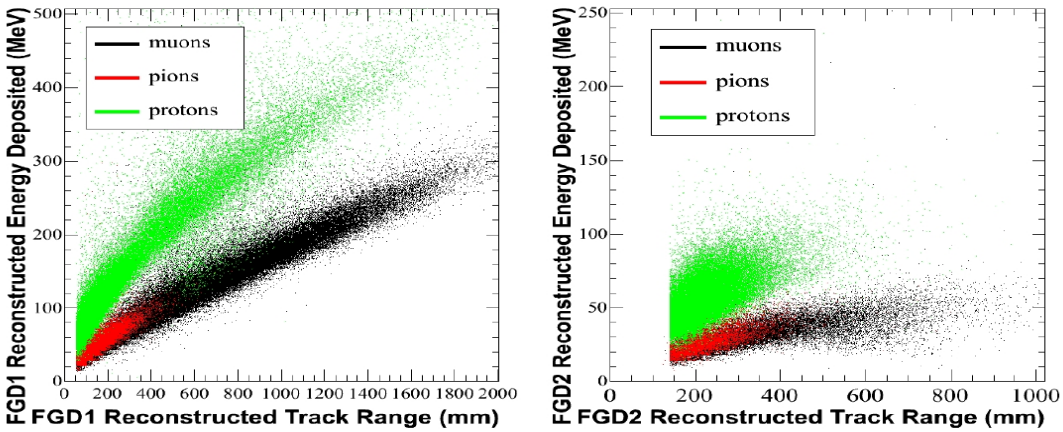

Figure 2.25: Reconstructed energy depositions as a function of the track length for muons, pions and protons in FGD1 (left) and FGD2 (right).

longer than the maximum time gap, the Michel electrons usually form an isolated time cluster. Typically, low momentum pions are fully contained in the FGD and decay into muons, this secondary muon (not to be confused with the primary muon of the CC interaction) also stops and decays in turn to a Michel electron. The tagging of such electron is made by seeking a delayed time cluster following the first time cluster associated to the initial neutrino interaction. Therefore, the Michel electrons are used to identify charged pions and characterize the neutrino interaction.
A sample of cosmics rays stopping in the FGD can be used to determine the detector capability to tag the Michel electrons by measuring the muon life time. The distribution of the time difference between two consecutive time clusters is described by an exponential decay:

$$f(\Delta T) = p_0 + p_1 \cdot e^{-\Delta T/p_2} \tag{2.12}$$

where p_0 accounts for any remaining flat background (i.e. a second coincident cosmic ray), p_1 is the normalization and p_2 the muon lifetime. The stopping muon sample is selected using the following criteria:

1. more than one delayed time cluster;

2. the number of hits in the delayed time cluster should be greater than 5 for FGD1 (6 for FGD2).

The measured Michel detection efficiencies in FGD1 is $\sim 56\%$ while it is evaluated to be $\sim 43\%$ in FGD2, this difference is due to the higher probability the Michel electron, if it was emitted in the water module. Figure 2.26 shows the measured μ^- lifetime for cosmic ray data. The fitted value of the lifetime is 1.87 ± 0.12 μs lower than expectation since they can also be absorbed. However the result is consistent with the measurements of μ^- capture lifetime on carbon [86].

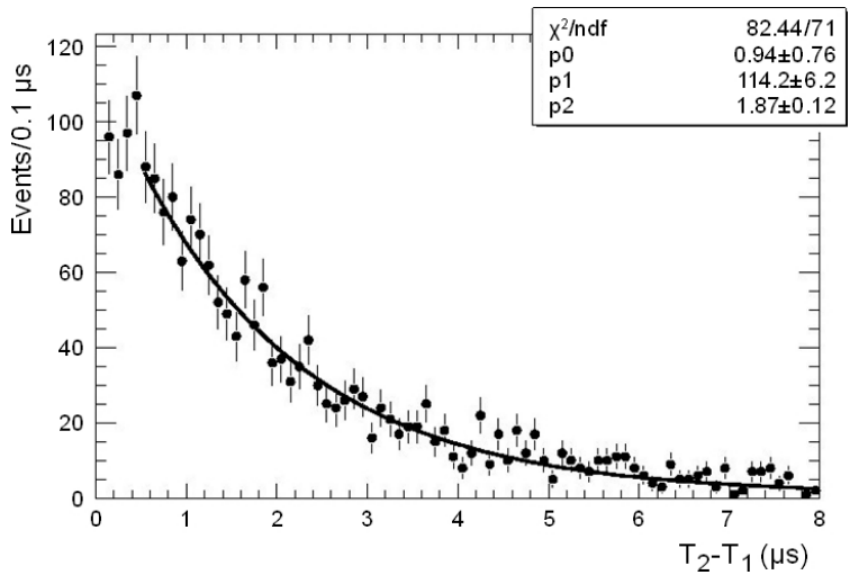

Figure 2.26: Measured lifetime distributions for negative stopping muons in the FGDs. The data are fitted with an exponential plus a flat background. Figure from [83].

Hit timing

One of the main features of the FGD detector is the possibility to determine the time of passage of a particle in the FGD and then provide the time of the neutrino interaction (T_0). The timing of a single hit is calculated by fitting the leading edge of the pulse waveforms up to the peak (see Fig 2.24 left). In this region the contributions to the pulse waveform due to after-pulsing and late photons (typically reflected from the mirrored end) are minimized. The fitted time hit is then corrected taking into account the travel time of the light inside the fiber and the different clocks of the electronic system components. The latter is corrected by looking at the asynchronous signal resulting from the simultaneously injection of an electronic signal (FGD timing markers). A detailed description of the electronic system can be found in Ref. [83]. Finally, after the calibration procedure, the time of a reconstructed track crossing the FGD is computed as an average time of the hits in the track. Figure 2.27 shows the time difference distribution between the FGD1 and FGD2 $\Delta t_{21} = t_{FGD2} - t_{FGD1}$ using a cosmic rays sample that crosses both the FGDs. The double peak is due to which FGD the cosmic muon hits first. The width of each peak gives an estimation of the timing resolution which is $\sigma_{\Delta t} \sim 1$ ns. Furthermore, the peak separation can be used to determine the track direction between the two FGDs. A track crossing both FGDs is tagged as backwards-going if the time difference is greater than $\Delta t_{21} > 3$ ns. Similarly, the FGD timing can be used to determine the direction of a track crossing the FGD and another fast detector of ND280 (PØD or electromagnetic calorimeters).

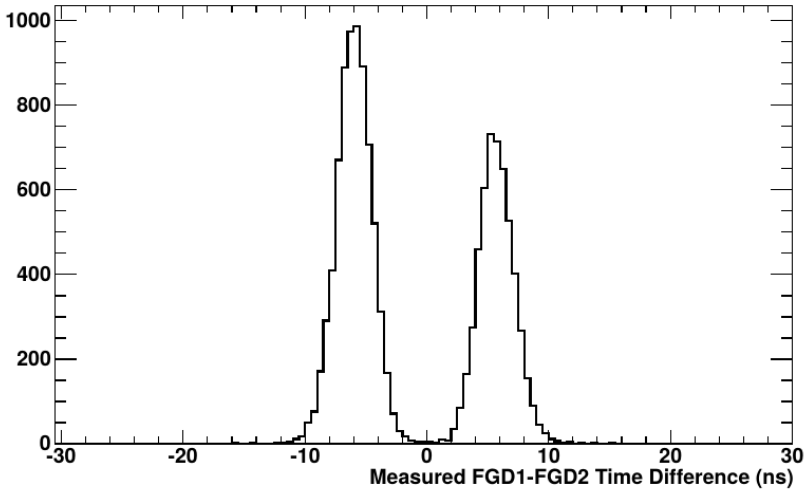

Figure 2.27: Averaged time difference of cosmic muons crossing both FGDs. The two peak structure is from cosmic muons hitting FGD1 or FGD2 first. Figure from [83].

2.6.5 The Electromagnetic calorimeters

The electromagnetic calorimeter (ECal) of ND280 surrounds the inner detectors (PØD, TPCs and FGDs) providing complementary information to the rest of the Tracker. They are used to detect and tag π^0 by measuring the direction and the energy of photons but also to provide measurements of particles (μ, p, π, e) in regions of the phase space without TPCs coverage. ECal exploits the same scintillator technology as the FGDs but with a lower granularity: coarse-grained bars with a 4×1 cm^2 section with a central hole in which the WLS fiber is inserted. Moreover the bars vary in length depending on the module they belong to and a lead absorber layer of 1.75 mm thickness is placed between the bars to contain electromagnetic showers and increase the probability for a photon to shower. As shown in Fig. 2.18 there are 13 independent ECal modules that can be sorted in three different types:

Barrel-ECal (Br-ECal): six modules surrounding the Tracker volume on its four sides parallel to the beam direction. Bottom and top side modules consist of two halves. It is composed of 31 layers at each side corresponding to 9.7 radiation length. In the side modules, bars 3.84 m long form the layer oriented in the z direction while 2.36 m long bars form the layer in the y direction. The bars running in z are read by two MPPCs while the bars perpendicular to them by one MPPC. Top and bottom modules are made of scintillator bars 1.52 m long alternately oriented in the z and x direction.

Downstream (Ds-ECal): one module covering the downstream part of the Tracker. It consists of 34 layers alternately oriented in the x or y direction for a total thickness of 10.6 radiation length. Each layer is composed of 50 bars 2.04 m long

read by two MPPCs.

PØD-ECal: six modules surrounding the PØD volume on its four sides parallel to the z-axis. It has higher granularity and is made of scintillator bars 2.34 m long parallel to the beam direction arranged in six scintillator planes. Bars are interleaved by a 4 mm thick lead absorber.

2.7 The Super-Kamiokande far detector

The far detector Super-Kamiokande (SK) is a Cherenkov detector with a mass of 50 ktons of pure water. It is located in the Mozumi mine of the Gifu prefecture in the west coast of Japan [87]. Housed underground the Kamioka mountain, the detector lies below 1000 m of rocks (2700 m water equivalent) which shields from cosmic rays up to 1 TeV reducing the flux of background muons from cosmic rays by about five orders of magnitude compared to a detector placed on surface. SK is in operation since April 1996. In 1998 SK discovered the oscillation of atmospheric neutrinos while SNO, slightly later, discovered the oscillation of solar neutrinos. For this reason the leading physicists of both collaborations, Takaaki Kajita (SK) and Arthur McDonald (SNO), received in 2015 the Nobel Prize in Physics for the discovery of neutrino oscillations. During its four major running periods (SK I-IV), SK has given a major contribution to the study of flavor oscillations of atmospheric and solar neutrinos [45, 88, 89, 90, 91]. Moreover it was successfully used as far detector for accelerator neutrinos in the K2K experiment [92].
Figure 2.28 shows a schematic view of the detector, the cylindrical tank has a size of 39 m in diameter and 36.2 m in height. It is filled with pure water. The tank consists of inner and outer regions separated by a cylindrical stainless steel structure. The inner detector (ID), the core of the far detector, is a cylindrical volume of 33.8 m in diameter and 36.2 m in height. The cylindrical surface is covered by 11.146 inward facing photomultipliers tubes (PMTs) of 50 cm diameter. Each PMT is spaced by 70.3 cm which corresponds to a 40% photocatode coverage of the ID surface [93]. The 2 m thickness cylindrical space concentric to the ID is called outer detector (OD). The internal surface of the OD is covered by 1885 outward facing PMTs of 20 cm diameter. The OD is used as an active veto to count (out)incoming particles entering(exiting) the ID. It serves also as additional passive shield for neutrons and γ rays from the rocks. A set of horizontal and vertical Helmholtz coils has been installed to reduce the Earth's magnetic field below 50 mG, so that the PMTs are not affected by it.
Water Cherenkov detectors as SK use the PMTs to collect the photons emitted, via Cherenkov effect [94], from a charged particle travelling through the water. The speed of light in a medium (v_l) depends on the refractive index (n) of the material $v_l = c/n$, where c is the speed of light in the vacuum. The Cherenkov effect occurs when a charged particle travels faster than the light in a medium: in this case the particle polarizes the atoms of the dielectric medium which promptly turn back to their ground state

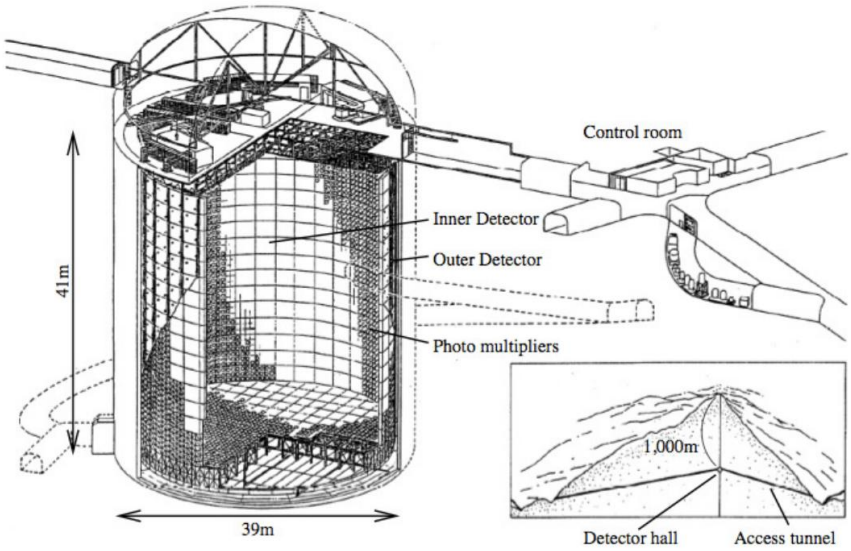

Figure 2.28: Diagram of the Super-Kamiokande far detector. Figure from [54].

emitting radiation (Cherenkov light). The emitted light propagates on the surface of a cone, around the particle path, of opening angle $\cos\theta = 1/n\beta$ where v is the speed of the particle in the medium and $\beta = v/c$. In water ($n = 1.33$) a relativistic particle ($\beta \sim 1$) has the maximum opening angle of $\sim 42°$. The cone axis corresponds to trajectory of the particle. If $\beta \sim 1/n$ the particle travels slower than the light in the medium and no Cherenkov light is produced. Therefore a particle, with mass at rest m_i, travelling through a dielectric medium with a given velocity v, must have a minimum energy E_i in order to produce Cherenkov light.

$$E_i = \frac{1}{\sqrt{1-\beta^2}} m_i c^2 = \frac{n}{\sqrt{n^2-1}} m_i c^2. \tag{2.13}$$

This threshold is a function of the mass of the particle m_i and of the crossing material. For instance in the water case the minimum energy is $E_i \sim 1.52\ m_i$ which corresponds to 775 keV for an electron (e), 160 MeV for a muon (μ), 212 MeV for a charged pion ($\pi^{\pm}$) and 1.42 GeV for a proton (p).
SK detects neutrino interactions thanks to the Cherenkov light emitted by the charged particles produced by the ν_μ or ν_e interactions with water. Inward and outward facing PMTs allows to identify entering/exiting particles rejecting backgrounds from outside the detector fiducial volume and tagging fully contained (FC) neutrino interactions. In a FC event the charged particles due to ν_μ or ν_e interactions with water must be produced and stop in the detector fiducial volume (2 m away from the ID wall for a total fiducial mass of 22.5 kton). Furthermore, as the particles cross the water, they lose energy and emit Cherenkov light which propagates towards the inward facing PMTs installed in the ID wall which record the charge and the time of the hits. The PMTs informations

are processed to reconstruct the vertex position, shape, size and orientation of the Cherenkov pattern (a ring if the particle is FC or a disk if the particle escapes the ID). The particle identification can be performed looking at the distinctive shape of the Cherenkov ring; muons propagate emitting just Cherenkov light which produces a single ring with well defined sharp edges while electrons tend to emit, during their propagation, photons via bremsstrahlung. The photons convert creating an electromagnetic shower which emits Cherenkov light at different angles generating then a ring with fuzzy edges. Additionally, given the small mass, an electron above few MeV will always produce a cone of maximal opening angle. SK has therefore a very good discrimination between e-like Cherenkov rings and μ-like Cherenkov rings which allows to separate ν_e from ν_μ interactions. Two example of FC contained events are shown in Fig. 2.29 a μ-like ring on the left (sharp edges) and a e-like ring on the right (fuzzy).
At T2K energy single ring events associated to the charged lepton produced by CC processes (see Fig. 1.2) are the most frequent neutrino interactions. The low momentum proton is not detected because it is below the Cherenkov threshold. However sometimes multi-ring events can occur in SK as well, when two or more Cherenkov rings are detected. The additional rings are due to the production of at least one second charged particle (pions) above the energy threshold.

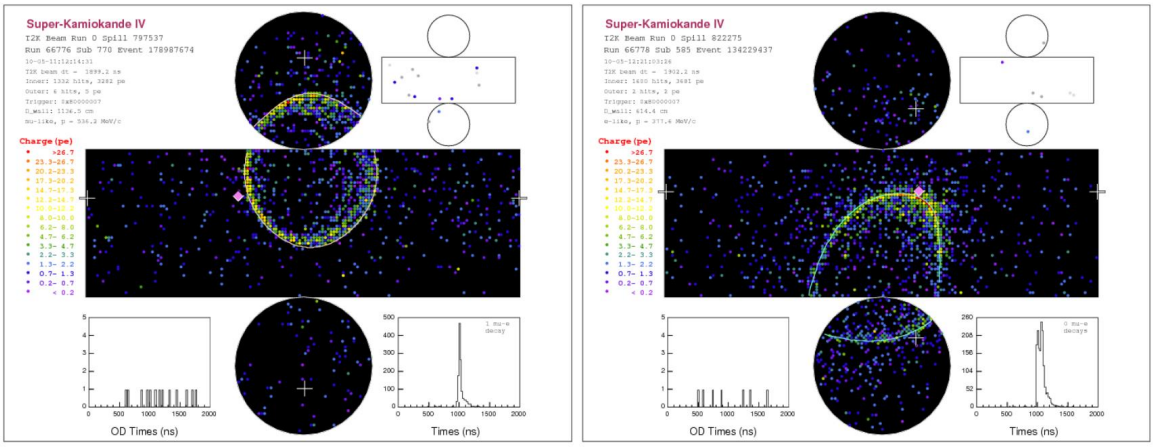

Figure 2.29: Reconstructed T2K events in Super-Kamiomande for a μ-like (left) and an e-like (right) ring. Figure from [54].

Chapter 3

The T2K Time Projection Chambers

In this Chapter an overview of the Time Projection Chambers (TPCs) [95] of the T2K experiment is provided. First the physical processes and working principles of gaseous tracking detectors will be summarized, then the ND280 TPCs and MicroMegas (MM) will be described as well as their performances.

3.1 Principles of gaseous tracking detectors

When a relativistic charged particle crosses a medium it can lose energy by exciting or ionizing the atoms according to the ionization potential of the surrounding material. Typically, for gaseous detectors gases with low primary ionization potentials (I) are chosen in order to facilitate the production of ionization electrons along the particle path. The mean energy loss per path length (dE/dx) is described by the Bethe-Bloch formula (Eq. 2.10) which relates the particle properties (m, β, z) to the composition (Z, A, I) of the traversing material. Since, gaseous detectors make precise measurement of the charged particles crossing their active volume exploiting the primary ionization electrons, in the following the motion of charged particle in the gas, the drift of the primary ionization electrons due to the ionization and the signal amplification are described.

3.1.1 Charged particle motion in the gas

When an electric field is applied, electrons and ions produced during the ionization process acquire, in addition to their random velocity v, a drift velocity v_d in the direction of the electric field. The drift velocity corresponds to the average distance covered by the drifting particles in the gas volume per time unit. It depends on the intensity of

the electric field, and can be written:

$$v_d = \frac{eE}{m}\tau \tag{3.1}$$

where E is the electric field and τ is the average time between two collisions. Along the drift electrons randomly change direction after scattering with the gas molecules, the momentum transfer per collision is not a constant. Excitation and ionization collisions between electrons and atoms, can cause a large energy loss which limits the maximum velocity they can reach. Thus the maximum velocity is attained when electron-atom collisions are minimized. Electrons with energies near the Ramsauer minimum [96] (Argon $\sim$ 0.23 eV) will have long mean free paths and as a consequence, would gain more energy before a collision occurs with the surrounding gas.

3.1.2 Amplification

In a gaseous detector the drift electrons are used to produce an avalanche in order to amplify the signal making it detectable. In the amplification region the electric field and the mean free path must allow the electrons from ionization to reach enough energy between collisions to be able to ionize the gas molecules. Usually gaseous detectors operate in the proportional mode: the signal is proportional to the number of primary electrons. The number of avalanche electrons N generated per path length dx is expressed by:

$$dN = \alpha N dx \tag{3.2}$$

the amplification factor α, also referred as gain coefficient, is the first Townsend ionization coefficient, that is a function of the electric field and of the gas density.

3.2 The Time Projection Chamber

The primary goal of a gaseous detector is to measure the particle ionization along the particle path in the detector active volume in order to reconstruct its properties thus performing tracking, particle identification and momentum measurement.
The Time Projection Chamber (TPC) is a gaseous detector invented in the late 1970's by David Nygren for the tracking of charged particles [97]. The track position is determined by the drift, along the field direction, of the ionization electrons to the extreme ends of the TPC (endplates) where they produce an electric signal which is readout. This provides a two dimensional projection of the track that combined with the time of arrival of the ionization cloud allows the reconstruction of the third coordinates and thus a 3D reconstruction of the track. The third coordinate is reconstructed as a function of the drift time which requires a precise knowledge of the drift velocity (constant for a uniform field) and of the time T_0 at which the particle crossed the detector. Typically, the T_0 is provided by an external trigger. In order to drift the electron in the desired

direction an electric field is applied between the extreme ends of the drift region: the cathode and the anode. Electrons drift towards the anode while ions drift to the cathode. The TPC normally exploits a uniform electric field oriented along the desired drift direction. Primary electrons exhibit a scattering in random directions along the drift affecting the resolution of the position of the track. Diffusion along the drift direction is called longitudinal diffusion while a diffusion perpendicular to the drift is referred to as transverse diffusion. The latter can be reduced introducing an external magnetic field oriented parallel or anti-parallel to the electric field, in this way any transverse diffusion has the Lorentz force counteracting it. Thus ionization electrons are bent around the line of the electric field. Moreover placing the TPC inside a uniform magnetic field allows also to measure the momentum of the charged particles from the curvature of the track, see Sec. 3.5.4 for more details.
Once the ionization electrons have crossed the drift region they arrive to the endplates where the readout is placed. Before reaching the anode the electrons need to be amplified to increase the amplitude of the signal over the electrical noise. Signal amplification can be accomplished using either wires in a Multi-Wire Proportional Chamber (MWPC) or an amplification region in Micro-Pattern Gaseous Detector (MPGD). The wires used in such chambers can break as a result of a spark and the ions produced together with the electrons near the wire usually drift back towards the cathode leading to a distortion of the electric field. On the contrary in a wireless TPC, most of the positive ions produced in amplification are collected immediately without distorting the electric field in the main drift volume, as will be explained later. For this reason T2K chose to use MPGD to amplify the electron signals and in particular a technology called *bulk MicroMegas*.

3.2.1 The micromesh Gaseous Detector

The T2K TPC was the first large scale TPC not using MWPC to detect the ionization electron signals. The T2K TPC uses micromesh Gaseous Detector, called MicroMegas (MM) [98]. The MicroMegas working principle is shown in Fig. 3.1.
A micromesh divides the gas volume in two separate regions: one where electrons drift (the drift region) and an amplification gap, of order of $\sim$ 100 μm, where electrons are amplified to produce a detectable signal. In the amplification stage, a very high electric field (20 to 70 kV/cm) is created by applying a voltage of few hundreds volts between the mesh and the anode. If the field ratio between the two regions, drift and amplification, is large enough and the mesh is thin enough, then the ionization electron are multiplied in an avalanche and collected by the anode with an efficiency of almost 100%. The anode can be segmented into strips or pads. When a charged particle passes through the TPC gas volume, the electrons produced by ionization along its trajectory drift towards the MM micromesh. In the amplification stage then the micromesh acts as cathode collecting all the ions produced by the gas ionization. In addition the smallness of the gap leads to a very fast signal. Usually, in absence of longitudinal diffusion,

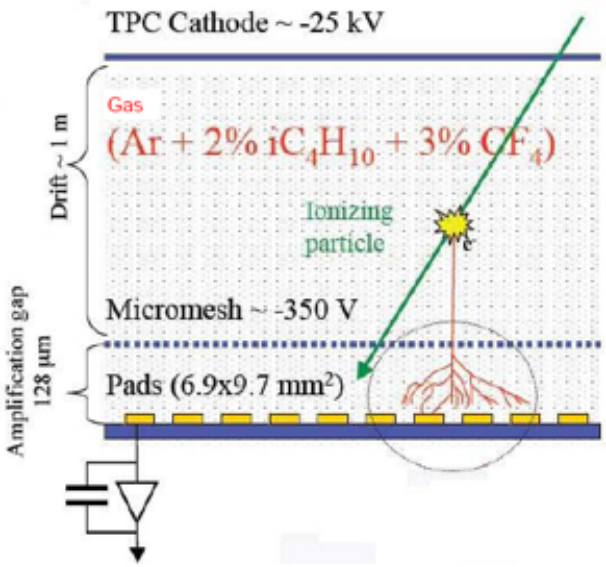

Figure 3.1: Schematic view of the MicroMegas detector used in T2K. The ionization electrons drift towards the micromesh that is placed $50 - 100$ μm above the anode. The micromesh is supported by short cylindrical pillars. Between the mesh and the anode, segmented to form pads, an avalanche is produced. Figure from [95].

electrons have a signal of few nanoseconds while ions have a signal of $\sim 50 - 100$ ns. Furthermore the fast signal and the high ion collection efficiency allow high rates to be sustained.

3.3 The T2K TPCs

As shown in Figure 2.18 three identical TPCs [95] are installed in the ND280 facility: the first one (TPC1) is placed downstream the PØD, the second (TPC2) is installed between the two FGDs while the last TPC3 is just in front of the FGD2 and upstream the downstream ECal. A simplified drawing of the TPC main components is shown in Fig. 3.2. Each TPC consists of a double box design which allows better electric isolation: an Inner Volume (IV) of a dimension of $1.808 \times 2.230 \times 0.854$ m^3 which contains the field cage and the drift volume filled with the gas mixture (see Sec. 3.3.2), and an Outer Volume (OV) which surrounds the IV. The dimension of the OV are 2.3×2.4 m^2 in the xy-plane perpendicular to the beam and 0.974 m along the beam direction z. The exterior of the OV is electrically grounded and consists of four walls and two endplates made of aluminum and aluminum/rohacell laminates for a total thickness of 15.2 mm. Moreover the volume between the outer and inner volumes is filled with CO_2 that serves as an electrical insulator for the high voltage used in the IV

thanks to its good dielectric rigidity. Figure 3.3 shows a detailed view of the OV and IV.

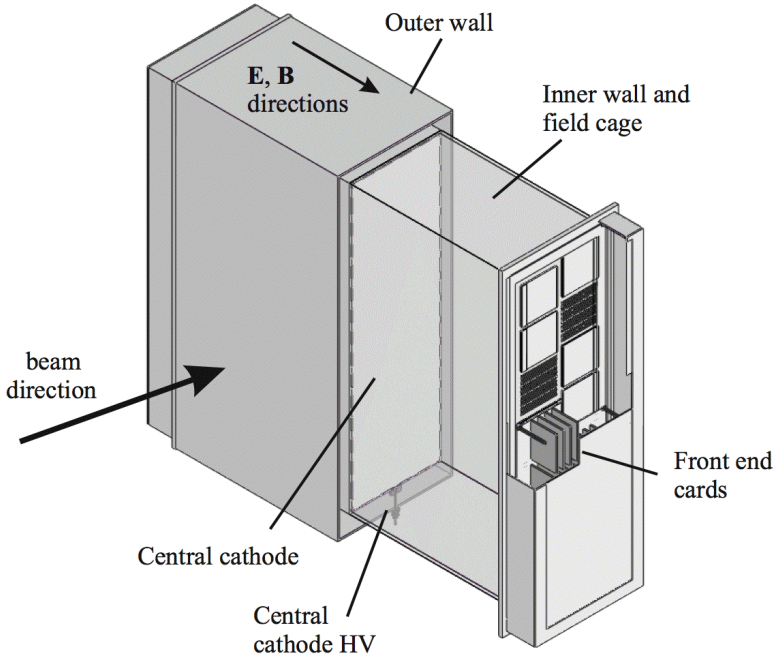

Figure 3.2: Schematic view of the T2K TPC detector. Figure from [95].

3.3.1 The Inner Volume

The IV consists of four walls and two endplates where the readout modules are installed. It is further divided by a central cathode in two separate volumes, the drift regions that contains the active volume of the TPC gaseous detector. During normal operation, under a magnetic field of 0.2 T, a voltage of -25 kV is applied to the central cathode. The walls, as well as the central cathode, are made of 1/32 inch of copper-clad G10 and G10/rohacell laminated onto both surfaces, giving a total thickness of 13.2 mm. The side walls are covered, on all sides, with a series of copper strips oriented parallel to central cathode of 10 mm width with a spacing of 1.5 mm. The strips are electrically connected to the central cathode via a precision resistor chain ($R = 20$ MΩ) in order to provide an uniform electric field inside the IV. According to the simulation the electric field is uniform to better than 10^{-4} for distance larger than 20 mm from the inner side wall. The IV is filled with a gas mixture Ar : CF_4 : iC_4H_{10} (95 : 3 : 2) and kept at a nominal pressure of 0.4 ± 0.1 mbar above the OV pressure. The TPC works at the atmospheric pressure. Finally at each extreme end of the IV 12 MicroMegas modules are installed in two columns of 6 modules each, as shown in Fig. 3.3.

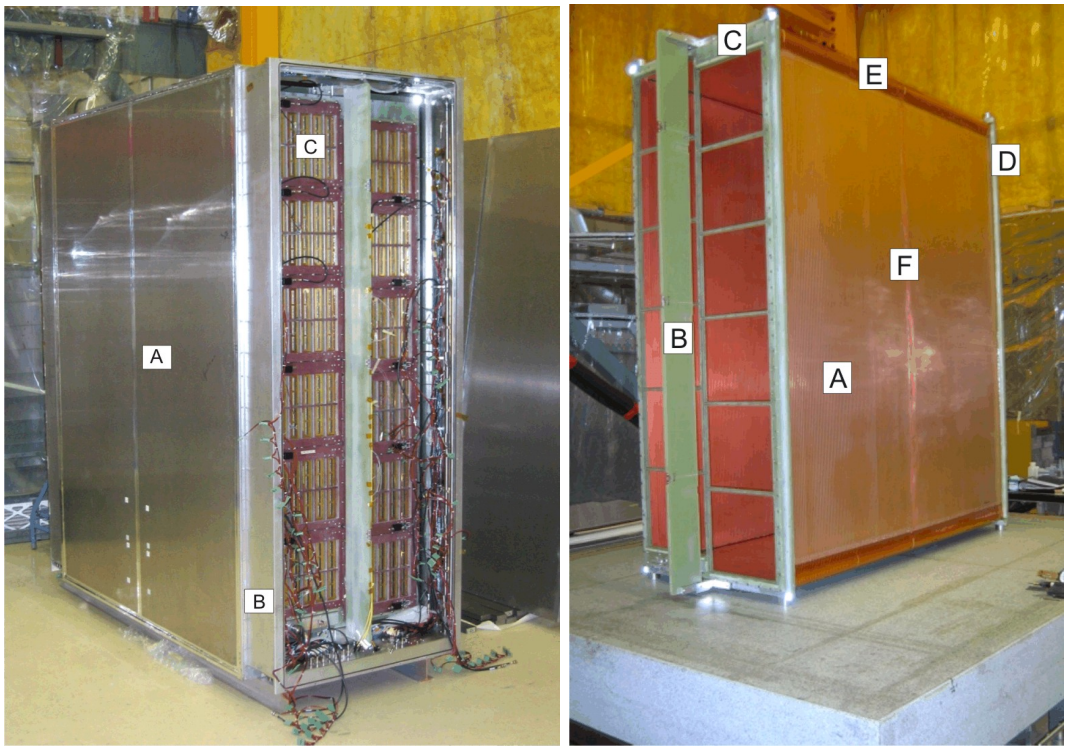

Figure 3.3: **Left:** outer box with the different components labeled. A: one of the outer box walls; B: service spacer; C: one of the MicroMegas modules inserted into the module frame. **Right:** picture of the Inner box. A: one of inner box walls; B: module frame stiffening plate; C: module frame; D: inner box endplate; E: field-reducing corners; F: central cathode location. Figures from [95].

3.3.2 The gas mixture

The gas mixture has been chosen to attain the best performances as possible in the determination of the momentum of the charged particles and their energy loss. Each gas component of the mixture plays a specific role in the TPCs operation. The Argon, which makes the majority of the mixture (95%), has a low primary ionization potential (15.8 eV) promoting the production of ionization electrons. Being a noble gas it reduces the possibility of re-absorption of the drifting electrons by another Ar nucleus since its valence shell is already filled by the electrons. Furthermore, given its natural abundance as 3^{rd} most abundant constituent of air, it is also reasonably cheap to purchase. The CF_4 (3%) serves to increase the drift velocity (7.8 cm/μs) in the drift region and to reduce the transverse diffusion (237 μm/$\sqrt{\text{cm}}$). In addition together with the isobutane $i\text{C}_4\text{H}_{10}$ (2%), the CF_4 is used as quencher to absorb photons emitted by the de-excitation of the Ar atoms. These photons, if not absorbed, can extract electrons from both the central cathode and the micromesh and start a new series of avalanches bringing the MM out of the proportional region. In this case new cascades will continuously be produced

making the detector blind to subsequent particles and damaging the equipment. In order to prevent this, polyatomic gases are added to the gas mixture to absorb those photons and dissipate the energy via elastic collisions and dissociation. Moreover, the gas system should also keep the oxygen contamination in the IV at the level of 10 ppm. A larger contamination would cause the phenomenon of attachment in the TPC gas and consequently a dependence of the signal on the drift distance. Therefore the gas is continuously recirculated and filtered.

3.3.3 The MicroMegas module

In the T2K TPCs the MicroMegas technology is used to detect the electrons from the gas ionization. For the modules production a new method developed in collaboration between CERN and CEA Saclay has been used [99]. This method, called Bulk technique, allows to produce in series robust detectors laminating a woven mesh on a PCB covered by a photo-imageable polyimide film. Each TPC is instrumented by 24 Bulk MicroMegas, 12 on each readout plane, arranged in a matrix of two columns of six modules each. The two columns are vertically staggered one respect to the other by 4.53 cm, to prevent as much as possible horizontal tracks to entirely cross the dead zone between two vertical modules. The dead zone between the two columns is 21 mm while it is of 7.7 mm between two modules belonging to the same column. Each module has a dimension of 349.3×359.1 mm^2 and consists of 1728 pads divided into 48 rows and 36 columns: 1726 active pads which collect the charge plus 2 pads located at one corner used for the micromesh high voltage connection from the backside of the PCB. Figure 3.4 on the left shows the pad grid with a zoom in the structure of the corner where the 2 pads deliver the voltage to the micromesh. Each pad has a dimension of 6.85×9.65 mm^2 for a total active area of ~ 3 m^2 per TPC and for a total number of channels of 124000 for the 3 TPCs. An average gain (~ 1600) is obtained by applying a high voltage of -350 V to the mesh. The number of sparks, electric discharges between the micromesh and the pads, is 0.1 sparks per module per hour of operation. A picture of the Bulk MicroMegas glued to the stiffener is shown in Fig. 3.4 on the right, its total thickness is 19.5 mm.
One advantage of the T2K MicroMegas modules is that they are completely independent and can be mounted or dismounted from the TPC endplate. In case of failure, this makes the detector replacement easier.

3.3.4 The Front-End electronic

The TPC electronic system must be able to record all the beam events. The nominal T2K event rate is 0.5 Hz which corresponds to the frequency of protons extraction from the Main Ring, thus the electronics is designed to read at a rate up to 20 Hz, providing a comfortable bandwidth to record cosmic rays triggers, pedestals and laser calibration events. The readout consists of two main parts: front-end electronics, directly mounted

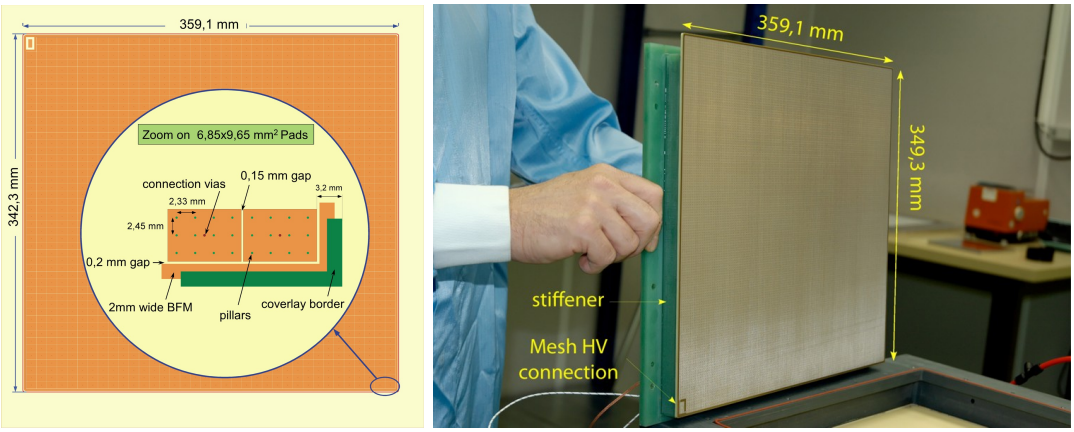

Figure 3.4: View of the PCB (left) from the anode pads side and a picture of a Bulk MicroMegas module for the T2K TPC (right). Figures from [95].

on the MicroMegas module and back-end electronics, housed in a standard rack. Each one of the 72 MicroMegas module is read by a set of six FEC (Front End Cards) connected together by a FEM (Front End Mezzanine) card, shown in Fig. 3.5. Each FEC is made up of four programmable ASIC chips called AFTER (Asic For TPC Electronic Readout), developed at CEA-Saclay. The purpose of this device is to shape and sample the signals coming from the MicroMegas pads. The large drift length of the TPC requires an accurate method to obtain the coordinate informations by continuously sampling pad signals in analogical memory arrays. The AFTER chip samples detector pad signals in a 511-bin Switch Capacitor Array (SCA) at a user defined frequency (up to 50 MHz). The sampling window can be adequately set through the sampling time (the time difference between two consecutive samples). In the case of the T2K TPCs the maximum drift distance is 90 cm. Given the electrons drift velocity in the gas mixture (7.8 cm/μs) this distance is covered in approximately 12 μs, adding 3 μs corresponding to the width of the T2K neutrino beam make an acquisition window of approximately 15 μs. In order to cover this window comfortably, the sampling time is set to 40 ns corresponding to an acquisition window of ≈ 20 μs. Moreover the AFTER chip is also characterized by its very low noise (600 e^-) giving an excellent signal-to-noise ratio of ≈ 200 for minimum ionization particle signal.
A total of 18 data Concentrator Cards (DCCs) are used to read information from the three TPCs. They are designed to supply the reference clock to the FEM and transmit signals from the FEMs via an Ethernet connection to an acquisition PC. The central software element of the DCC is a command server program which receives orders from the TPC data acquisition PC over an Ethernet connection. It decodes, translates and posts the corresponding commands to the front-end electronics over its optical communication links, receives the responses from the front-end, encapsulates them in Ethernet frames, and finally returns this information to the client PC. The requested acquisition rate is 20 Hz.

The Front-End Mezzanine is connected to 6 FECs and its main tasks are: to receive clock, trigger and synchronization information from its DCC, duplicate the signals to the six FECs and receive event data digitized by the ADCs of the FECs to deliver event fragments to its DCC. The required input bandwidth is one of the challenging aspects of the FEM: given a 20 MHz conversion rate for the quad-channel 12-bit ADC of each FEC, the FEM has to receive and store an aggregate data flow of 5.76 Gbit/s. Transmission to and reception from the DCC occurs at 2 Gbit/s each way. The core of the FEM is a large Field Programmable Gate Array (FPGA) device that has to provide a few million gates, a couple of hundred I/O pins with an aggregate bandwidth of 20 Gbit/s.
A summary of the main TPC characteristics is shown in Table 3.1.

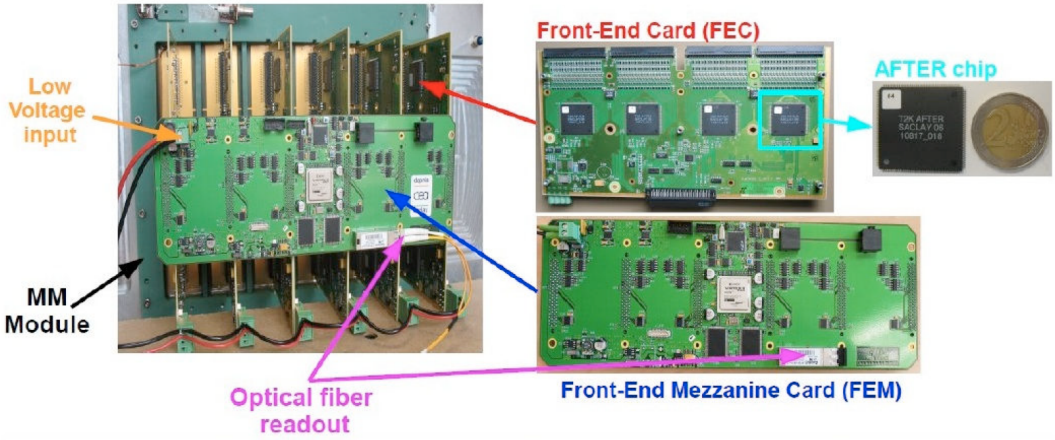

Figure 3.5: External view picture of a MicroMegas module read by 6 FEC connected by a FEM. Figure from [95].

Maximum drift distance	90 cm
Gas mixture	$Ar : CF_4 : iC_4H_{10}$ (95 : 3 : 2)
Ionization potential Ar	15.8 eV
Cathode high voltage	-25 kV $\rightarrow E \sim 280$ V/m
Drift velocity	7.9 cm/μs
Transverse diffusion coefficient	237 $\mu/\sqrt{\text{cm}}$
Total number of readout channels	124272
Pad dimensions	6.9×9.7 mm^2
MicroMegas high voltage	-350 V $\rightarrow E \sim 27$ kV/m
MicroMegas Gain	~ 1500 (at 350 V)
ASIC sampling time	40 ns
ASIC peaking time	200 ns

Table 3.1: List of the TPC main design parameters in the default running conditions with a magnetic field of 0.2 T.

3.4 The TPC calibration

To keep uniform performance in time, the TPC must operate in stable conditions regarding the gas properties, the electric and magnetic fields, the MicroMegas gain and the Front-End Electronics. To monitor the TPCs two different systems are used: a laser calibration system and a gas monitor chamber. This system allow to continuously monitoring the effects which affects the electron drift.

3.4.1 Laser Calibration System

A UV-laser based calibration system is installed in the TPC providing a real-time calibration of each TPC during data taking. A pattern of dots of 88 mm of diameter and strips 4 mm wide in aluminum are glued to the copper cathode surface. A diagram of the laser pattern is shown in Fig. 3.6 left while the laser setup is shown on the right. A Nd:YAG UV-laser is located on the floor below the detector, the laser pulse is then transported and injected in the TPC through the readout planes by 18 quartz optical fibers. Each readout plane has 3 injection points, each one covers a region of the central cathode measured by 4 MicroMegas modules. When the dots and strips on the cathode are illuminated by the laser pulse they release electrons via photoelectric effect, electrons drift then towards the readout plane where they are amplified and detected producing an image of the aluminum pattern. Any distortion in the electron drift would lead to a relative displacement with respect the expected pattern.

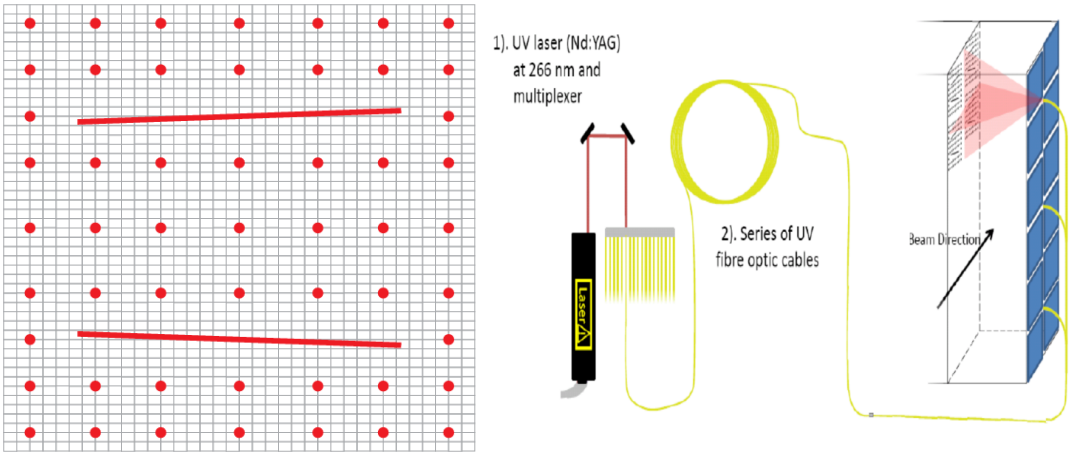

Figure 3.6: **Left:** pattern of aluminum dots and strips for one MicroMegas module on both sides of the central cathode. The grid pads gives the readout pads projection onto the cathode. **Right:** the laser system setup. Figure from [95].

3.4.2 Gas Monitoring System

The Gas Monitor System (GMS) measures the properties of the gas entering and exiting the TPCs. It consists of two mini-TPCs designed to have the same features as the T2K TPCs in terms of gas ionization, electron drift under a static electrical field and electron amplification. The MicroMegas used by the GMS are smaller but produced in the same way. They are installed in the same gas line that feeds the three TPCs: one chamber samples the gas mixture before being sent to the TPCs while the other receive the gas returning from them.
The gain is measured by using a source of ^{55}Fe. It decays into ^{55}Mn by electron capture emitting a γ ray of 5.9 keV of energy, the photon interacts inside the GMS producing a well known number of electrons that drift towards the MicroMegas. The gain is then calculated comparing the measured and expected number of electron from the emission of 5.9 keV photon.
The drift velocity monitoring is done by comparing the drift time between two tracks perpendicular to the drift field originated at a well defined separation distance. To accomplish that two sources of ^{90}Sr are used. The method exploits the β-decay of the ^{90}Sr to ^{90}Y. The emitted electron produce a track in the chamber, if the electron reaches the scintillating fibre below one of the sources a drift velocity is measured. Figure 3.7 shows a picture of the GMS and its experimental setup.

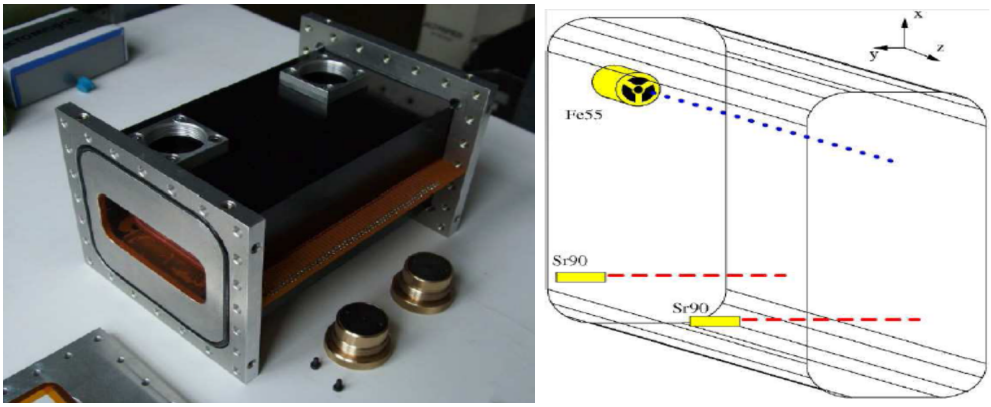

Figure 3.7: Picture of one gas monitor chambers on the left and the layout of the experimental setup on the right.

3.5 The TPC performances

3.5.1 Track reconstruction

The reconstruction of the tracks in the TPCs is based on the information recorded on the different pads of the MicroMegas modules. The signal of each pad is processed individually, by applying the gain calibration constants as a function of the ambient

temperature and pressure variations and removing dead and noisy channels. The output of this process is a waveform corresponding to the temporal distribution of the charge obtained, after amplification, from the electron cloud reaching a pad. Track reconstruction can be split in two main steps: the clustering and the likelihood method. The characteristic waveform is shown in Fig. 3.8 on the lef.

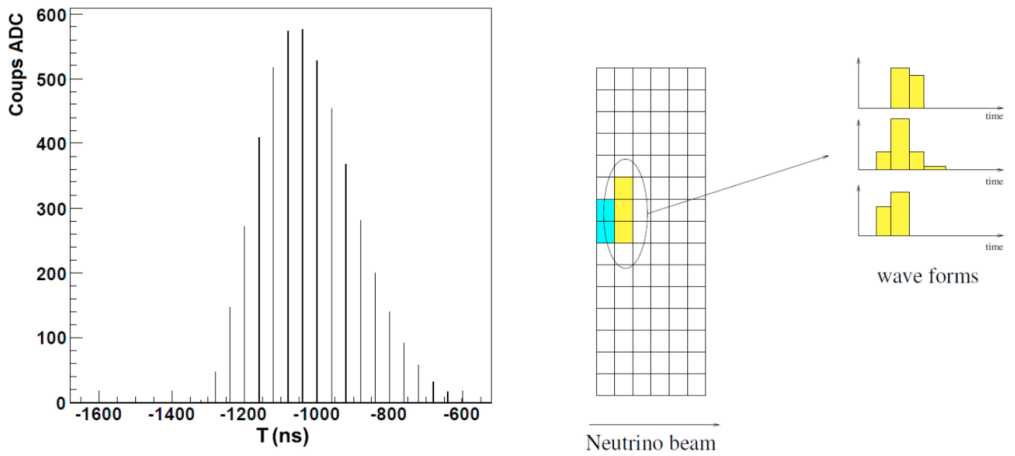

Figure 3.8: **Left:** characteristic waveform signal associated to a charge deposition in a pad. **Right:** schematic explanation of the clustering criteria of connectivity and time coincidence. Pad associated at the same cluster are displayed in the same color.

Clustering

The first step in the track reconstruction consists in clustering the waveforms of the pads following a simple criterion of connectivity: waveforms have to be in adjacent pads in space and in temporal coincidence. Since the particles originating from neutrino interactions are mainly emitted in the forward region, the clustering is done within vertical pad columns. For high angle tracks instead, because of the proximity to the vertical direction, the clustering can be done in horizontal pad rows. Due to the transverse diffusion of electrons in the gas, several pads can collect part of the electron-deposited charge of a primary track. Therefore the number of pads contained in a cluster depends on the drift distance. It is usually two for horizontal tracks crossing the center of the drift region but it can be one for tracks entering the TPC near the readout plane or three for tracks close to the cathode. A cluster is then defined by the following criteria (i.e. horizontal tracks):

Connectivity: neighboring pads must belong to the same column. The distance in y between the center of two pads must not be greater than the height of two pads.

Time coincidence: the difference in time between two waveforms must be lower than 80 ns, equivalent to two sampling time units.

Figure 3.8 shows on the right the clustering process and the waveforms of pads that satisfy the connectivity and time coincidence criteria. Clusters are then connected using a pattern recognition algorithm to form a track segment. Once that segments are connected, the reconstruction program selects the combination that provides the longest reconstructed track segment that is identified as the primary track left by a charged particle. In this way it is possible to identify branches that leave the main track and have a minimum number of independent segments. They could correspond to interactions in the TPC volume.

Likelihood method

The likelihood method is based on the comparison between the observed charge within a cluster and the charge predicted assuming a given track angle and position. Track's predictions are based on a simple model of electron drift and uniform charge deposition on a pad along the z-axis. The number of primary electrons n_i measured by a pad i with a gain g_i is defined as:

$$n_i = \frac{ADC_i \cdot C_i}{g_i} \tag{3.3}$$

where ADC_i is the charge collected in ADC units while C_i is the equivalent number of electrons per ADC channel. The likelihood function is then defined as:

$$log\mathcal{L} = \sum_i n_i log\ p_i + const \tag{3.4}$$

where p_i is the probability of a primary electron to be associated to the pad i, p_i is defined by the following formula:

$$p_i = \frac{Q_i(\vec{x}, \vec{p}, \sigma)}{\sum_j Q_j(\vec{x}, \vec{p}, \sigma)} \tag{3.5}$$

where $Q_i(\vec{x}, \vec{p}, \sigma)$ is the predicted charge deposited in the pad i by a track of coordinate $\vec{x}$, momentum $\vec{p}$ and electron cloud width σ which is a function of the drift distance. The sum is over all the pads of the cluster including the pad i. The charge deposited in a single pad can be described by a gaussian and defined as:

$$Q(x) = \frac{Q_0}{\sqrt{2\pi\sigma^2}}\ e^{-\frac{x^2}{2\sigma^2}}. \tag{3.6}$$

where σ is the charge width at the pad plane which is a function of the drift distance. Finally the likelihood is maximized in order to obtain the track coordinates.
While the y and z coordinates are determined by the pad, the x coordinate is computed using the drift time of the electrons, hence it is necessary to know at which time the track was created. This time, called T_0, must be obtained by matching the track passage with fast detectors, such as FGD or ECal. For instance when a particle crosses the

TPC and the FGD, the TPC tracks is matched to the FGD signal which can provide a time measurement with a resolution of few nanoseconds. Moreover is also possible to determine the T_0 when the track passes through the cathode located at the center of the TPC. The T_0 is then obtained by subtracting the maximum drift time of approximately 12 μs from the arrival time of the electrons on the pads corresponding to the position in the YZ-plane where the track crossed the cathode.
In the TPC coordinate system, due to the electron drift in a magnetic field, the trajectory of the track can be parametrized by a three-dimensional helix where x and y are expressed as a function of z while the corresponding slopes t_x and t_y are given by the relations:

$$x = x_0 - \frac{t_{x_o}}{\rho \cos\phi_0} \left(-\phi_0 + \arcsin\left(-\delta_z \rho + \sin\phi_0\right)\right) \tag{3.7}$$

$$t_x = \frac{t_{x_0} \cos\phi_0}{\sqrt{1 + \delta_z \rho - \sin^2\phi_0}} \tag{3.8}$$

$$y = y_0 + \frac{1}{\rho}\sqrt{1 + \delta_z \rho - \sin^2\phi_0 - \cos\phi_0} \tag{3.9}$$

$$t_y = \tan\left(\arcsin\left(\sin\phi_0 - \delta_z \rho\right)\right) \tag{3.10}$$

where x_0 and y_0 are the initial coordinates of the track, ρ is its curvature, t_{x_0} is the projection of the tangent in the XZ-plane. ϕ_0 is the angle in the YZ-plane and finally $\delta_z = z - z_0$ is the distance from the origin of the track on the z-axis. Once the likelihood is determined, the track reconstruction is performed independently in the three TPCs. After the individual track segments have been found, a Kalman filter algorithm [100] is used to match the segments in the TPCs and the reconstructed tracks in the others detectors, in particular the FGD and ECal. This algorithm takes into account the material distribution and the reconstructed track momentum to predict the track coordinates, angle and momentum at the matching plane. In the case of a track that crosses two TPCs and the FGD between them, the matching plane is defined as the center of the FGD. The matching follows a standard quality criterion that computes the χ^2 of the matching. If several tracks fulfill the requirement, the one with the best quality is selected. Eventually, tracks are refitted together in order to improve the momentum resolution. Once the track of the particle has been reconstructed the particle identification method, described in Sec. 3.5.3, is applied.

3.5.2 Spatial resolution

As previously described, the deposited charge due to a charged particle crossing a TPC can be spread over a few pads. The spatial resolution is obtained through the comparison of the y (transverse) coordinate calculated by the global fit of the track trajectory to the one resulting from a single cluster fit. The distribution of the residuals is then described by a Gaussian which gives the resolution and possible bias due to the

charge collection in the TPC. The distribution is obtained with a large number of track. Figure 3.9 shows the spatial resolution obtained with T2K data considering all clusters and any number of pads per cluster. The loss of spatial resolution at short drift distance is due to the large number of clusters involving only one pad, since the electron transverse diffusion is low. Therefore the resolution is limited by the pad size. The spatial resolution reaches a minimum of about 600 μm for drift distances of the order of 25 cm and increases up to about 700 μm for the maximum drift distance ($\sim$ 90 cm) when the track is close to the central cathode, due to larger diffusion. Figure 3.9 also shows the spatial resolution as a function of the angle of the track with respect to the horizontal plane for all drift distances or number of pads per cluster. The resolution deteriorates with the angle due to ionization fluctuations along the track. These fluctuations increase the uncertainties in the charge collected by neighboring pads of the same cluster when the angle is larger.

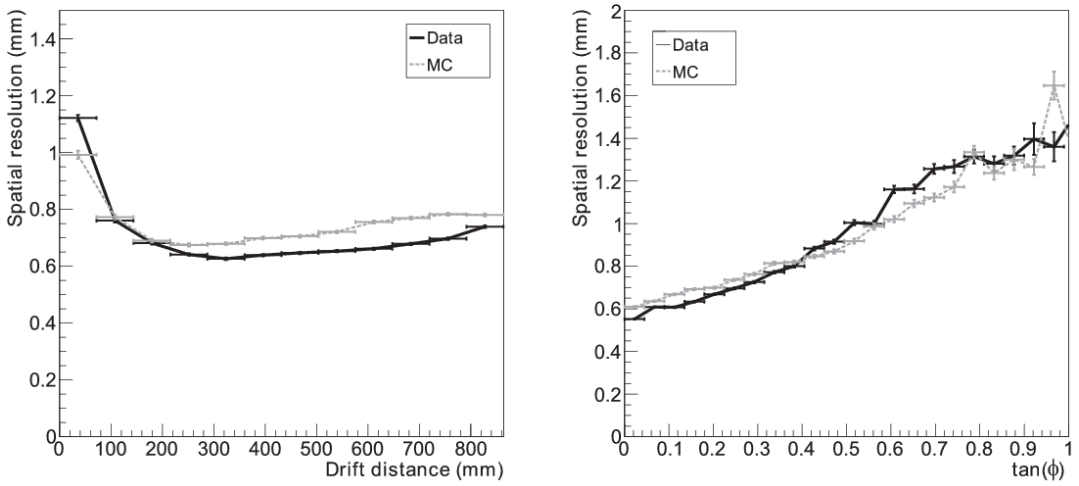

Figure 3.9: Spatial resolution per cluster as function of the drift distance (left) and of the tangent of the angle (right) with respect to the horizontal plane. Black continuos line/points show the results computed from data while grey dashed line/points show the results from simulations. Figures from [95].

3.5.3 Particle identification

According to Eq. 2.10 the loss of energy is a function of the particle speed β and hence of its momentum (p) and its mass (m), $p = m\beta$. Therefore, the joint measurement of the particle momentum and loss of energy in the TPC allows to determine the mass of the particle and thus to identify it. The particle identification (PID) in the TPC is performed by measuring the charge collected, cluster by cluster, by the MicroMegas modules. The method is based on the measurement of the truncated mean of the energy

loss from ionization [101]. The identification algorithm is calibrated to take into account all the factors that may affect the measurement of the deposited charge, such as the length and angle of the track or the electron drift conditions or the gain of the modules. In order to identify a particle, the measured energy loss of the track is compared to the expected value under the assumption of different particle type (electron, muon, pion and proton). This comparison is expressed through a pull which represents the difference between the measured value and the expected value for a given particle hypothesis:

$$Pull_i = \frac{(dE/dx)_{meas} - (dE/dx)_{exp,i}}{\sigma_{(dE/dx)_{exp,i}}} \tag{3.11}$$

where $(dE/dx)_{meas}$ is the measured energy loss of the reconstructed track while $(dE/dx)_{exp,i}$ is the one expected for the particle $i = e, \mu, \pi, p$ at such measured momentum. Finally $\sigma_{(dE/dx)_{exp,i}}$ is the uncertainty in the expected dE/dx for the particle i. The pull measures the standard deviation of the measured dE/dx from the expected value for a particle i. Figure 3.10 shows the measured energy loss in the TPCs, as a function of the measured track momentum compared with the expected curve for a particle with given mass and charge. Particles with similar mass, like muons ($m_\mu = 105.66$ MeV/c^2) and pions ($m_\pi = 139.57$ MeV/c^2) show a similar behavior, while lighter and heavier particles as electrons ($m_e = 0.511$ MeV/c^2) and protons ($m_p = 938.27$ MeV/c^2) have very different energy losses. Finally, in order to determine which particle hypothesis is the most likely for the reconstructed track, the pull are used to calculate a test statistic:

$$\mathcal{L}_i = \frac{e^{-Pull_i^2}}{\sum_l e^{-Pull_l^2}}, \tag{3.12}$$

where $\sum_l$ is the sum over all hypotheses. The probability of identifying a muon as an electron, for tracks below 1 GeV/c and a pull in the electron hypothesis of $-1 < Pull_e < 2$, is 0.2%. This proves the excellent discrimination power of the TPC to identify the intrinsic ν_e contamination in the ν_μ beam in charge current interactions which produce, respectively, an electron or a muon in the final state.

3.5.4 Momentum measurement

With the reconstruction algorithm described above, see Sec. 3.5.1, the curvature of the track, and thus its momentum, can be measured. Given a particle with charge q and momentum $\vec{p} = (p_x, p_y, p_z)$ moving in the horizontal plane, in the TPC it is curved under the action of the uniform axial magnetic field of magnitude $\vec{B} = (B_x, 0, 0)$ parallel to the drift and perpendicular to the cathode and anode plates. The projected trajectory of the track in the perpendicular plane to the field is then an arc of a circle of radius:

$$R = \frac{p_t}{qB_x}, \tag{3.13}$$

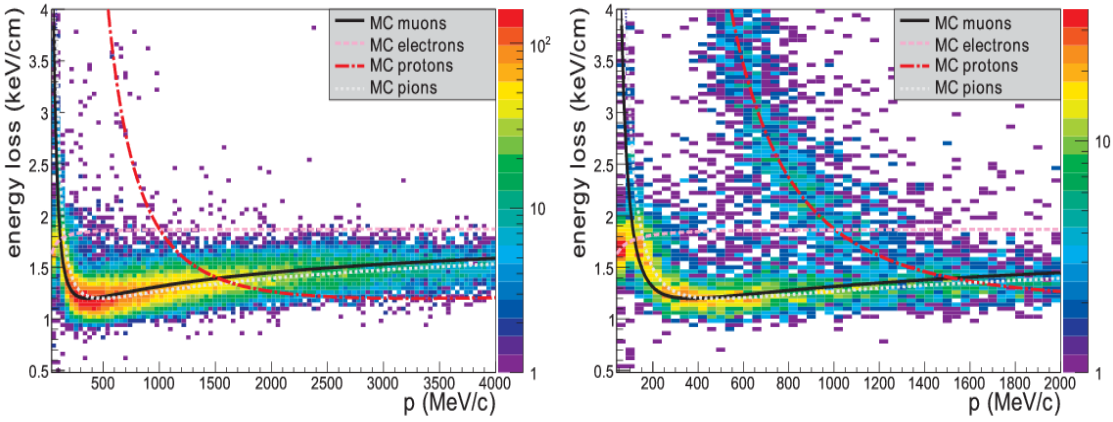

Figure 3.10: Comparison of the measured dE/dx as a function of the momentum of the track for negative (left) and positive (right) particles. The expected value for different particle hypothesis is also shown. Figures from [95].

where $p_t = \sqrt{p_y^2 + p_z^2}$ is the transverse momentum which can also be written as $p_t \sim 0.3 B_x R$ considering energy in units of GeV/c, radius in meters and field in Tesla. The radius R is connected to the sagitta s of the arc formed by the trajectory of the particle, as shown in Fig. 3.11. For large track momentum ($s \ll l$):

$$p_t \approx \frac{qB_x l^2}{8s}. \tag{3.14}$$

The resolution of the momentum can be estimated using the Gluckstern formulas [102]. Under the hypothesis of track composed of N_p equidistant points and neglecting multiple scattering, the relative uncertainty on the measurement of the transverse momentum is equal to the relative uncertainty in the measurement of the sagitta and is given by:

$$\frac{\sigma_{p_t}}{p_t} = \frac{\sigma_s}{s} = \sigma_{yz} \frac{p_t}{qB_x l^2} \sqrt{\frac{720}{N_p + 4}}, \tag{3.15}$$

where σ_{yz} is the spatial resolution in the transverse plane. Finally to calculate the total particle momentum knowing its transverse momentum and the polar angle θ between the track and the direction of the magnetic field $\vec{B}$ is given by:

$$p = \frac{p_t}{\sin\theta}. \tag{3.16}$$

The resolution on the measurement of the polar angle θ depends on the resolution in the drift direction x, on N_p and on the track length l

$$\frac{\sigma_\theta}{\theta} = \frac{\sigma_x}{l} \sqrt{\frac{12(N_p - 1)}{N_p(N_p + 1)}}. \tag{3.17}$$

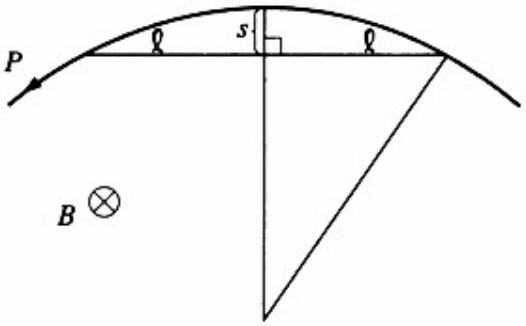

Figure 3.11: Measurement of the sagitta of a curved track under the action of a uniform axial magnetic field.

Usually a reconstructed horizontal track which entirely crosses one TPC has 72 clusters. Given the nominal magnetic field $B = 0.2$ T, assuming a track length of $l = 72$ cm and a spatial resolution of $\sigma_{yz} = 700$ μm which correspond to a medium drift length in the gas volume (see Fig. 3.9) the expected resolution for a track of transverse momentum of 1 GeV/c is $\sim 10\%$. This track would have a sagitta of approximately 4 mm, thus to control the momentum scale measurement to better than 2%, it is necessary to be able to understand variations of the curvature of the track at 0.1 mm level.
Three sources of error can affect the determination of the momentum in the TPC:

1. inhomogeneities of the magnetic field which lead to distortions in the drift of electrons of the trajectory in the MicroMegas reading planes;

2. inhomogeneities of the electric field affecting the drift of electrons;

3. misalignments of the MicroMegas modules introducing an error in the determination of the curvature of the particle.

In order to estimate the error in the determination of the track momentum introduced by magnetic field distortions, a mapping of such inhomogeneities has been integrated into the model describing the electron drift process. This mapping was obtained from measurements of the magnetic field made with Hall probes before the installation of the detectors inside the magnet [103]. It also takes into account the calibration data using the laser calibration system. Figure 3.12 shows the distortion map in the YZ-plane in the TPC region. The magnetic field in the TPC has inhomogeneities of the order of a few 10^{-4} and mostly affect the most downstream TPC which is placed closer to the extreme end of the magnet.
Similarly to the magnetic field, the reconstruction of the curvature can be biased by inhomogeneities of the electric field. The transverse diffusion of the electron cloud due to the electric field variations had been studied thanks to the laser calibration system in absence of magnetic field and are estimated to be lower than the spatial resolution.

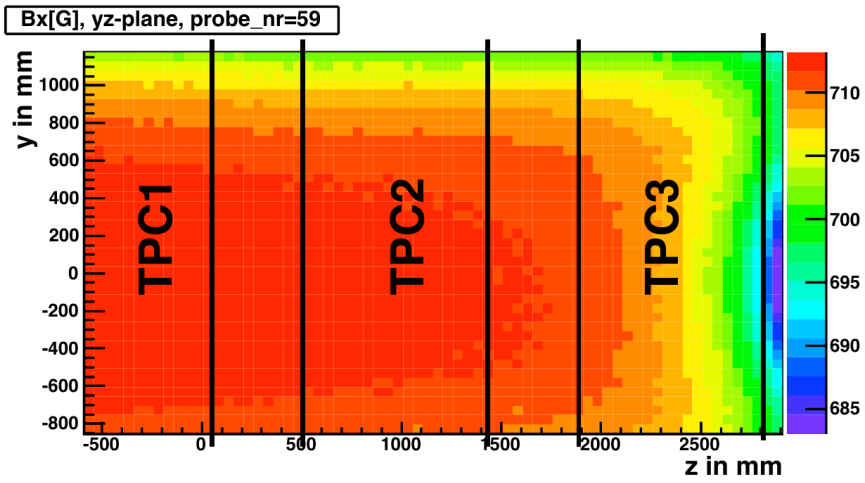

Figure 3.12: Magnetic field map (in Gauss) in the TPC region. The neutrino beam is entering from the left. Modified from [103] to highlight the TPCs.

Recently a new approach studied electric field distortions in the TPCs, exploiting a hit resolution study performed using information from the track reconstruction. It selects tracks crossing the TPC and measures the difference in the transverse direction (y) between the fitted and the hits positions in each pad column of the MicroMegas. Assuming that the magnetic field was properly corrected previously, such distributions should be centered at zero. Consequently, any deviation from zero can be caused by electric field distortions. Since electric field distortions are highly correlated with module misalignments this study was performed with alignment correction enabled.
Finally, misalignment of the MicroMegas modules can introduce an error in the measurement of the radius of curvature of the particle. In the following Chapter 4, the determination of the misalignment between MicroMegas modules is described.

Chapter 4

Alignment of the MicroMegas modules

In this Chapter, the method used to determine the relative orientation and position of the MicroMegas (MM) modules that instrument each readout plane of the ND280 TPC will be described. The method is based on the comparison of the segments belonging to the same track projection and traversing two adjacent modules. The reconstruction algorithm has been modified such that each segment is considered as an independent track and its parameters are determined by performing an independent reconstruction in each module. As shown in Fig. 4.1, the relative difference (residual) in orientation ($\Delta\phi$) and translation (Δy) of the projection of the track on the YZ-plane is calculated, for a pair of modules, at fixed z coordinate in the middle plane between the two MM detector columns. Thus the misalignments associated with rotations ($\delta\phi$) and relative shifts (δy and δz) between the two modules in the YZ-plane completely define the distributions of the residuals ($\Delta\phi$, Δy).
To determine the misalignment of MM modules, data taken without magnetic field ($|\vec{B}| = 0$) are used. This configuration allows to use track parametrized by straight lines, decoupling misalignment effects from magnetic field inhomogeneities. Furthermore neither $\vec{B}$ nor $\vec{E}$ field corrections are applied in the track reconstruction process in order to not introduce potential bias due to external corrections in the MM alignment procedure. The residuals $\Delta\phi$ and Δy are used as input to a fit to extract the rotational and translation MM correction constants. The fit is validated via MC test geometries where a well known MM misalignment is simulated in the detector. Finally, a study on the impact of the new alignment corrections on the momentum measurement in comparison to the optical corrections constants currently in use in ND280, will be quantified.

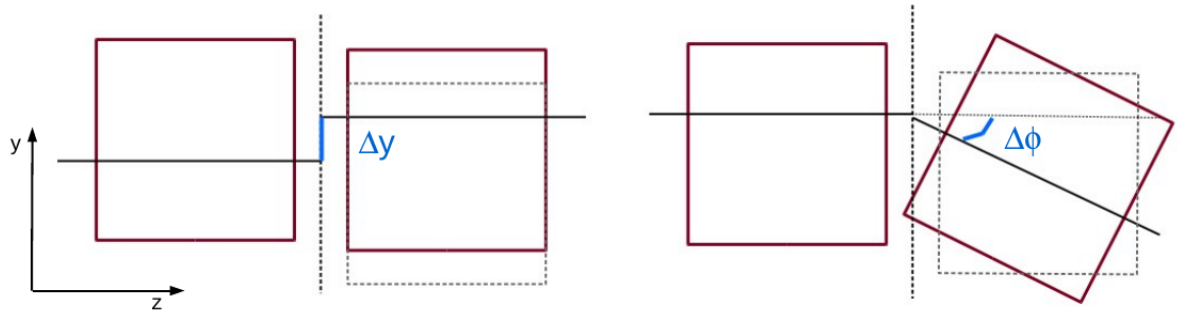

Figure 4.1: Schematic view of residuals extrapolation: translation residual Δy on the left, rotational residual $\Delta\phi$ on the right.

4.1 Geometry and enumeration

As already discussed in the previous Sec. 3.3.3, in the T2K TPCs the MicroMegas technology has been chosen to detect the drift electrons produced by charged particles passing through the TPC gas volume. Each TPC is read by 24 MM modules, 12 on each readout plane arranged in a matrix of two columns of six modules each, placed in the end plates EP0 (EP1) at the fixed coordinate $x = -(+)1000$ mm in the ND280 coordinate system XYZ (see Fig. 2.18). In this coordinate system the three TPCs cover the volume $x \in [-1150, 1150]$ mm, $y \in [-1170, 1230]$ mm, and $z \in [-885, 89]$, $[474, 1448]$, $[1833, 2807]$ mm for TPC1,2,3 respectively. The different MMs of a single readout plane (EP0 or EP1) are enumerated from 0 to 11: the top one is MM0, the bottom one is MM11. The modules MM0-MM5 belong to the column lifted up (column 0) while MM6-MM11 to the other column (column 1), as shown in Fig. 4.2. The enumeration has been chosen to reflect the mirror geometry between the EPs. Thus one MM can be characterized by 3 numbers, for instance the top MicroMegas in column 1 instrumenting the readout plane 1 (EP1) of the last TPC (TPC3) will be identified in an unambiguous way by TPC3_EP1_MM6.
Each MM module is composed of 1728 pads arranged in a 48×36 matrix. Each pad is identified by row and column indexes. In column 0, pad column numbers run from 0 to 35 while pad row numbers from 0 to 47, in column 1 instead, columns run from 1 to 36 while rows from 1 to 48. Enumeration is specular in the readout planes.

4.2 Optical alignment precision

The MM alignment in use in T2K is based on a optical survey (Survey Alignment) performed during the TPCs assembling, prior to the electronics installation. Therefore the Survey alignment does not take into account possible later deformations of the mechanical structure of the TPCs due to the electronics. For these measurements

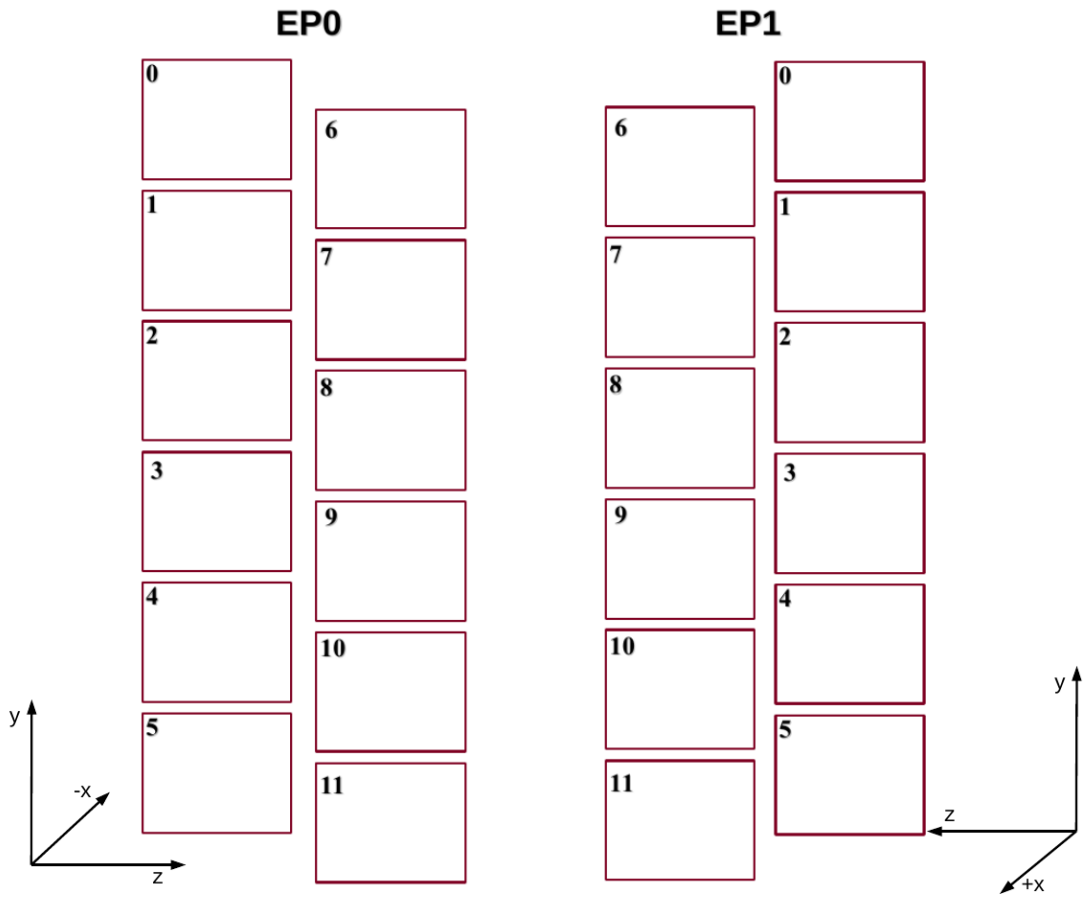

Figure 4.2: Schematic view of the MM geometry in each TPC readout plane. The two columns are vertically staggered by $\sim$ 5 cm, MMs enumerate from 0 to 11. EP0 left, EP1 right.

an high-precision optical system was used [104]. Alignment corrections are extracted by looking at the relative positions with respect to MM design locations in the TPC coordinate system. The TPC coordinate system is defined by the average of the survey of the 36 MM modules on end plate 1 (EP1). The EP are assumed to be flat. The orientation of a module is defined by a simple rotation in the EP1 plane ($+x$-direction), around the center of each module, followed by translations in y and z. Care must be taken when comparing with rotations and translations in the ND280 coordinate system. Results on the MM alignment via Survey are summarized in Tab. 4.1. The comparison between the optical survey and the new method measurements will be discussed in Sec. 4.8.

TPC1 EP1	dy (mm)	dz (mm)	dϕ (mrad)	**TPC1 EP0**	dy (mm)	dz (mm)	dϕ (mrad)
MM00	0.274	-0.156	-0.894	MM00	-0.091	0.510	0.317
MM01	0.386	-0.054	-0.726	MM01	-0.082	0.149	0.385
MM02	0.213	0.198	0.085	MM02	-0.520	0.541	1.458
MM03	0.257	0.014	-0.439	MM03	-0.452	0.525	0.933
MM04	0.169	0.001	-0.373	MM04	-0.299	0.542	0.575
MM05	0.250	0.010	-0.567	MM05	-0.358	0.389	0.650
MM06	-0.138	0.003	0.258	MM06	-0.464	0.333	0.263
MM07	-0.292	0.048	0.800	MM07	-0.593	0.281	-0.679
MM08	-0.109	0.113	0.034	MM08	-0.575	0.291	-0.606
MM09	-0.344	-0.156	0.916	MM09	-0.697	0.380	-1.311
MM10	-0.171	-0.081	-0.396	MM10	-0.952	0.624	-0.658
MM11	-0.310	-0.141	-0.092	MM11	-0.648	0.283	-0.290
TPC2 EP1	dy (mm)	dz (mm)	dϕ (mrad)	**TPC2 EP0**	dy (mm)	dz (mm)	dϕ (mrad)
MM00	0.297	0.058	-0.799	MM00	-0.005	-0.407	-0.406
MM01	0.052	0.110	-0.915	MM01	0.334	-0.280	-0.343
MM02	0.082	0.191	-0.369	MM02	0.068	-0.169	-0.120
MM03	0.208	0.093	-0.134	MM03	-0.016	0.001	-0.092
MM04	0.090	0.105	-0.183	MM04	0.059	0.230	-0.633
MM05	0.159	-0.063	0.421	MM05	0.006	0.456	-0.212
MM06	0.026	-0.100	0.344	MM06	-0.113	-0.480	-0.608
MM07	-0.074	-0.154	0.843	MM07	-0.159	-0.229	-1.372
MM08	-0.106	-0.021	0.581	MM08	-0.172	0.078	-0.229
MM09	-0.138	-0.165	0.320	MM09	-0.207	0.236	-1.011
MM10	-0.256	-0.174	0.599	MM10	-0.034	0.448	-1.513
MM11	-0.140	-0.100	0.175	MM11	-0.287	0.558	-1.083
TPC3 EP1	dy (mm)	dz (mm)	dϕ (mrad)	**TPC3 EP0**	dy (mm)	dz (mm)	dϕ (mrad)
MM00	0.060	0.108	-0.731	MM00	0.488	-0.428	0.123
MM01	0.142	0.176	-0.427	MM01	0.291	-0.363	-0.124
MM02	0.115	0.010	-0.787	MM02	0.346	-0.258	0.213
MM03	-0.022	0.053	-0.389	MM03	0.304	-0.149	0.347
MM04	0.052	0.075	-0.616	MM04	0.318	-0.083	0.419
MM05	0.121	0.045	-0.621	MM05	0.113	-0.074	-0.295
MM06	0.027	-0.007	0.374	MM06	0.135	-0.212	-0.326
MM07	-0.002	-0.164	0.578	MM07	0.050	-0.171	-0.481
MM08	0.029	-0.083	0.944	MM08	0.249	-0.123	-0.086
MM09	-0.012	-0.127	0.468	MM09	0.002	-0.061	-0.537
MM10	-0.019	-0.067	0.013	MM10	0.018	-0.072	0.041
MM11	-0.131	0.053	0.636	MM11	-0.063	-0.120	-0.459

Table 4.1: Alignment correction extracted using the Survey of the MM modules respect to the design locations. The rotation is around the center of the module and about the +x direction, followed by a translation in the TPC design coordinate system.

4.3 Cosmic rays and simulated samples

The data sample for this analysis includes cosmic rays collected in ND280 Run II-IV with magnetic field off ($|\vec{B}| = 0$). The data were taken using two trigger systems: the FGD trigger, in which a cosmic track must pass through both FGDs, and the Trip-t trigger where two fast-triggered detectors (FGD , ECal or SMRD) are activated in coincidence. The coverage of the three TPCs for these two trigger types is shown in Fig. 4.3.

Since TPC2 is sandwiched between the FGDs, the FGD trigger provides good coverage of the TPC2 center. However the top and bottom of each TPC are poorly covered. On the other hand the Trip-t trigger provides a more uniform coverage, however the number of Tript-t tracks does not allow the same statistical precision for the modules located on the top and bottom of the TPCs as provided by FGD trigger for those placed at the center.

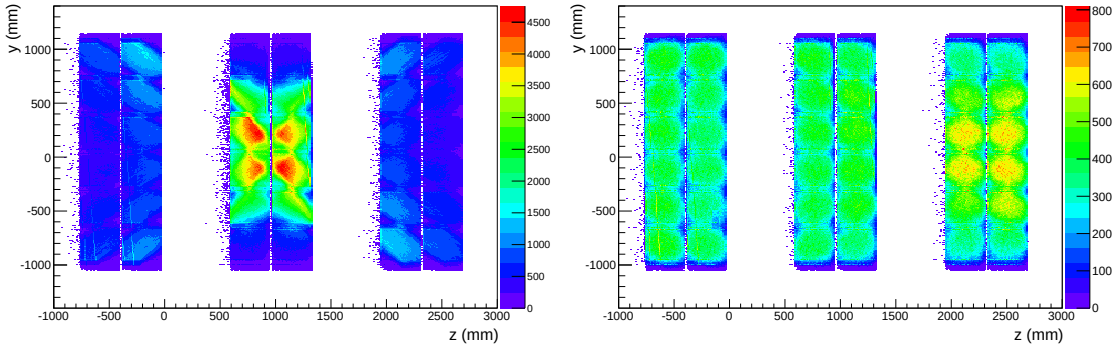

Figure 4.3: TPC coverage in the YZ-plane using FGD (left) and Trip-t (right) triggers.

In order to ensure sufficient accuracy in the determination of the track parameters, only good quality tracks with minimum 20 clusters and good χ^2 on each module are taken into account. High angle tracks $\left(|\phi^{track}| > 75°\right)$ are not included in this study because of the poor reconstruction. Selection cuts are listed in Table 4.2.

Quality track	$10^{-5} < \chi^2 < 0.5$
Number of hits	$20 < n_{hits} < 50$
Horizontal tracks	$\|\phi^{track}\| < 60°$
Angular residual	$\|\Delta\phi\| < 15.$ mrad
Translational residual	$\|\Delta y\| < 2.5$ mm

Table 4.2: List of selection cuts for the tracks used for the alignment study.

By geometrical consideration selected tracks correspond to trajectories passing through two MM modules positioned in different columns and vertically offset by at most one module. Thus it is possible to split them in two samples: tracks crossing modules in different columns and same row constitute the Horizontal sample while tracks crossing a MM pair in different columns and rows are the Diagonal sample. Since the aim of this study is to extract corrections between adjacent modules only the Horizontal sample is used. However the Diagonal sample can be used to cross-check the consistency of the results from MC validation studies.
The cosmic ray sample was collected during T2K RunII-IV data taking periods (see Fig. 2.2), Tab. 4.3 details the magnetic field off ND280 run and sub-run numbers as well as the total number of horizontal tracks after selection cuts.
A MC sample is produced with several muon particle-gun sources placed upstream TPC1 so as to cover with enough statistics all the MM modules of the TPCs. It is used for MC validation studies (Sec. 4.4 and 4.6) and consists of muons of 1.2 GeV energy, randomly generated inside a cone of maximum opening angle of 45°. Figure 4.4 (left) shows a side view of the detector, the muon source is placed in the top half ($y = 900$ mm) with respect the beam center, the other 4 sources are placed respectively one at the

T2K Run II	**ND280 run number**	**sub-run**
	00006606	0000-0038
	00006646	0000-0017
	00007714	0000-0102
Horizontal tracks	$\sim 33k$	
T2K Run III	**ND280 run number**	**sub-run**
	00008215	0000-0111
	00008306	0000-0097
	00008465	0000-0071
	00008520	0000-0040
	00008765	0000-0016
	00008783	0000-0044
Horizontal tracks	$\sim 37k$	
T2K Run IV	**ND280 run number**	**sub-run**
	00009730	0000-0017
	00009731	0000-0025
	00009732	0000-0005
	00009738	0000-0002
	00009739	0000-0038
	00009748	0000-0038
Horizontal tracks	$\sim 18k$	

Table 4.3: Cosmic rays data sample used for the alignment study.

beam center ($y = 0$ mm) while the other three are one in the top half ($y = 0.5$ mm) and two in the bottom half ($y = -450$ mm and $y = -850$ mm). As shown in Fig. 4.4 on the right with this configuration the first TPC will be more covered than TPC2 and TPC3. The effect of this different coverage leads the fit to be more sensitive in TPC1. However the generated statistics is enough to have a good sensitivity in all the TPCs.

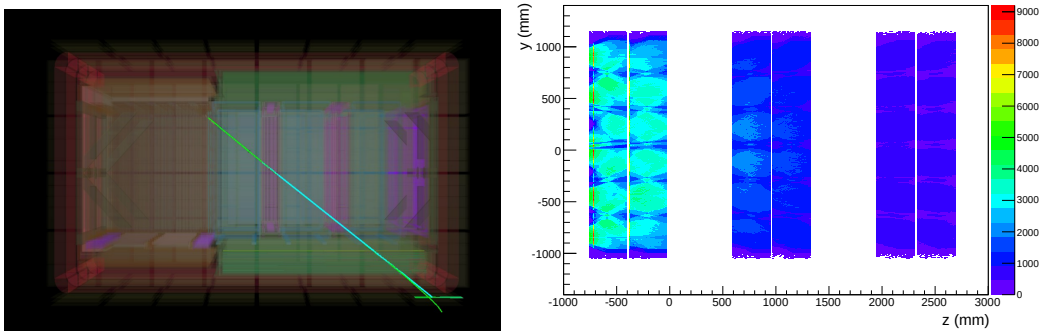

Figure 4.4: **Left:** side view of muon particle-gun source in the ND280 detector. The source are placed in 5 different positions upstream the first TPC. **Right:** TPC coverage of the MC sample.

4.4 Residuals extraction

The MMs alignment strategy in each TPC readout plane is based on the matching, at a fixed position, of the straight segments of a track passing through two adjacent MM module pairs belonging to the same row. The difference in position and angle of the two track segments is measured by their extrapolation in the middle plane (MP) between MM columns, as already shown in Fig. 4.1. The residual is the relative difference in angle ($\Delta\phi$) or position (Δy). The MPs are located at fixed $z = -398, 958, 2318$ mm for TPC1, TPC2, and TPC3 respectively. The magnetic field off configuration allows to decouple misalignment effects in the momentum determination from other sources of error but also to disentangle rotational and translation degrees of freedom. In this way is possible to independently extract the residuals and correct separately the relative orientations and translations between MM pairs. Track segments in absence of magnetic field appear as straight lines that can be parametrized, in the YZ-plane, by a linear function:

$$y^{track} = y_{L,F} + \left(z_{L,F} - z^{track}\right) \tan\phi^{track} \tag{4.1}$$

where y^{track}, z^{track} are the reconstructed track coordinates while ϕ^{track} is the reconstructed angle of the track with respect to the z-axis. The $y_{F,L}$ and $z_{F,L}$ are the start (first F) and end position (last L) of the reconstructed track segment.

4.4.1 Rotations

The rotational misalignment in the YZ-plane is completely uncorrelated from the relative position of the modules. Thus the angular residual $\Delta\phi$ is extracted directly from the difference in angle between the two track segments:

$$\Delta\phi = \phi^{track}_{MM_i} - \phi^{track}_{MM_j} \tag{4.2}$$

where $\phi^{track}_{MM_{i(j)}}$ is the angle of the track in MM module i or j, respectively. The uncertainty on the measurement of the angle strongly depends on the number of clusters and therefore on the value of the angle itself. To reduce this uncertainty, tracks with an angle less than 1 rad with respect to the horizontal direction, in the y and z projection, are selected (see Tab. 4.2). Figure 4.5 shows two examples of residual distributions for a given MM pair under the perfect geometry hypothesis, for the Horizontal and Diagonal samples. The parameters $p_{1,4} = \mu_{1,2}$ are the means and $p_{2,5} = \sigma_{1,2}$ are the resolution of the two gaussians used to fit the distribution. The parameters of the narrower gaussian (μ_1, σ_1) are assumed as the mean value and the resolution of the MM pair, for instance in the left plot $\mu_1 = 0.078$ mrad and $\sigma_1 = 1.735$ mrad. Diagonal tracks are used as additional check in the $\Delta\phi$ residual extraction since corrections are computed between module belonging to the same MM row taking as reference the module positioned in column 0. For this reason in each readout plane 6 pairs of modules are taken into account for a total of 36 pairs of MM for the three TPCs.

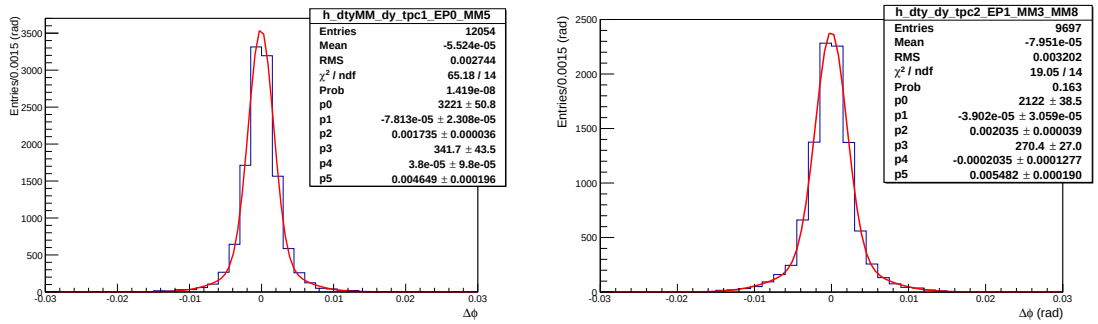

Figure 4.5: Example of $\Delta\phi$ distribution for a pair of modules under perfect geometry hypothesis. For horizontal (left) and diagonal (right) tracks.

Figure 4.6 shows the distribution of the mean value of the residual ($\overline{\Delta\phi}$) obtained from the set of 36 pairs of modules under perfect geometry. The mean of such distribution $\mu_{\overline{\Delta\phi}} = 0.022 \pm 0.058$ mrad is compatible with the perfect geometry hypothesis ($\mu = 0$) while the standard deviation gives an estimation of the precision and goodness of the method in the reconstruction of this kind of tracks (Horizontal).

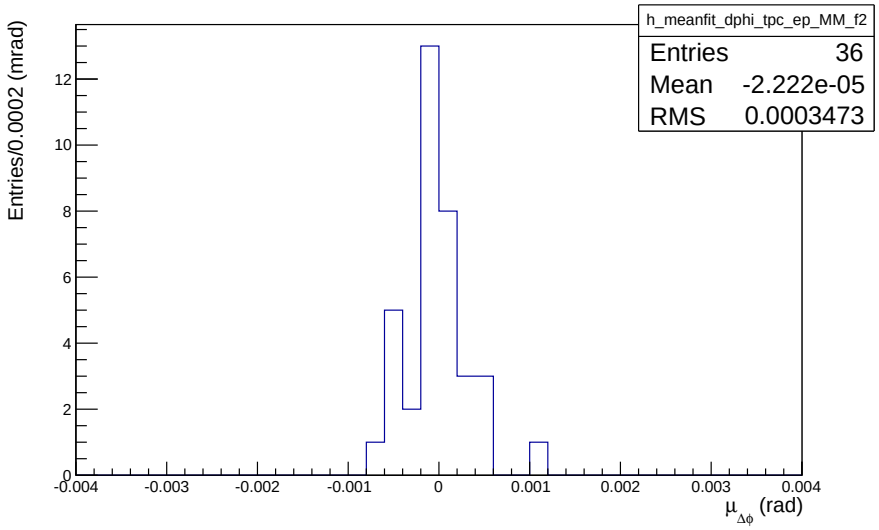

Figure 4.6: Distribution of the residual mean value $\overline{\Delta\phi}$ for all 36 MM pairs under perfect geometry.

4.4.2 Translations

The relative shifts in the YZ-plane between MM pairs are determined by the residual Δy which also depends on the angular misalignments. However this dependency is

negligible if low angular residuals ($\overline{\Delta\phi} \sim 0$) are considered.
For this reason Δy is computed after rotational misalignments correction to disentangle translations from rotations. To compute the translational residual the track segments are propagated and matched in the MP between the MM columns, as shown in Fig. 4.1 (left). According to Eq. 4.1 the track y coordinate in the MP (y_{MP}) can be estimated by the following linear equation:

$$y_{MP} = y_{L,F} - (z_{L,F} - z_{MP}) \tan\phi, \tag{4.3}$$

where z_{MP} is the fixed z coordinate of the MP between the MM columns in the three TPCs and ϕ is the angle of the segment with respect to the horizontal axis (z). The matching between MM is performed by propagating the last (L) or the first (F) fitted track position ($z_{L,F}, y_{L,F}$) in each MM segment with Eq. 4.3 and the residual is defined as:

$$\Delta y = y_{MP}^{MM_i} - y_{MP}^{MM_j}, \tag{4.4}$$

where $y_{MP}^{MM_{i(j)}}$ are the y_{MP} coordinate computed as in Eq. 4.3 for the two MM modules i and j.
Figure 4.7 shows two examples of residual distributions for a given MM pairs under perfect geometry hypothesis using horizontal (left) and diagonal (right) tracks. Following the same notation used for rotations, the parameters $p_1 = \mu_1$ and $p_2 = \sigma_1$ are the mean value and the resolution of the residual distribution of the MM pairs.

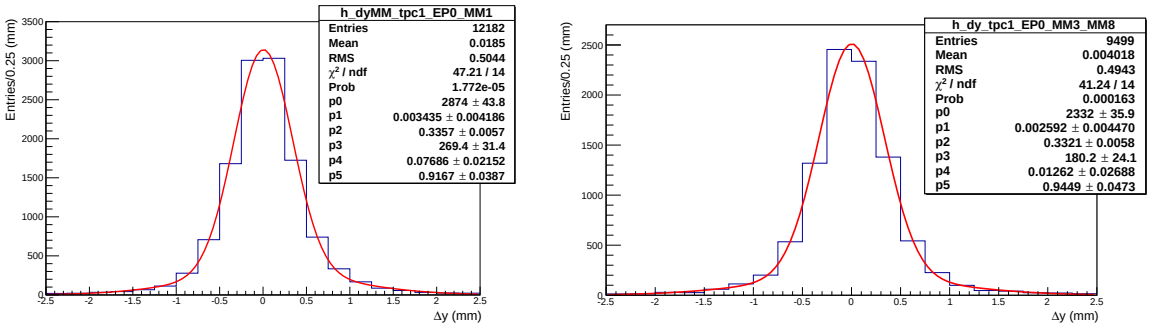

Figure 4.7: Example of Δy distribution for a pair of modules under perfect geometry hypothesis. For horizontal (left) and diagonal (right) tracks.

Figure 4.8 shows the distribution of the means $\overline{\Delta y}$ for all the 36 MM pairs using horizontal tracks. The mean value of this distribution is compatible within the error with the perfect geometry hypothesis ($\mu_{\overline{\Delta y}} = -0.009 \pm 0.010$ mm). The mean value is also estimated via a two gaussians fit to the residual distribution.

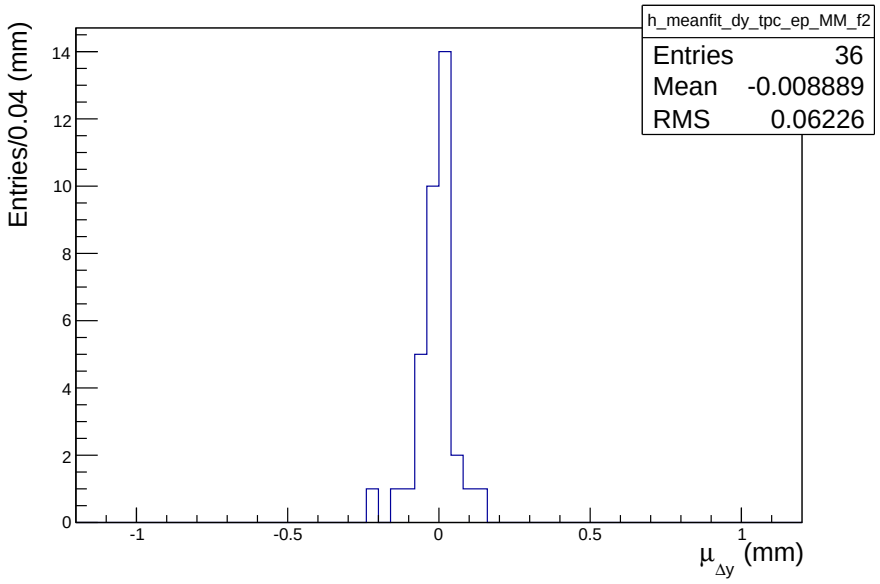

Figure 4.8: Δy distribution for all 36 MM pairs under perfect geometry.

4.5 Fit strategy

The numerical minimization and error analysis code MINUIT [105] is used to extract alignment corrections. The fit is performed using the MIGRAD minimization method. The chi-square between the fitting function and the residuals for given values of the parameters is defined as:

$$\chi^2 = \chi^2_{\Delta\phi} + \chi^2_{\Delta y} = \sum^{n_{tracks}} \left(\frac{\Delta\phi + f_{\Delta\phi}}{\sigma_{\Delta\phi}} \right)^2 + \sum^{n_{tracks}} \left(\frac{\Delta y + f_{\Delta y}}{\sigma_{\Delta y}} \right)^2 \tag{4.5}$$

where $\Delta\phi$ and Δy are the single track residuals for rotations and translations respectively, as defined in Sec. 4.4, whereas $f_{\Delta\phi}$ and $f_{\Delta y}$ are the corresponding correction functions used to describe the dependency of the residuals as a function of the free parameters. Correction functions will be described in Sec. 4.5.1. Finally σ_Δ is the resolution on the residuals extracted via a two gaussians fit to the residual distributions (Fig. 4.5 and 4.7). The χ^2_Δ is computed summing all over the selected tracks (n_{tracks}). Using a 3-dimensional vector $\vec{x} = (z, y, \phi)$ to describe the MM degree of freedom in the global coordinates system, the free parameters in the fit can be defined as:

$$\delta_{\vec{x}} = \vec{x}_{MM_i} - \vec{x}_{MM_j} = (z, y, \phi)|_{MM_i} - (z, y, \phi)|_{MM_j}. \tag{4.6}$$

The alignment procedure is only sensitive to relative displacements between two adjacent modules, thus in the fit the parameters describing the MM position in one column are kept fixed while parameters of the other column are free to vary. For instance

given a MM pair (MM_3, MM_9) if the parameters $\vec{x}_{MM_3}$ related to MM_3 are fixed, the parameters $\vec{x}_{MM_9}$ of the MM_9 module are extracted by the fit and vice versa.
As already stated the magnetic field off configuration allows to disentangle rotational and translation residuals, then in order to avoid dependence of the translation corrections on rotational misalignment a two step procedure is implemented.

First step: the fit considers only rotational alignment constants.
The chi-square is defined as:

$$\chi^2 = \chi^2_{\Delta\phi} \tag{4.7}$$

in this case the free parameters are the parameters which describe MM angular positions in one column while all the others are kept fixed (translations in both columns + rotations in the other one).

Second step: the fit is performed considering translation and rotational alignment constants.
Once rotational corrections are applied, reconstructing the sample with the corrections extracted in the First step, the fit extracts translation corrections. In this step the chi-square function to minimize is defined as in Eq. 4.5:

$$\chi^2 = \chi^2_{\Delta\phi} + \chi^2_{\Delta y} \tag{4.8}$$

All parameters in one column are fixed while translation and rotational parameters in the other one are free to vary. In this way the fit checks whether angular corrections effectively worked ($\overline{\Delta\phi} \sim 0$).

Closure test step: all the alignment correction constants (translations + rotations) are applied to the sample. The fit runs for the last time as closure test using the same configuration as in the second step.

4.5.1 Correction formulas

The functions f_Δ in Eq. 4.5 describes the misalignments dependency on the track parameters. In this section this parametrization is discussed.

Rotations

The mutual orientations between the MMs are the easiest misalignments to correct, the uncorrelation from the relative module position leads the correction formula f_Δ equal to the residual definition (Eq. 4.2). The angular misalignments are simply defined as:

$$f_{\Delta\phi} = \delta_\phi = \phi_{MM_i} - \phi_{MM_j} \tag{4.9}$$

where $\phi_{MM_{i,j}}$ are the free parameters matching the orientation of the module, δ_ϕ is then the relative correction between two MMs.

Translations

The relative position between the MM modules depends on the difference in position $\delta_{\vec{x}}$ of all the coordinates $\Delta y = f_{\Delta y}\left(\delta y, \delta z, \delta\phi, \phi^{track}\right)$. The total translation correction formula can be parametrized as:

$$\begin{aligned} f_{\Delta y} &= \delta_y - \delta_z \tan\phi^{'} - \delta_\phi \left(\frac{d+L}{2} - y_{MP}\tan\phi^{'}\right) \\ &= \left(y_{MM_i} - y_{MM_j}\right) - \left(z_{MM_i} - z_{MM_j}\right)\tan\phi^{'} - \left(\phi_{MM_i} - \phi_{MM_j}\right)\left(\frac{d+L}{2} - y_{MM_i}\tan\phi^{'}\right) \end{aligned} \tag{4.10}$$

where δ_y and δ_z are the free parameters related with the y and z correction constants, d and L are the modules distance and the MM length in the z-direction.
Particular attention should be given to the term $\tan\phi^{'} = \tan(\phi^{track} - \delta_\phi)$, the angle $\phi^{'}$ is the angle in the rotated framework. The first two terms in Eq. 4.10 describe the translation misalignment in the YZ-plane while the third term describes the contribution to Δy given by a rotation in the YZ-plane, as detailed in appendix B. Since rotational correction constants are already extracted in the first step ($\overline{\Delta\phi} \sim 0$), at the first order, the last term in Eq. 4.10 is negligible.

4.6 Validation of the alignment fit

4.6.1 Simulate a new MicroMegas geometry

The whole ND280 detector is simulated using the GEANT4 software [106]. In this environment, each part of the detector is simulated as an independent object (volume). Each MicroMegas module volume can be moved in the simulated structure of the TPCs. The GEANT4 geometry is then converted in a ROOT file [107] provided as an input to the reconstruction algorithm. A new geometry of the MM module in the TPCs can thus be generated to validate the alignment method and test its accuracy. Figure 4.9 shows an event display of the broken tracks and the Δy distribution observed after changing the MM geometry by 10 mm along the y-axis. Next Sec. 4.6.2 and 4.6.3 will present the fit validation via simulated misalignments in the MM geometry.

4.6.2 Formulas validation

Since the Survey alignment (Tab. 4.1) gives correction constants of the order of few hundreds microns for translations and a couple of milliradians for rotations, the fit has to be sensitive to this level of precision. Introducing a well known geometry in the MM and using the muons MC sample is then possible to validate and test the fit. In this first validation step only one pair of adjacent MM at time is considered, parameters related to the misaligned MM_i are free while all the others related to MM_j are fixed

$$\delta_{\vec{x}} = \vec{x}_{MM_i}|_{free} - \vec{x}_{MM_j}|_{fixed} = (z, y, \phi)_{MM_i}|_{free} - (z, y, \phi)_{MM_j}|_{fixed}. \tag{4.11}$$

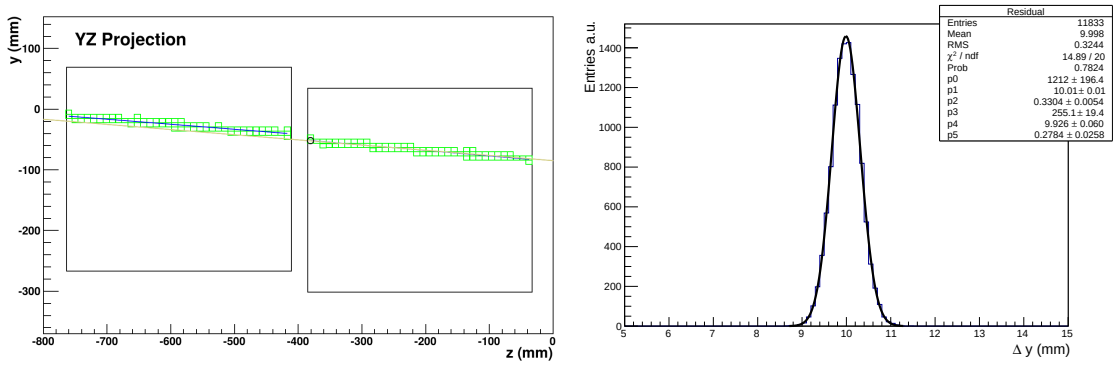

Figure 4.9: Broken track event display (left) and corresponding residual distribution of the MM couple (right). The true track is displayed by the gold line while the reconstructed track is in blue. The green box represents the track pad hit.

Misalignments δ_z, δ_y, δ_ϕ are introduced by step in the MM geometry, Fig. 4.10 shows fit results for elementary configurations when just one degree of freedom at time is tested. As can be seen, the alignment fit gives correct results within uncertainties of $5-20$ μm and $20-50$ μrad.

In the second step of the formula validation more than one misalignment is introduced on the YZ-plane, see Fig. 4.11 left. The example shows a configuration where a misalignment along the y-direction is forced in MM1 and one along z in MM7. The value of the residual Δy depends on both δ_y and δ_z misalignments with the following linear relation:

$$f_{\Delta y}(\delta_y, \delta_z) = \delta y + \delta_z \tan\phi \tag{4.12}$$

which corresponds to the first two terms of the translation correction formula (Eq. 4.10). It is then possible to extract the values of the misalignments between two modules by fitting by hand the Δy distribution as a function of $\tan\phi$ with Eq. 4.12, as shown in Fig. 4.11, right. The points represent the mean of the Δy distribution, extracted by a two gaussians fit in steps of 0.04 in $\tan\phi$. The slope (p_1) gives the δ_z value while the intercept (p_0) is δ_y. The angle value used for the calculation is taken as the average of the angle measured on each of the two track segments.

Unfortunately this simplified method, to determine δ_y and δ_z, is limited for two reasons: firstly it requires much more statistics in each angular bin for the determination of δ_y and δ_z than the MINUIT fit; secondly it does not parametrize at all the relative rotation between the MMs, thus it works only in total absence of angular misalignment as shown in Fig. 4.12 in which the fit cannot recover the misalignment configuration.

For these reasons it is used just as a rough cross-check on the MINUIT fit formula once rotational corrections are applied. However the MINUIT fit, thanks to the third term in Eq. 4.10, is able to recover the correct misalignment values also in presence of rotational misalignment. The sign of the third term is tested and validated using the most simple configuration where just a rotation is forced in the geometry, as shown in

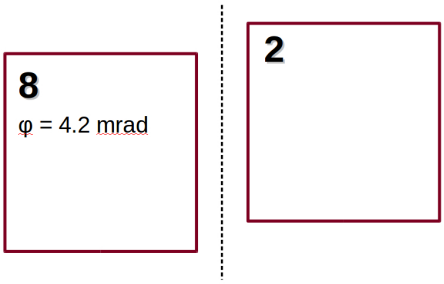

	δ_ϕ (mrad)	δ_y (mm)	δ_z (mm)
MM2-MM8	-4.141 ± 0.045	0.001 ± 0.008	-0.015 ± 0.019

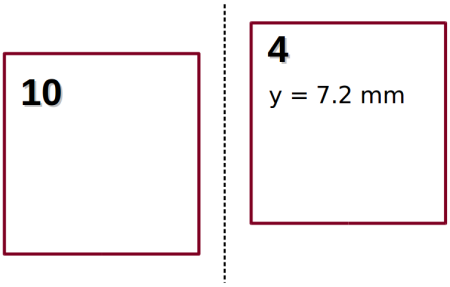

	δ_ϕ (mrad)	δ_y (mm)	δ_z (mm)
MM4-MM10	-0.035 ± 0.023	7.198 ± 0.006	0.035 ± 0.012

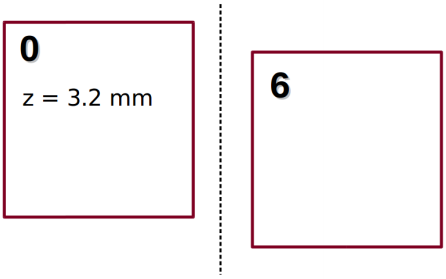

	δ_ϕ (mrad)	δ_y (mm)	δ_z (mm)
MM0 -MM6	-0.041 ± 0.033	0.008 ± 0.006	3.253 ± 0.013

Figure 4.10: **Top**: Simulated rotational lack between MM8 and MM2 and relative fit results letting free MM2 parameters. Residual Δ = MM2 - MM8.
Center: Simulated misalignment in y direction between MM10 and MM4. Fit results on the table for free parameters in $MM4$. The residual Δ = MM4 - MM10
Bottom: Misalignment in z direction in the module pairs MM6, MM0, fixed parameters in MM6. The residuals Δ = MM0 - MM6

Fig. 4.13.
The table lists the fit results for the corrections extraction using only the translation formula. Although it gives the correct value for the angular correction, translations still have a small dependency on it. For this reason a two-step procedure is applied to

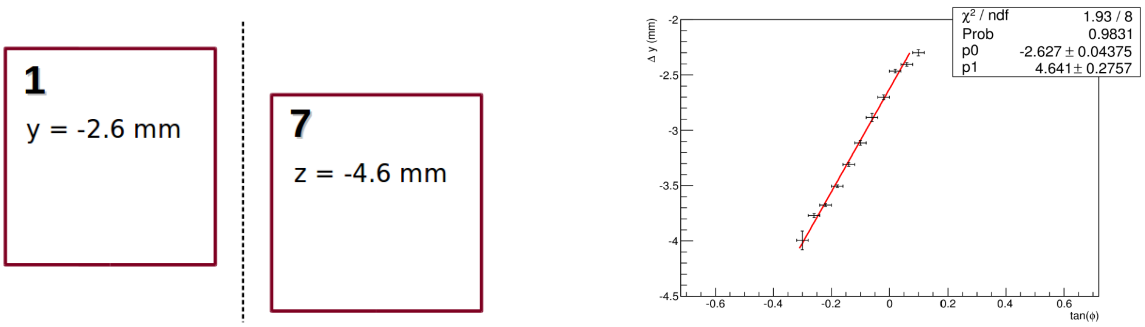

Figure 4.11: Schematic view of a generic translation misalignment for MM pair MM1-MM7 on the left. On the right a linear fit to the Δy residuals as a function of the track angle.

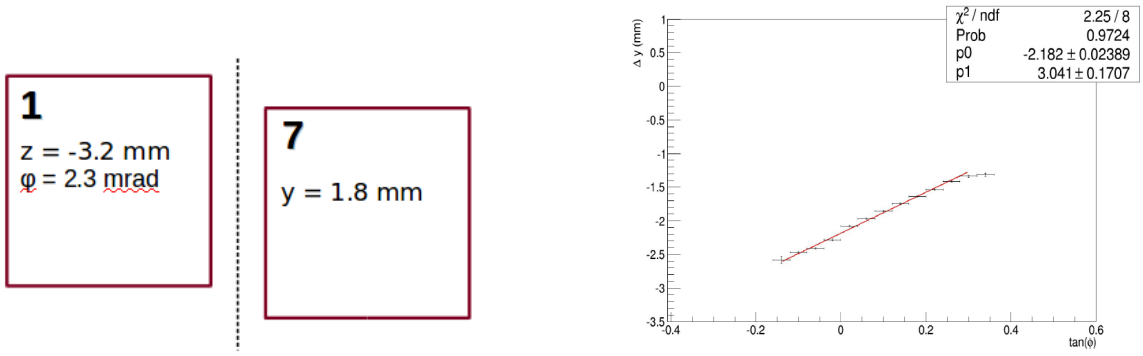

Figure 4.12: Generic translation + rotational misalignment topology on the left. Linear fit formula result on the right.

minimize the dependency on the rotational misalignment.
The full set of correction formulas is finally validated using a general configuration where translation and rotational misalignments are introduced at the same time in the MM pair geometry. Figure 4.14 shows the final test.

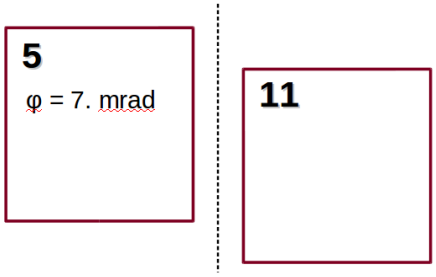

MM5 -MM11	δ_ϕ (mrad)	δ_y (mm)	δ_z (mm)
1 - 2	6.945 ± 0.021	-1.367 ± 0.004	0.000 ± 0.009
1 - 2 - 3	6.945 ± 0.021	-0.072 ± 0.005	0.000 ± 0.009

Figure 4.13: Cross-check of the sign of the rotational terms in the translation correction formula.

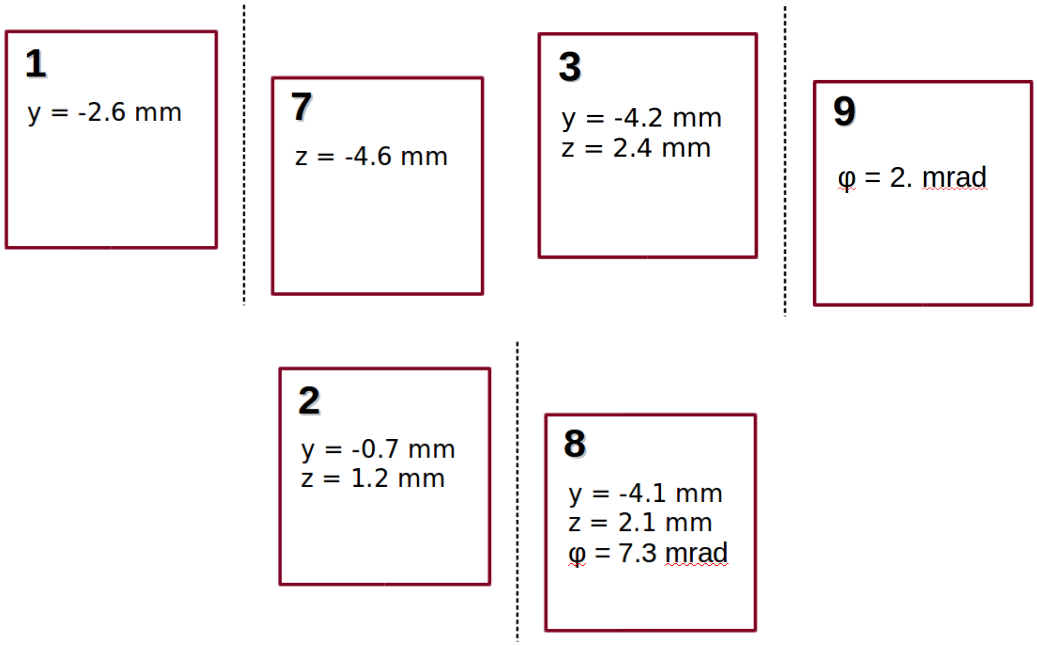

	δ_ϕ (mrad)	δ_y (mm)	δ_z (mm)
MM1-MM7	0.010 ± 0.025	-2.584 ± 0.004	4.627 ± 0.015
MM3-MM9	-1.921 ± 0.032	-4.206 ± 0.006	2.375 ± 0.010
MM2 -MM8	-7.227 ± 0.050	3.445 ± 0.012	-1.033 ± 0.038

Figure 4.14: Final step of the validation test for the full set of correction formulas.

4.6.3 Monte-Carlo test geometries

The next step in the validation process is to check more complex geometries which involves misalignments of many MM pairs of each TPC readout plane at the same time. Unfortunately the ND280 code does not allow to reconstruct the MC sample applying the alignment corrections. Thus it is not possible to test the two steps procedure in the MC. To solve this issue a set of two connected geometries **A** and **B** is generated as follow:

- Test geometry **A**: rotational and translation MM misalignments are introduced at the same time in the geometry
- Test geometry **B**: under the assumption of fully corrected rotational misalignments ($\overline{\Delta\phi} = 0$ inside the resolution), the same translation misalignments as in geometry **A** are introduced.

In this way the two step procedure is properly reproduced in the validation study. Geometry **A** fully mimic the first step where the modules are not aligned neither in angle nor in y and z directions. The fit will look then only for rotational corrections. In geometry **B** instead, translation and residual angular corrections are extracted using the full set of formulas as in the second step. In order to validate the method two distinct sets of misalignment geometries are studied: a *Simple* and a *Survey-like* geometry.

4.6.4 Simple geometry

The Simple geometry takes into account small and very large module displacements in order to test the sensitivity in all conditions. Several misalignments are introduced at the same time in the MM geometry of each readout plane. In Tab. 4.4 the fit results compared with the introduced geometry between the MM pairs are listed. The agreement between them is very good in both readout planes of all TPCs.
Figures 4.15, 4.16, 4.17 show a direct comparison between the fit and the geometry assumption for all the MM pairs belonging to each readout plane of each TPC. Similarly Fig. 4.18, 4.19 and 4.20 show the bias between the fit results and the test geometry. Bias with the associated mean value and width of the distribution are shown in Fig. 4.21 for translational (left and center) and rotational (right) corrections.

TPC1 EP0	$\delta\phi$ (mrad)	Nominal (mrad)	δz (mm)	Nominal (mm)	δy (mm)	Nominal (mm)
MM0-MM6	-0.013 ± 0.032	0.000	-0.077 ± 0.017	0.000	-0.003 ± 0.003	0.000
MM1-MM7	-2.004 ± 0.030	-2.100	-0.035 ± 0.010	0.000	-2.303 ± 0.003	-2.300
MM2-MM8	-0.013 ± 0.036	0.000	-0.015 ± 0.008	0.000	0.004 ± 0.003	0.000
MM3-MM9	-2.469 ± 0.035	-2.500	-1.602 ± 0.010	-1.600	-1.389 ± 0.003	-1.400
MM4-MM10	-1.809 ± 0.038	-1.900	-0.034 ± 0.010	0.000	1.206 ± 0.002	1.200
MM5-MM11	0.055 ± 0.033	0.000	-0.040 ± 0.008	0.000	-0.013 ± 0.002	0.000
TPC1 EP1	$\delta\phi$ (mrad)	Nominal (mrad)	δz (mm)	Nominal (mm)	δy (mm)	Nominal (mm)
MM0-MM6	0.000 ± 0.041	0.000	0.048 ± 0.011	0.000	0.000 ± 0.003	0.000
MM1-MM7	-6.086 ± 0.036	-6.300	3.289 ± 0.011	3.200	1.804 ± 0.003	1.800
MM2-MM8	-0.011 ± 0.033	0.000	0.095 ± 0.009	0.000	-0.026 ± 0.003	0.000
MM3-MM9	-4.716 ± 0.033	-5.100	2.398 ± 0.009	2.400	-4.276 ± 0.003	-4.200
MM4-MM10	0.012 ± 0.031	0.000	0.019 ± 0.010	0.000	-0.012 ± 0.003	0.000
MM5-MM11	-2.242 ± 0.038	-2.300	2.120 ± 0.012	2.100	-0.597 ± 0.003	-0.600
TPC2 EP0	$\delta\phi$ (mrad)	Nominal (mrad)	δz (mm)	Nominal (mm)	δy (mm)	Nominal (mm)
MM0-MM6	2.214 ± 0.062	2.200	-0.0587 ± 0.029	0.000	-3.406 ± 0.007	-3.400
MM1-MM7	0.031 ± 0.052	0.000	4.669 ± 0.020	4.800	2.677 ± 0.005	2.700
MM2-MM8	-0.043 ± 0.042	0.000	-0.110 ± 0.016	0.000	-0.022 ± 0.004	0.000
MM3-MM9	1.422 ± 0.049	1.400	3.214 ± 0.015	3.200	0.015 ± 0.004	0.000
MM4-MM10	0.043 ± 0.044	0.000	0.093 ± 0.016	0.000	-0.043 ± 0.005	0.000
MM5-MM11	-0.996 ± 0.049	-1.100	-1.098 ± 0.021	-1.200	-0.051 ± 0.006	0.000
TPC2 EP1	$\delta\phi$ (mrad)	Nominal (mrad)	δz (mm)	Nominal (mm)	δy (mm)	Nominal (mm)
MM0-MM6	0.064 ± 0.058	0.000	-0.102 ± 0.022	0.000	-0.052 ± 0.007	0.000
MM1-MM7	-4.290 ± 0.045	-4.400	1.630 ± 0.016	1.600	1.388 ± 0.005	1.400
MM2-MM8	1.244 ± 0.041	1.400	-2.303 ± 0.014	-2.400	3.201 ± 0.004	3.200
MM3-MM9	-0.043 ± 0.040	0.000	0.069 ± 0.015	0.000	0.000 ± 0.004	0.000
MM4-MM10	-1.877 ± 0.048	-1.900	2.124 ± 0.020	1.900	0.374 ± 0.005	0.400
MM5-MM11	0.159 ± 0.072	0.000	0.151 ± 0.028	0.000	-0.006 ± 0.006	0.000
TPC3 EP0	$\delta\phi$ (mrad)	Nominal (mrad)	δz (mm)	Nominal (mm)	δy (mm)	Nominal (mm)
MM0-MM6	0.066 ± 0.078	0.000	0.087 ± 0.043	0.000	0.031 ± 0.011	0.000
MM1-MM7	-0.051 ± 0.071	0.000	0.023 ± 0.037	0.000	-2.806 ± 0.008	-2.800
MM2-MM8	-0.828 ± 0.060	-0.800	-0.897 ± 0.033	-0.900	3.351 ± 0.006	3.400
MM3-MM9	0.010 ± 0.083	0.000	-0.029 ± 0.033	0.000	-0.025 ± 0.006	0.000
MM4-MM10	7.219 ± 0.075	7.400	-0.086 ± 0.034	0.000	-3.392 ± 0.007	-3.400
MM5-MM11	0.024 ± 0.065	0.000	0.323 ± 0.036	0.300	-0.070 ± 0.010	0.000
TPC3 EP1	$\delta\phi$ (mrad)	Nominal (mrad)	δz (mm)	Nominal (mm)	δy (mm)	Nominal (mm)
MM0-MM6	-1.115 ± 0.063	-1.200	-0.170 ± 0.036	0.000	-0.074 ± 0.010	0.000
MM1-MM7	-6.279 ± 0.078	-6.400	-0.078 ± 0.034	0.000	-0.061 ± 0.008	0.000
MM2-MM8	-0.021 ± 0.099	0.000	-1.839 ± 0.032	-1.700	1.373 ± 0.006	1.400
MM3-MM9	0.009 ± 0.057	0.000	-0.006 ± 0.032	0.000	-0.010 ± 0.006	0.000
MM4-MM10	-1.495 ± 0.064	-1.500	-1.669 ± 0.036	-1.800	4.177 ± 0.007	4.200
MM5-MM11	-0.018 ± 0.091	0.000	0.034 ± 0.042	0.000	-0.011 ± 0.010	0.000

Table 4.4: Fit results for each readout plane under the simple geometry configuration hypothesis.

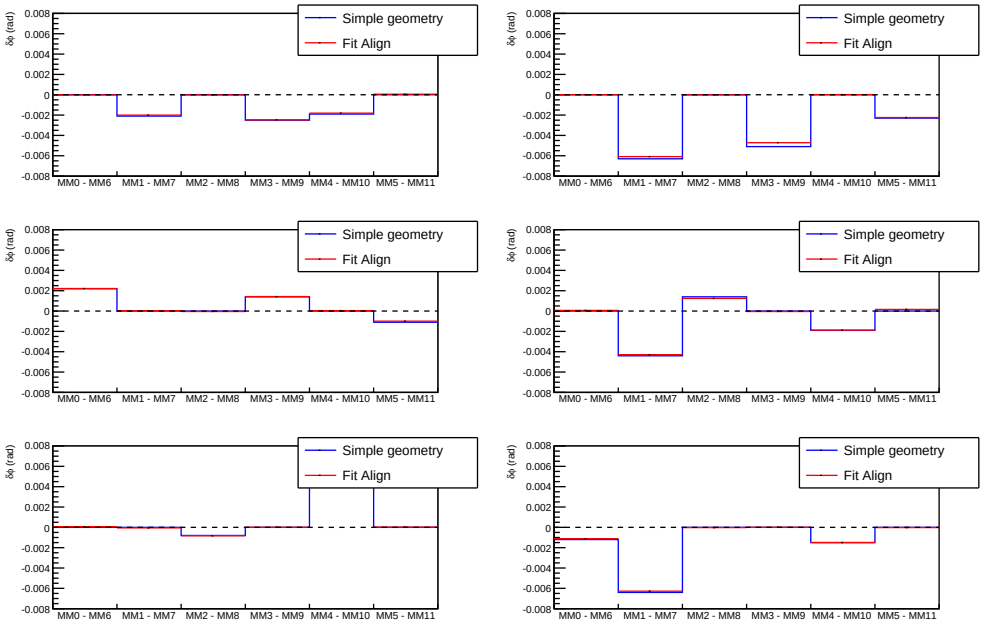

Figure 4.15: Simple geometry results on rotation δ_ϕ. In blue the simulated misalignments in the Simple geometry, in red the fit results. From the top to the bottom the three TPCs (TPC1 top, TPC2 center, TPC3 bottom). Left plots show the EP0, the right plots the EP1.

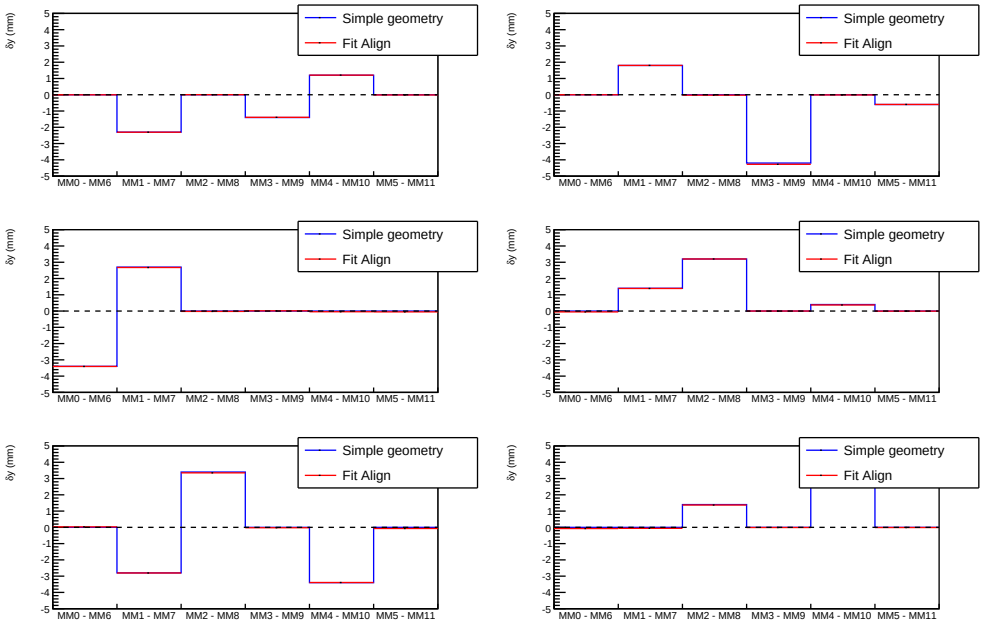

Figure 4.16: Results on translation corrections δ_y. In blue the simulated misalignments, in red the fit results.

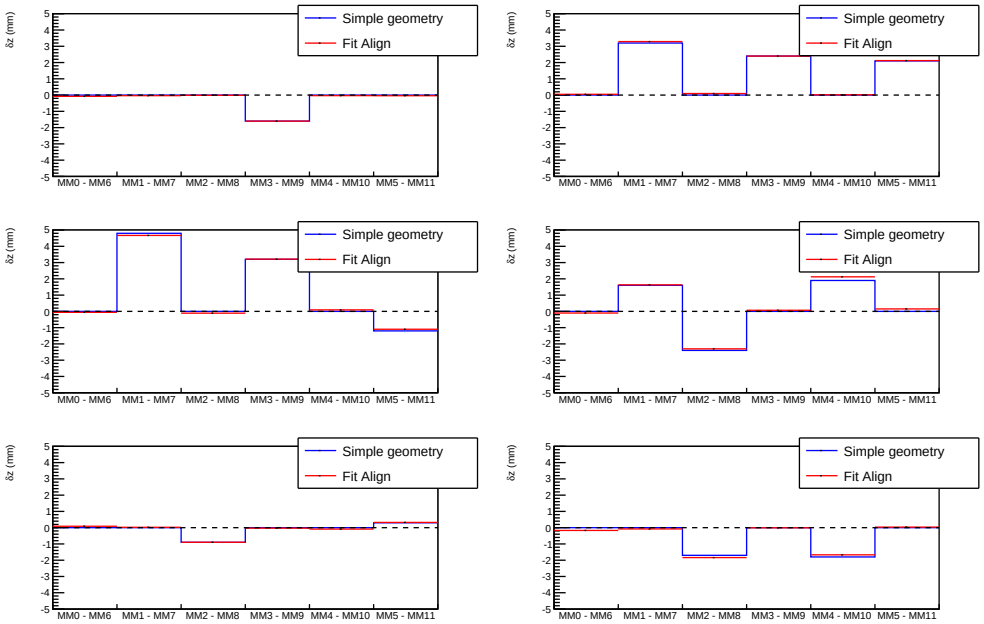

Figure 4.17: Test geometry results on translation δ_z. The simulated misalignments in blue, in red the fit results instead.

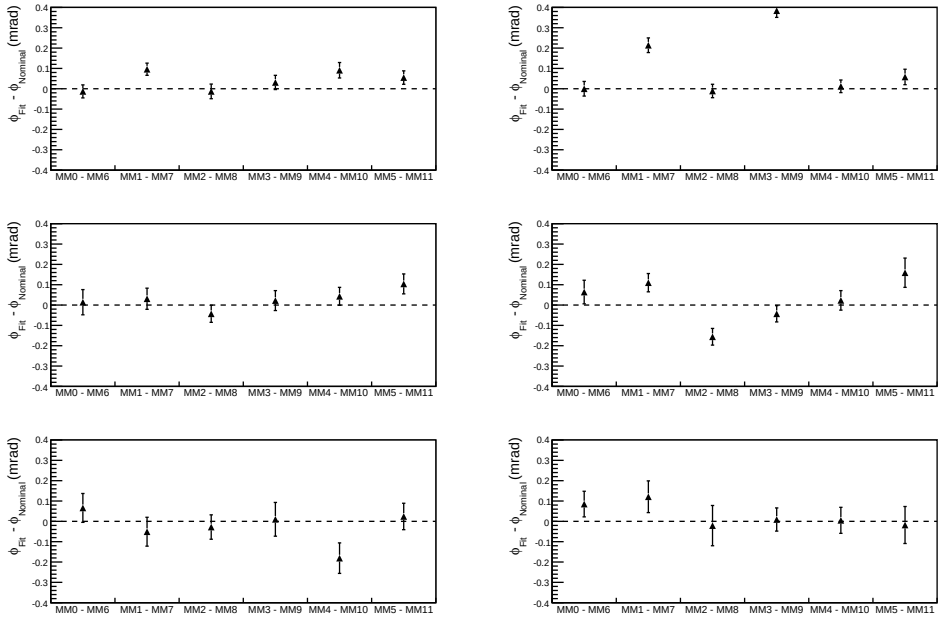

Figure 4.18: Bias between the test geometry and the fit results for rotation δ_ϕ for the six MM couples of each TPC readout plane.

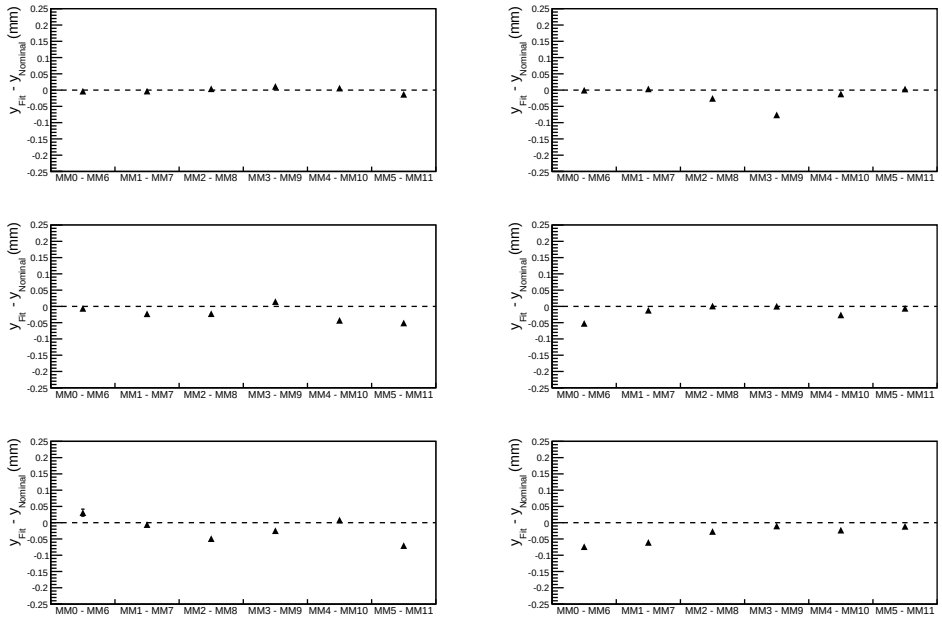

Figure 4.19: Simulated geometry fit results bias for translation in the y direction δ_y.

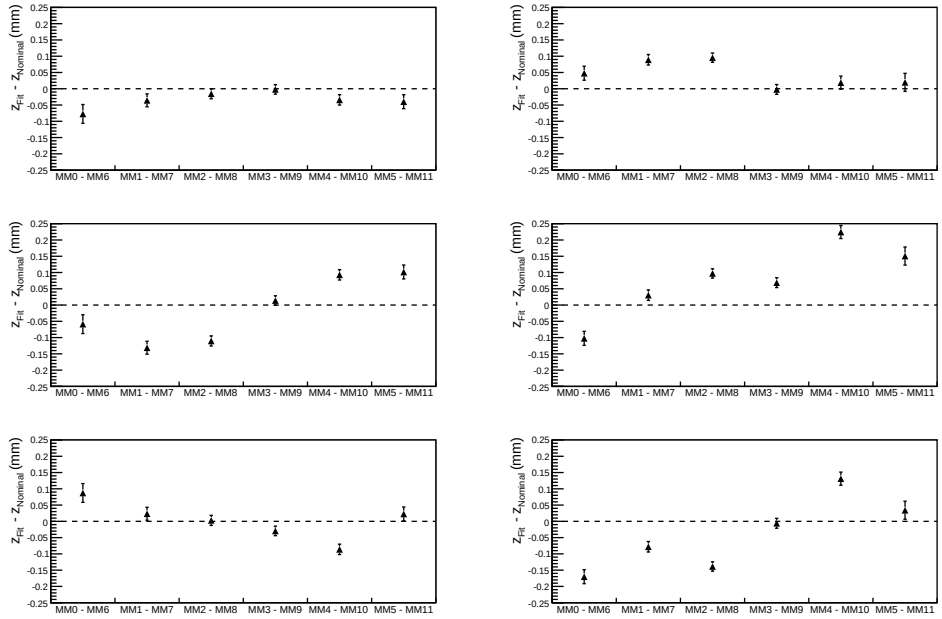

Figure 4.20: Translational correction bias δ_z between the introduced Simple geometry and the fit results.

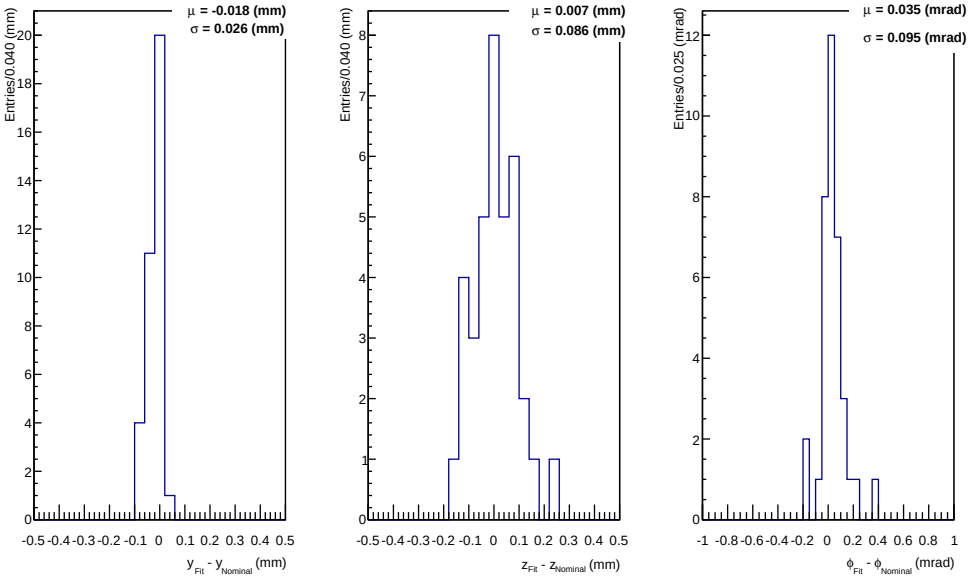

Figure 4.21: Bias distributions for the three correction constants. Translation corrections δ_y on the left, δ_z in the center while rotation corrections δ_ϕ on the right.

4.6.5 Survey-like geometry

The final test is performed reproducing in the TPC geometry measured by the optical Survey, as listed in Tab. 4.5. This configuration represents the most realistic test including multiple (translation + rotational) misalignments within the MM pairs. The fit results are shown in Fig. 4.22, 4.23, 4.24: the fit perfectly reproduces the test Survey-like geometry. The comparison between the simulated geometry and the fit is shown in Fig. 4.25, 4.26, 4.27. Small biases are visible in the results for translations in the z direction where the fit is less sensitive because of the absence of vertical tracks in the sample. Figure 4.28 show the bias distributions for translational (left and center) and rotational (right) corrections. The mean and the width of such distributions are also displayed.

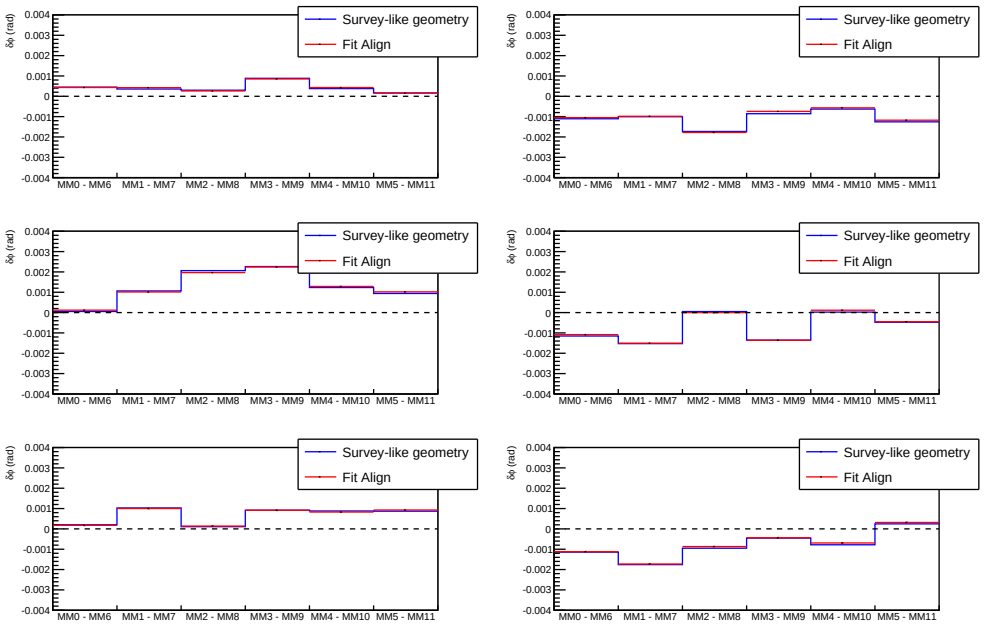

Figure 4.22: Survey-like test geometry results on rotation δ_ϕ. In blue the test Survey geometry, in red the fit results.

TPC1 EP0	$\delta\phi$ (mrad)	Nominal (mrad)	δz (mm)	Nominal (mm)	δy (mm)	Nominal (mm)
MM0-MM6	0.432 ± 0.018	0.449	-0.319 ± 0.018	-0.216	0.350 ± 0.004	0.353
MM1-MM7	0.424 ± 0.016	0.357	-0.256 ± 0.010	-0.192	0.233 ± 0.004	0.241
MM2-MM8	0.263 ± 0.013	0.299	-0.183 ± 0.009	-0.135	0.084 ± 0.003	0.097
MM3-MM9	0.852 ± 0.018	0.884	-0.160 ± 0.010	-0.088	0.298 ± 0.004	0.302
MM4-MM10	0.430 ± 0.014	0.378	-0.079 ± 0.010	-0.011	0.307 ± 0.004	0.300
MM5-MM11	0.153 ± 0.017	0.164	-0.005 ± 0.010	0.046	0.174 ± 0.004	0.175
TPC1 EP1	$\delta\phi$ (mrad)	Nominal (mrad)	δz (mm)	Nominal (mm)	δy (mm)	Nominal (mm)
MM0-MM6	-1.049 ± 0.021	-1.105	0.173 ± 0.011	0.115	0.044 ± 0.004	0.033
MM1-MM7	-0.983 ± 0.013	-1.005	0.377 ± 0.012	0.340	0.152 ± 0.004	0.144
MM2-MM8	-1.779 ± 0.019	-1.731	0.138 ± 0.008	0.093	0.057 ± 0.003	0.086
MM3-MM9	-0.743 ± 0.013	-0.857	0.210 ± 0.009	0.180	-0.004 ± 0.003	-0.010
MM4-MM10	-0.567 ± 0.014	-0.629	0.187 ± 0.011	0.142	0.091 ± 0.005	0.071
MM5-MM11	-1.176 ± 0.014	-1.257	0.068 ± 0.013	-0.008	0.252 ± 0.005	0.252
TPC2 EP0	$\delta\phi$ (mrad)	Nominal (mrad)	δz (mm)	Nominal (mm)	δy (mm)	Nominal (mm)
MM0-MM6	0.119 ± 0.027	0.064	0.042 ± 0.030	0.177	0.350 ± 0.010	0.373
MM1-MM7	1.031 ± 0.024	1.064	-0.246 ± 0.021	-0.132	0.488 ± 0.008	0.511
MM2-MM8	1.943 ± 0.022	2.064	0.229 ± 0.016	0.250	0.038 ± 0.007	0.055
MM3-MM9	2.222 ± 0.024	2.264	0.076 ± 0.015	0.145	0.236 ± 0.007	0.245
MM4-MM10	1.243 ± 0.030	1.233	-0.139 ± 0.016	-0.082	0.633 ± 0.007	0.653
MM5-MM11	1.012 ± 0.033	0.994	0.074 ± 0.021	0.106	0.291 ± 0.009	0.300
TPC2 EP1	$\delta\phi$ (mrad)	Nominal (mrad)	δz (mm)	Nominal (mm)	δy (mm)	Nominal (mm)
MM0-MM6	-1.084 ± 0.034	-1.152	-0.092 ± 0.022	-0.159	0.407 ± 0.010	0.412
MM1-MM7	-1.505 ± 0.019	-1.526	0.040 ± 0.017	-0.102	0.671 ± 0.008	0.678
MM2-MM8	-0.001 ± 0.026	0.051	0.135 ± 0.015	0.085	0.294 ± 0.007	0.322
MM3-MM9	-1.361 ± 0.018	-1.355	0.210 ± 0.016	0.170	0.570 ± 0.007	0.601
MM4-MM10	0.117 ± 0.024	0.023	0.194 ± 0.020	0.082	0.331 ± 0.008	0.340
MM5-MM11	-0.447 ± 0.038	-0.475	0.224 ± 0.028	0.151	0.522 ± 0.010	0.560
TPC3 EP0	$\delta\phi$ (mrad)	Nominal (mrad)	δz (mm)	Nominal (mm)	δy (mm)	Nominal (mm)
MM0-MM6	0.174 ± 0.056	0.202	-0.025 ± 0.045	0.073	0.120 ± 0.0135	0.108
MM1-MM7	1.002 ± 0.049	1.209	-0.133 ± 0.038	-0.051	0.485 ± 0.032	0.493
MM2-MM8	0.138 ± 0.046	0.109	-0.318 ± 0.035	-0.247	0.230 ± 0.030	0.240
MM3-MM9	0.916 ± 0.044	0.919	-0.331 ± 0.034	-0.235	0.179 ± 0.031	0.191
MM4-MM10	0.829 ± 0.045	0.880	-0.224 ± 0.034	-0.218	0.089 ± 0.031	-0.025
MM5-MM11	0.928 ± 0.046	0.871	-0.087 ± 0.037	-0.102	0.275 ± 0.033	0.293
TPC3 EP1	$\delta\phi$ (mrad)	Nominal (mrad)	δz (mm)	Nominal (mm)	δy (mm)	Nominal (mm)
MM0-MM6	-1.121 ± 0.047	-1.143	0.282 ± 0.037	0.158	0.272 ± 0.034	0.271
MM1-MM7	-1.728 ± 0.045	-1.758	0.218 ± 0.035	0.264	0.104 ± 0.032	0.126
MM2-MM8	-0.870 ± 0.044	-0.950	0.245 ± 0.034	0.212	0.172 ± 0.031	0.188
MM3-MM9	-0.435 ± 0.045	-0.454	0.357 ± 0.034	0.258	0.302 ± 0.030	0.346
MM4-MM10	-0.693 ± 0.048	-0.782	0.337 ± 0.037	0.279	0.338 ± 0.032	0.346
MM5-MM11	0.315 ± 0.054	0.246	0.150 ± 0.043	0.037	0.272 ± 0.034	0.299

Table 4.5: Fit results for each readout plane under the Survey-like geometry configuration hypothesis.

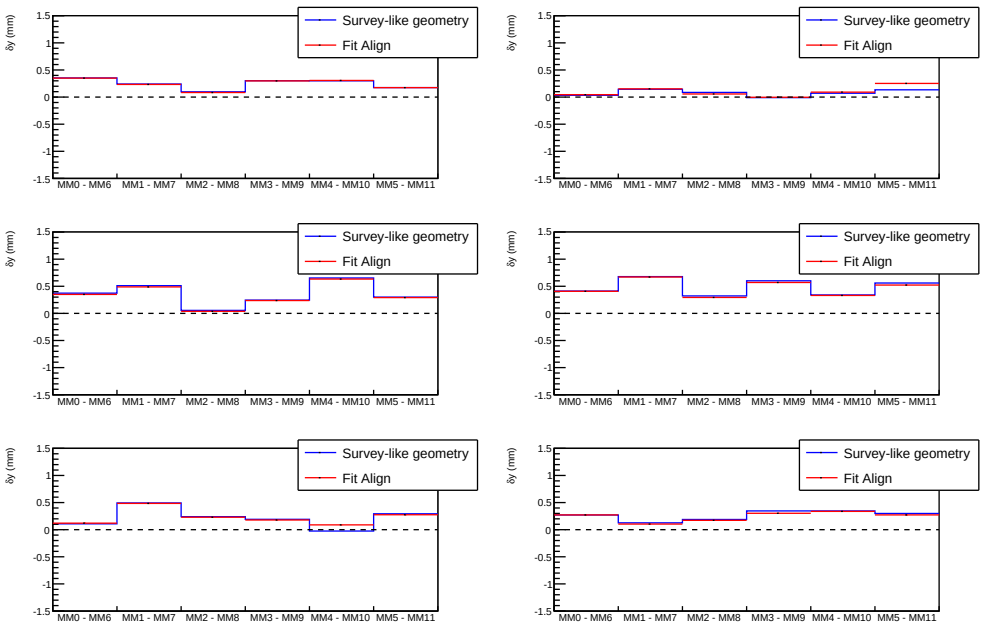

Figure 4.23: Results on translation corrections δ_y. In blue the test Survey-like geometry, in red the fit results.

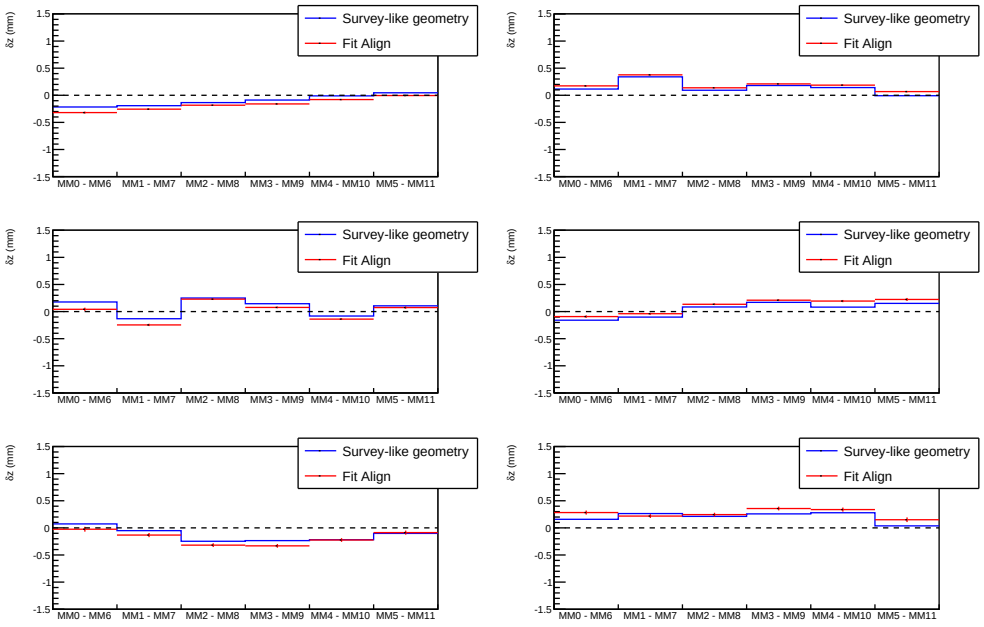

Figure 4.24: Results on translation corrections δ_z. In blue the test Survey-like geometry, in red the fit results.

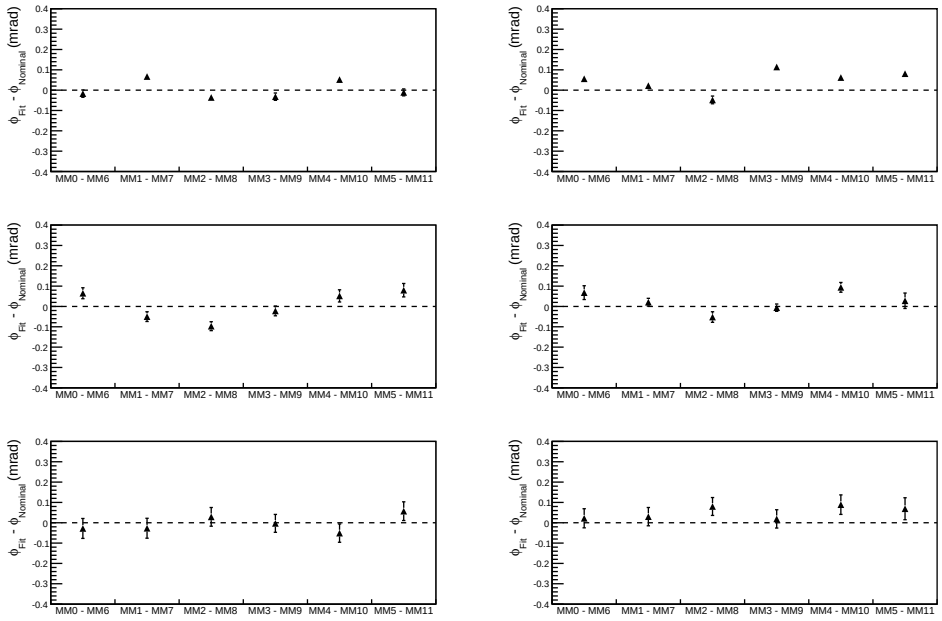

Figure 4.25: Bias between the Survey-like and the fit results for δ_ϕ corrections.

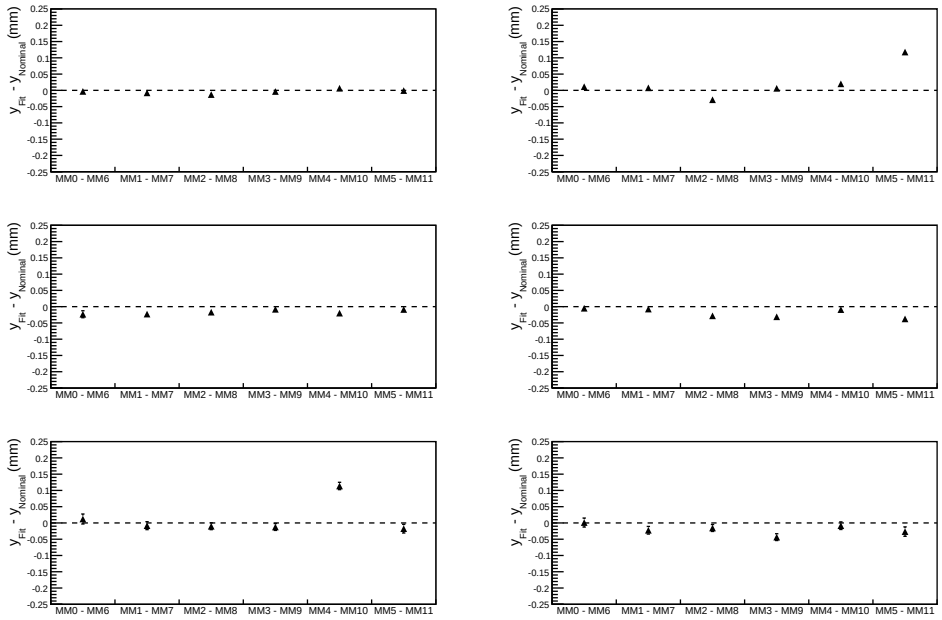

Figure 4.26: Bias between the Survey-like and the fit results for δ_y corrections.

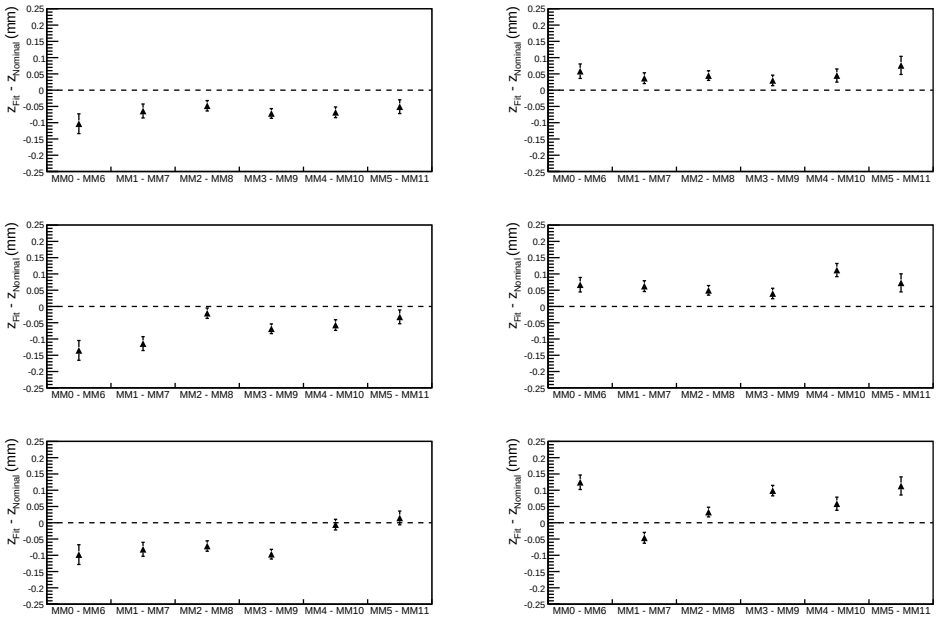

Figure 4.27: Bias between the Survey-like and the fit results for δ_z corrections.

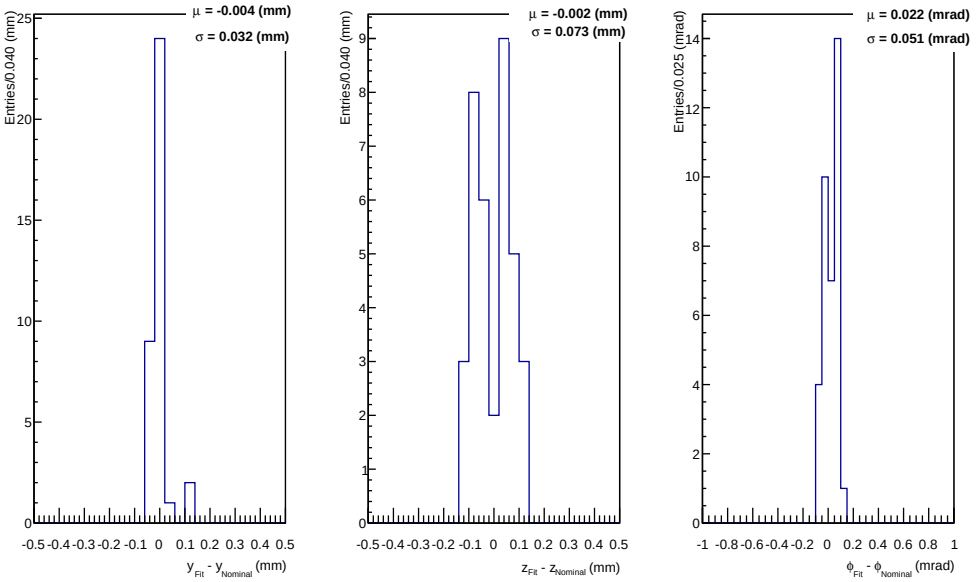

Figure 4.28: Bias distributions for the three correction constants.

4.7 MicroMegas alignment results on data

In this Section the alignment procedure is applied to the data sample of cosmics in RunII-IV (Tab. 4.3). Selection cuts described in Sec. 4.3 are applied to the data sample, as listed in Tab. 4.2.

4.7.1 1^{st} step: rotation corrections

The first step of the alignment procedure consists in the extraction of rotational correction constants letting free to vary the angular parameters in the column 0 (MM0-5). All the parameters related to translations are fixed as well as ϕ angles in the second column (MM6-11). The extracted corrections for angular misalignments (δ_ϕ) are listed in Tab. 4.6.

TPC1 EP0	δ_ϕ (mrad)	**TPC2 EP0**	δ_ϕ (mrad)	**TPC3 EP0**	δ_ϕ (mrad)
MM0-MM6	1.197 ± 0.053	**MM0-MM6**	0.779 ± 0.096	**MM0-MM6**	1.532 ± 0.083
MM1-MM7	1.112 ± 0.056	**MM1-MM7**	0.915 ± 0.042	**MM1-MM7**	1.092 ± 0.066
MM2-MM8	0.924 ± 0.058	**MM2-MM8**	2.965 ± 0.040	**MM2-MM8**	0.783 ± 0.058
MM3-MM9	1.383 ± 0.067	**MM3-MM9**	2.037 ± 0.041	**MM3-MM9**	0.796 ± 0.052
MM4-MM10	0.164 ± 0.074	**MM4-MM10**	1.004 ± 0.045	**MM4-MM10**	0.654 ± 0.050
MM5-MM11	0.485 ± 0.078	**MM5-MM11**	1.741 ± 0.119	**MM5-MM11**	0.539 ± 0.054
TPC1 EP1	δ_ϕ (mrad)	**TPC2 EP1**	δ_ϕ (mrad)	**TPC3 EP1**	δ_ϕ (mrad)
MM0-MM6	-1.636 ± 0.071	**MM0-MM6**	-1.277 ± 0.108	**MM0-MM6**	-1.106 ± 0.061
MM1-MM7	-1.149 ± 0.069	**MM1-MM7**	-1.464 ± 0.045	**MM1-MM7**	-1.771 ± 0.056
MM2-MM8	-1.424 ± 0.064	**MM2-MM8**	0.524 ± 0.041	**MM2-MM8**	0.520 ± 0.055
MM3-MM9	-1.085 ± 0.062	**MM3-MM9**	0.024 ± 0.042	**MM3-MM9**	-1.641 ± 0.059
MM4-MM10	0.070 ± 0.061	**MM4-MM10**	-1.100 ± 0.045	**MM4-MM10**	0.916 ± 0.063
MM5-MM11	0.102 ± 0.061	**MM5-MM11**	0.079 ± 0.102	**MM5-MM11**	0.917 ± 0.074

Table 4.6: Angular correction constants δ_ϕ for rotational misalignments for each MM pairs.

4.7.2 2^{nd} step: translation corrections

The angular corrections determined in the first step (Tab. 4.6) are then applied to reconstruct the tracks used in the second step for the evaluation of translation corrections δ_y and δ_z. The parameters related to translations and rotations are now free to vary in one column (column 0) and fixed in the other one (column 1). The extracted translation corrections, are listed in Tab. 4.7. After the application of the angular correction constants, the mutual rotation between the MM pair is impressively reduced. To test if residual rotational misalignments are properly evaluated, the fit runs again letting free, this time, just the angular parameters in one column. All the translation parameters are fixed. Results are compared in Fig. 4.29: a good agreement between the first and second configuration is shown, proving the robustness and reliability of the fit in the angular correction constants determination.

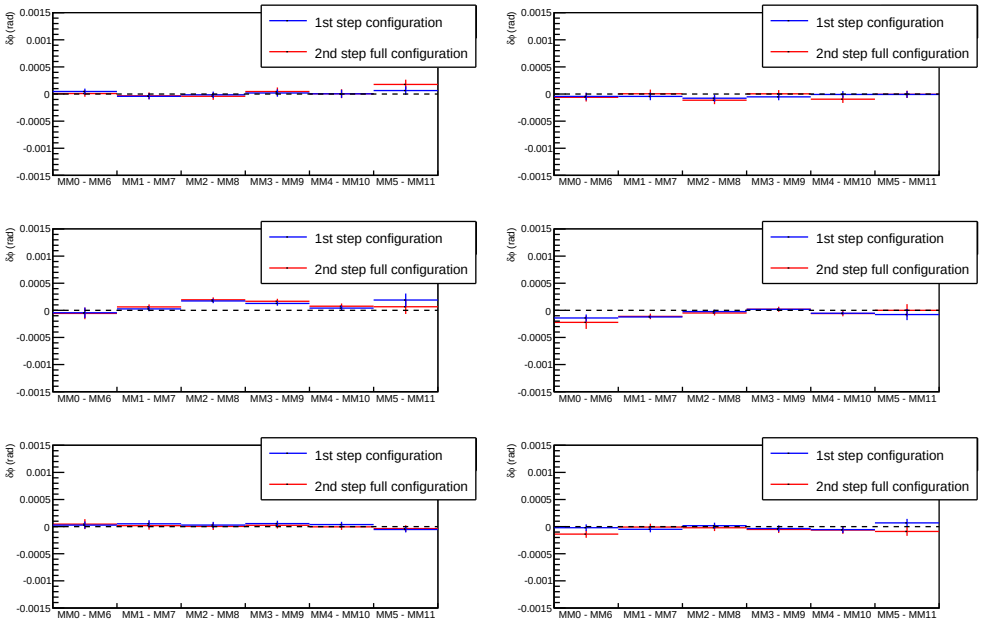

Figure 4.29: Angular corrections comparison extracted running two times the fit with different configuration: translation + rotational in red, only rotational in blue.

TPC1 EP0	δ_z (mm)	δ_y (mm)	δ_ϕ (mrad)
MM0-MM6	0.109 ± 0.029	0.472 ± 0.018	0.009 ± 0.059
MM1-MM7	0.401 ± 0.030	0.546 ± 0.018	-0.033 ± 0.063
MM2-MM8	0.548 ± 0.030	0.242 ± 0.017	-0.041 ± 0.066
MM3-MM9	0.316 ± 0.030	0.302 ± 0.017	0.046 ± 0.075
MM4-MM10	0.480 ± 0.030	0.065 ± 0.020	0.006 ± 0.082
MM5-MM11	0.211 ± 0.028	0.095 ± 0.021	0.177 ± 0.088
TPC1 EP1	δ_z (mm)	δ_y (mm)	δ_ϕ (mrad)
MM0-MM6	-0.342 ± 0.027	0.177 ± 0.019	-0.060 ± 0.078
MM1-MM7	-0.244 ± 0.028	0.267 ± 0.019	0.005 ± 0.077
MM2-MM8	-0.405 ± 0.030	0.129 ± 0.017	-0.114 ± 0.073
MM3-MM9	-0.450 ± 0.029	-0.060 ± 0.017	0.004 ± 0.069
MM4-MM10	-0.214 ± 0.031	-0.033 ± 0.019	-0.095 ± 0.069
MM5-MM11	-0.084 ± 0.028	-0.043 ± 0.020	-0.005 ± 0.068
TPC2 EP0	δ_z (mm)	δ_y (mm)	δ_ϕ (mrad)
MM0-MM6	-0.214 ± 0.049	0.069 ± 0.028	-0.057 ± 0.107
MM1-MM7	0.090 ± 0.016	0.496 ± 0.012	0.063 ± 0.047
MM2-MM8	0.388 ± 0.014	0.552 ± 0.011	0.194 ± 0.045
MM3-MM9	0.158 ± 0.014	0.630 ± 0.011	0.167 ± 0.046
MM4-MM10	-0.154 ± 0.017	0.810 ± 0.012	0.076 ± 0.050
MM5-MM11	0.456 ± 0.050	0.646 ± 0.031	0.066 ± 0.133
TPC2 EP1	δ_z (mm)	δ_y (mm)	δ_ϕ (mrad)
MM0-MM6	0.038 ± 0.044	0.635 ± 0.028	-0.222 ± 0.121
MM1-MM7	-0.315 ± 0.016	1.030 ± 0.012	-0.112 ± 0.051
MM2-MM8	-0.476 ± 0.014	0.672 ± 0.011	-0.049 ± 0.046
MM3-MM9	-0.074 ± 0.014	0.462 ± 0.011	0.020 ± 0.047
MM4-MM10	-0.248 ± 0.017	0.818 ± 0.012	-0.059 ± 0.051
MM5-MM11	0.009 ± 0.046	0.297 ± 0.029	0.000 ± 0.114
TPC3 EP0	δ_z (mm)	δ_y (mm)	δ_ϕ (mrad)
MM0-MM6	0.047 ± 0.034	0.631 ± 0.022	0.046 ± 0.092
MM1-MM7	0.062 ± 0.028	0.686 ± 0.018	0.018 ± 0.074
MM2-MM8	-0.236 ± 0.025	0.402 ± 0.015	0.004 ± 0.066
MM3-MM9	0.171 ± 0.027	0.551 ± 0.015	0.025 ± 0.059
MM4-MM10	0.111 ± 0.029	0.576 ± 0.017	-0.004 ± 0.056
MM5-MM11	-0.033 ± 0.032	0.452 ± 0.020	-0.036 ± 0.061
TPC3 EP1	δ_z (mm)	δ_y (mm)	δ_ϕ (mrad)
MM0-MM6	0.005 ± 0.033	0.252 ± 0.022	-0.138 ± 0.068
MM1-MM7	-0.359 ± 0.027	0.0130 ± 0.017	-0.008 ± 0.062
MM2-MM8	-0.232 ± 0.024	-0.086 ± 0.015	-0.021 ± 0.061
MM3-MM9	0.113 ± 0.024	0.530 ± 0.015	-0.052 ± 0.066
MM4-MM10	0.443 ± 0.027	0.491 ± 0.017	-0.063 ± 0.070
MM5-MM11	-0.007 ± 0.034	0.372 ± 0.021	-0.089 ± 0.081

Table 4.7: 2^{nd} step results for the extraction of translation corrections δ_y and δ_z.

4.7.3 Alignment results

The last step (closure test) of the procedure consists in reconstructing the tracks applying all the evaluated corrections at the same time (translation + rotation) and running the fit again. It can be summarized as follow:

- **Alignment corrections:** $\delta\phi$ from the 1^{st} step and δy, δz from the 2^{nd} step
- **Run the fit:** looking at possible residual misalignments on the reconstructed sample.

The applied correction constants are listed in Tables 4.6 for rotations and 4.7 for translations. Figures 4.30, 4.31, 4.32 show alignment results before (blue lines) and after (red lines) the MM alignment procedure for the full set of correction constants δ_ϕ, δ_y and δ_z. The distributions of the residuals before and after the alignment are shown in Fig.4.33 and summarized in Tab. 4.8. The corrections worked properly allowing to achieve the desired precision of the order of 0.1 mrad in ϕ and 30(50) μm in $y(z)$ direction.

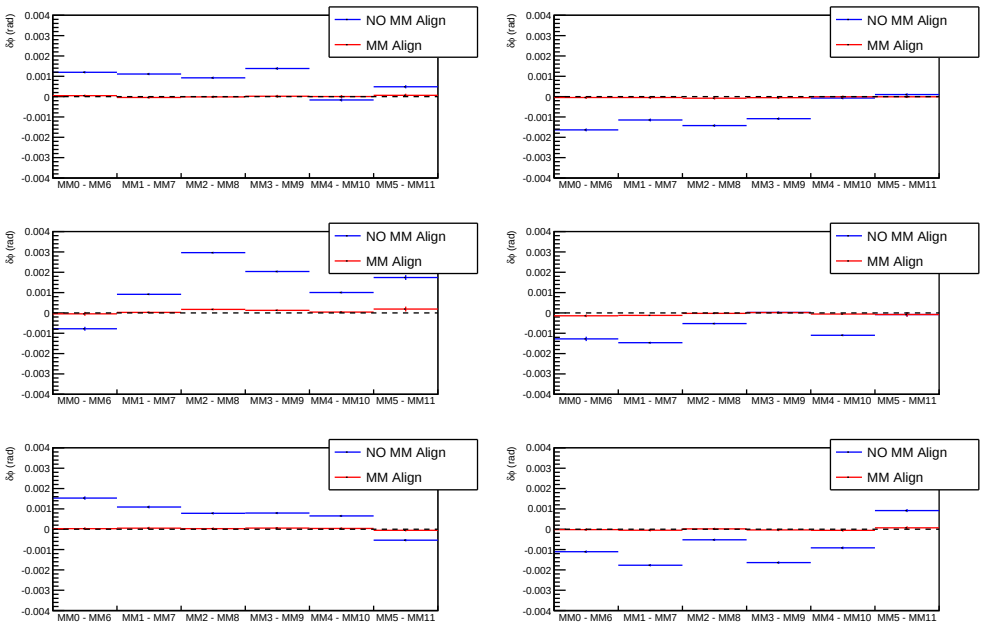

Figure 4.30: First step alignment results for angular corrections. In blue (NO MM Align) the extracted corrections, in red the results after applying them.

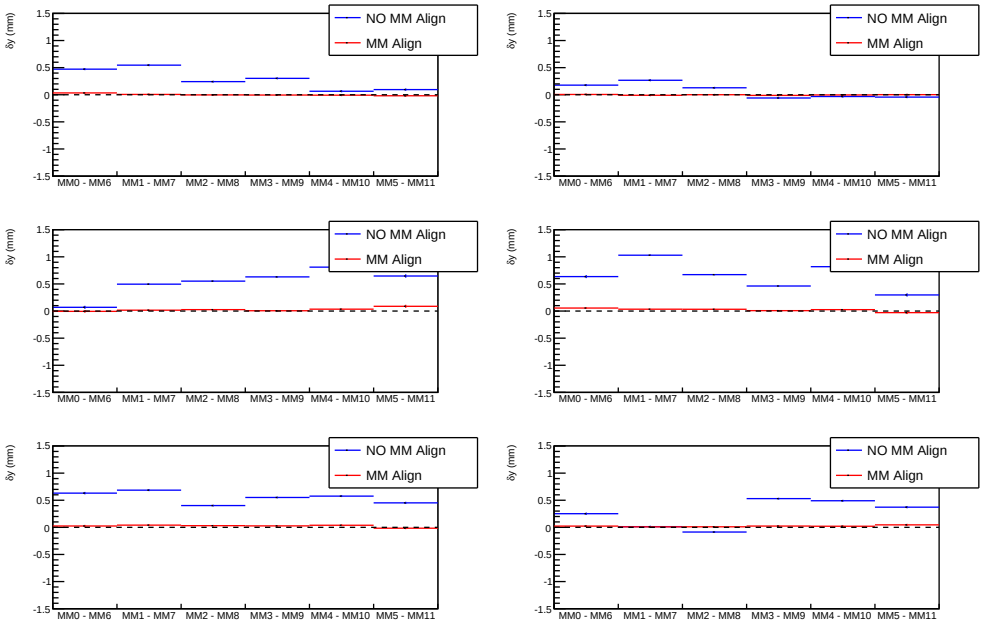

Figure 4.31: Second step alignment results for the translation in the y direction before and after applying corrections.

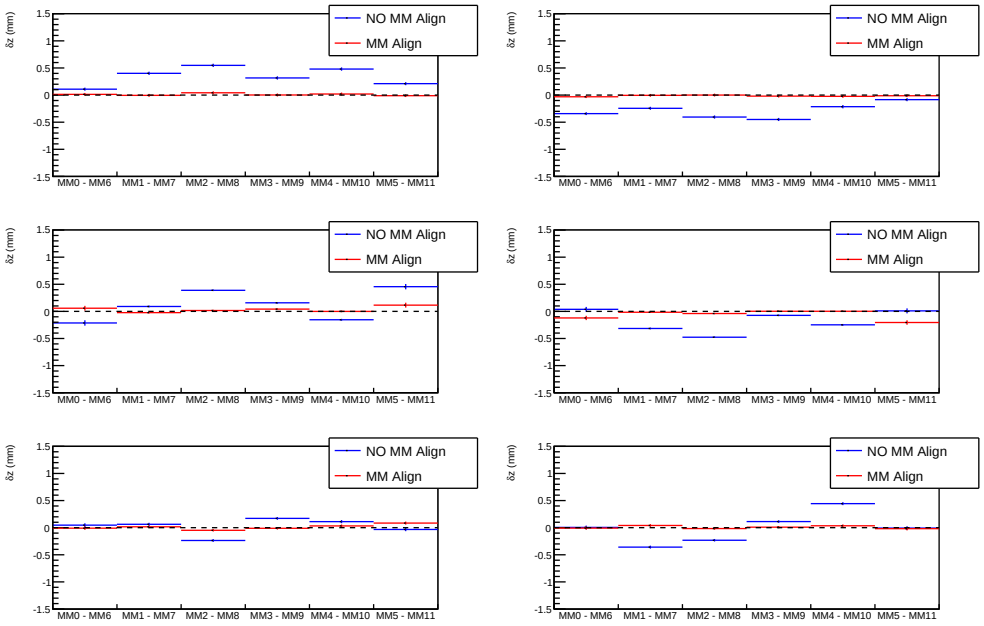

Figure 4.32: Second step alignment results for the translation in the z direction before and after applying corrections.

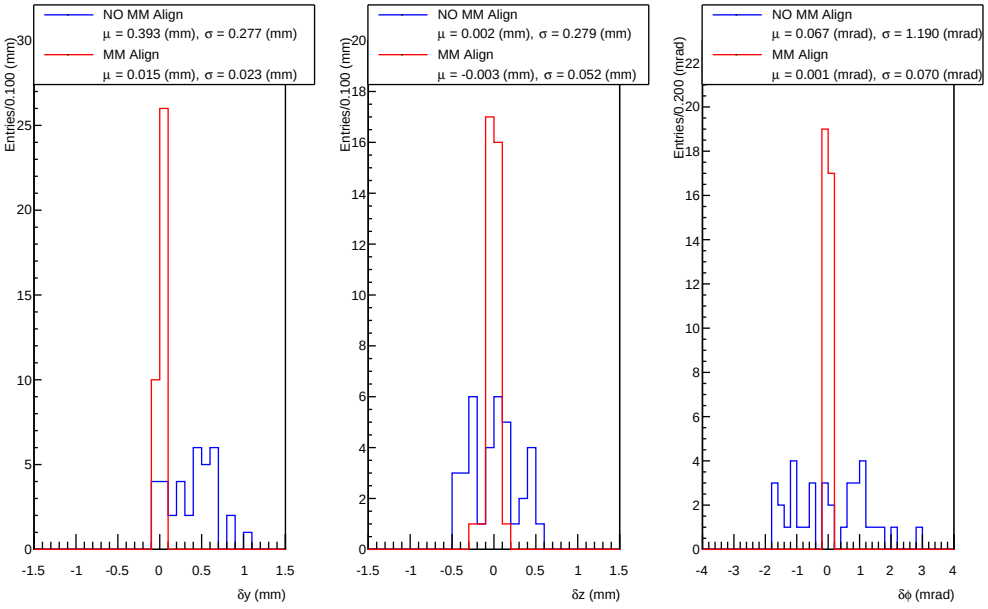

Figure 4.33: Residual distributions before in blue and after in red the two step alignment procedure. The δ_y on the left, the δ_z in the center and the rotations δ_ϕ on the right.

	NoMMAlign δ_z (mm)	MMAlign δ_z (mm)	NoMMAlign δ_y (mm)	MMAlign δ_y (mm)	NoMMAlign δ_ϕ (mrad)	MMAlign δ_ϕ (mrad)
TPC1 EP0						
MM0-MM6	0.109 ± 0.028	0.013 ± 0.026	0.472 ± 0.018	0.034 ± 0.017	1.197 ± 0.053	0.047 ± 0.053
MM1-MM7	0.401 ± 0.030	-0.005 ± 0.027	0.546 ± 0.018	0.006 ± 0.016	1.112 ± 0.056	-0.042 ± 0.056
MM2-MM8	0.548 ± 0.030	0.042 ± 0.027	0.242 ± 0.017	-0.003 ± 0.015	0.924 ± 0.058	-0.014 ± 0.059
MM3-MM9	0.316 ± 0.030	0.001 ± 0.028	0.302 ± 0.017	-0.005 ± 0.016	1.383 ± 0.067	0.019 ± 0.068
MM4-MM10	0.480 ± 0.030	0.020 ± 0.027	0.065 ± 0.020	-0.008 ± 0.018	-0.164 ± 0.074	0.004 ± 0.075
MM5-MM11	0.211 ± 0.028	-0.011 ± 0.025	0.095 ± 0.021	-0.019 ± 0.019	0.485 ± 0.078	0.064 ± 0.079
TPC1 EP1						
MM0-MM6	-0.342 ± 0.027	-0.031 ± 0.024	0.177 ± 0.019	0.005 ± 0.017	-2.636 ± 0.071	-0.044 ± 0.071
MM1-MM7	-0.244 ± 0.028	-0.005 ± 0.026	0.267 ± 0.019	-0.010 ± 0.017	-1.149 ± 0.069	-0.044 ± 0.070
MM2-MM8	-0.405 ± 0.030	0.000 ± 0.026	0.129 ± 0.017	0.001 ± 0.015	-1.424 ± 0.064	-0.077 ± 0.065
MM3-MM9	-0.450 ± 0.029	-0.019 ± 0.026	-0.060 ± 0.017	-0.012 ± 0.015	-1.085 ± 0.062	-0.052 ± 0.063
MM4-MM10	-0.214 ± 0.031	-0.023 ± 0.027	-0.033 ± 0.019	-0.004 ± 0.017	-0.070 ± 0.061	-0.008 ± 0.062
MM5-MM11	-0.084 ± 0.028	-0.012 ± 0.025	-0.043 ± 0.020	0.002 ± 0.018	0.102 ± 0.061	-0.008 ± 0.062
TPC2 EP0						
MM0-MM6	-0.214 ± 0.050	0.058 ± 0.044	0.069 ± 0.028	-0.006 ± 0.025	-0.779 ± 0.096	-0.045 ± 0.097
MM1-MM7	0.090 ± 0.016	-0.023 ± 0.015	0.496 ± 0.012	0.016 ± 0.010	0.915 ± 0.042	0.026 ± 0.043
MM2-MM8	0.388 ± 0.014	0.0161 ± 0.013	0.552 ± 0.011	0.026 ± 0.010	2.965 ± 0.040	0.173 ± 0.041
MM3-MM9	0.158 ± 0.015	0.042 ± 0.013	0.630 ± 0.011	0.006 ± 0.010	2.037 ± 0.041	0.127 ± 0.042
MM4-MM10	-0.154 ± 0.017	-0.000 ± 0.015	0.810 ± 0.012	0.035 ± 0.011	1.004 ± 0.045	0.041 ± 0.045
MM5-MM11	0.456 ± 0.050	0.115 ± 0.045	0.646 ± 0.031	0.087 ± 0.028	1.741 ± 0.119	0.190 ± 0.120
TPC2 EP1						
MM0-MM6	0.038 ± 0.045	-0.121 ± 0.040	0.635 ± 0.028	0.055 ± 0.015	-1.277 ± 0.108	-0.141 ± 0.065
MM1-MM7	-0.315 ± 0.016	-0.016 ± 0.014	1.030 ± 0.012	0.034 ± 0.006	-1.464 ± 0.045	-0.122 ± 0.025
MM2-MM8	-0.477 ± 0.014	-0.040 ± 0.012	0.672 ± 0.011	0.033 ± 0.008	-0.524 ± 0.041	-0.023 ± 0.035
MM3-MM9	-0.074 ± 0.014	0.002 ± 0.012	0.462 ± 0.011	0.008 ± 0.006	0.024 ± 0.042	0.018 ± 0.027
MM4-MM10	-0.248 ± 0.016	0.002 ± 0.014	0.818 ± 0.012	0.026 ± 0.007	-1.100 ± 0.045	-0.054 ± 0.028
MM5-MM11	0.009 ± 0.046	-0.205 ± 0.041	0.297 ± 0.029	-0.029 ± 0.026	-0.079 ± 0.102	-0.078 ± 0.103
TPC3 EP0						
MM0-MM6	0.047 ± 0.034	-0.009 ± 0.031	0.631 ± 0.022	0.025 ± 0.020	1.532 ± 0.083	0.028 ± 0.083
MM1-MM7	0.062 ± 0.028	0.016 ± 0.025	0.686 ± 0.018	0.041 ± 0.016	1.092 ± 0.066	0.052 ± 0.067
MM2-MM8	-0.236 ± 0.025	-0.048 ± 0.023	0.402 ± 0.015	0.031 ± 0.014	0.783 ± 0.058	0.029 ± 0.059
MM3-MM9	0.171 ± 0.026	-0.012 ± 0.023	0.551 ± 0.015	0.027 ± 0.014	0.796 ± 0.052	0.056 ± 0.053
MM4-MM10	0.111 ± 0.029	0.032 ± 0.027	0.576 ± 0.017	0.038 ± 0.015	0.654 ± 0.050	0.038 ± 0.051
MM5-MM11	-0.033 ± 0.032	0.085 ± 0.028	0.452 ± 0.020	-0.016 ± 0.018	-0.539 ± 0.054	-0.053 ± 0.054
TPC3 EP1						
MM0-MM6	0.005 ± 0.033	-0.008 ± 0.030	0.252 ± 0.022	0.023 ± 0.020	-1.106 ± 0.061	-0.020 ± 0.062
MM1-MM7	-0.359 ± 0.027	0.041 ± 0.025	0.013 ± 0.017	0.009 ± 0.015	-1.771 ± 0.056	-0.049 ± 0.056
MM2-MM8	-0.232 ± 0.024	-0.016 ± 0.021	-0.086 ± 0.015	0.010 ± 0.013	-0.520 ± 0.055	0.017 ± 0.056
MM3-MM9	0.113 ± 0.024	0.009 ± 0.022	0.530 ± 0.015	0.024 ± 0.014	-1.641 ± 0.059	-0.035 ± 0.059
MM4-MM10	0.443 ± 0.027	0.035 ± 0.025	0.491 ± 0.017	0.020 ± 0.016	-0.916 ± 0.063	-0.055 ± 0.064
MM5-MM11	-0.007 ± 0.034	-0.018 ± 0.031	0.372 ± 0.021	0.046 ± 0.019	0.917 ± 0.074	0.069 ± 0.074

Table 4.8: Alignment corrections (NOMMAlign) and residuals after MicroMegas modules alignment (MMAlign) on data RunII-IV for each MM pair of adjacent modules of each TPC readout plane.

4.8 Validation of the alignment results

Finally in order to test the goodness and reliability of the new set of correction constants the new MM geometry, determined in the previous section, is introduced in the reconstruction algorithm.

4.8.1 Spatial resolution

To observe the effect on the spatial resolution, the residual per column between the y position of the fitted track and the corresponding cluster is computed at fixed z. Thus, the hit resolution variable Δy can be obtained for each reconstructed segment in the TPC as:

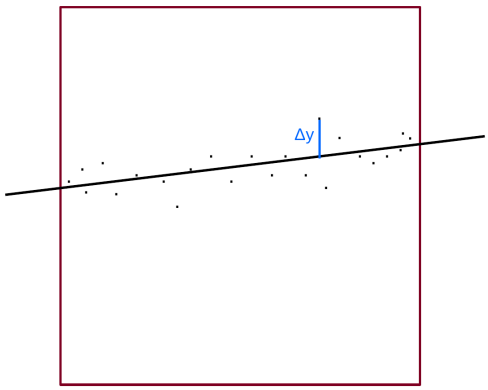

$$\Delta y = y_{fit}^{track} - y_{hit}^{track} \tag{4.13}$$

where y_{hit}^{track} is the y coordinate of the hit of the track in the YZ-plane and y_{fit}^{track} is the related y position after the track reconstruction at the same z coordinate. The sample still consists of cosmic rays from RunII-IV collected with magnetic field off. Tracks parameter are now computed using the ND280 standard reconstruction without breaking tracks in a single MM module as described in Sec. 3.5.1. Neither $\vec{B}$ nor $\vec{E}$ field corrections are applied. It is possible to produce three different geometry samples which differ thanks to the sets of alignment constants applied to the cosmic rays data:

NO MM Alignment: no corrections are applied

Survey Alignment: the ND280 default alignment constants (optical alignment see Sec. 4.2)

MINUIT Fit Alignment: the new correction alignment constants extracted by the fit in the previous sections.

Only good reconstructed tracks and tracks with a reasonable number of hits are taken into account. Poor reconstruction is also avoid adding a cut on the residual value. The list of cuts is summarized in the Tab. 4.9. A single horizontal track which entirely crosses a TPC will leave at least 72 hits. Finally the track fit-hit residual is averaged per column via a two gaussian fit to the projected distribution obtained by dividing in

Quality track	$10^{-5} < \chi^2 < 0.5$
Number of hits	$40 < n_{hits} < 90$
Residual	$\|\Delta y\| < 3$ mm

Table 4.9: Selection cuts for alignment validation.

slice of pad column the pad column-residual distribution. The residual Δy is averaged for each TPC separately. Figure 4.34 shows the fit-hit residual mean value as a function of the pad column in the three TPCs for each considered sample, the EP0 on the top while EP1 on the bottom. A green line divides the three TPCs: TPC1 0-71, TPC2 72-143, TPC3 144-215. The mean value obtained before correction of the geometry (NO MM Alignment) is shown in blue, the one from the optical measurements (Survey Alignment) are presented in black while in red there are the values obtained after the MM alignment procedure according to the constants determined by the fit.
Since no field corrections are applied the residual mean values closer to the MP between columns must be compared. When no alignment corrections are applied a clear gap is present between the two MM columns of each EP of the TPCs. This gap is considerably reduced (~ 50 μm) when an alignment geometry is introduced. When the modules are well aligned, this difference tends to be zero for clusters close to the column, the residual values are typically less than 100 μm. The Fit Alignment is slightly better than the Survey in the EP0 of the three TPCs (top plot) where the two distributions overlap, however, it is much better in the EP1 (bottom) where the gap in the Fit case is negligible in the three readout planes (i.e. TPC3 EP1). No electric field correction is applied to the sample, this leads the residuals to have the classic S shape due to distortions in the field. The S shape is more pronounced looking at the tracks crossing just one MM pair. For this reason, in order to probe the new alignment correction constants effects on the TPC performances, they must be studied coupled with electric field distorting corrections.
As additional cross-check for the goodness of the Fit Alignment, also the track-hit residual pad column correlation between a single MM pair are studied to see if also locally the fit is better than survey. Figures 4.35, 4.36, 4.37 show this behavior for MM pairs in TPC1, TPC2 and TPC3 respectively. The column number runs from 0 to 71 while the green line represents the MP between the MMs. Even locally track fit-hit residuals are better for the Fit Alignment, the gap is impressively reduced and it is negligible in the most of the MM couples, which satisfy the zero gap condition more than Survey Alignment case. In the next section a study of the impact on the momentum measurement of the new geometry together with the electric field distortion correction will be shown.

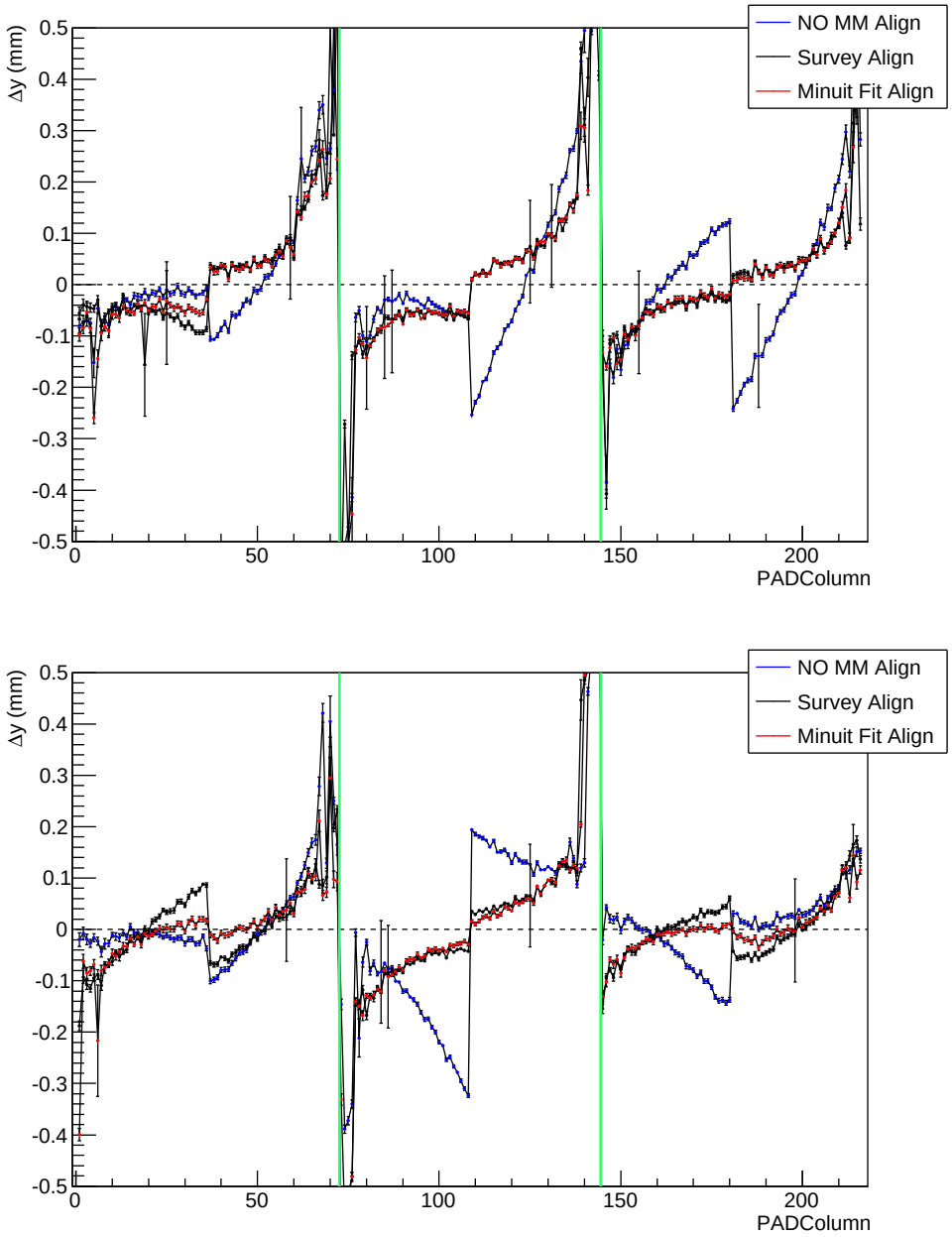

Figure 4.34: Track fit-hit residuals mean value as a function of the column number for the EP0 on the top and EP1 on the bottom. The green lines divide the three TPCs.

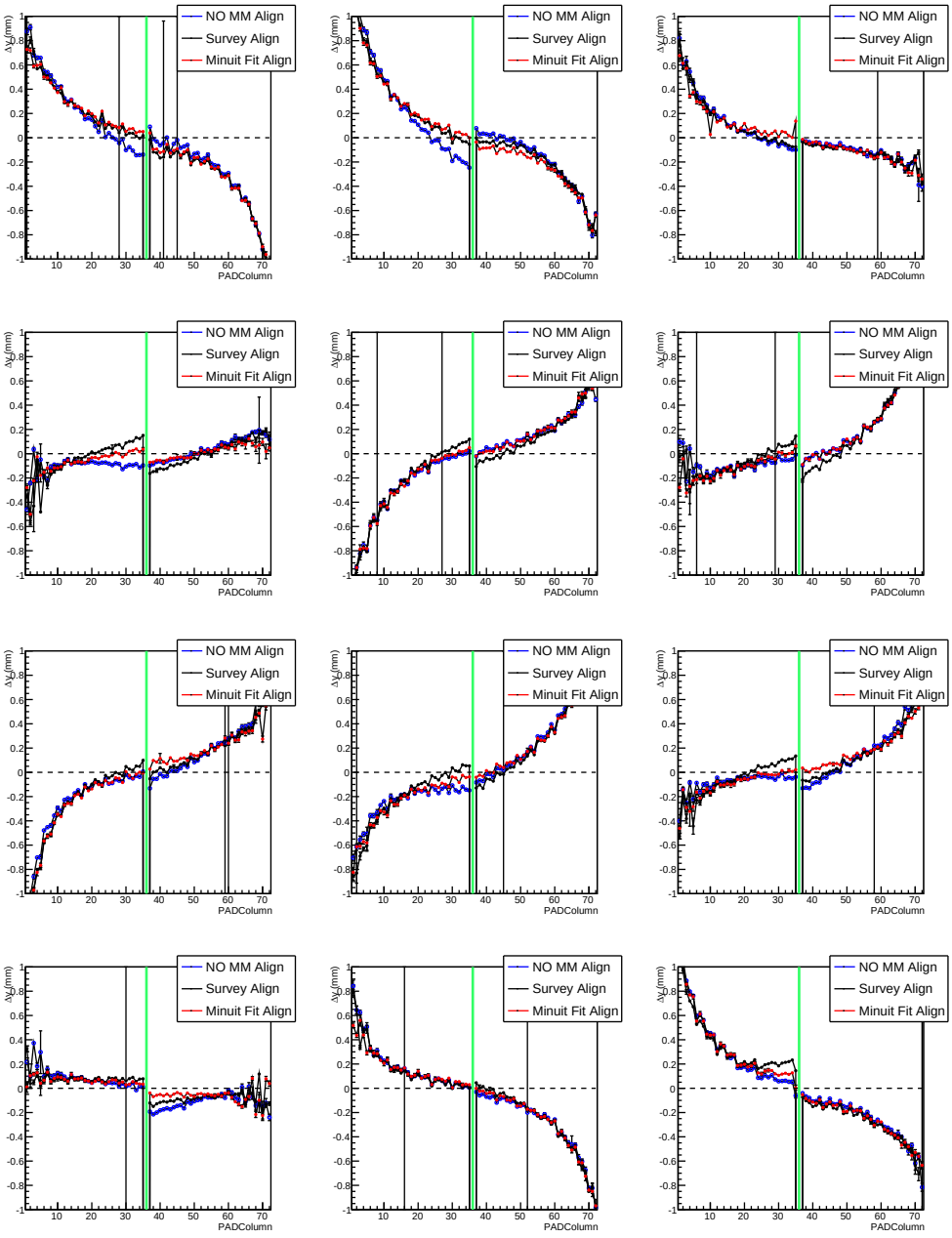

Figure 4.35: Track fit-hit residuals mean value as a function of the column number for all the MM pairs in the TPC1 EPs. The EP0 in the first two rows and EP1 in the last two rows. The green lines is the middle plane between two adjacent MM modules.

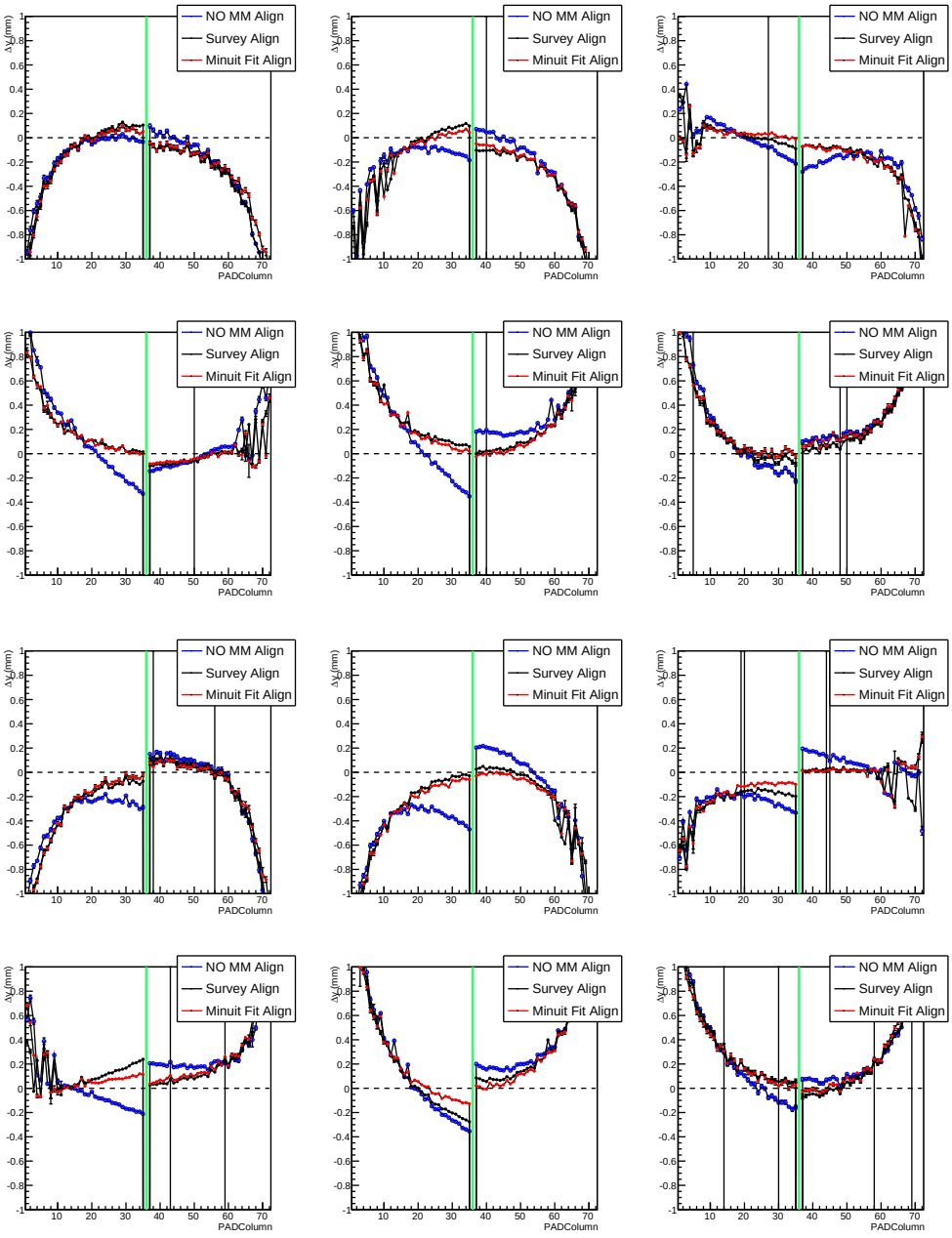

Figure 4.36: Track fit-hit residuals mean value as a function of the column number for all the MM pairs in the TPC2 EPs. The EP0 in the first two rows and EP1 in the last two rows. The green lines is the middle plane between two adjacent MM modules.

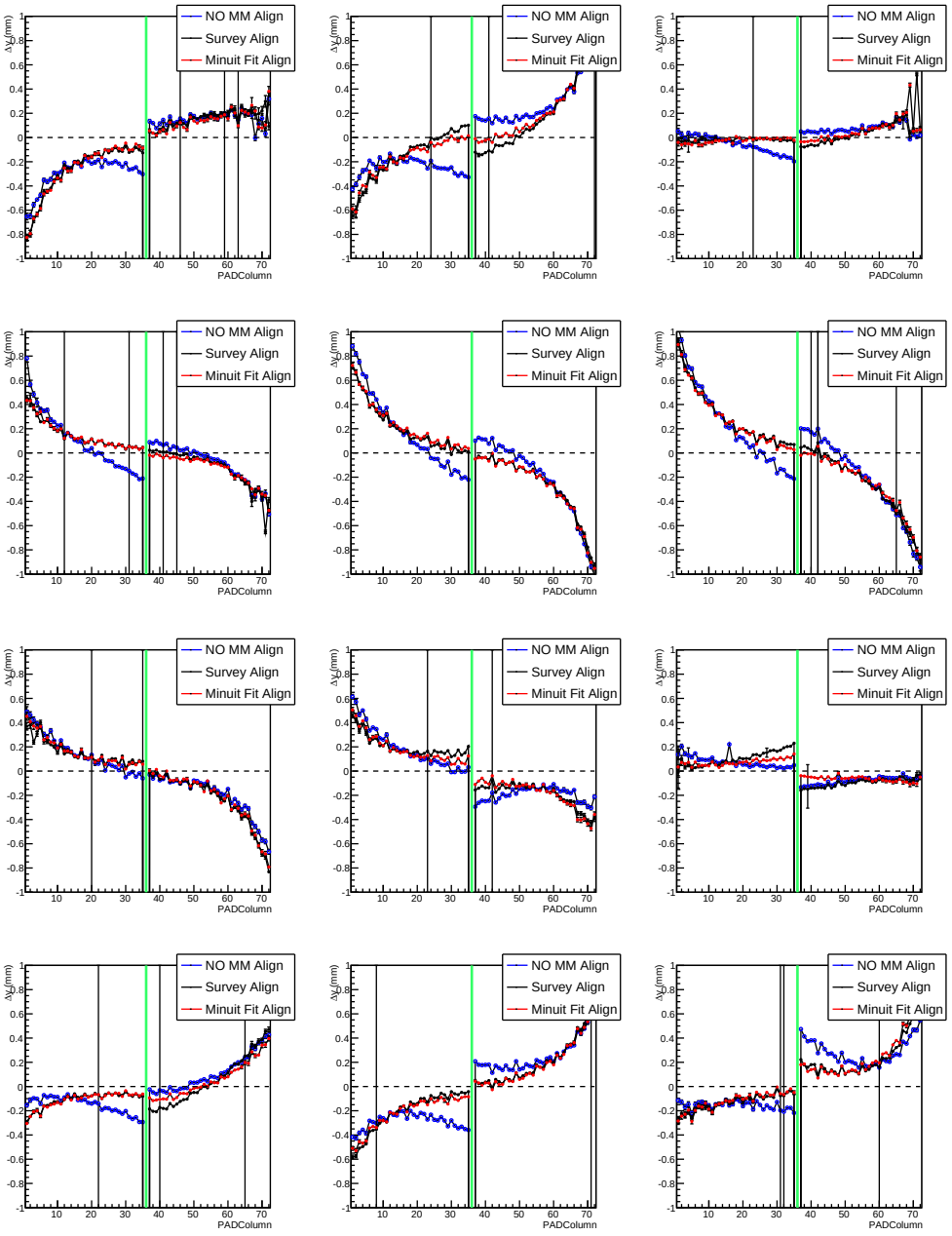

Figure 4.37: Track fit-hit residuals mean value as a function of the column number for all the MM pairs in the TPC3 EPs. The EP0 in the first two rows and EP1 in the last two rows. The green lines is the middle plane between two adjacent MM modules.

4.8.2 Momentum resolution

Micromegas misalignments have an effect on the momentum reconstruction. In this section, the impact of the alignment corrections together with electric field correction on the momentum resolution is studied in detail. A comparison with optical alignment result is also shown. The first step for this study is the design of a suitable control sample. The data sample consists of neutrino beam interactions from ND280 RunIII collected with magnetic field on $\vec{B} = (0.2, 0, 0)$ T. The MC is obtained using the corresponding RunIII simulation (for more details see Sec. 6.1.1). In order to get a clean sample of very horizontal tracks parallel to the MM plane coming from ν_μ interactions in the detector, the following selection criteria are applied:

1. **Event quality:** the event must be in time with the beam trigger and have good detector and good beam flags.
2. **Number of TPC tracks:** the global track must cross at least two TPC tracks, but no more than one in each TPC.
3. **TPC and global track quality:** the number of vertical pad columns hit should be higher than 18 in each TPC segment and more than 60 for all TPC segments in global track.
4. **Negative track:** only one negative global track.
5. **Muon PID:** the global track must be identified as muon-like.
6. **Long FGD segment:** a minimal length for the track pass through the FGD $L > 320$ mm, to avoid tracks coming from the side of the detector (i.e. cosmics).
7. **Restricted Fiducial Volume:** the interaction must occur in the defined Fiducial Volume $z > -3000$ mm, $|x, (y)| < 950$ mm.
8. **Momentum:** the transverse momentum higher than 3 GeV/c. This condition is included to use only very straight tracks.
9. **Track distance:** the distance along x between the beginning and the end of the segment must be $\Delta x < 45$ mm and the cathode is not crossed.

This selection selects events with tracks having very small angles in the x-direction. Different samples are produced according to the fields and alignment correction constants applied in the reconstruction:

MC RunIII: perfect MM geometry, no field distortions neither in the $\vec{E}$ nor in $\vec{B}$.

DATA MM SurveyAlign: optical alignment applied together with electric and magnetic field distortion corrections.

DATA MM FitAlign: new alignment constants applied together with electric and magnetic field distortion corrections.

The use of the global reconstruction is mandatory in this analysis since track segments associated to global track have to be matched to each other. The study of the TPC global momentum resolution has been performed using tracks crossing multiple TPCs which allow to build a fully reconstructed observable sensitive only to the intrinsic TPC resolution. The aim of the method is to measure the momentum resolution from the data themselves. The reconstructed observable is defined as the difference between the inverse transverse momentum (p_t) reconstructed using the two TPC segments of the same global track

$$\Delta(1/p_t) = \frac{1}{p_t^{(2)}} - \frac{1}{p_t^{(1)} - \Delta p_t^{(FGD)}} \tag{4.14}$$

where $p_t^{(1)}$ and $p_t^{(2)}$ are the transverse momenta measured in the first and second TPC respectively while $\Delta p_t^{(FGD)}$ is the transverse momentum loss in the intermediate FGD. The latter takes into account the dependency of $\Delta(1/p_t)$ resolution on the energy loss in the FGD. Such variable will be a gaussian distributed with mean value $\langle\Delta(1/p_t)\rangle$ and standard deviation $\sigma[\Delta(1/p_t)]$.
The $\Delta(1/p_t)$ can be expressed as a function of the track kinematic variables: the transverse momentum (p_t), the angle in the y-direction ($\cos\theta_y$) and the position (x and y). The resulting distributions for different kinematic ranges can be then fitted with a gaussian function in order to extract resolution $\sigma[\Delta(1/p_t)]$. Figures 4.38 and 4.39 compare the momentum resolution and bias for the different samples distinguishing between the two available TPC couples (TPC1-TPC2 and TPC2-TPC3). Several conclusions can be drawn from these plots:

- The Fit MM alignment improves the momentum resolution in all the kinematic variables and reduce the discrepancy between data and MC especially in y-coordinate which is the one more affected by MM misalignments. An improvement in the resolution is also observed in both TPC couples mainly in p_t and x.

- The difference between data and MC is quite uniform in y and $\cos\theta_y$ and even in p_t except at very low momentum due to an incomplete description of energy loss. However that difference is more complicated as a function of x. It seems that $\sigma[\Delta(1/p_t)]$ is almost 0 at the pad plane ($x \sim 900$ mm) and increases with the drift distance and then it decreases when approaching the cathode.

- The momentum is overcorrected in the x-coordinate probably because the electric field correction, which is more sensitive to this coordinate, is extracted using a sample which includes the optical MM alignment.

- The improvement is more significant in TPC2-TPC3 couple where also field distortion are more pronounced (see Fig. 3.12).

- The discrepancies between data and MC are not completely solved with the new MM alignment. This might point to the the fact that electric field corrections includes the optical alignment, thus electric field distortion must be computed using the new set of constants for the MM alignment. Futhermore also the misalignment between the TPCs in the tracker introduce a bias, for this reason a similar fit should be performed in order to improve their alignment.

As shown in Fig. 4.38, the global momentum resolution is better in the MC. This effect introduces a systematic error on any event selection using the ND280 tracker. Thus the ultimate goal of this study is to look at the discrepancy between data and MC in order to find a systematic parameter (the smearing factor) that would be propagated in any event selection to make data match with the MC. For the momentum measurement systematics in ND280 tracker the smearing of the observable $(1/p_t)^{smear.}$ is done track by track as a function of the x-coordinate according to the following equation:

$$(1/p_t)^{smear.} = (1/p_t)^{true}_{MC} + (1+\alpha)\cdot\left[(1/p_t)^{reco}_{MC} - (1/p_t)^{true}_{MC}\right], \tag{4.15}$$

where $(1/p_t)^{true}_{MC}$ and $(1/p_t)^{reco}_{MC}$ are the true and reconstructed value of the observable. The coefficient α is the fractional difference in momentum resolution between data and MC that can be extracted from $2nd$ row plots in Fig. 4.38.

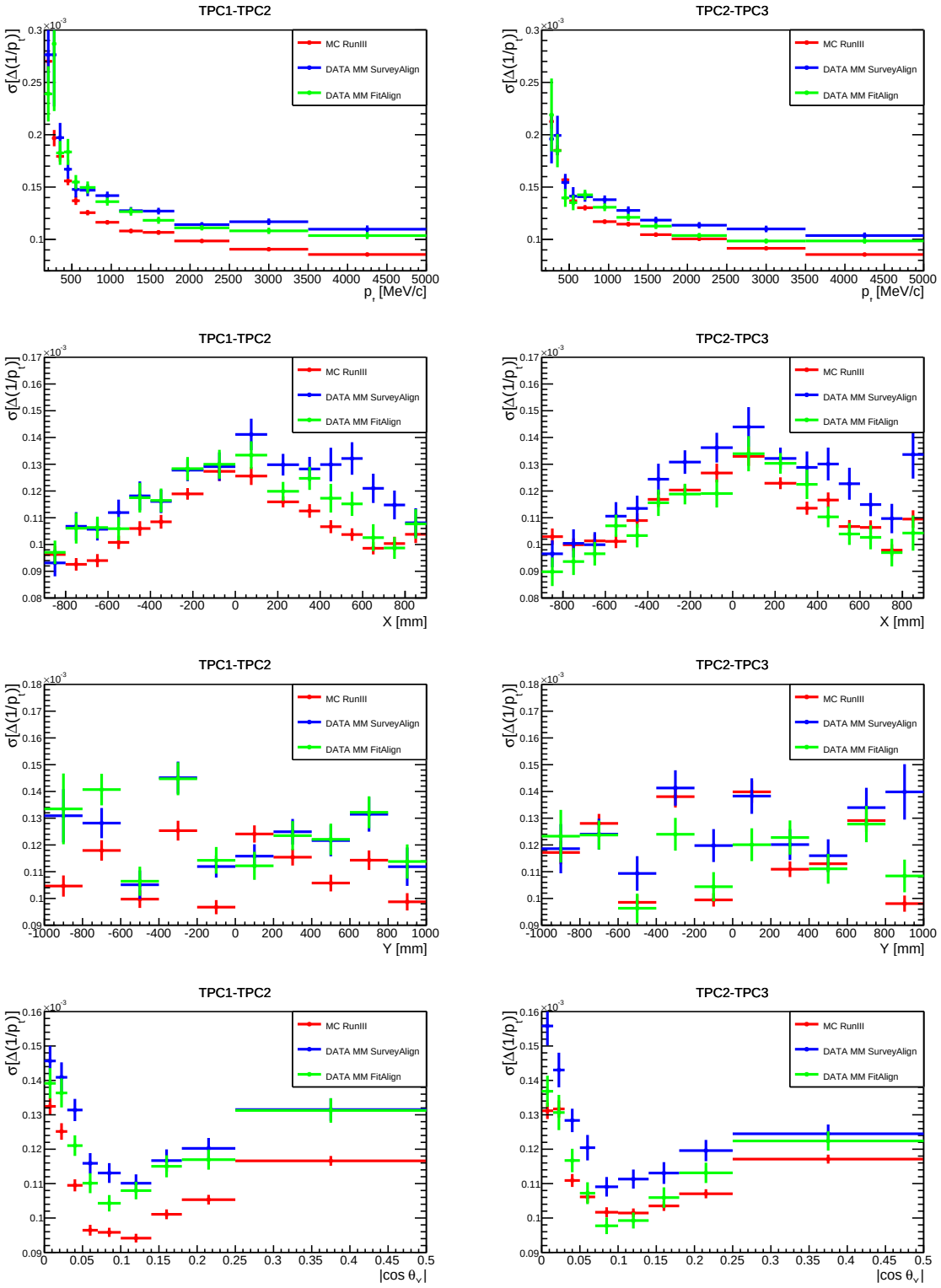

Figure 4.38: Momentum resolution as function of the transverse momentum, the cosino of the angle in the y-direction and positions x and y using TPC1-TPC2 (left) and TPC2-TPC3 (right). Colors indicates the different samples.

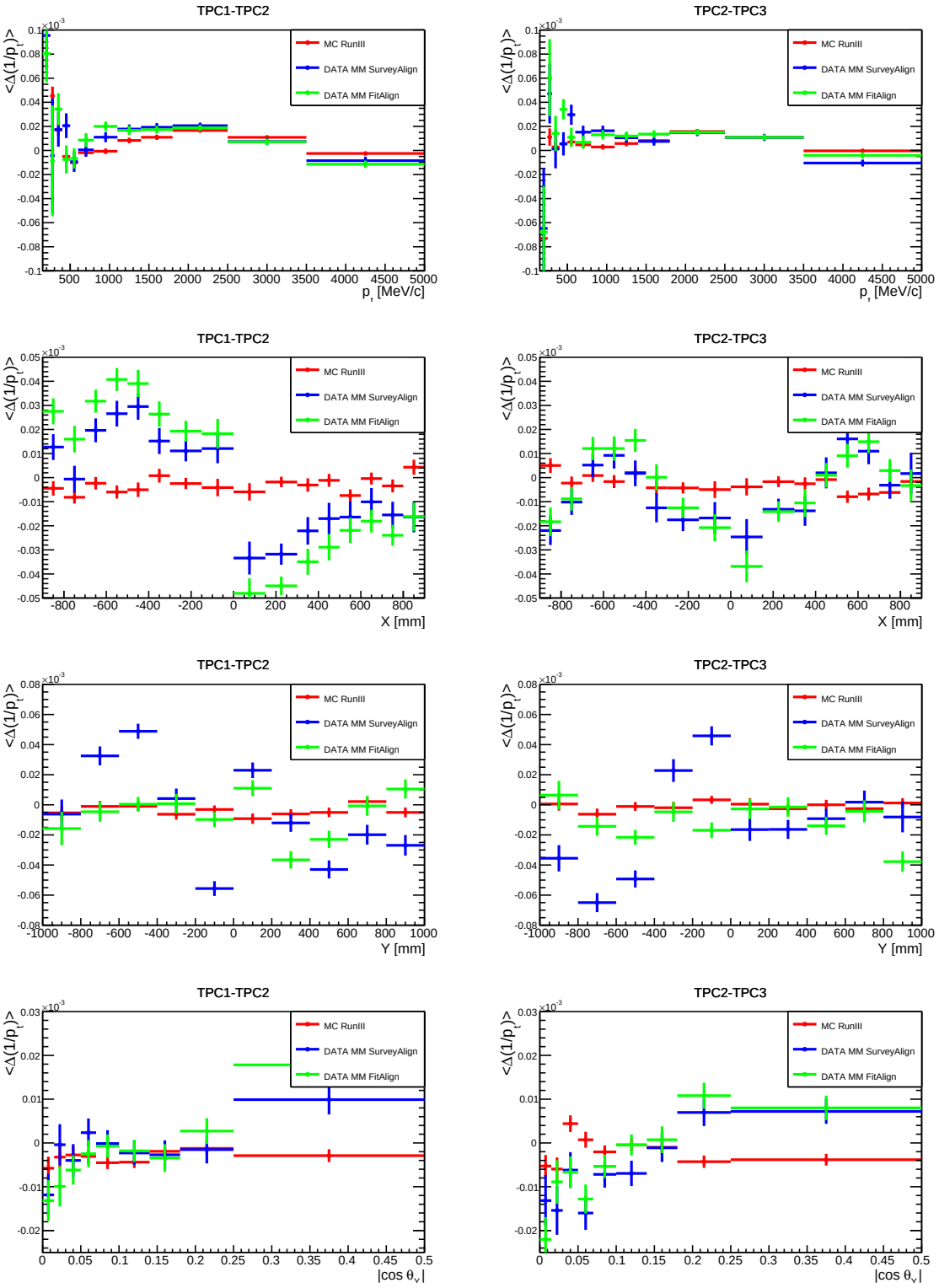

Figure 4.39: Momentum bias as function of the transverse momentum, the cosine of the angle in the y-direction and positions x and y using TPC1-TPC2 (left) and TPC2-TPC3 (right). Colors indicates the different samples.

4.9 Conclusions

MicroMegas modules misalignments in the TPC of ND280 have been studied in detail because they introduce a source of systematic error in the measurement of the particle momentum. For this reason a method to determine the value of the misalignments between modules belonging to the same readout plane has been proposed. It relies on the comparison of the track segments of a straight track reconstructed in adjacent modules. The performance of the fit is satisfactory, it reaches a good precision in both translation and rotational misalignments. Rotations are constrained with a precision better than 0.1 mrad while determination of misalignment between modules in the transverse direction (y) is ~ 20 μm. However the same accuracy is not achieved along the beam axis (z), where it stands at ~ 50 μm; the current reconstruction algorithm does not allow to measure with sufficient precision particle trajectory close to the vertical. An improvement for future study would be to include vertical tracks and align all the MM starting from the top module.
Track hit and momentum resolution studies show an improvement with respect to the optical measurements. Nevertheless, this correction is not able to totally reduce the observed discrepancies between data and MC in momentum resolution and bias. Currently the momentum resolution study has one problem: the MM misalignments are strongly correlated with electric field correction which relies to the optical measurements. In order to further improve the impact of the new alignment constants it would be necessary to repeat electric field distortion study using the new constants.

Chapter 5

Neutrino interactions with matter

As previously stated in Chapter 1 neutrinos are colorless, neutral fermions which only interact with matter through the weak force by exchanging a Z^0 or $W^{\pm}$ boson via:

Charge Current interactions (CC): mediated by the charged bosons $W^{\pm}$, they produce a charged lepton according to the flavor of the interacting neutrino (see Fig. 1.2 left). Since leptons have a very characteristic signature in particle detectors they are used to tag the incoming neutrino flavor.

Neutral Current interactions (NC): mediated by the Z^0 boson (see Fig. 1.2 right), they do not involve any charge exchange. The outgoing product is still a neutrino, therefore it is impossible in the detector to tag the neutrino flavor.

Neutrino oscillation experiments measure the CC and NC event rates which can generically be expressed as:

$$N(\vec{x}) = \sum_{i}^{process} \sum_{j}^{target} \Phi(E_\nu) \times \sigma_i(E_\nu, \vec{x}) \times \epsilon(\vec{x}) \times T_j \times P(\nu_\alpha \to \nu_\beta) \tag{5.1}$$

where $N(\vec{x})$ is the event rate of all the interaction processes as a function of the kinemtic variables $\vec{x}$ of the outgoing particles, $\Phi(E_\nu)$ is the neutrino flux which depends on neutrino energy E_ν, $\sigma_i(E_\nu, \vec{x})$ is the cross-section of a given CC or NC process, $\epsilon(\vec{x})$ describes the detector response and T_j is the number of nucleon targets of a given nucleus j in the detector fiducial volume. Finally, $P(\nu_\alpha \to \nu_\beta)$ is the neutrino oscillation probability.
In long baseline experiments the neutrino oscillation parameters are measured by comparing the neutrino interaction rate in Eq. 5.1 at near and far detectors. Such rate is the convolution of the neutrino flux and the neutrino interaction cross-section which must be propagated from the near to the far detector. Due to differences in geometrical acceptance and elemental composition of the detectors but also in neutrino energy spectrum and flavor composition because of ν oscillation, the extrapolation of the neutrino interaction rate from the near to the far detector is not trivial. However, the

near detector measurement of the neutrino rate can be used to constrain the systematics at the far detector. Table 5.1 shows the systematic uncertainties on the number of muon N_μ and electron N_e neutrino events predicted at SK with and without the ND280 measurements of the neutrino flux and cross-sections parameters (ND280 constraints) [108]. The neutrino sample benefits from this improvement by reducing the flux $\times$ cross-section uncertainty to $\sim 3\%$ which is comparable with the total SK uncertainty. Furthermore ND280 constrains the cross-section parameters uncertainty to $\sim 4\%$. This allows the overall uncertainty on the prediction to be reduced from $\sim 12\%$ to $\sim 5.4\%$. Figure 5.1 shows the uncertainty on the ν_μ and ν_e rate prediction at SK as a function of the neutrino energy.

	$\delta N_\mu/N_\mu$		$\delta N_e/N_e$	
Systematics Source	w/o ND280	w/ ND280	w/o ND280	w/ ND280
Flux	7.62%	3.60%	8.94%	3.64%
Cross Sections	9.74%	4.00%	7.17%	4.13%
Flux + Cross Sections	11.3%	2.79%	11.4%	2.88%
Final State/Secondary interaction Super-K	1.48%	1.48%	2.50%	2.50%
Super-K detector	3.86%	3.86%	2.39%	2.39%
Total	12.0%	5.03%	11.9%	5.41%

Table 5.1: Systematic uncertainties at SK on the predicted event rates of the ν_μ and ν_e samples with and without ND280 data.

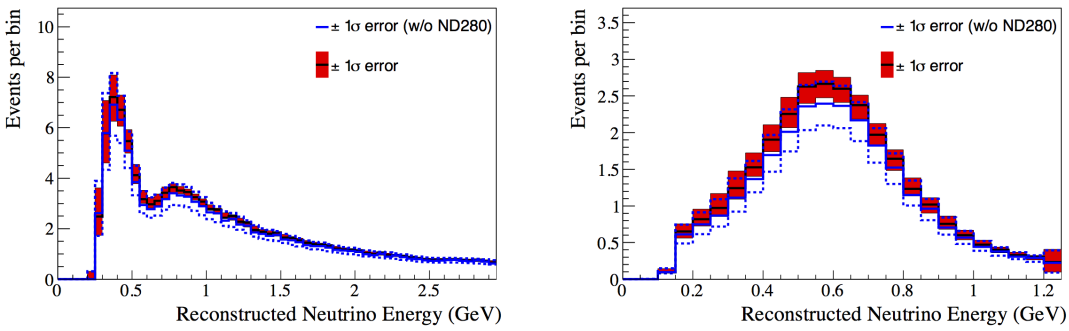

Figure 5.1: Predicted energy spectrum for ν_μ (left) and ν_e (right) events at SK, with and without ND280 constraints.

Therefore the precision of current and next generation neutrino oscillation experiments is limited by the knowledge of how neutrinos interact with matter. Thus, an accurate understanding of neutrino-nucleus interactions for different nuclear targets and as a function of the neutrino energy and of the kinematics of the outgoing particles is required.
In this chapter the most relevant neutrino interaction processes at the T2K energy and

their models are detailed in Sec. 5.1, Sec. 5.2 explains the nuclear effects while the generators currently in use in T2K are described in Sec. 5.4.

5.1 Neutrino-nucleus interaction at T2K

The T2K experiment lies in the intermediate energy range $\langle E_\nu \rangle = 600$ MeV. The neutrino interaction modes include: CC and NC quasi-elastic, CC and NC resonant and coherent pion production, deep inelastic scattering as shown in Fig. 5.2.

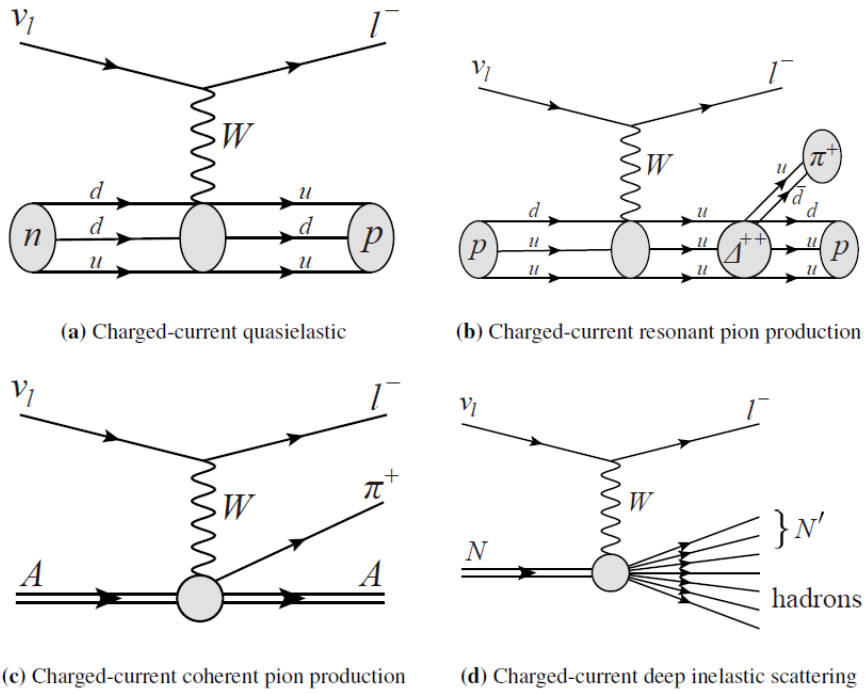

(a) Charged-current quasielastic

(b) Charged-current resonant pion production

(c) Charged-current coherent pion production

(d) Charged-current deep inelastic scattering

Figure 5.2: Diagrams of neutrino charged current interactions.

Below 1 GeV, CC quasi-elastic interaction dominates the cross-section: only a lepton and an outgoing nucleon are produced in the final state (Fig. 5.2.a). It is called *"quasi"* because the nucleon is transformed into another nucleon. Above 1 GeV resonant pion production (Fig. 5.2.b) becomes important: the target nucleon can be excited into a baryonic resonance (mostly Δ) which decays producing a pion. Figure 5.2.c shows the coherent pion production where the neutrino scatters on the entire nucleus leaving it unchanged and producing a single pion. Finally, above few GeV deep inelastic scattering dominates the neutrino cross-section: the neutrino has enough energy to resolve the individual quark constituents of the nucleon producing a hadron shower (Fig. 5.2.d), the nucleon is broken apart. Figure 5.3 summarizes some of the existing measurements of CC neutrino cross sections per nucleon in the energy range $0.1-300$ GeV for differents

interaction modes. In the T2K energy range, displayed by the orange shaded region, CC quasi-elastic interactions dominate the total CC cross-section.

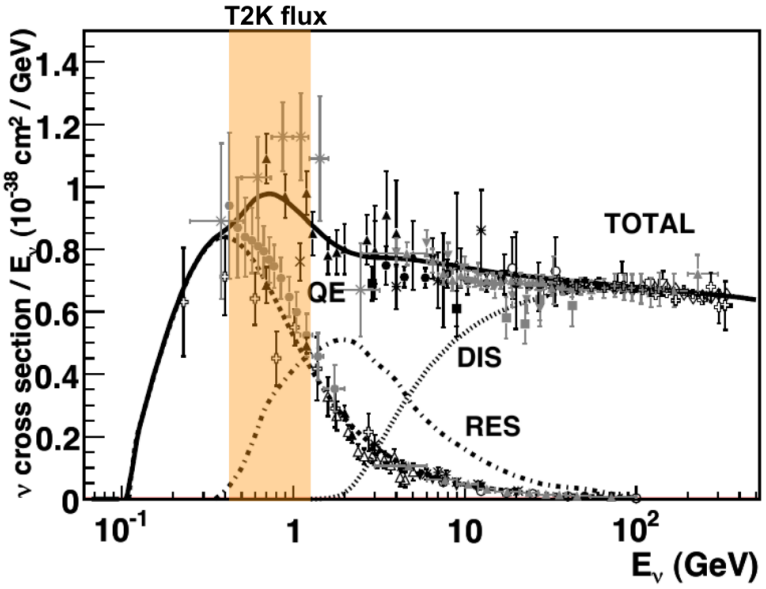

Figure 5.3: CC neutrino cross sections per nucleon as a function of the energy. The coherent contribution is not shown as it is negligible compared to the other channels. Figure modified from [109] to highlight the energy region around the T2K flux peak.

5.1.1 Quasi-Elastic interactions

Charged-current quasi-elastic (CCQE) neutrino-nucleon scattering is the dominant process for neutrino interactions in the GeV region:

$$\begin{aligned} \nu_l + n &\rightarrow p + l^-, \\ \overline{\nu}_l + p &\rightarrow n + l^+, \end{aligned} \tag{5.2}$$

where $\nu_l(\overline{\nu}_l)$ and $l^{-(+)}$ are a (anti-)neutrino and lepton of the same flavor, while n and p are the neutron and proton respectively. Assuming simple two-body kinematics and the nucleon at rest, the initial neutrino energy E_ν can be calculated as:

$$E_\nu = \frac{(m_n - E_B)\, E_l + \left(2m_n E_B - E_B^2 - m_l^2 + m_p^2 - m_n^2\right)}{2\left(m_n - E_B - E_\mu + P_l cos\theta_l\right)} \tag{5.3}$$

where m_p, m_n are the proton and neutron mass and m_l is the mass of the outgoing lepton of energy E_l, momentum p_l and angle θ_l with respect to the neutrino direction. The term E_B denotes the binding energy of the nucleon target in the nucleus, see Sec. 5.2.1.

Following the Llewellyn-Smith formalism which assumes the neutrino to be massless and the neutron (proton) to be at rest [110], the (anti-)neutrino-nucleon cross-section for the CCQE process can be written as:

$$\frac{\partial\sigma_{CCQE}}{\partial Q^2} = \frac{G_F^2(M_A^{QE})^2\cos\theta_c}{8\pi E_\nu^2}\left[A(Q^2) \pm B(Q^2)\frac{s-u}{(M_A^{QE})^2} + C(Q^2)\frac{(s-u)^2}{(M_A^{QE})^4}\right], \quad (5.4)$$

where the $(-)+$ refers to (anti-)neutrino scattering, G_F is the Fermi coupling, E_ν is the energy of the incident neutrino, M_A^{QE} is the axial nucleon mass, θ_c is the Cabibbo mixing angle and Q^2 is the squared four-momentum transfer [109]. The quantities $s = (p+k)^2$ and $u = (k-p')^2$ are the Lorentz-invariant Mandelstam variables which correspond respectively to the center of mass and the squared of four-momentum transfer $(s-u) = 4M_A^{QE}E_\nu - Q^2 - m_l$. The factors $A(Q^2), B(Q^2), C(Q^2)$ are functions of the vector $F_1(Q^2), F_2(Q^2)$, axial $F_A(Q^2)$, and pseudo-scalar $F_p(Q^2)$ form factors of the target nucleon. They account for the charge distribution in the nucleus and depend on the interaction. The vector form factors are well understood thanks to electron scattering experiments, and are directly related to the electromagnetic form factors [109]. On the contrary, axial and pseudo-scalar form factors are not well known since they are more difficult to measure experimentally. They can only be measured in neutrino interactions. $F_A(Q^2)$ and $F_p(Q^2)$ can be related by [111]:

$$F_p(Q^2) = \frac{2(M_A^{QE})^2}{m_\pi^2 + Q^2}F_A(Q^2). \quad (5.5)$$

In general, it is common to express the axial form factor as a dipole assuming that the weak axial charge follows an exponential distribution in the nucleon:

$$F_A(Q^2) = \frac{F_A(0)}{\left(1 + \frac{Q^2}{(M_A^{QE})^2}\right)^2}. \quad (5.6)$$

At the value $Q^2 = 0$, $F_A(0) = 1.2694 \pm 0.0028$ [109]. It has been determined through $\beta-$decay experiment. Only one parameter, the nucleon axial mass M_A^{QE}, remains free. A complete description of the cross-section calculation and the parametrization of each form factor can be found in [109]. As shown in Eq. 5.6 and 5.4, the axial form factor shape and the cross-section σ_{CCQE}, can be considered as a function of a single parameter M_A^{QE} which can be constrained using neutrino-nucleon scattering data. Old neutrino-deuterium scattering in bubble chamber fixed its value to $M_A^{QE} = 1.026 \pm 0.021$ GeV/c^2 [112].

Due to the two-body kinematics which allows to easily infer the energy of the incoming neutrino and to its dominating cross-section in the GeV region, the CCQE channel has been chosen in T2K as the main signal to investigate neutrino oscillations. Moreover it is the cleanest and most abundant channel to characterize the neutrino beam at the

near detector before oscillation (see Fig. 5.3). The ND280 detector provides a high-statistics sample of CCQE interactions which can be used to constrain the cross-section as a function of the variables p_μ and $\cos\theta_\mu$ describing the kinematics of the outgoing muon. Figure 5.4 shows the most recent T2K results on the CCQE-like double differential cross-section measurement for water and carbon [113] targets. For brevity only one double differential bin in $\cos\theta_\mu - p_\mu$ is shown. The measurements are performed in muon kinematics since they are directly observable in the detector: the neutrino energy measured with the two body approximation (Eq. 5.3) would introduce a model dependency since it has to be corrected for nuclear effects. Currently no model describes perfectly the nuclear effects and different models give different predictions. An overview is given in Sec. 5.2.

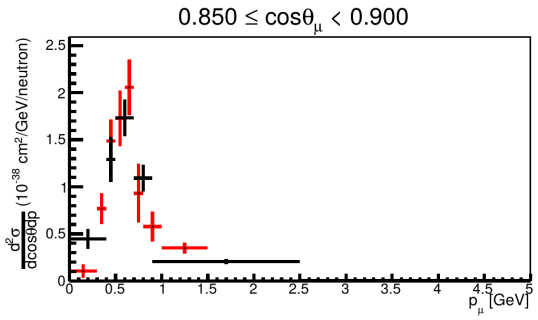

Figure 5.4: Double differential CCQE-like interaction cross-section $\frac{\partial^2\sigma}{\partial cos\theta_\mu \partial p_\mu}$ is measured for forward muons on water (black) and carbon (red) at T2K. Figure from [113].

In the last decade a tension between model predictions and neutrino data in CCQE interactions has been observed. The NOMAD [114] and the MiniBooNE [115] experiments observed a significant discrepancy in the cross-section measured at different energies. NOMAD was a magnetized tracking detector made mainly of carbon which can detect both muons and protons from a CCQE interaction. It used a neutrino beam with an energy in the range $3-10$ GeV. Conversely MiniBooNE is a 800 ton spherical mineral oil Cherenkov detector, exploiting a carbon target like NOMAD but with a neutrino beam peaking around 1 GeV. MiniBooNE could only detect muons, since protons are below the Cherenkov threshold (see Sec. 2.7).
Both experiments measured the effective axial mass M_A^{QE}. Figure 5.5 shows the model prediction which best fits the value of M_A^{QE} compared with the experimental data of both collaborations:

$$\begin{aligned} &M_A^{QE}(\text{NOMAD}) = 1.05 \pm 0.02\ (stat.) \pm 0.06\ (syst.)\ \text{GeV/c}^2, \\ &M_A^{QE}(\text{MiniBooNE}) = 1.35 \pm 0.17\ \text{GeV/c}^2. \end{aligned} \tag{5.7}$$

While NOMAD results are consistent with the deuterium bubble chambers data ($M_A^{QE} = 1.026 \pm 0.021$ GeV/c^2), MiniBooNE requires a higher value of the axial mass. This sig-

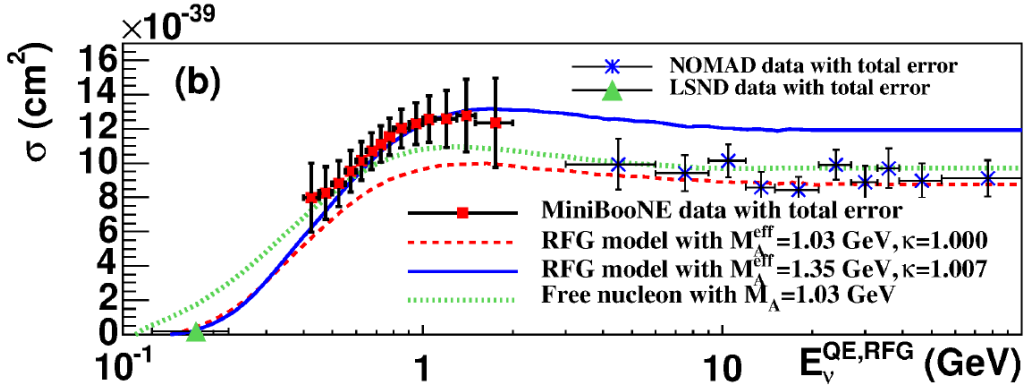

Figure 5.5: Comparison between the neutrino MiniBooNE and NOMAD CCQE cross-section measurements and model predictions with different M_A^{QE} values. Figure from [115].

nificant difference in the CCQE cross-section measured at different energies called for a more sophisticated modelization of the interaction. Although both experiments have the same target they differ in the selection, MiniBooNE does not detect the outgoing nucleon, making pure CCQE indistinguishable from interactions that involves the emission of more than one nucleon. Multi-nucleon emission could be a possible cause of such tension, as will be shown in Sec. 5.2.3.

More recently, the MINERνA experiment released several CCQE differential cross-sections. MINERνA is a tracker scintillator detector at Fermilab which measures neutrino interactions at energies between 1.5 and 10 GeV on a carbon-based target. Both muons and protons can be detected in the final state. MINERνA results on neutrino [116] and antineutrino [117] cross-sections measured, like NOMAD, an axial mass consistent with bubble chambers. In the analysis they only require a muon candidate and no pions in the final state and do not include energy near the vertex in order not to bias the measurements to the number of nucleons emitted in the CCQE interaction candidate. The μ-only data are then compared with the prediction of models which include or not multi-nucleon emission suggesting, in neutrino mode, a transverse enhancement of the cross-section that prefer final states including more than one outgoing nucleon. The measurement of the vertex activity is more sensitive to the kinematics of the emitted protons, suggesting final states with an extra proton below 225 MeV in $25 \pm 1(stat.) \pm 9(syst.)\%$ of the events [116]. Therefore, in both cases event distributions are consistent with the multi-nucleon hypothesis. Moreover MINERνA has also published a CCQE measurement as a function of the proton kinematics [118] based on a final state with one muon, no pions and at least one proton. In this case the proton kinematic results for CCQE interactions are more consistent with a model which does not include additional multi-nucleon effects, in contrast with previous results based on muon kinematics [118]. Therefore MINERνA shows the need of a model which reproduces both the leptonic and hadronic kinematics since both affect the neutrino energy reconstruction.

Once again these results highlighted the shortcomings of the current modelization of the neutrino-nucleus interactions, suggesting the need of a more sophisticated model.

5.1.2 Pion resonant production

In addition to the CCQE scattering, the second largest neutrino-nucleon cross-section at T2K energy is the resonant channel (RES) in which, in addition to the muon and the nucleon, a pion is produced. The resonant channel can be accessed through both CC and NC when the center of mass of the neutrino-nucleon interaction has enough energy to excite the target nucleon into a baryonic resonance, mostly $\Delta(1232)$. The NC and CC processes are:

$$\begin{aligned} \nu_l + n &\rightarrow l^- + n + \pi^+ \\ &\quad + p + \pi^0 \\ \nu_l + p &\rightarrow l^- + p + \pi^+ \\ \nu_l + p &\rightarrow \nu_l + n + \pi^+ \\ &\quad + p + \pi^0. \end{aligned} \tag{5.8}$$

Resonant neutrino-nucleon scattering usually is calculated using the Rein-Sehgal model [119] which includes resonance up to 2 GeV and the cross-section contains interference terms between them as well as non-resonant background. Moreover it accounts also for a non-resonant production term which is small but not negligible. Like in the CCQE case, the CCRES cross-section can be written as a function of vector $C^V(Q^2)$ and axial $C^A(Q^2)$ form factors. Vector form factors can be constrained using electron scattering data whereas the axial part can only be constrained using neutrino-nucleon scattering. The axial part can be determined using two free parameters: the axial mass for resonance interactions M_A^{RES} and the normalization of the axial form factor $C_5^A(0)$. A priori there is no reason to set different axial mass for CCQE and CCRES interactions, however in order to get good agreement with data they need to be tuned to different values.
Several measurements of the charged current pion production cross-section have been performed in the last years. Figure 5.6 shows the MINERνA (left) measurement on a CH target [120] and the T2K (right) measurement on a H_2O target [121], as a function of the angle of the outgoing pion with respect the neutrino direction, compared with different event generators (see Sec. 5.4). FSI stand for Final State Interactions in the nucleus which are addressed in Sec. 5.2.5.

5.1.3 Coherent pion production

In Coherent production of single pion, the neutrino scatters on the whole nucleus which stays unchanged. This process is characterized by a very low or no energy transfer to the nucleus producing no nuclear recoil and a more forward-scattered pion compared

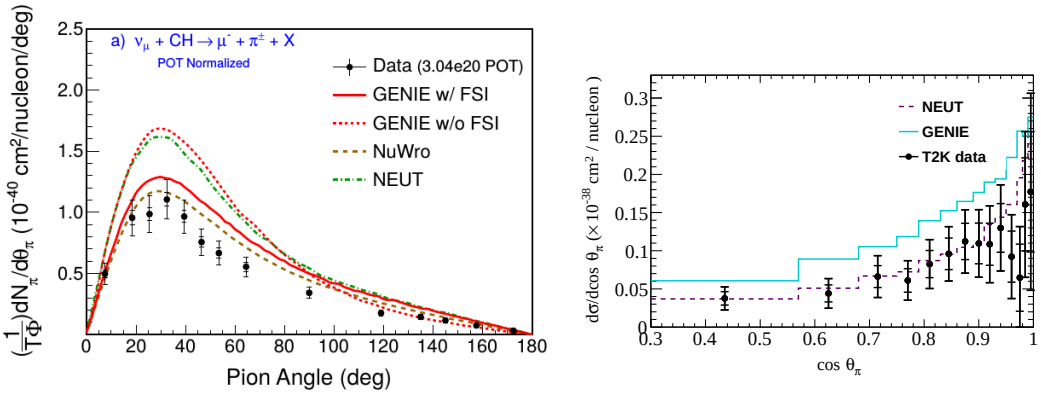

Figure 5.6: Single differential pion production cross section as a function of the pion angle from MINERνA (left) [120] and T2K (right) [121] collaborations. Results are compared with different neutrino interactions generators. The inner (outer) error bars correspond to the statistical (total) uncertainty on the data.

to resonance interactions [109]. Both CC and NC interactions are possible:

$$\begin{aligned} \nu_l + A &\rightarrow \nu_l + \pi^0 + A \\ \nu_l + A &\rightarrow l^- + \pi^+ + A \end{aligned} \tag{5.9}$$

where A is the target nucleus unchanged after the neutrino scattering. Like the pion resonant production, a common theoretical approach for coherent pion production cross-section uses a Rein-Sehgal model [122] based on Adler's assumption of partial conservation of the axial-vector current (PCAC theorem) [123]. This model successfully describes coherent interactions at high energy, however it is not satisfactory for low energy data ($E_\nu < 2$ GeV) where the cross-section is much lower than the predictions [109]. Indeed the PCAC model, relates neutrino-nucleus coherent pion production to pion-nucleus elastic scattering assuming $Q^2 = 0$. This is a good approximation in the high energy limit, however decreasing the energy the transverse momentum is not negligible and the $Q^2 = 0$ assumption is not satisfied. More recently, MINERνA measured neutrino and antineutrino coherent pion production [124] showing a better agreement with the Berger-Sehgal model [125]. This model establishes that the coherent pion production process gives a very small contribution to neutrino-nucleus cross-section at low energy because it is strongly suppressed due to kinematic reasons [125].

5.1.4 Deep Inelastic Scattering

Increasing further the energy ($Q^2 > 2$ GeV) the incident neutrino has enough energy to resolve the individual quarks in the nucleon, breaking up the original nucleon. Due to color confinement, quarks cannot exist isolated and hence cannot be observed directly [126]; the knocked out quarks give rise to an hadronization process where a collimated

collection of particles (jet) is produced. Deep Inelastic Scattering is allowed for both CC and NC:

$$\begin{aligned} \nu_l + N &\to l^- + X \\ \nu_l + N &\to \nu_l + X \end{aligned} \tag{5.10}$$

where X denotes the hadronic shower and N is the struck nucleon.
The cross-section calculation of this process is based on the Bjorken and Paschos model [127] which describes the nucleon as composed of point-like constituents, *"partons"*, which are incoherently scattered by an high energetic probe. Each of these point-like constituents, now identified as gluons and quarks, carry a fraction x of the nucleon momentum $\vec{P}$. Therefore the cross-section will depend on the probability of hitting a parton i with momentum $\vec{p_i} = x\vec{P}$. This probability is called the parton distribution function.
The DIS cross-section for the CC interaction in Eq. 5.10 is then the incoherent sum over all the neutrino-parton scattering and is given by the formula:

$$\left(\frac{\partial^2\sigma_{DIS}}{\partial x \partial Q^2}\right)_{\nu N \to l^- X} = \sum_i \int dx\ e_i q_i(x) \left(\frac{\partial^2\sigma_{DIS}}{\partial x \partial Q^2}\right)_{\nu q_i \to l^- q_i} \tag{5.11}$$

where $q_i(x)$ is the parton distribution function of the parton i with charge e_i inside the nucleon target.

5.2 Nuclear models

In the previous section the description of the CC and NC neutrino interactions has been reduced to equations that only depend on few form factors and masses. But the kinematics and cross-section of any neutrino-nucleon interactions are affected by the motion of the nucleons inside the nuclear potential. Moreover nucleons are bound in the nuclei, hence nuclear effects must be taken into account in the modelization of interaction cross-sections. Nuclear effects includes Fermi motion of the initial nucleons, Pauli blocking, nucleon-nucleon correlations and re-interactions in the nuclear medium of the products of the neutrino interaction. Because of the complexity and variety of nuclear effects, several models have been developed so far. A summary of some of them will be given in this section.

5.2.1 Relativistic Fermi Gas

The simplest model describing the most important features of nuclear dynamics is the Relativistic Fermi Gas model (RFG) [128]. In the RFG, the nucleus is considered as an ideal gas of weakly interacting fermions, the nucleons. Neutrons and protons are then considered as indistinguishable fermions which obey the Fermi-Dirac statistics and the Pauli exclusion principle. Pauli blocking prevents identical fermions from occupying the same quantum state in a nucleus. Therefore nucleons can only move to a state

which is not already filled, limiting the available phase space and hence reducing the cross-section. In the RFG all the possible particle states up to the Fermi momentum are filled, so the produced outgoing nucleon cannot occupy any of them. This leads to a limit on the momentum of the outgoing nucleon, the so called Fermi momentum p_F; only interactions in which the outgoing nucleon has a momentum higher than p_F are allowed. Moreover nucleons are bounded in the nucleus, thus to be ejected they need to receive enough energy to cross the energy gap between the nuclear potential and their energy level. This energy is called binding energy E_B. So in summary, the RFG model depends on two nucleus parameters which scale with the nucleus size: p_F the momentum of the most energetic nucleon and the nucleon binding energy E_B. Figure 5.7 shows the nuclear ground state of non-interacting nucleons for both protons and neutrons. The proton potential and neutron potential shapes differ because of the electrostatic repulsion between protons which leads the neutrons to have deeper ground state [129]. The RFG model is generally used as simplified approach to model CCQE interactions since the distribution of momentum of the initial nucleons is assumed flat up to p_F (the maximal allowed momentum). A more sophisticated model of nuclear effects is needed to match the precision of modern neutrino scattering data. An improvement of the RFG model is the Local Fermi Gas (LFG) approach [130], where the initial nucleon momentum depends on its radial position inside the nucleus. The Fermi momentum depends on the local proton or neutron density $\rho_{p,n}$ of the nucleus:

$$p_F(r) = [3\pi^2 \rho_{p,n}(r)]^{\frac{1}{2}} \tag{5.12}$$

where r is the nucleon distance from the center of the nucleus.

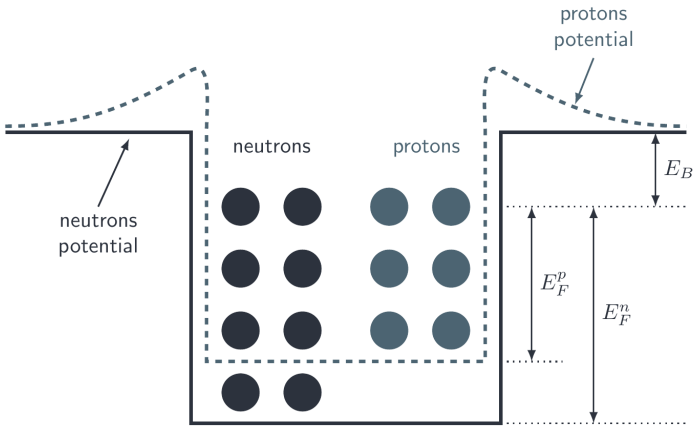

Figure 5.7: Protons and neutrons in a Fermi gas potential. Figure from [129].

5.2.2 Spectral Function

The Spectral Function (SF) is a more sophisticated model than the RFG or LFG, and provides a more realistic description of the momentum and energy distributions of the initial nucleons within the nucleus. It relies on a function which describes the probability distribution $\mathcal{F}(\vec{p}, E)$ for a nucleon, in a finite nucleus, to have a momentum $\vec{p}$ and energy E [131].
The SF depends on the size of the nucleus, therefore it must be computed for each nucleus. The spectral function consists of two terms:

$$\mathcal{F}(\vec{p}, E) = \mathcal{F}_{MF}(\vec{p}, E) + \mathcal{F}_{corr.}(\vec{p}, E), \tag{5.13}$$

a mean field term $\mathcal{F}_{MF}(\vec{p}, E)$ for single nucleons occupying energy levels in the nucleus and a correlation term $\mathcal{F}_{corr.}(\vec{p}, E)$ which describes nucleon-nucleon pairs interactions. The latter term accounts for $\approx 20\%$ of the total SF. The correlation term leads to long-range correlation which results in the ejection of a second nucleon in presence of ν interactions. Figure 5.8 shows the oxygen Spectral Function compared with the equivalent flat distribution shown for the RFG model. The long tail in the SF distribution is due to the correlation term.

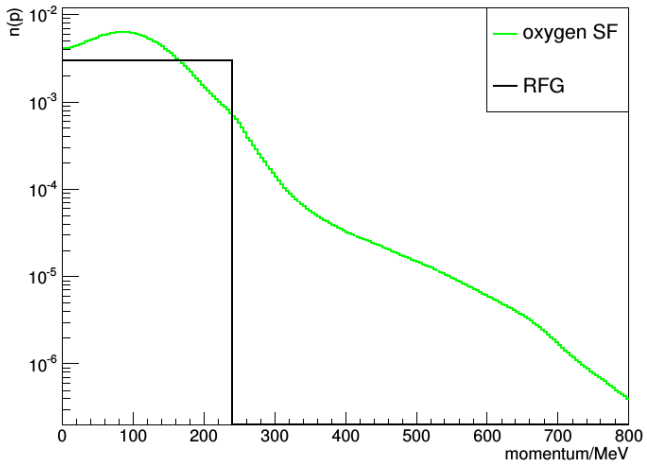

Figure 5.8: Spectral Function for oxygen (green line) nucleus compared to a RFG model (black line) with $p_F = 220$ MeV/c. Figure from [131].

5.2.3 Random Phase Approximation

The Random Phase Approximation (RPA) is a non-perturbative method to describe microscopic quantum mechanical interactions in complex systems of many bodies. The RPA for neutrino-nucleus interactions is used as a correction to the model based on RFG or LFG to account for medium and long-range correlations between nucleons within a

nucleus [132, 133, 134]. Such effects induce a correction to the overall neutrino-nucleus interaction cross-section as of Q^2. The RPA descriptions by Nieves [133] and Martini [134] of the medium polarization effect rely on the LFG as the underlying model of the nucleus. The correlations between nucleons described by the RPA, result in a correction to the pure CCQE cross-section obtained on a single nucleon in motion in the nucleus potential. They are described via the propagation of particle-hole excitation (*1 particle - 1 hole* or 1p-1h), through the nuclear medium and accounts for long-range correlations.
When the electroweak interaction takes place in the nucleus, the first order RPA correction to the $1p-1h$ medium polarization leads to change in the strength of the electroweak coupling altering the CCQE free nucleon prediction. Higher order corrections to the W-boson self-energy are not described by RPA, however they are included in both Nieves and Martini models: this class of interactions are often referred as "*n-particle n-hole*" ($np-nh$) since multiple particle-hole pairs are propagated in the nucleus. Of particular interest are the $2p-2h$ interactions which involve multi-nucleon emissions from a neutrino-nucleus interaction.

5.2.4 Multi-nucleon interactions

As shown in Sec. 5.1.1 the tension in CCQE cross-section measurements observed by MiniBooNE and NOMAD (see Fig. 5.5) points towards nuclear effects which are not taken into account in simplified neutrino interaction models. At low Q^2, when the neutrino interacts with a target with a large number of nucleons ($A > 4$), the presence of correlations between nucleons gives rise to multi-nucleon emissions which can mimic the pure CCQE interaction when nucleons in the final state escape undetected or are re-absorbed by the nucleus (see Sec. 5.2.5). This process is also called *2p2h*. Figure 5.9 illustrates some of the diagrams responsible for the 2p2h: the W boson excites more than one pair of particles and holes connected by a virtual meson propagator. For this reason sometimes 2p2h is referred as *meson exchange current* (MEC). It should be noted that the MEC diagrams are only a subsample of the 2p2h process because they do not include nucleon-nucleon correlation contribution.

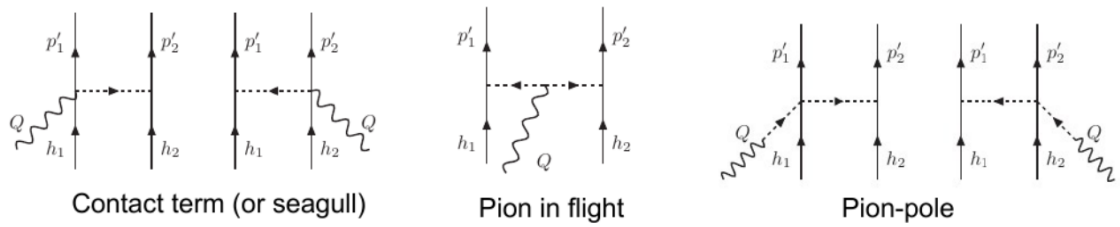

Figure 5.9: Set of 2p2h/MEC diagrams. Single solid lines represent nucleons, the shaded lines are pions and curly lines represent the W boson. Figure adapted from [135].

Figure 5.10 shows the MiniBooNE CCQE double differential cross-section in terms of

the muon kinematics (left) and the cross-section as a function of the neutrino energy (right). Note how the inclusion of RPA + $2p2h$ corrections to the CCQE interactions helps to fill the discrepancy observed in the MiniBooNE measurements since multi-nucleon events contribute to the measured CCQE cross-section. Experimental data are compared with the classical description of QE interaction and with QE + multi-nucleon interactions predicted by Nieves and Martini. The Martini model starts from different approximations and neglects some diagrams which are included in Nieves model. This translates in cross-section predictions for the 2p2h process which differ up to a factor of two in some regions [134].
Although important steps forward in neutrino interactions understanding have been made in the last decade, the present understanding is far to be satisfying. Thus additional efforts on both theoretical models implementation and on dedicated cross-section measurements are needed.

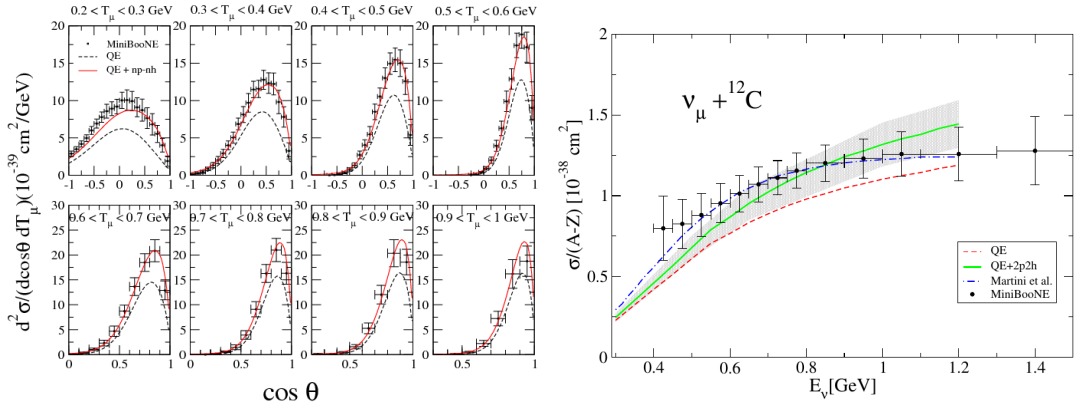

Figure 5.10: **Left:** MiniBooNE [136] ν_μ CCQE double differential cross-section measurement on carbon. The dashed line is the pure CCQE model calculated in RPA, solid red line is the same model with the inclusion of np-nh component. Figure from [137]. **Right:** MiniBooNE data as a function of neutrino energy compared with Nieves [132] and Martini [134] predictions. Figure from [132].

5.2.5 Final state interactions

The final hadrons produced by neutrino scattering propagate through the nuclear medium before they can leave the nucleus and thus be detected. In particular nucleons from CCQE or pion from resonant interactions, due to the strong force, can easily undergo re-interactions within the nucleus. These effects, called *Final State Interactions* (FSI), can alter the observed number of hadrons and their kinematics. Once a charged pion has been produced by a neutrino-nucleon interaction, it passes through the nuclear medium in which it can either scatter or be absorbed or convert via charge-exchanging into a neutral pion:

$$\pi^+ + n \rightarrow \pi^0 + p. \tag{5.14}$$

MINERνA measurement of pion resonant production (see Fig. 5.11 left) shows the importance of pion FSI processes in determining the cross-section of pion production and the shape of the distribution in pion kinematic variables. They are largely determined by the fact that more than 50% of the produced pions re-interact before escaping the nucleus.
As pions, also protons undergo FSI. Electron-scattering data on different nuclei show that the nuclear transparency T, the probability for a proton to escape the nucleus unchanged, does not strongly depend on the transfer momentum Q^2 but decreases for heavy nuclei [138]. Figure 5.11 shows the transparency as a function of the Q^2 for different nuclei, of particular interest is the result on carbon target C which quantify the FSI correction for proton production ($\sim$ 40%). Therefore the FSI are not negligible in neutrino-nucleus interactions on relatively heavy nuclei like ^{12}C: the content and kinematics of the outgoing hadron may change the final state of the interaction, leading to a misidentification of the reaction type. Furthermore, since they scale with the nucleus size, in T2K their propagation from the near to the far detectors must be treated carefully.

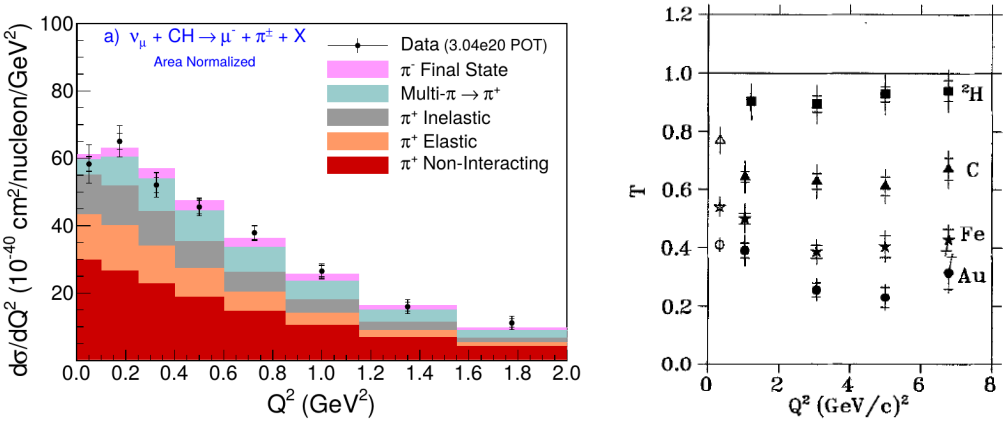

Figure 5.11: **Left:** Pion FSI processes within the nucleus. Figure from [120]. **Right:** Nuclear transparency for electron-nucleus scattering as a function of the Q^2 for different nuclei. Figure from [138].

5.3 Impact of O and C cross-section measurements

As described in the previous sections the nuclear effects are also significant for relatively heavy targets like Carbon (^{12}C) and Oxygen (^{16}O). Such effects obviously depend on the size of the target. The target nucleus at the far detector of T2K is oxygen while the near detector contains both carbon and oxygen, this introduces some issues in using neutrino cross-section measurement on carbon to understand interaction rates at Super-Kamiokande. Therefore the oscillation analyses must take into account uncertainties due to potential differences between target nuclei. Indeed the oscillation parameters are extracted using the reconstructed energy distribution of the incoming neutrino which is inferred using the kinematics of the outgoing particles (see Eq. 5.3). This method requires an accurate understanding of the nuclear effects.
Figure 5.12 demonstrates the importance of developing an accurate theoretical description of nuclear effects for the targets [139]. It shows the effect on the T2K disappearance analysis of assuming a oxygen (shaded areas) or carbon (solid regions) model to predict and fit the event rate at the far detector made of oxygen. The best fit obtained from the carbon-based model is shown by the black triangle while the true value from the oxygen-based model is the red dot.

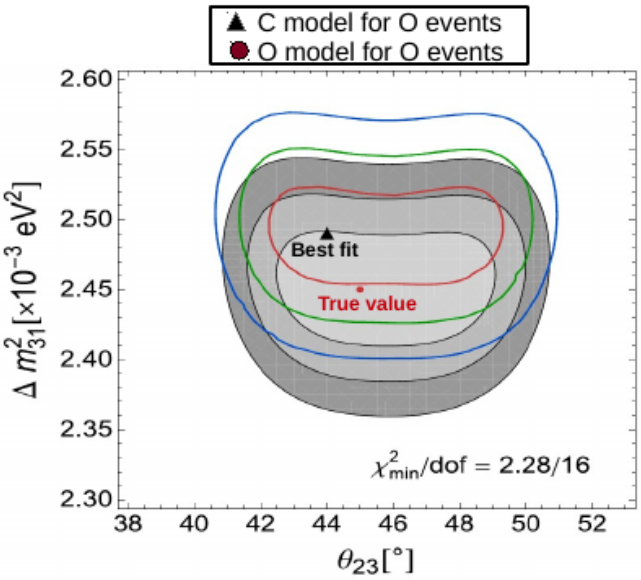

Figure 5.12: Confidence regions in the $\theta_{23} - \Delta m^2_{31}$ plane obtained by fitting oxygen data using carbon-based (solid lines) and oxygen-based (shaded areas) models. Figure has been modified from [139] to highlight the used model, the best fit (black triangle) and the true value (red dot).

The difference between the fitted and true values of the oscillation parameters is non-negligible when carbon and oxygen differences are not taking into account. However, in

a experiment like T2K, which employs different neutrino targets between the near and far detectors, such differences are corrected including oxygen and carbon cross-section parameters to predict the event rate at Super-Kamiokande. In order to reduce oscillation analysis uncertainties, such parameters are constrained using samples of neutrino interactions on oxygen and carbon at the near detector. The difference between carbon and oxygen interactions are parametrized in the oscillation analysis using different values of Fermi momentum (p_F) and binding energy (E_B). Also the overall normalizations for the 2p2h/MEC contributions are split by target.
A sophisticated approach, employing the SuperScaling Approximation (SuSA) [140, 141] to describe the CCQE and 2p2h/MEC interactions, tuned with electron scattering data for different nuclear targets is shown in Fig. 5.13. It estimates the expected impact of such nuclear effects on the oxygen over carbon cross-section ratio. Figure 5.13 shows preliminary results of such model as a function of the muon kinematics for different values of p_F on oxygen which is set to $p_F = 216$ MeV/c (red) or $p_F = 230$ MeV/c (orange). The difference between p_F hypothesis are highlighted by the blue shaded region. The CCQE (dashed-dotted lines) and MEC (dashed lines) interactions shows an opposite behavior for the ratio (when CCQE goes up, MEC goes down and viceversa), however these effects compensate in the total cross-section ratio (CCQE + MEC) resulting in O−C differences around few % in most of the phase space. The ratio shows a large effect in the very low muon momentum region ($p_\mu < 200$ MeV/c) where the differece is up to 10% while it is quite flat for the muon angle.
For these reasons, a measurement of the cross-section on oxygen and of the oxygen-carbon difference at the near detector is crucial to test the T2K modelling of nuclear effects in carbon and oxygen interactions and thus minimize the uncertainty in the oscillation analysis.

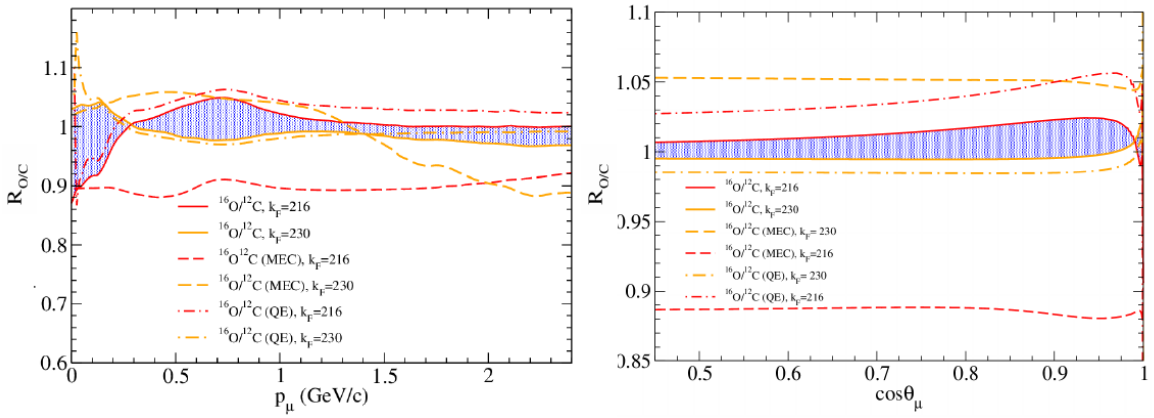

Figure 5.13: SuSA preliminary predictions of the oxygen over carbon cross-section ratio as a function of the muon momentum (left) and direction (right). The red and orange lines correspond to different values of the Fermi momentum for the oxygen target while dashed and solid lines correspond to different neutrino interactions.

5.4 Neutrino interactions generators

All oscillation experiments rely on Monte-Carlo generators to simulate neutrino interactions at the near and far detectors. Unfortunately, for the moment an unified framework able to describe all neutrino interactions in a broad energy range does not exist. Therefore each generator needs to combine various models. Due to nuclear effects which depend on the target nucleus (see Sec. 5.2) and to detector inefficiency which depends on the experimental apparatus, accurate simulations of the interactions in the specific detector are necessary to properly evaluate selection efficiencies and signal purities. For this reason an event generator needs to provide the kinematics of all the produced particles after FSI (see Sec. 5.2.5) for each interaction process.
In the T2K near detector ND280 neutrino interactions are simulated from few MeV up to 30 GeV, according to the estimated neutrino flux and the outgoing particles are propagated through a simulation of the detector. Events are simulated on all the materials crossed by the neutrino beam including the magnet yoke and all the material surrounding the detector. T2K relies on the NEUT generator [142] as a primary neutrino-nucleus interactions simulation and GENIE [143] as secondary generator for cross-checks and fake data studies. A description of the cross-section models used by both generators will be given in the following Sec. 5.4.1 and 5.4.2.

5.4.1 NEUT Monte-Carlo generator

The NEUT Monte-Carlo generator simulates charged and neutral current processes for (anti-)neutrinos in a broad energy spectrum from 10 MeV to 100 TeV. It was originally developed for the Kamiokande experiment and then updated and adapted to Super-Kamiokande and long-baseline experiments like K2K and T2K. NEUT models CC and NC quasi-elastic interactions through the Llewellyn-Smith model [110] using the Smith Moniz RFG model [128] to account for bounded nucleons in the nucleus. The axial form factor of the nucleon $F_A(Q^2)$, see Eq. 5.6, is described by a dipole shape with $M_A^{QE} = 1.21$ GeV/c^2 whereas the BBBA05 implementation [144] for the vector form factors $F_1(Q^2)$ and $F_2(Q^2)$ is used. The Fermi momentum cutoff for the outgoing nucleon is fixed at $p_F = 217$ MeV/c for carbon and $p_F = 225$ MeV/c for oxygen. It accounts for the Pauli blocking. Moreover the binding energy is fixed at $E_B = 25$ MeV/c^2 for carbon and $E_B = 27$ MeV/c^2 for oxygen, this leads to modify the cross-section differently for the two nuclei at low Q^2. Nieves model [133, 132] is used to describe multi-nucleon interaction while the inclusion of RPA correction is done using [132]. The full SF [131] implementation of the initial state of the nucleus is also available as an alternative model to the RFG. Therefore two different models can be considered: the SF and RFG+RPA.
The resonant pion production modelization relies on the Rein-Sehgal model [119] which considers 18 different baryon resonances with masses $W < 2$ GeV/c^2 including their interference terms and the non-resonant contribution. The resonant axial mass M_A^{RES}

is set to 0.95 GeV/c^2, while the normalization of the axial form factor $C_5^A(0)$ is updated to the Graczyk-Sobczyk form factor [145] and fixed to 1.01. The normalization of the isospin non-resonant $I_{1/2}$ is set to 1.30. These parameters are fixed using low energy neutrino-deuterium single pion production data [146, 147]. Coherent pion production is simulated, for both NC and CC channels, using the Rein-Sehgal model, including the PCAC lepton mass correction for CC interactions [122]. Multi-pion production (DIS) is simulated according to the Bodek and Yang model [148] where the DIS processes uses the *GRV98* parton distribution functions [149]. Furthermore, in order to avoid double counting with the single pion resonant production, in the DIS model only multiple pion production processes are considered for hadronic invariant mass below 2 GeV/c^2. Conversely hadronic shower at high invariant mass ($>$ 2 GeV/c^2) is simulated using PYTHIA/JETSET [150].
The transport in the nucleus of the products of neutrino interactions is simulated according to an intranuclear cascade [149] using the Woods-Saxon distribution to model the nuclear density [151]. In this FSI modelization each particle is propagated, according to its free mean path, in finite steps inside the nucleus. The allowed pion interactions inside the nucleus include: charge exchange, absorption where the pion is absorbed through two or three body processes, pions production due to inelastic scattering and elastic scattering where the pion only exchanges momentum and energy. If an interaction occurs, new and modified particles are also added to the intranuclear cascade. The probability of nuclear interactions is calculated at each step until all particles involved are either absorbed or escape the nucleus.

5.4.2 GENIE Monte-Carlo generator

GENIE is currently used in the T2K experiment as an alternative event generator for neutrino-nucleus interactions. Since it has been built in a modular way, it allows the implementation of new cross-section models, fluxes and detector geometries providing a more general framework than NEUT, valid over a large range of experiments, targets and neutrino energies. Therefore it is often used as a baseline to compare results from experiments with different neutrino flux or targets. Essentially GENIE uses the same models as NEUT to describe the neutrino-nucleus cross-sections, however the implementation of such models is slightly different and different default values are used for some theoretical parameters. For these reasons the predicted cross-sections can differ.
Like NEUT, in the quasi-elastic interactions, GENIE relies on the Llewellyn-Smith model [110], although it uses the Bodek and Ritchie formulation of the RFG [152] which includes a high-momentum tail to account for nucleon-nucleon correlations as predicted by the SF model. The value of the axial masses for quasi-elastic interaction is set to $M_A^{QE} = 0.99$ GeV/c^2, according to the value found by deuterium experiments. The resonant pion production still uses the Rein-Sehgal model [119], but it considers 16 resonances and neglects interference terms between them in the parametrization. The axial mass is fixed at $M_A^{RES} = 1.12$ GeV/c^2. Coherent pion production relies on the

Rein-Sehgal parametrization [122], however it uses more updated pion-nucleus scattering to tune the model. The Bodek-Yang model [148] used to simulate DIS interactions includes the AGKY parametrization [153] for low invariant mass (< 2 GeV/c^2) and, like NEUT, the PYTHIA/JETSET [150] for high invariant mass above 2 GeV/c^2. Finally, the intranuclear transport of the produced hadrons are propagated using a cascade model tuned to similar data-sets to the ones used in NEUT, although there are some differences in the implementation.

Chapter 6

Neutrino-nucleus O/C cross-section ratio: data selection and source of systematics

The charged current quasi-elastic (CCQE) interaction is the most relevant process at T2K neutrino energies [61]. As previously described in Chapter 5, the measurements of CCQE interactions on relatively heavy nuclear targets (like carbon) do not agree with predictions based on data from bubble chambers on hydrogen and deuterium targets and with nuclear models developed so far. Moreover, the measured final state does not match the true neutrino interaction because of physics (i.e. FSI) and experimental effects (i.e. reconstruction). For instance due to FSI a pion resonant production event can mimic a CCQE event if the pion is absorbed inside the nucleus. Furthermore a CCQE interaction is characterized by the presence of a muon and a single proton in the final state, however reconstructing nucleons (protons or neutrons) is experimentally challenging. The proton has often very low momentum and, if it exits the nucleus, it may escape undetected. Moreover multi-nucleon interactions generate in the final state more than one outgoing nucleon which often are not detected, mimicking hence a pure CCQE event.
For these reasons a definition of the interaction corresponding to what is actually observed in ND280 is needed in order to avoid a model depend measurement. The signal considered consists of Charge Current Zero Pions interactions (CC0π) where a muon, any number of nucleons and no pions are detected in the final state. The aim of the analysis described in this manuscript is the measurement of the CC0π cross-section ratio on oxygen over carbon in order to reduce the total uncertainty on the oscillation analysis due to the near to far detector extrapolation. Since the far detector SK is a water Cherenkov detector, ND280 must precisely constrain the neutrino interaction rates on oxygen. Neutrino cross-sections indeed, depend on the target nucleus through nuclear effects (FSI, 2p2h) which are not well described by the theory. Therefore the interaction rates must be measured on oxygen at the near detector.

In ND280 water targets are present in the FGD2 and in the PØD subdetectors. The latter consists of water bags that can be filled either with water or be empty, therefore cross-section extraction in oxygen can be achieved using a method based on a statistical subtraction of events. This method does not identify water interactions individually but infers them taking data with and without water in the detector [113]. Since the FGD2 consists of uninstrumented water module and of plastic scintillator bars, an alternative method relies on finding the interaction vertex position in the active material in order to constrain the water interactions [121]. This analysis uses a combination of both those methods: vertex determination plus subtraction of the oxygen component by comparing interactions in the scintillator layers. However the measurement of the cross-section in water with the statistical subtraction is also possible in FGD2 by comparing the interaction rate between the FGDs. Indeed being the FGD1 made up entirely of plastic scintillators (carbon based), it can be used to accurately model the non-water rate in FGD2 (carbon + water). However, here the FGD1 will be used as control sample to constrain the systematics. A schematic drawing of the layer structure of the two FGDs is shown in Fig. 6.1.
In this Chapter a detailed description of the used samples and selection for CC0π interactions as well as the analysis strategy and a full assessment of the systematic errors are given.

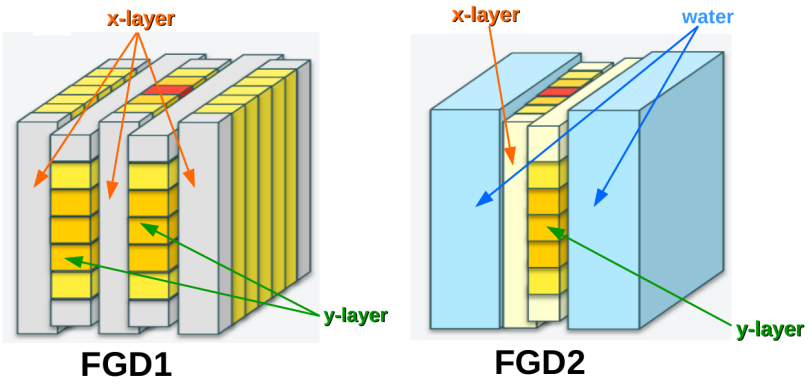

Figure 6.1: Schematic drawing of the layer structure of the two FGDs. The neutrino beam goes from left to right.

6.1 Samples and event selection

6.1.1 Real Data and Monte Carlo samples

Figure 2.2 summarizes the eight T2K data taking periods, the total Protons on Target (POT) collected so far (up to 7 April 2017) as well as the beam power and the horn current. The data sample used for this analysis includes RunII-IV corresponding to the

neutrino mode (forward horn current). Table 6.1 lists the POT corresponding to each run period for real data and MCs. The MC generators for the neutrino interactions with nuclei are based on *NEUT 5.3.2* [142] and *GENIE 2.8.0* [143]. NEUT has been chosen as the official MC in the T2K experiment and in this analysis, GENIE is used as benchmark to validate the analysis against possible biases due to MC mismodeling. The real data sample corresponds to 5.800×10^{20} POT and contains events which passed the *"good"* quality spill and all ND280 sub-detectors and magnet were in operation and labelled as *"good"* (see Sec. 6.1.2). RunI is not used because of global reconstruction issues and less accurate calibration constants of some sub-detectors, in addition the ECal Barrel modules were not installed yet. Moreover RunI recorded a total statistics of 0.167×10^{20} POT, negligible compared to the total number of POT from RunII-IV. Each run period can be further split into different samples as a result of different beam and detector conditions, as shown in Table 6.1. PØD contains water bags that can be empty (air) or filled with pure water, according to that the run period is labelled *"air"* or *"water"*. In addition during RunIIIb the magnetic horns were operating at a current of 205 kA, rather than the nominal 250 kA. Overall, for each run period, the MC statistics is more than 10 times larger than the data statistics and is reweighted in order to match the run conditions of the T2K data taking periods.

T2K Run	ND280 runs	DATA POT ($\times 10^{20}$)	MC NEUT POT ($\times 10^{20}$)	MC GENIE POT ($\times 10^{20}$)
RunII (water)	6462-7663	0.433	5.215	12.847
RunII (air)	7664-7754	0.359	9.385	9.861
RunIIIb (air)	8309-8453	0.217	3.216	4.538
RunIIIc (air)	8550-8753	1.364	27.219	28.238
RunIV (water)	8983-9413	1.643	16.620	24.153
RunIV (air)	9426-9796	1.783	35.026	37.289
Total		5.800	96.901	117.14

Table 6.1: Definition of the ND280 runs and the corresponding amount in POT for the data and MC samples used in the analysis.

6.1.2 Event selection

The overall data sample contains many events not caused by CC0π interactions in the FGD2. In order to produce a measurement of the muon-neutrino cross-section in a specific channel, it is necessary to first prune the sample of all reconstructed events into the ones relevant for this analysis. This procedure is simply referred to as the "event selection" and its purpose is to provide a filtered sample of events mostly occurring in the FGD2 fiducial volume and in the CC0π interaction channel. The selection is based entirely on reconstructed information and therefore can be applied to both real data and MC. Since a blind analysis is performed, it was tested first using only MC samples. This section describes the Charge Current (CC) selection criteria, the so called "*CC-inclusive*", which includes the analysis signal CC0π, as well as, single pion production

and deep inelastic scattering. This analysis uses the same selection described in Ref. [154]. The ν_μ CC-inclusive selection criteria are the following:

1. **Data Quality:** the event must be within the bunch time and the full spill must have a good ND280 data quality flag. The beam spill is constituted of eight bunches with a total width of 5.6 μs (see Sec. 2.2), tracks are then grouped together in bunches according to their timing. The good quality flag requires that all detectors must be in full operational mode.

2. **Total Multiplicity:** at least one reconstructed track crossing the TPC.

3. **Muon candidate identification:** among all tracks originated in FGD2 which enter the TPCs, the muon candidate is identified as the highest momentum negatively-charged (HMNT) one. The negative charge is identified using the track curvature in the solenoidal magnetic field. The HMNT must start inside the FGD2 fiducial volume and must have more than 18 vertical clusters in the TPC in order to reject short tracks for which the momentum reconstruction is less accurate. The Fiducial Volume (FV) is defined as the detector volume where the events are accepted. It is smaller than the total detector volume to reduce the fraction of events corresponding to ν_μ interactions outside the FGD (i.e. TPC walls or dark box). The FGD2 FV begins 58 mm inward from the edges in x ($|x_{vertex}| < 874.51$ mm) and in y ($|y_{vertex} - 55| < 874.5$ mm) which allow to accept tracks with a vertex 5 scintillator bars distant from the edges. Longitudinally FV is defined cutting 7.5 mm inward from the upstream FGD2 edge in z ($1481.45 < z < 1807.05$ mm) which leads to exclude the most upstream scintillator layer (first x-layer). A schematic view of the FGD2 FV definition is shown in Fig. 6.2.

4. **External veto:** this cut rejects the muon candidates originated upstream of FGD2 FV which are wrongly reconstructed as two separate tracks. These events are removed looking at the second highest momentum track. If its start position is more than 150 mm upstream of the muon candidate (outside the FV), then the event is rejected. Additionally, for FGD2 selection, the event is vetoed if there is a potential muon candidate in FGD1.

5. **Broken track veto:** it is used to reject tracks which are broken into a short track fully contained in the FGD (FGD-only track) and originated from the same selected vertex of the FGD-TPC matched track (muon candidate) and starting in the last two layers of the FGD. The FGD-only tracks are defined as tracks with segments in the FGD and no segments in any TPC. In order to remove these events, the muon candidate track and the reconstructed FGD-only track have a start position 425 mm far from the upstream edge of the FGD. A schematic example of a broken track is shown in Fig 6.3.

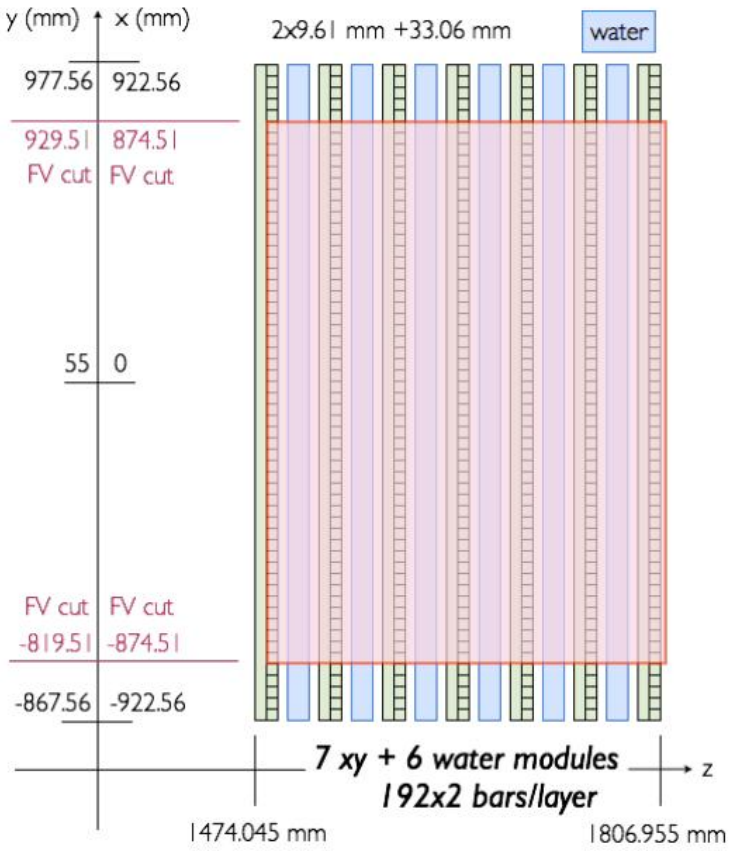

Figure 6.2: Side view of FGD2 subdetector and definition of the fiducial volume (FV). The FV is delimited by the red box.

6. **Muon particle identification (PID):** HMNT must be identified as μ^- track according with the method described in Sec. 3.5.3 which uses the truncated mean of the charge collected in the TPC to calculate pulls (Eq. 3.11) for each particle hypothesis ($l = \mu, e, \pi, p$). In order to reject other particles hypothesis the following cut are applied to the TPC PID likelihood (Eq. 3.12):

$$\mathcal{L}_\mu > 0.05 \tag{6.1}$$

All the events passing these requirements make the ν_μ CC-inclusive selected sample in the FGD2. The ν_μ CC-inclusive sample can be split further into three sub-samples defined by the number of reconstructed pions in the final state:

- CC0π: no pions in the final state;
- CC1π^+: one reconstructed positively charged pion π^+;
- CC-Others: more than a π^+ or any other number of pions (charged $\pi^\pm$ or neutral π^0) in the final state.

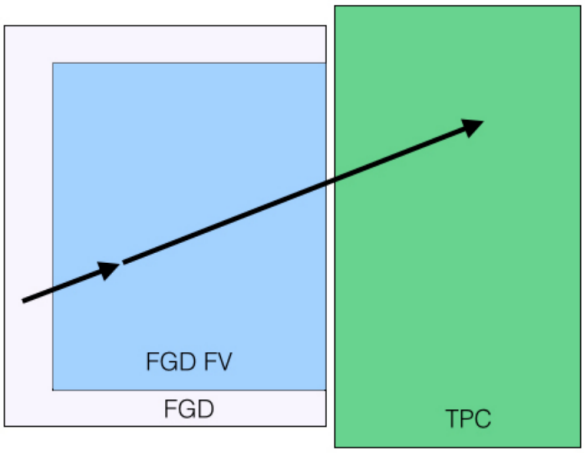

Figure 6.3: Example of a broken track. The long track is reconstructed as two different tracks, one FGD-only track starting outside of the FGD FV, and one FGD-TPC track.

Therefore additional cuts looking at the number and type of pions are required in the FGD2 selection. In the ND280 tracker, pions are reconstructed in the TPC or FGD. Charged and neutral pion selection can be summarized as follow:

Charged pion: presence of a charged secondary track in the final state of the interactions.

1. Data Quality: secondary track in the same bunch timing as the muon candidate.

2. Secondary particle identification:

   (a) **TPC criteria**: they are applied when the secondary track enter in the TPC:

      i. Track Quality: track must start in the FGD2 FV and has more than 18 clusters in the TPC (same quality cut as for the muon candidate).

      ii. TPC PID: to identify the particle type, the TPC PID likelihood (Eq. 3.12) is calculated for each particle hypothesis according to the track charge:

         - for negative charged tracks $l = \ e^-, \pi^-$ whereas in case of positive tracks $l = \ p, \ e^+, \ \pi^+$;
         - particles are tagged with the type that has the highest probability. The probability is defined as the ratio of the probability for a given particle type i over the sum of the probabilities of all the possible particle type hypotheses ($P_i = L_i / \sum_l P_l$). Pulls are defined using the measured and predicted energy loss (Eq. 3.11).

(b) **FGD criteria**: the FGD information is used for secondary track identification when the momentum of the particle is too low or its angle is to high to enter the TPC. In this case two methods are used for the PID according to the track length:

i. Michel electron tagging: the track does not leave enough hits in the FGD to be reconstructed as an independent track. Pions can be identified by the presence of a Michel electron originating from the muon produced by the pion decay at rest. since it is the product of the pion decay at rest. As explained in Sec. 2.6.4.1, the Michel electrons are found by looking at the delayed signals due to the decay time of muon (≈ 2.19 μs) which is required to be outside the bunch timing. In addition the track must have at least 6 hits in FGD2.

ii. FGD PID: the particle produces a reconstructed secondary track in the FGD which is in the same bunch time of the muon candidate and fully contained in FGD. In this case, to be tagged as a pion, its pull must be $-2 < Pull_{\pi} < 2.5$. As in the TPC, pulls are defined using Eq. 3.11.

Neutral pion: since the lifetime of a neutral pion is extremely short ($\approx 10^{-16}$ s), they decay very quickly in the detector into a pair of γ rays. Therefore the π^0 candidate are identified by tagging the e^+/e^- showers in ECal. Neutral pions objects are tagged if:

- there are isolated objects in the ECal in the same time bunch as the muon candidate;
- the likelihood to distinguish MIPs and showers is compatible with an electromagnetic shower;
- it leaves hits in the 5 layers of the ECal;
- the distance between the muon candidate and the isolated ECal object must be larger than 70 cm. This allows to avoid tagging the muon candidate that might have reached the ECal as a π^0;
- the distance between all TPC positive tracks and the isolated ECal object must be larger than 70 cm. This prevents positive pion reaching the ECal and to be misidentified as a π^0.

Therefore this veto manages to reject CC interactions producing a π^0 in the final state, hence the event is moved to the CC-Other sample.

6.1.3 Signal definition

The signal definition for this analysis is the ν_μ CC0π interaction which produces a muon, any number of nucleons and no pions exiting the nucleus after final state interactions. As described in Sec. 2.6.4 and shown in Fig. 6.1, FGD2 consists of 7

scintillator XY-modules interleaved with 6 water modules. The scintillator module is made of polystyrene bars alternately oriented in the x and y direction, an active volume allowing the tracking of the charged particles. The water module is not instrumented and operates a passive volume, reproducing the same target as Super-K for measurements of neutrino interactions in water. In this active/passive structure the z position of an interaction can only be reconstructed in the scintillator layers.

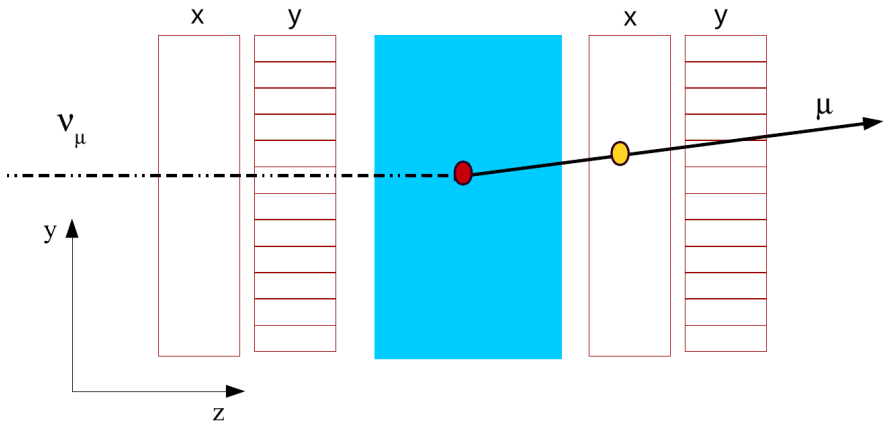

Figure 6.4: Schematic side view of FGD2 scintillator-water structure (x-layer, y-layer and water module). A CC0π water interaction is shown, the muon neutrino (dashed line) interacts in water (red circle) then the first reconstructed hit (orange circle) of the outgoing muon (black line) is seen in the upstream x-layer.

Therefore, when the neutrino interacts in the water passive volume, the first reconstructed hit will lie in the downstream (or upstream) scintillator active layer as shown in Fig. 6.4. Hence, mostly the downstream x-layer and partially the upstream y-layer will be enhanced with interactions in water. Since neutrinos tend to produce forward-going muons.
The goal of this analysis is to estimate the neutrino interactions with water and scintillator in order to extract the CC0π cross-section ratio between oxygen and carbon which is directly related to the rate of interaction in the water and the scintillator modules. Figure 6.5 shows the final state of reconstructed events as a function of the scintillator layer number. The layers are progressively enumerated from 30 to 43: even numbers correspond to x-layers, odd numbers to y-layers. Layer number 30, which is the most upstream x-layer, is outside of the FV. The x-layers are more populated than the y-layers because they contain most of the water interactions since the muons tend to go forward.
Figure 6.6 shows the momentum and angle distributions of the muon candidate in the selected CC0π sample divided by true final state. As explained, the true ν_μ CC-inclusive final state is defined by looking at the number of outgoing pions after the final state interactions CC(0, 1, oth)π. The non-ν_μ CC interactions due to the electronic neutrino (ν_e) and anti-neutrino ($\bar{\nu}$) contamination in the ν_μ flux and the NC interactions are

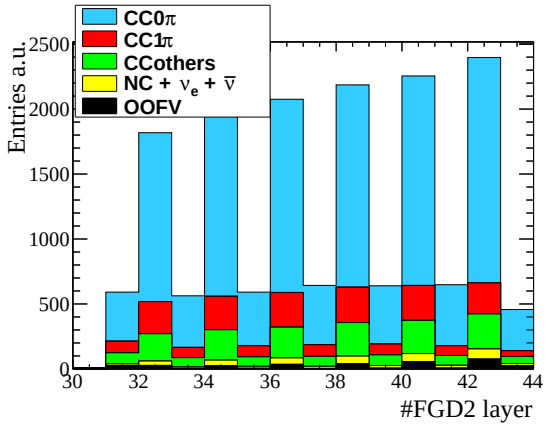

Figure 6.5: Selected CC0π interactions true final state as a function of the layer number.

classified as backgrounds to the CC-inclusive sample (NC + (ν_e) + ($\bar{\nu}$)). An additional source of background is due to all the interactions happening outside the FGD2 FV (OOFV).

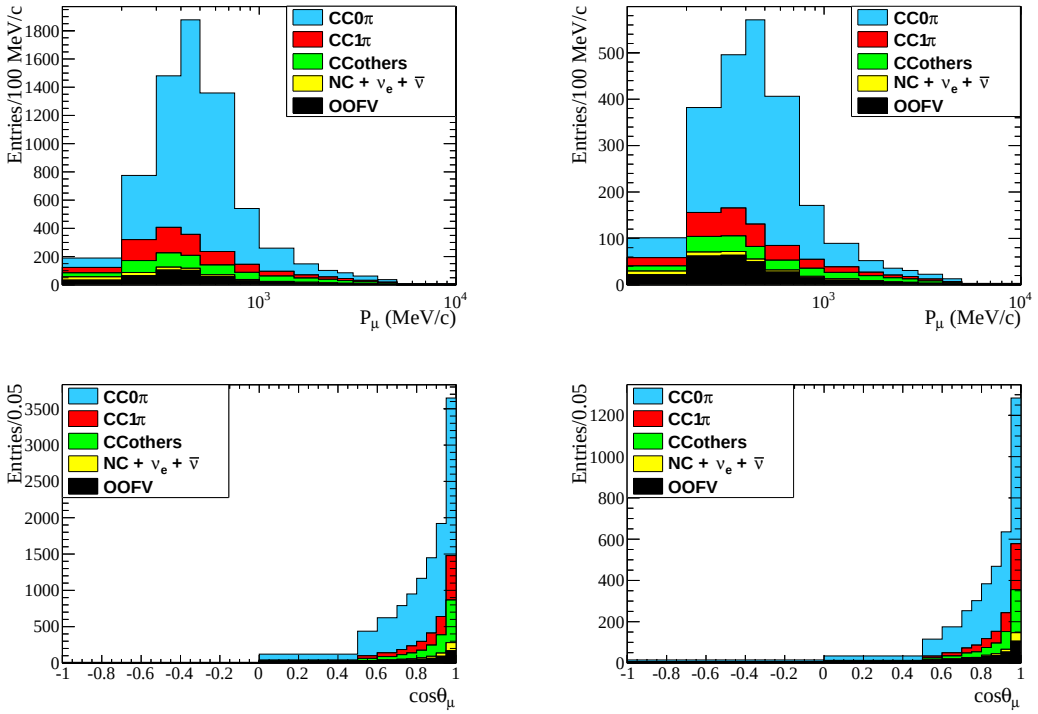

Figure 6.6: Muon candidate in events selected as CC0π as a function of reconstructed momentum (top) and angle (bottom) normalized to data POT and split in the different true final states for the x-layer (left) and y-layer (right).

6.1.4 CC1π and CC-Others sample

The CC1π^+ sample is defined by reconstructed events with just one positive pion candidate track and no other pions, charged or neutral, in the final state. The CC-others final state contains instead all the ν_μ CC events not selected neither as CC0π nor as CC1π^+. These events contain, in addition to the muon candidate, more than one light meson, mostly charged or neutral pions, in the final state. Figures 6.7 and 6.8 show the distributions of the momentum and angle of the muon candidate track in these samples, split into the true final states, both have a very low contamination coming from true CC0π events.

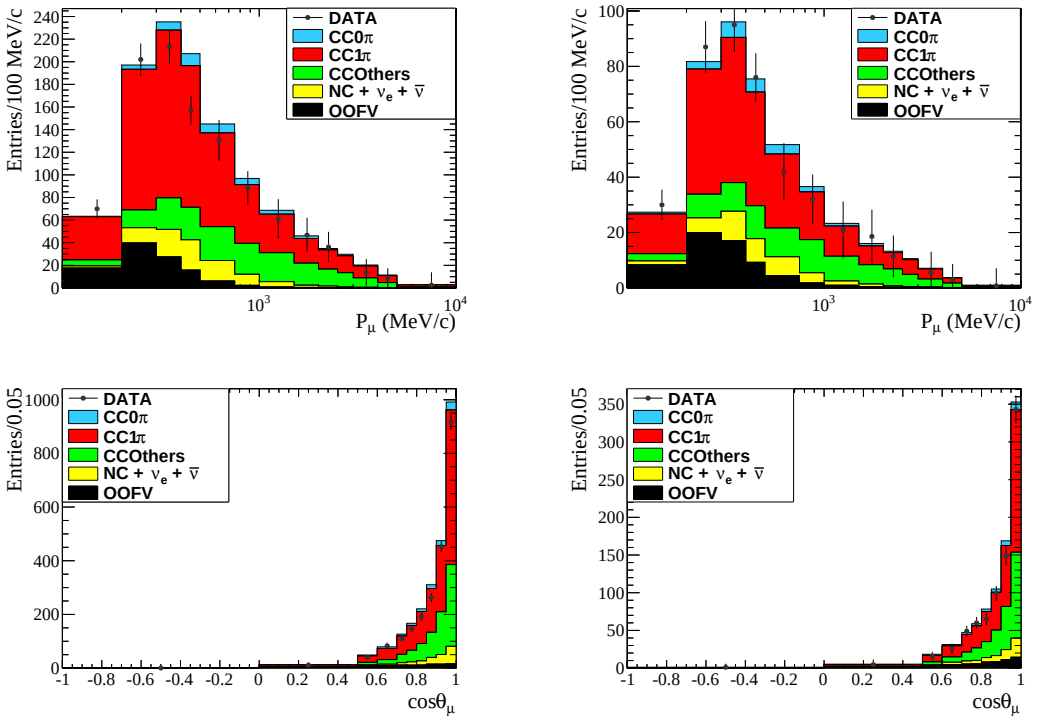

Figure 6.7: Number of events selected as CC1π^+ as a function of reconstructed momentum (top) and angle (bottom) of the muon candidate, normalized to data POT and split in the different final states for the x-layer (left) and y-layer (right). The Black dots are the real data sample.

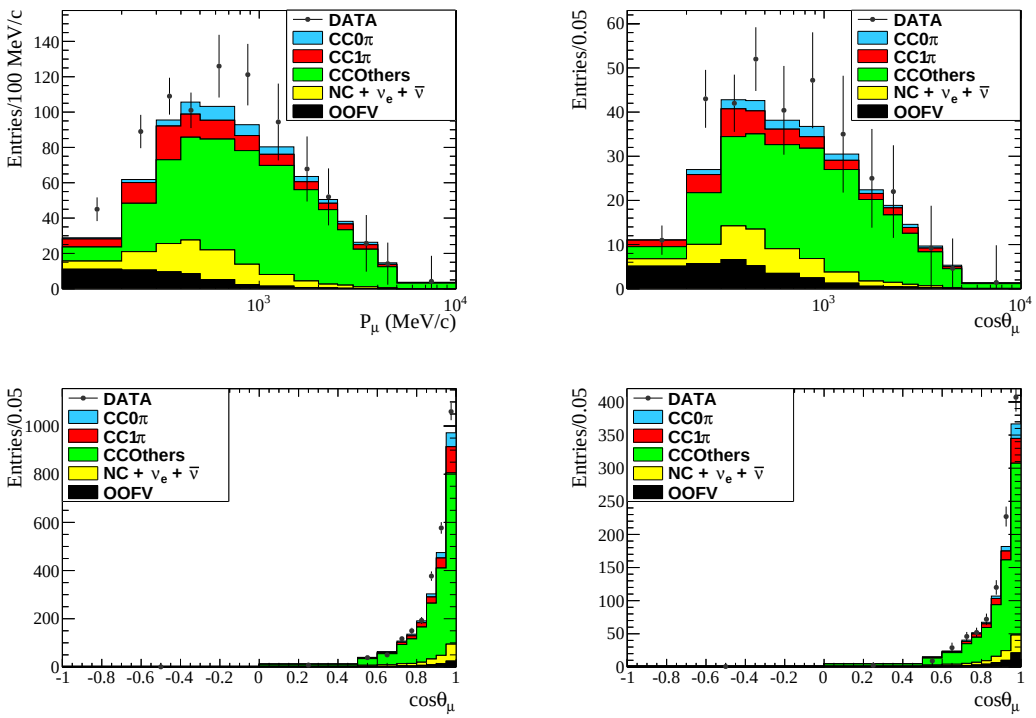

Figure 6.8: Number of events selected as CC-Others as a function of reconstructed momentum (top) and angle (bottom) of the muon candidate, normalized to data POT and split in the different final states for the x-layer (left) and y-layer (right). The Black dots are the real data sample.

6.2 Analysis strategy

Ideally, the neutrino interaction vertex could be measured with sufficient accuracy to determine whether a given interaction happened in the water or in the scintillator module. However, this information will never be available for events with a single reconstructed track. This means that the selection can only distinguish between carbon and oxygen events statistically rather than on an event-by-event basis.
The number (N_{signal}) of neutrino interactions in the FGD2 fiducial volume, can be expressed as the convolution of the signal cross-section σ_{signal} with the integrated flux Φ of incident neutrinos per unit area, normalized by the number of target in the fiducial volume T_{FV}:

$$N_{signal} = \int \sigma_{signal}(E_\nu) \cdot \Phi_\nu(E_\nu) \cdot T_{FV} \cdot dE_\nu. \tag{6.2}$$

The number of selected CC0π candidates must be corrected by the detector efficiency ϵ and by the signal purity $f^{CC0\pi}$ which is the fraction of true CC0π events in the events reconstructed and selected as CC0π in the detector. The number of reconstructed and selected CC0π events is then given by:

$$N_{CC0\pi} = \frac{N_{signal} \cdot \epsilon}{f^{CC0\pi}}. \tag{6.3}$$

The simulation is used to estimate the sample purity and the detector efficiency. Hence, given Eq. 6.2 and 6.3, the flux integrated cross-section for the ν_μ CC0π interactions is:

$$\sigma_{signal} = \int \frac{N_{CC0\pi} \cdot f^{CC0\pi}}{\epsilon \cdot T_{FV}} \Phi_\nu(E_\nu) dE_\nu \tag{6.4}$$

Therefore using Eq. 6.2 and 6.3 and a condensed notation, the CC0π Oxygen over Carbon cross-section ratio $R_{O/C}$ can be extracted by solving the following linear system:

$$\begin{cases} \frac{N_x f_x^{CC0\pi}}{\Phi} = & \epsilon_w f_{w\to x} \left(\sigma_O T^{O,wm} + \sigma_C T^{C,wm}\right) + \epsilon_x f_{x\to x} \left(\sigma_C T^{C,x} + \sigma_O T^{O,x}\right) + \\ & \epsilon_y f_{y\to x} \left(\sigma_C T^{C,y} + \sigma_O T^{O,y}\right) \\ \frac{N_y f_y^{CC0\pi}}{\Phi} = & \epsilon_w f_{w\to y} \left(\sigma_O T^{O,wm} + \sigma_C T^{C,wm}\right) + \epsilon_y f_{y\to y} \left(\sigma_C T^{C,y} + \sigma_O T^{O,y}\right) + \\ & \epsilon_x f_{x\to y} \left(\sigma_C T^{C,x} + \sigma_O T^{O,x}\right) \end{cases} \tag{6.5}$$

where Φ is the integrated neutrino flux, N_x and N_y are the number of reconstructed events in the x and y layers estimated by applying the so-called *"transfer matrix"*, relating the number of reconstructed events to the true numbers of events. It is obtained from MC, see Sec. 6.2.1. The $f_{x,(y)}^{CC0\pi}$ are the signal purities (the fraction of true CC0π over all the selected events in the x(y)-layer). The cross-section σ_C is the cross-section in pure carbon (C) while σ_O is the cross-section in pure oxygen (O). Since the water module consists of pure water and a carbon-like structure, it includes also

carbon interactions, for this reason the fractions $f^{w}_{x(y)}$ are divided in two contributions $\sigma_O T^{O,wm}$ and $\sigma_C T^{C,wm}$. The targets $T^{O,wm}$ and $T^{C,wm}$ are then the number of pure water and carbon-like targets in the water module. In the same way the scintillator module contains also oxygen targets: $\sigma_C T^{C,x(y)}$ and $\sigma_O T^{O,x(y)}$. Finally $T^{C,x}$ and $T^{C,y}$ are the number of carbon targets in the x and y layers while $T^{O,x(y)}$ is the number of oxygen targets in the scintillator modules. The terms $f_{a\to b}$ take into account the *"migration of vertex"*: the reconstruction of vertex in a different module than the one in which the true interaction occurred. The $f_{a\to b}$ that for notation reason now will be called f^{b}_{a}, is then the fraction of true CC0π in module a which are reconstructed in module b (where a can indicates x,y or water module and b can indicates x or y active layers). Solving the linear system as a function of $R = \sigma_O/\sigma_C$, the final formula for the cross-section ratio is:

$$\mathrm{R}^{CC0\pi}_{O/C} = \frac{N_x f_x^{CC0\pi}\left(\epsilon_w f_y^w T^{C,wm} + \epsilon_y f_y^y T^{C,y} + \epsilon_x f_y^x T^{C,x}\right) - N_y f_y^{CC0\pi}\left(\epsilon_x f_x^x T^{C,x} + \epsilon_y f_x^y T^{C,y} + \epsilon_w f_x^w T^{C,wm}\right)}{N_y f_y^{CC0\pi}\left(\epsilon_w f_x^w T^{O,wm} + \epsilon_x f_x^x T^{O,x} + \epsilon_y f_x^y T^{O,y}\right) - N_x f_x^{CC0\pi}\left(\epsilon_w f_y^w T^{O,wm} + \epsilon_y f_y^y T^{O,y} + \epsilon_x f_y^x T^{O,x}\right)}. \tag{6.6}$$

The ν_μ CC0π oxygen over carbon cross-section ratio will be measured as a function of true muon kinematics momentum p_μ and angle $\cos\theta_\mu$.

6.2.1 Transfer matrix

The distribution of any observable is distorted due to experimental limitations of the detector. A MC-based procedure is therefore needed to estimate the truth level spectrum, the spectrum that would be measured with an ideal detector (without resolution effects). The ND280 TPC has a good resolution in momentum and angle of the muon from neutrino interactions, as shown in Fig. 6.9 and Fig. 6.10. Moreover most of the detector effects are known to be the same for interactions in the x and y layers, hence any data-MC discrepancy is expected to cancel out in the ratio. Furthermore, the simulation is known to reproduce well the detector performances and any known data-MC discrepancy is included in the systematics. As a consequence, a simple Reco-True transfer matrix based on MC is used to correct detector effects.
The Reco-True transfer matrix is defined as follows. The number of events in the i^{th} true bin $\left(N_i^{True}\right)$, given the number of reco events $\left(N_j^{Reco}\right)$ in the j^{th} reco bin, is calculated as:

$$N_i^{True} = \sum_{j=1}^{N_{bin}} w_{ij} \cdot N_j^{Reco} \tag{6.7}$$

where the coefficient w_{ij} is the corresponding correction factor: the probability for a true muon with a given momentum p_μ (or direction $\cos\theta_\mu$) in the true bin i to be reconstructed in the bin j. The calculation of w_{ij} is based on the MC sample after

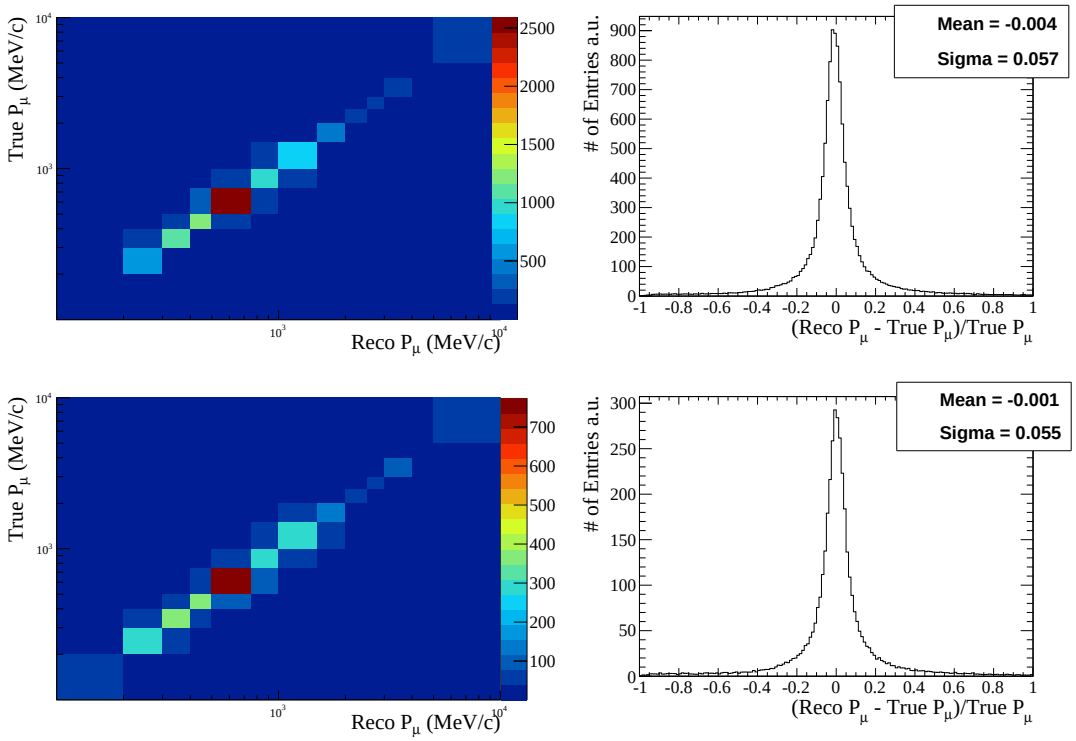

Figure 6.9: True vs Reco muon momentum (left) and muon momentum resolution (right) of the selected CC0π interactions in the x-layer (top) and y-layer (bottom).

applying all the cuts for the CC0π selection. It is defined as:

$$w_{ij} = \frac{U(True, Reco)_{ij}}{\int_1^{N_{bin}} N(Reco) dN} \tag{6.8}$$

where the True-Reco matrix $U(True, Reco)$ is built from the numbers of true and reconstructed MC events in terms of the muon kinematic variables (momentum in Fig. 6.9 and direction in Fig. 6.10). The transfer matrix which models the correction factor for the x and y layers are shown in Fig. 6.11. The chosen binning for the transfer matrix is shown in Table 6.2.

Observable	Bins
p_μ (MeV/c)	[100, 200, 300, 400, 500, 750, 1000, 1500, 2000, 2500, 3000, 4000, 5000, 10000]
cosθ_μ	[-1, 0., 0.5, 0.6, 0.7, 0.75, 0.8, 0.85, 0.9, 0.95, 1]

Table 6.2: Binning of the cross-section ratio in the kinematic variables.

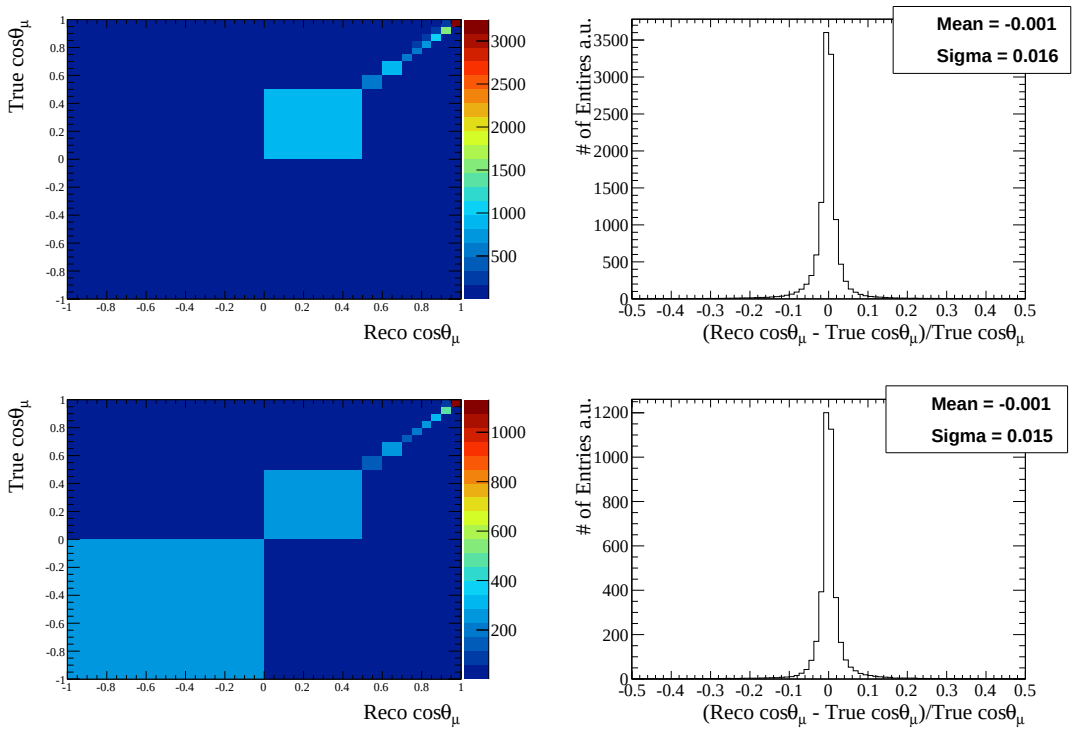

Figure 6.10: True vs Reco muon direction (left) and muon direction resolution (right) of the selected CC0π interactions in the x-layer (top) and y-layer (bottom).

6.2.2 Efficiency and Purity

The efficiency for the selection of CC0π interactions reported in eq. 6.6 is defined as:

$$\epsilon_{CC0\pi}^{water(x,y-layer)} = \frac{N_{sel.}^{true\ CC0\pi\ in\ water(x,y-layer)}}{N_{gen.}^{true\ CC0\pi\ in\ water(x,y-layer)}}, \tag{6.9}$$

the ratio between the number of selected true CC0π ($N_{sel.}^{true,CC0\pi}$) and the number of the generated CC0π events ($N_{gen.}^{true,CC0\pi}$) in the FV of the FGD2 for the CC0π interactions in water and x and y scintillator layers. The true CC0π efficiencies in each module are are: $\epsilon_w = 50.2\%$ in the water modules, $\epsilon_{x-layer} = 49.8\%$ and $\epsilon_{y-layer} = 47.0\%$ for scintillator interactions. They are dominated by the loss of events in the backward angle and in low momentum regions. Efficiencies are averaged over all the x-layers or y-layers or water modules.
Figure 6.12 shows the selection efficiencies as a function of the true muon momentum and direction and true vertex position along the z-axis. Scintillator module loses efficiency in the first and last xy-module which leads the y-layer to have an efficiency slightly lower than water and x-layer (bottom plot). Otherwise the efficiencies in different modules are very similar and increase with the z-position. The selection requires

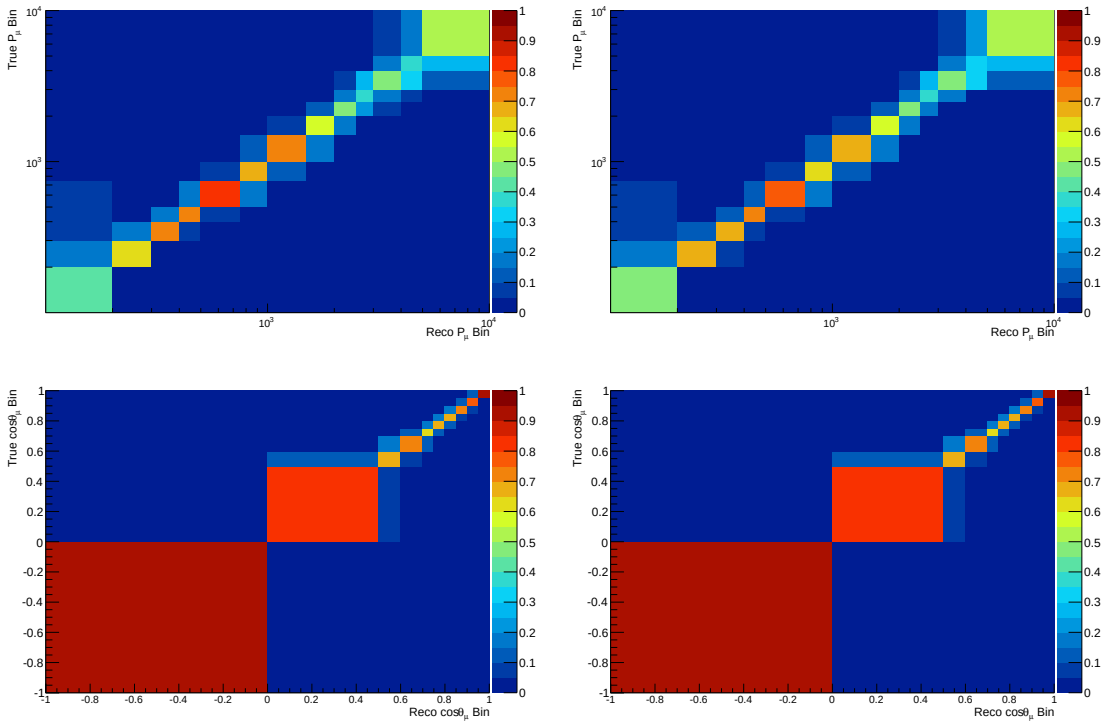

Figure 6.11: Correction factor True-Reco matrices for the muon momentum (top) and angle (bottom) of the selected CC0π event in the x-layer (left) and y-layer (right).

a muon candidate track in the TPC with at least 18 clusters, hence tracks closer to downstream TPC3 have more probability to pass the selection. The low efficiency in the backward region ($\sim 7\%$) is due to reconstruction effects, backward-going event are tagged thanks to the timing information between the FGDs. The muon candidate to be reconstructed as backward must enter in the upstream TPC2 and reaches FGD1 leaving some hits but usually backward muons have very low momentum and do not even escape FGD2. The statistical uncertainty on the efficiency due to the MC statistics is computed taking into account the MC weight w of each event, using the following formula:

$$\delta_\epsilon = \frac{\sqrt{\sum_{j=1}^{N_{bin}} \sum^{sel.} w^2 \left(\sum^{unsel.} w\right)^2 + \sum^{unsel.} w^2 \left(\sum^{sel.} w\right)^2}}{\left(\sum^{sel.+unsel.} w\right)^2}. \tag{6.10}$$

The uncertainty (Fig. 6.13) is of the order of a few percent in each bin and becomes larger in the very low/high momentum and backward/high angle regions where the data statistics also has large uncertainty.

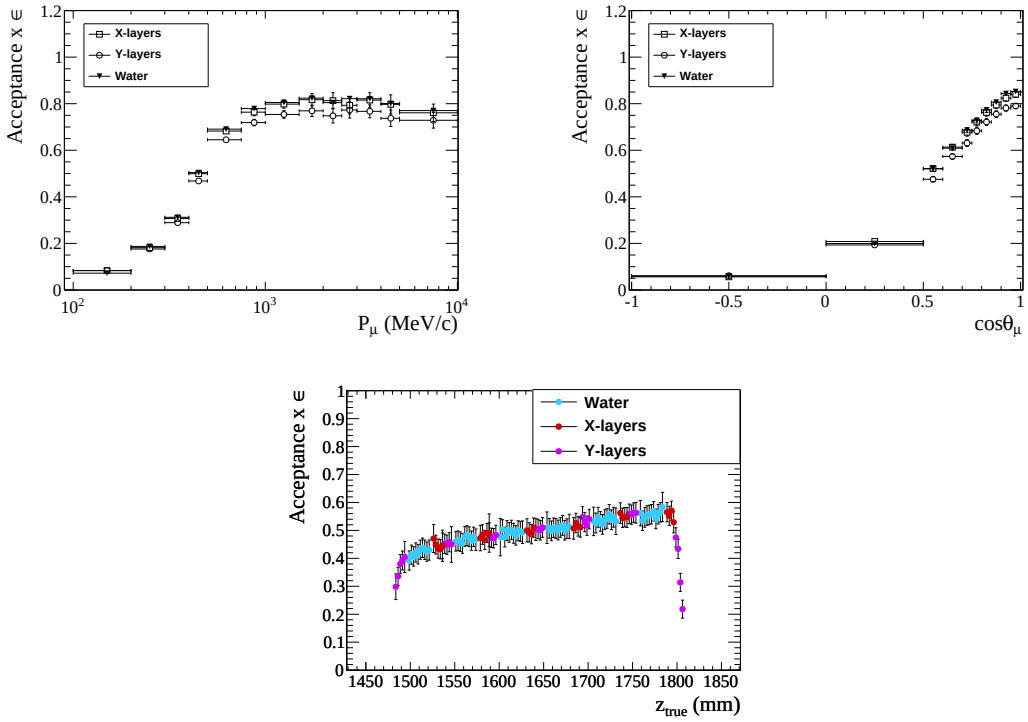

Figure 6.12: Selection efficiency as a function muon true momentum (top left) and angle (top right). The bottom plot shows the efficiency as a function of the true vertex position along the z-axis; blue, red and magenta dots represent water, x and y-layers efficiencies.

The CC0π purity is defined as:

$$f^{CC0\pi}_{x(y)-layers} = \frac{N^{true\ CC0pi}_{sel.\ x(y)-layers}}{N_{sel.\ x(y)-layers}} \tag{6.11}$$

the ratio between the true selected CC0π interactions ($N^{true\ CC0pi}_{sel.\ x(y)-layers}$) and all the events selected as CC0π $\left(N_{sel.\ x(y)-layers}\right)$ in the x or y layers. The uncertainty on the purity is computed as in Eq. 6.10. Table 6.3 summarizes the true composition of the selected CC0π sample in the x and y layers, which was already reported in Fig. 6.6. The integrated true CC0π purity is about 69% and 64% for the x and y layer respectively. The CC1π sample is the main background source of the order of 15%. It is mainly due to detector inefficiency, i.e. the outgoing pion being undetected or misidentified. The contamination coming from the CC-Others sample is not negligible ($\sim$ 8%), more pions are not detected or misidentified, and from the OOFV when the vertex is reconstructed in the FV but the ν_μ interacts outside the fiducial volume. The OOFV contribution is different in the x ($\sim$ 6%) and y ($\sim$ 11%) layers because of the definition of FV itself, see Fig. 6.2. In the FGD2 only the first x-layer is removed from the FV, thus the first y-layer contains the events coming from the upstream x-layer.

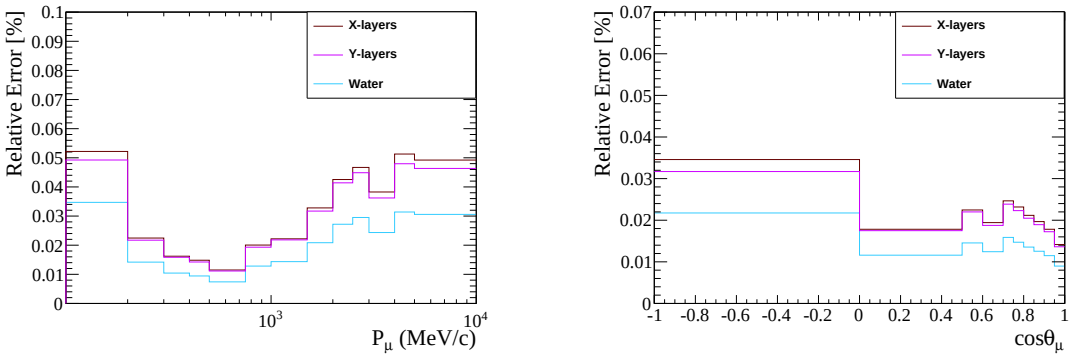

Figure 6.13: Relative uncertainty of CC0π selection efficiencies due to MC statistics for the water modules in blue, x-layers in red and y-layers in violet as a function of muon momentum (left) and angle (right).

	$CC0\pi$ [%]	$CC1\pi$[%]	$CC-Others$ [%]	$NC\ +\ \nu_e$ [%]	$OOFV$ [%]
FGD2 x-layer	68.7	14.7	8.05	2.36	6.19
FGD2 y-layer	63.5	15.1	8.32	2.45	10.6

Table 6.3: True final state composition of the selected CC0π sample.

6.2.3 Water and Scintillator module interactions

The analysis relies on the ability to disentangle the interactions in the water module from the interactions in scintillator. Figure 6.14 shows the selected CC0π reconstructed (left) and true (right) vertex position in FGD2 for signal interactions in water, x and y layers and for backgrounds.
Considering only true CC0π events which pass the selection, the fraction of neutrino interactions in the water module, in the x-layers and is reconstructed in active x or y layers can be defined as:

$$f_{x(y)}^{water(x,y-layers)} = \frac{N_{sel.\ x(y)-layers}^{true\ CC0\pi\ in\ water(x,y-layers)}}{N_{sel.\ x(y)-layers}^{true\ CC0\pi}}. \tag{6.12}$$

Similarly it is possible to define also another fraction $f_{x(y)}^{dead}$ which represents the fraction of the true selected CC0π interactions which takes place neither in the x-layer nor in the y-layer nor in water. The dead material/gap is due to the glue skin between the scintillator bars, the G10 spacers, the air and any other passive material within the water or scintillator module structure. A detailed discussion about the gap composition will be presented in Sec. 6.4.3. Since dead materials contains mainly carbon and oxygen nuclei, those interactions are included in the ratio extraction in order to do not lose statistics.
Moreover, it is not possible to disentangle CC0π events in pure water from events in the

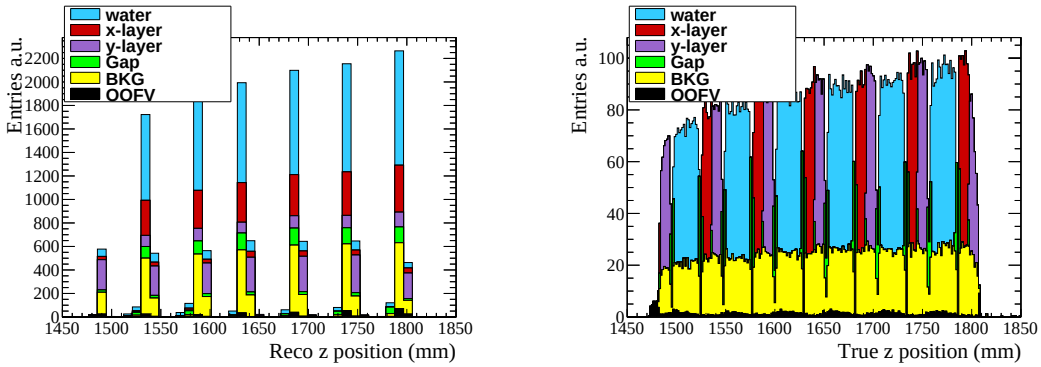

Figure 6.14: Selected CC0π reconstructed (left) and true (right) vertex position in FGD2 for signal interactions in water, x and y layers and for backgrounds.

panel ($C_{16}H_{14}O_3$), for this reason the water fraction (f^{water}) includes both. This effect is taken into account by including the composition of the module, as will be explained in Sec. 6.4.3. Figure 6.15 shows the fraction of true CC0π reconstructed in each material, statistical errors are computed as in Eq. 6.10. The x-layer is dominated by water events and by interactions which took place in the x-layer itself but there is also a small contribution from y-layer due to detector effects resulting in the reconstruction of the interaction vertex in a different module than the one in which the true interaction took place (vertex migration). The y-layer instead is dominated by y-layer events with a small contribution from interactions coming from the x-layer wrongly reconstructed in y and by a small water contamination which tends to be larger for low momentum, backward muons. Similarly the pollution of true x(y) interactions reconstructed in y(x)-layers tends to increase for low momentum, backward muons. Integrated values for the x and y-layers are listed in Tab. 6.4.

MC	**Water** [%]	**x-layer** [%]	**y-layer** [%]	**Dead** [%]
x-layer	60.0	24.4	7.38	8.22
y-layer	17.9	9.19	67.7	5.25

Table 6.4: Module composition of the true CC0π selected sample.

6.2.3.1 Events migrations

As shown in Eq. 6.6 it is crucial for this analysis to separate true interactions which take place in the water and scintillator modules and are detected in x or y active layers. The number of detected events $N_{x,(y)}$ is given by the sum of events generated in the water and scintillator module and contains *"migrated events"*. Therefore migrations between layers must be deeply studied.
Two kinds of migrations can misreconstruct the vertex of the interaction: forward and backward migrations.

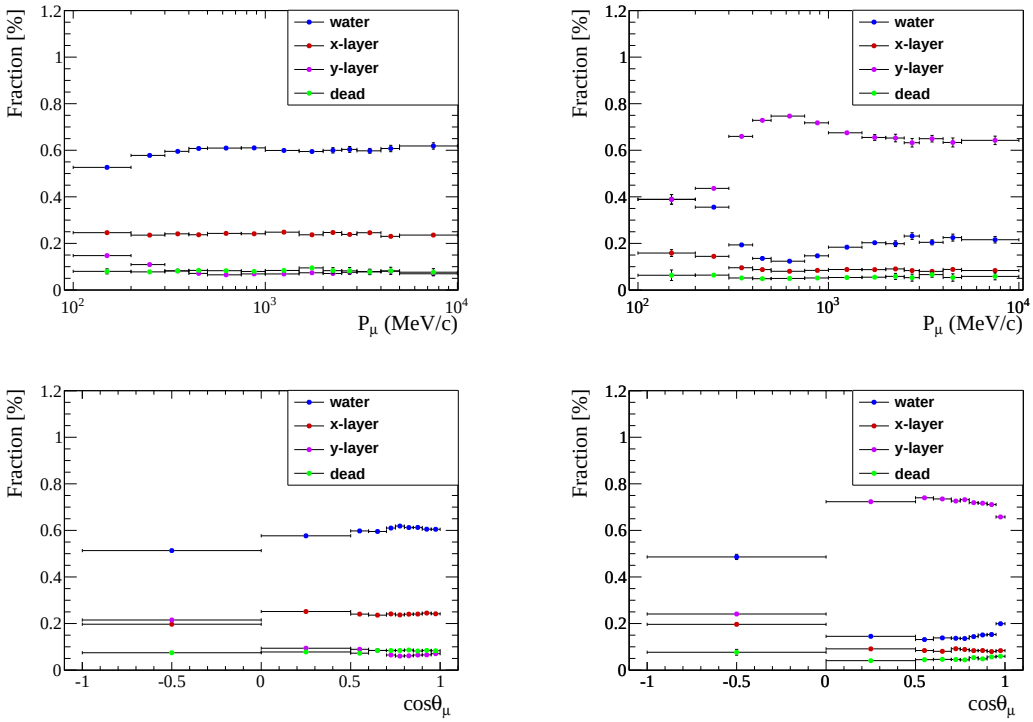

Figure 6.15: Selected true CC0π events divided by interaction in the true module type as a function of the muon candidate true momentum (top) and angle (bottom) for the x-layers (left) and y-layers (right).

- Interactions in the water module:
  - not migrated: the first hit is in the first downstrem x-layer ($\sim 90\%$);
  - forward migrations: water interactions are reconstructed in the downstream y-layer ($< 1\%$);
  - backward migrations: water interactions are reconstructed in the upstream y-layer ($\sim 9\%$).
- Interactions in the x-layer:
  - not migrated: the interactions happen in the same x-layer where it is reconstructed ($\sim 89\%$);
  - forward migrations: x-layer interactions are reconstructed in the downstream y-layer ($\sim 9\%$);
  - backward migrations: x-layer interactions are reconstructed in the upstream y-layer ($\sim 2\%$).
- Interactions in the y-layer:

- not migrated: the interactions happen in the same y-layer where it is reconstructed ($\sim 73\%$);
- forward migrations: y-layer interactions are reconstructed in the downstream x-layer ($\sim 10\%$);
- backward migrations: y-layer interactions are reconstructed in the upstream x-layer ($\sim 17\%$).

The migration/not migration events fractions $f_{j\to i}$ are defined as the fraction of events generated in the module $j = x-layer,\ y-layer,\ water$ and reconstructed in the layer $i = x-layer, y-layer$ (averaged on the layer number). They are defined as:

$$\begin{aligned} f_{x(y)\to x(y)} &= \frac{N_{x(y)\to x(y)}}{N^{True\ x(y)-layer}_{reconstructed}}, \\ f_{x(y)\to y(x)} &= \frac{N_{x(y)\to y(x)}}{N^{True\ x(y)-layer}_{reconstructed}}, \\ f_{w\to x(y)} &= \frac{N_{w\to x(y)}}{N^{True\ water}_{reconstructed}}, \end{aligned} \tag{6.13}$$

where $N_{j\to i}$ is the number of events generated in j and reconstructed in i and $True$ means *vertex generated in...*, for instance $N^{True\ water}_{reconstructed}$ is the number of reconstructed events generated in the water module and passing the CC0π selection. Splitting each sample according to those definitions gives a estimate of migrated and not migrated events, hence by definition the following relations are satisfied:

$$\begin{aligned} f_{x\to x} + f_{x\to y(fwd)} + f_{x\to y(bkw)} &= \frac{N_{x\to x} + N_{x\to y(fwd)} + N_{x\to y(bkw)}}{N^{True\ x-layer}_{reconstructed}} &&= 1 \\ f_{y\to y} + f_{y\to x(fwd)} + f_{y\to x(bkw)} &= \frac{N_{y\to y} + N_{y\to x(fwd)} + N_{y\to x(bkw)}}{N^{True\ y-layer}_{reconstructed}} &&= 1 \\ f_{w\to x} + f_{w\to y} &= \frac{N_{w\to x} + N_{w\to y}}{N^{True\ water}_{reconstructed}} &&= 1. \end{aligned} \tag{6.14}$$

Figures 6.16 and 6.17 show the migration fractions of each module as a function of the true muon momentum and direction.
Table 6.5 details the migration fractions for each true vertex.

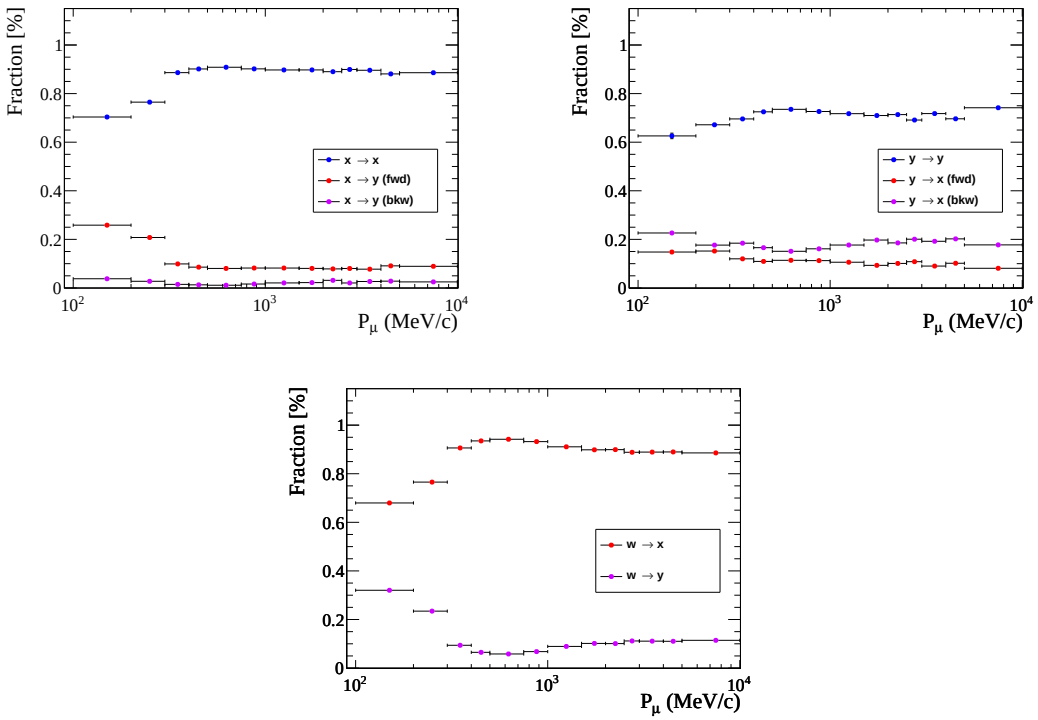

Figure 6.16: Migration fractions in FGD2 as a function of muon momentum. Top left: true interaction in the x-layer. Top right: true interaction in the y-layer. Bottom: event generated in the water module.

Forward migrations

Forward migrations in both water and scintillator module reconstruct the vertex in the downstream layer because of missing hits, due to detector reconstruction inefficiency. In the water module case this happens when the vertex is reconstructed in the downstream y-layer or any layer after the first x-layer. Migrations of more than one layer (i.e. from one x(y)-layer to the following x(y)-layer) are $\sim 0.6\%$. Figure 6.18 shows a schematic view of forward migrations in the FGD2 structure where the reconstructed vertex (first hit in orange) is downstream the true vertex of the interaction (red). The forward migrations between neighboring layers in the scintillator interactions are more common

Migration $j \to i$		
$f_{x\to x} = 0.891 \pm 0.009$	$f_{x\to y(fwd)} = 0.093 \pm 0.002$	$f_{x\to y(bkw)} = 0.016 \pm 0.001$
$f_{y\to y} = 0.718 \pm 0.008$	$f_{y\to x(fwd)} = 0.112 \pm 0.002$	$f_{y\to x(bkw)} = 0.169 \pm 0.003$
$f_{w\to x} = 0.912 \pm 0.009$	$f_{w\to y} = 0.088 \pm 0.002$	

Table 6.5: List of migration fractions. The first index represents the true interaction module, the second one the reconstructed vertex.

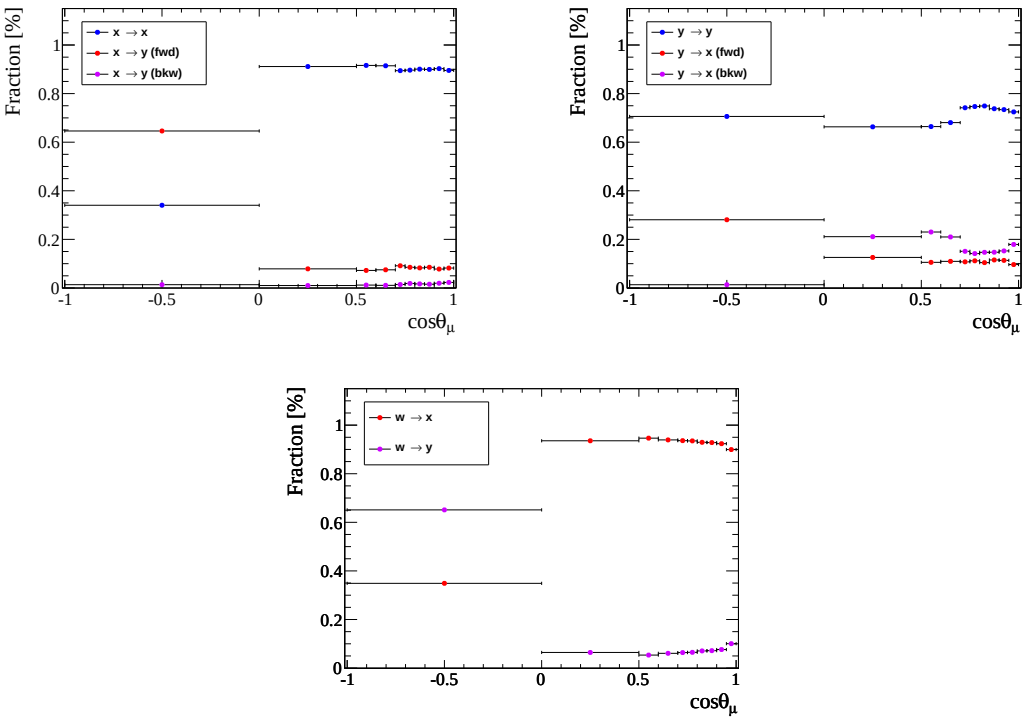

Figure 6.17: Migration fractions in FGD2 as a function of muon direction.

than water forward migrations to the first downstream y-layer. In case of scintillator to scintillator migration (top left and right in Fig. 6.18), forward migrations can happen if the interaction takes place at the edge of the scintillator. For water interactions instead the track must entirely cross the first downstream x-layer, therefore the probability of missing a hits in the whole x-layer and reconstructing then the track in the downstream y-layer (bottom) is very unlikely ($< 1\%$). For this reason the y-layer enhancement with water interactions, the f_y^w in Eq. 6.6, is mostly due to backward tracks. In summary, forward migration is a second order effect due to detector issues and not to the physics of the interaction itself and it is fully dominated by the migration between scintillator modules.

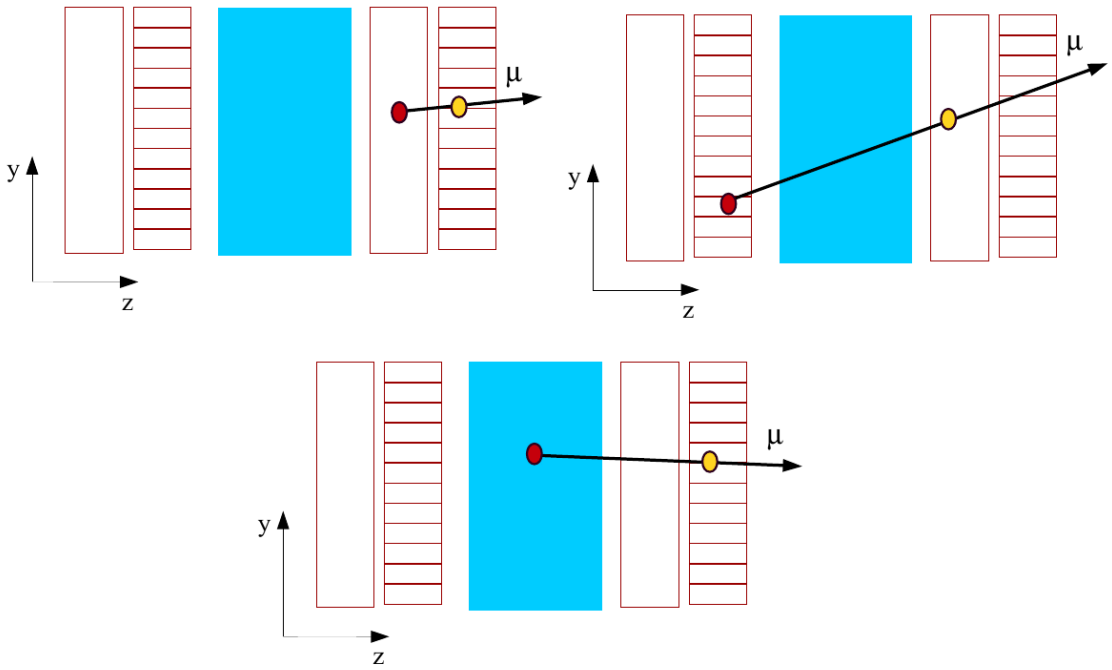

Figure 6.18: Schematic view of forward migrations in the FGD2 structure with the true interaction vertex (red vertex) and reconstructed vertex (orange vertex).

Backward migration

Backward migrations can happen when a low energetic particle, produced in the interaction, travels backward leaving some hits which are fitted together with the forward muon candidate or when the muon candidate itself is backward. Figure 6.19 shows a schematic view of backward migrations in the FGD2, the true vertex interaction is yellow while the first reconstructed hit is orange. Similarly to forward migrations, backward migrations are divided in scintillator to scintillator and water to scintillator migrations. The scintillator to scintillator backward migration happens when the true interaction in the x(y)-layer is reconstructed in the upstream y(x)-layer (top left and right in Fig. 6.19) as a result of backward going particle due to detector resolution, when the interaction takes place at the edge of the module or because the first hit of the backward going muon is missing. However, the water to scintillator migrations reconstructed in the upstream y-layer (bottom) are more interesting because they are a mix of oxygen and carbon interactions. The MC has large uncertainty in modeling the backward tracks from neutrino interactions. Backward going particles could be nucleons produced by FSI/2p2h effects or muons traveling backward. The amount of backward particles is small ($\sim$ 10% in NEUT) but has a large modeling uncertainty. For this reason it must be constrained from a control sample on data, as explained in the next Sec. 6.3. Effects of the second order with combination of backward particles

and detector inefficiencies, causing a migration of more than one layer (from x(y) to the upstream x(y)-layer) are very unlikely $\sim 0.7\%$.

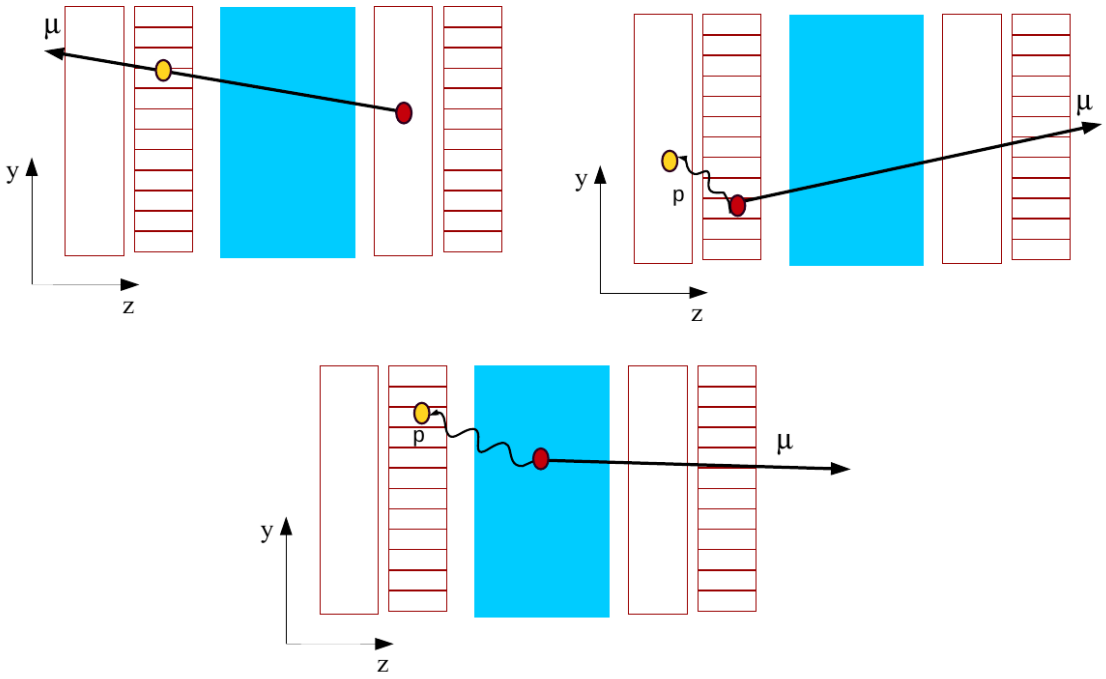

Figure 6.19: Schematic view of FGD2 structure with the true interaction vertex (red vertex) and reconstructed vertex (orange vertex) of backward migrations.

6.3 The control sample

While the two FGDs are very similar in their structure and electronics, the active/passive structure of FGD2, where 7 XY-modules are interleaved with 6 water modules, causes a degradation in vertex resolution with respect to the fully active FGD1. For these reasons a fully active FGD1 cannot be used as control sample as it is, since it does not reproduce the active/passive effects present in the FGD2. Thus, it is possible to alter the FGD1 configuration masking one XY-module every two so that it becomes much more comparable to FGD2. In the following this reduced FGD1 will be named *"Hybrid FGD1"*.
This Section presents then, an exhaustive description of the Hybrid FGD1 control sample, which is used in order to prove the reliability and the robustness of the analysis for the extraction of the oxygen over carbon CC0π cross-section ratio in the FGD2 as well as to constrain the systematics on migrations due to backward tracks.

6.3.1 The Hybrid FGD1

Discarding all hits in some modules, it is possible to produce FGD1 with 8 active XY-modules interleaved with 7 passive XY-modules acting as if they were uninstrumented. For this study the reconstruction has been modified in order to remove all hits in two consecutive layers. In this way if the neutrino interaction occurs in one of them the vertex will be reconstructed in the first non-masked layer, upstream or downstream the masked module. While this is not exactly a FGD2, because of the larger width of the water modules, it is possible to directly compare the Hybrid FGD1 with FGD2 results in both MC and data in order to constrain the systematic effects taking into account the difference between the two FGDs. The most significant difference between the Hybrid FGD1 and FGD2 is in the amount of dead material between modules. A water module in FGD2 has 2.8 g/cm^2 of dead material, while a masked XY module has 2.1g/cm^2, however this effect is well modelled by the simulation. Moreover, the radiation lengths are similar $\lambda = 36.08$ cm and $\lambda = 41.31$ cm for water and plastic scintillator respectively [155].
Due to the large size of the files and due to the time to re-run the full reconstruction chain, only 20% of the total MC sample has been used. This statistics corresponds to approximately 3 times the data statistics.
A side view of an event occurring in the masked module (red circle) and detected in the downstream x-layer (orange circle) in the Hybrid FGD1 is shown in Fig. 6.20 left. The right plot shows the distribution of the reconstructed CC0π events as a function of the layer number. This distribution matches the one in Fig. 6.5 in which x-layers are enriched by interactions coming from the upstream passive module. The first two layers are OOFV, while the layers number 3 and 4 correspond to the first XY-module switched off. Some events are reconstructed in the passive module because of reconstruction effects in the extrapolation of the vertex which is one of the sources of the OOFV systematic. These effects affect also the FGD2 (see Fig. 6.14), those events are treated as forward and included in the downstream x-layer.
The ratio formula in the Hybrid FGD1 can be written as:

$$\mathrm{R}_{C/C}^{CC0\pi} = \frac{N_x f_x^{CC0\pi}\left(\epsilon_{XY} f_y^{XY} T^{C,XY} + \epsilon_y f_y^y T^{C,y} + \epsilon_x f_y^x T^{C,x}\right) - N_y f_y^{CC0\pi}\left(\epsilon_x f_x^x T^{C,x} + \epsilon_y f_x^y T^{C,y} + \epsilon_{XY} f_x^{XY} T^{C,XY}\right)}{N_y f_y^{CC0\pi}\left(\epsilon_{XY} f_x^{XY} T^{C,XY} + \epsilon_x f_x^x T^{C,x} + \epsilon_y f_x^y T^{C,y}\right) - N_x f_x^{CC0\pi}\left(\epsilon_{XY} f_y^{XY} T^{C,XY} + \epsilon_y f_y^y T^{C,y} + \epsilon_x f_y^x T^{C,x}\right)}, \tag{6.15}$$

where *"XY"* denotes the passive module. The ratio formula for the Hybrid FGD1 is equal to the one in Eq. 6.6 for the FGD2 except that it is a passive scintillator XY-module over active scintillator (XY-module) ratio. Therefore, the expected value for the ratio should be equal to 1 (carbon over carbon ratio).

6.3.1.1 Efficiency and Purities

As for the FGD2, the total efficiency and sample purity are estimated in the Hybrid FGD1 from MC. Figures 6.21 and 6.22 show the efficiency times acceptance and the distribution of CC0π events as a function of the muon candidate reconstructed momentum

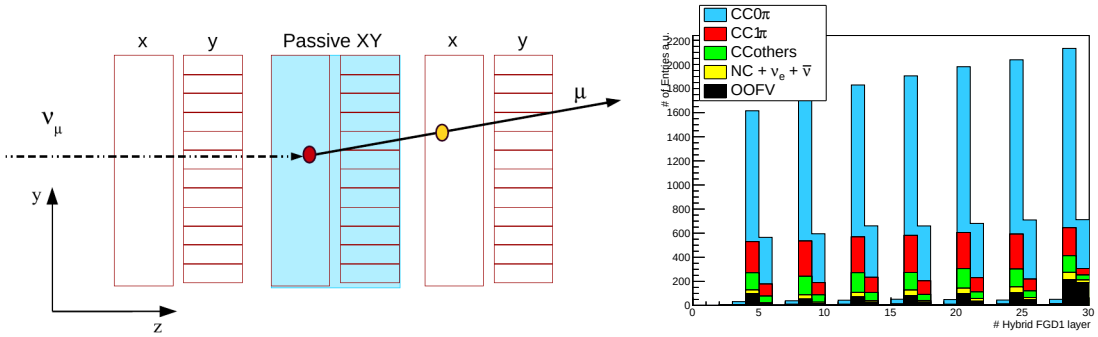

Figure 6.20: Schematic view of the FGD1 after the masking of the XY-modules (left). On the right the number of CC0π interactions as a function of the layer number in the Hybrid FGD1 (layers 0,1 are OOFV).

and angle. The black dots represent the data before applying the transfer matrix. The final efficiencies are 47.8% for events in the passive modules, 48.3% for the x-layer and 47.6% for the y-layers. The fractions of events in x, y, passive layers or dead material and reconstructed in the x-layer (left) and y-layer (right) are shown in Fig. 6.23. Tables 6.6 and 6.7 summarize the integrated sample purities and the true vertex location for reconstructed tracks in x-layers and y-layers.

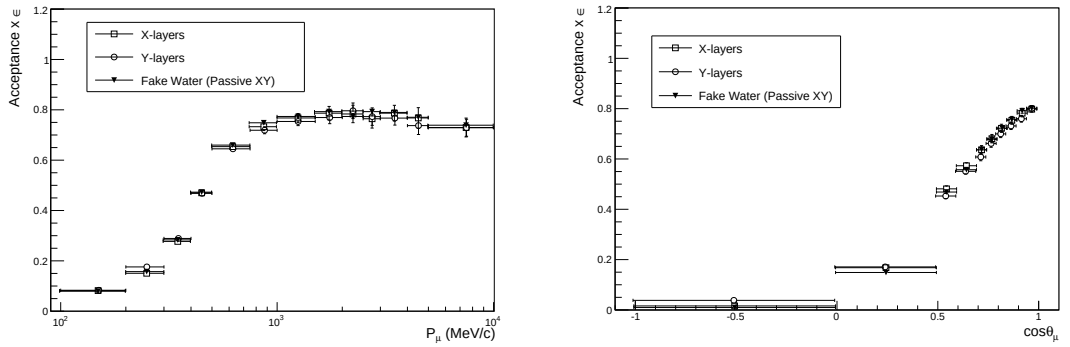

Figure 6.21: Passive XY and x-, y-layers selection efficiency (left) as a function of the muon momentum (left) and angle (right) in the Hybrid FGD1

	$CC0\pi$ [%]	$CC1\pi$[%]	$CC-Others$ [%]	$NC\ +\ \nu_e$ [%]	$OOFV$ [%]
Hybrid FGD1 x-layer	69.7	14.9	7.90	2.25	5.29
Hybrid FGD1 y-layer	66.3	15.5	8.31	2.34	7.56

Table 6.6: Topology composition of the selected CC0π sample.

Similarly to FGD2 the ratio formula (Eq. 6.15) corrects for event migration between

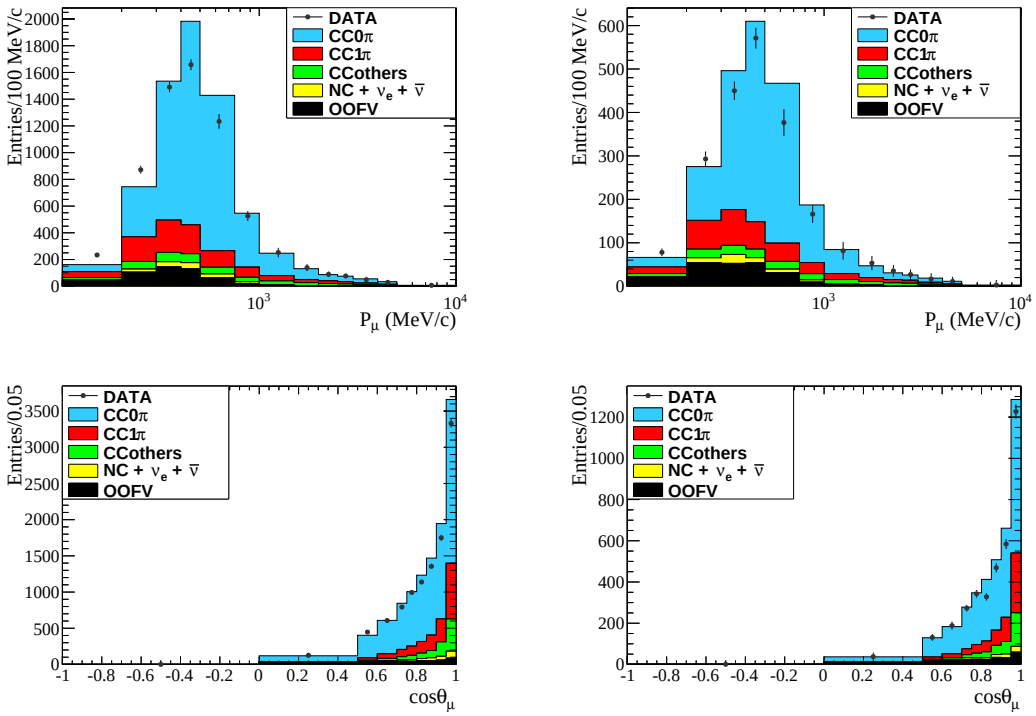

Figure 6.22: CC0π muon candidate in the Hybrid FDG1 as a function of muon reconstructed momentum (top) and angle (bottom) normalized to data POT and split in the different final states for the x-layer (left) and y-layer (right). Black dots represent the data before applying the Reco-True transfer matrix.

layers. Figures 6.24 and 6.25 show the migration/not migration events fractions as a function of muon momentum and direction for each module type.

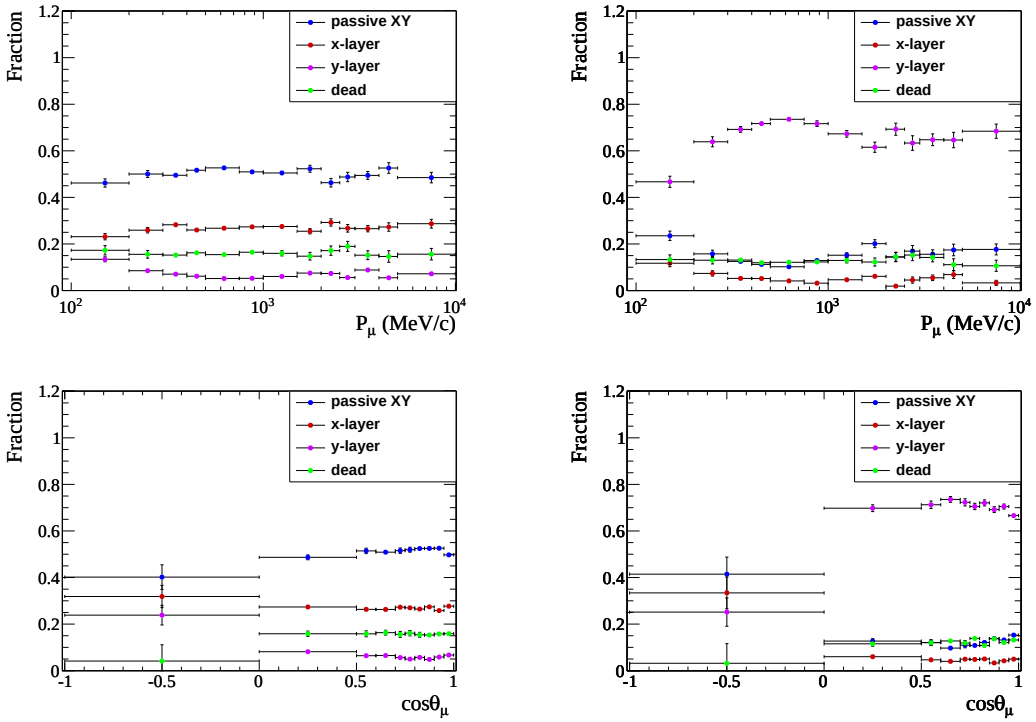

Figure 6.23: CC0π sample divided in true vertex locations reconstructed in the x-layer (left) and y-layer (right) as a function of muon true kinematics: momentum (top) and angle (bottom).

	Passive XY-module	X-layer	Y-layer	Dead
Hybrid FGD1-x	51.2	26.9	6.14	15.8
Hybrid FGD1-y	12.9	4.65	69.9	12.5

Table 6.7: True vertex location fraction in the true CC0π sample in the Hybrid FGD1 layers.

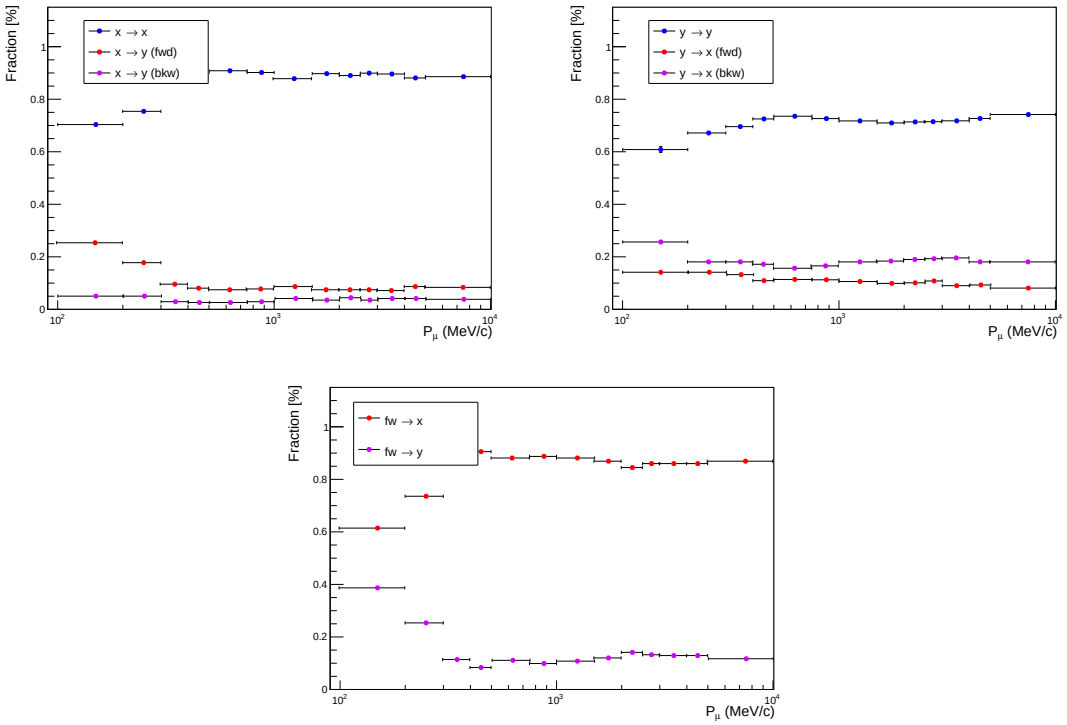

Figure 6.24: Migration fractions in the Hybrid FGD1 as a function of the muon momentum.

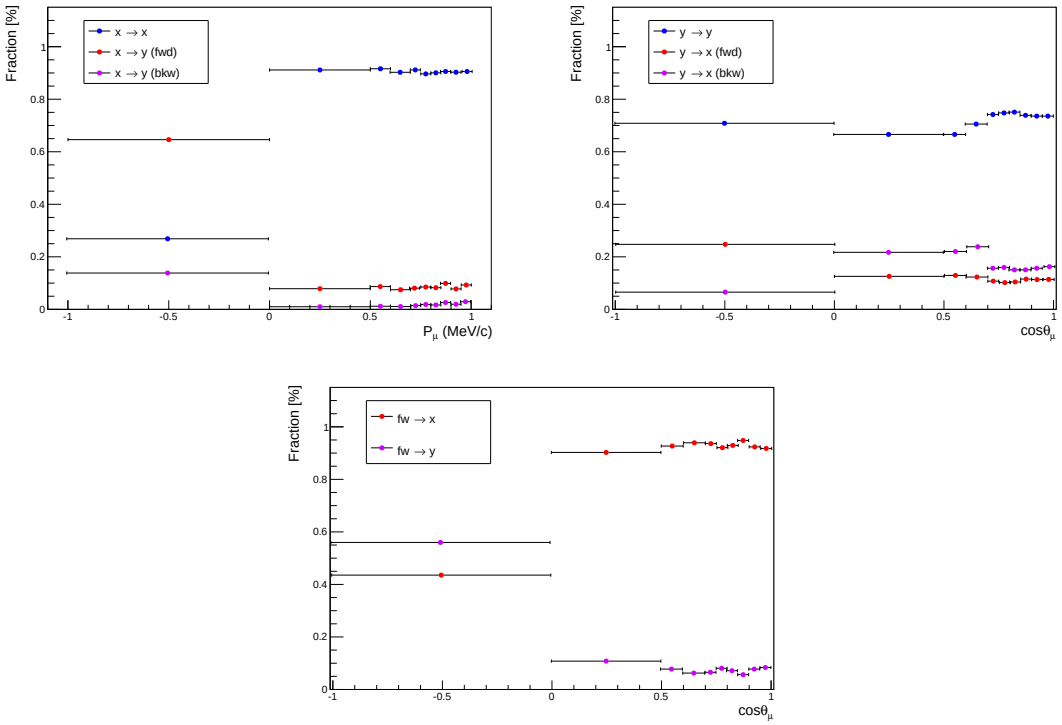

Figure 6.25: Migration fractions in the Hybrid FGD1 as a function of the muon direction.

6.3.1.2 Migration study

In order to quantify the sensitivity of the ratio formula to the migration of events due to backward tracks, a reweighting study of the backward sample is performed in FGD1, Hybrid FGD1 and FGD2. Since FGD1 consists of only active material, it is possible to test only migrations between active layers, the effect of migrations is expected to be different in FGD2 because of the passive material. The total uncertainty is a combination of passive to active migrations plus reconstruction effects modified by the presence of passive material.
The sample of backward tracks is reweighted using three different values: 20%, 50% and 100%. For instance, the +100% reweighting corresponds to doubling the total amount of backward tracks, while −100% removes all of them. Therefore such reweighting would model an uncertainty of 100% on the total amount of backward tracks. The results of this study are listed in Tab 6.8. Comparing FGD1 with FGD2 the introduced bias on the cross-section ratio scales with the reweighting but it is very different in the two cases: the 100% reweighting leads to an uncertainty of 1.7% and 4.2% for the FGD1 and FGD2 respectively. On the other hand, changing the amount of backward tracks in the MC by the 100%, 50% or 20% leads to similar results for the FGD2 and Hybrid FGD1.

Reweight	**FGD1**	**Hybrid FGD1**	**FGD2**
20%	0.4%	1.2%	0.9%
50%	0.9%	2.3%	2.0%
100%	1.7%	4.4%	4.2%

Table 6.8: Cross-section ratio relative uncertainties for the backward tracks reweighting study in FGD1, Hybrid FGD1, FGD2.

Since the ratio in the Hybrid FGD1 must be 1 (carbon to carbon rate), any deviation from 1 measured in the Hybrid FGD1 data can be interpreted as a bias due to backward track mismodeling. The expected bias on the ratio is 4%, 2% or 1% if the MC simulation has an uncertainty on the backward tracks by 100%, 50% or 20% respectively.

6.3.1.3 Real data RunII-IV results on Hybrid FGD1

The $R_{C/C}$ CC0π cross-section ratio calculated in the Hybrid FGD1 for NEUT generator is shown in Fig. 6.26 as a function of the muon momentum and angle. The results are represented by the black filled circles while the dashed black line is NEUT prediction. The NEUT results are in agreement within the error with the true prediction. Results on real data from RunII-IV for the Hybrid FGD1 control sample are shown in Fig. 6.27. The total cross section ratios obtained by the integration of one of the variable (p_μ or cosθ_μ) for NEUT and real data are:

$$\begin{aligned} R_{C/C}^{NEUT} &= 0.981 \pm 0.032(stat.) \pm 0.009(syst.) \\ R_{C/C}^{DATA} &= 1.012 \pm 0.050(stat.) \pm 0.009(syst.), \end{aligned} \tag{6.16}$$

while NEUT true prediction is $R_{C/C}^{Truth\ NEUT} = 0.994$. Results on both MC and data are compatible, within the error, with the prediction and also with the initial unitary assumption of the ratio. The bias due to backward tracks cannot be larger than the total uncertainty on data ($\sim$ 5%) which corresponds to an uncertainty on backward tracks of $\sim$ 100% (see Tab. 6.8). Note that in this case the total uncertainty does not include the systematics due to the detector mass and the uncertainty due to the theoretical cross-section models in the MC.

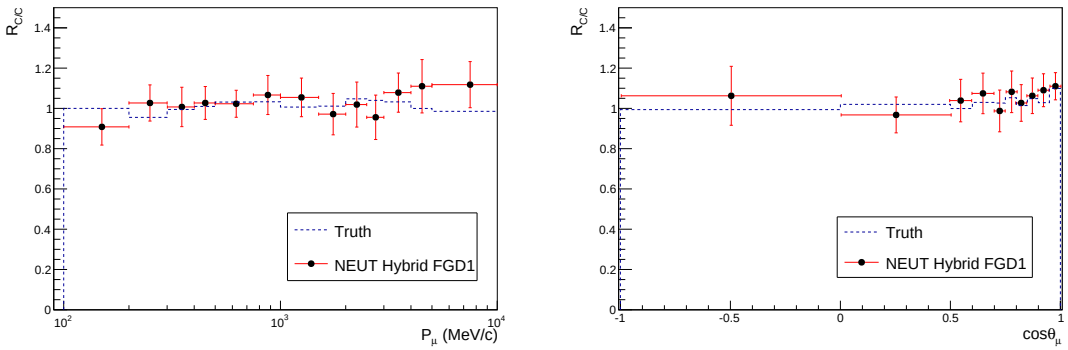

Figure 6.26: CC0π passive carbon over carbon ratio using the NEUT generator as a function of muon true momentum (left) and angle (right).

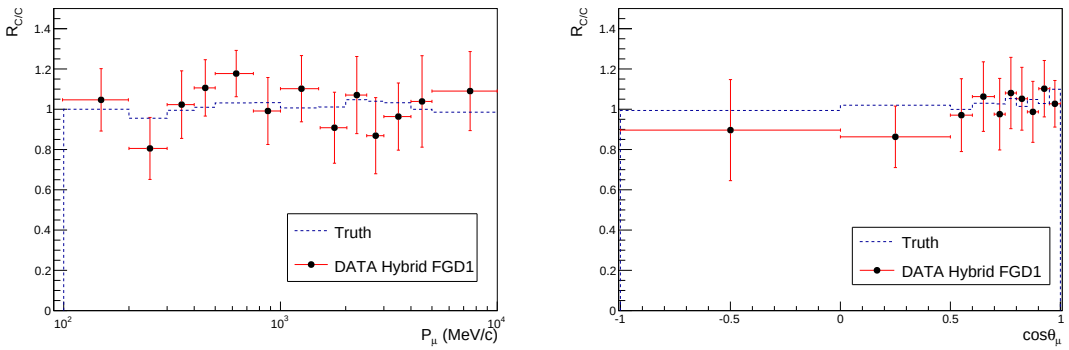

Figure 6.27: CC0π passive carbon over carbon ratio DATA results as a function of muon true momentum (left) and angle (right).

6.4 Source of uncertainties

The statistical uncertainty is due to the number of collected data in each bin (N_i) and to the amount of simulated events which affect the purities $f^{CC0\pi}$ and efficiencies ϵ. Systematics uncertainties on the oxygen over carbon cross-section ratio are a direct consequence of the limited knowledge of neutrino interactions and of the incomplete understanding of the detector apparatus. The sources of uncertainties can be summarized as:

- neutrino flux uncertainty due to beam composition and to the neutrino energy spectrum;
- detector uncertainties involved in the event reconstruction affecting the p_μ and $\cos\theta_\mu$ resolution, the amount of OOFV, the efficiency and acceptance;
- number of neutron targets in the detector FV definition;
- cross-section and FSI models used to simulate the signal and background processes.

The effects of these uncertainties are calculated using toy pseudo-experiments (throws) where the parameters describing the systematics are simultaneously varied taking into account their correlations. Each pseudo-experiment corresponds to an alternative hypothesis of the parameter set. The cross-section ratio is estimated for each pseudo-experiment and the final uncertainty is extracted from the RMS of the distribution of the ratio values over all the pseudo-experiments.

6.4.1 Statistical uncertainty

The statistical uncertainty is due to the fluctuations of the number of total reconstructed events in each bin ($N_{x,y}$) and to the MC statistics used to evaluate fractions

(f) and efficiencies (ϵ) of Eq. (6.6).
In order to evaluate the statistical uncertainty due to the limited data statistics, $N_{x,y}$ are varied assuming poissonian fluctuations in each p_μ ($\cos\theta_\mu$) bin. Therefore each toy MC sample will give a value of the ratio $R_{O/C}$. A set of 1000 toy MC simulations are performed, where the MC sample is renormalized to the POT in data. The statistical uncertainty due to the number of signal events reconstructed in each bin is then estimated as the RMS of the CC0π oxygen over carbon cross-section ratio distribution in that bin.
The MC statistical uncertainty has been evaluated with the error propagation theory using the following formula:

$$\sigma^2_{R_{O/C}} = \sum_i \left(\frac{\partial R_{O/C}}{\partial f_i}\right)^2 \sigma^2_{f_i} + 2\sum_{ij} \frac{\partial^2 R_{O/C}}{\partial f_i \partial f_j}\rho_{ij} \tag{6.17}$$

where the f_i are the fractions and the efficiencies in Eq. 6.6 and σ_{f_i} is the associated uncertainty from Eq. 6.10. The coefficient ρ_{ij} takes into account $f^{water}_{x(y)}$ and $f^{scint}_{x(y)}$ correlation. Finally the expected statistical uncertainty is extracted by summing in quadrature the MC statistical uncertainty ($\sim 1.\%$) given by Eq. 6.17 and the statistical fluctuations of the data sample ($\sim 4.6\%$). The estimated total relative statistical error (data + MC) is 4.8%. The statistical uncertainty in each p_μ ($cos\theta_\mu$) bin is shown in Fig. 6.35.

6.4.2 Detector systematic uncertainties

The ND280 detector consists of many sub-detectors, the uncertainty on the reconstruction and selection of events comes from the limitated knowledge of underlying physical properties of the detector apparatus and of the reconstruction method. The detector performances are modeled by MC which predicts the resolution and acceptance of the selection. Therefore the systematics effects are evaluated as the difference between the data and Monte Carlo simulation. The systematic uncertainties mainly fall into two categories: "*variation*" and "*weight*" systematics. Table 6.9 details the list of the detector systematic uncertainties considered in this analysis divided by source and category.

Variation systematics

The variation systematics modify the reconstructed observables (track momentum, PID, etc..) leading to a migration of events between different selected samples or between bins. These observables may have different mean value or resolution, in data and MC. The difference in the mean value is the bias that has to be corrected, differences in resolution are also corrected by applying further smearing in the MC simulation. When a variation systematic is estimated, the reconstructed observables are corrected and

	Category
TPC related	
Magnetic Field distortion	variation
TPC Momentum Resolution	variation
TPC Momenmtum Scaling	variation
TPC Particle IDentification	variation
TPC Cluster Efficiency	weight
TPC Track Reconstruction	weight
Charge IDentification	weight
FGD related	
Particle Time of Flight	variation
FGD Particle IDentification	variation
FGD Hybrid Track Reconstruction	weight
TPC-FGD Matching Efficiency	weight
Michel Electron Detection	weight
Layer Migration	
Background	
Out Of Fiducial Volume Events	weight
Event Pile-Up	weight
MC Modeling	
Pion Secondary Interactions	weight
FGD Mass	

Table 6.9: List of detector systematic error sources and category for the ND280 detector.

smeared and the event selection is re-run on the modified event:

$$x_{smear.} = x_{true} + (s + \alpha \cdot \delta_s)(x_{reco}^{MC} - x_{true}) \tag{6.18}$$

where $x_{smear.}$ is the smeared observable while x_{true} and x_{reco}^{MC} are the generated and reconstructed values, s is the scale factor, δ_s its uncertainty and α a random variable distributed following a *pdf* (usually flat or gaussian distributed with mean equal 0 and width of 1). The scale factor s is defined as the ratio between the data and MC resolutions. The only exception is the systematic related to the magnetic field distortions.

Weight systematics

Weight systematics do not affect the observables but only re-weight the event to increase or reduce its contribution to the selection. There are two differents types of implementation for weight systematics:

Normalization systematics associated to the total event normalization for specific sub-samples of the selection. They are applied by reweighting the event according to the variation suggested by systematic uncertainties studies. This weight is calculated as:

$$w_{event} = 1 + \alpha \cdot \delta, \tag{6.19}$$

where α is the random variable to propagate the systematic variations and δ is the systematic error associated to a category of events. An unitary weight is applied when events are not part of the systematic category.

Efficiency-like systematics correspond to specific reconstruction or detection probabilities. They use studies comparing MC predictions with data measurement for well-known control samples that fulfill specific requirements. Indeed, tracking and matching efficiencies can be easily computed using the redundancy between detectors. Control samples do not necessarily include all the features that would be present in the physics analysis, however they are designed to be sufficiently representative of the selection. In general, the predicted efficiency in a given sample is given by:

$$\epsilon_{data} = \frac{\epsilon_{data}^{CS}}{\epsilon_{MC}^{CS}} \epsilon_{MC}, \tag{6.20}$$

where ϵ_{data}^{CS} and ϵ_{MC}^{CS} are the efficiencies in the control samples for data and MC while ϵ_{MC} is the efficiency in the MC analysis sample. Since control sample efficiencies are known with a limited precision, their statistical uncertainties must also be taken into account in the propagation of the systematic error. The smeared value of the predicted efficiency in data analysis is then:

$$\epsilon_{data}^{'} = \left(r^{CS} + \alpha \cdot \delta_r^{CS}\right) \epsilon_{MC} \tag{6.21}$$

where r^{CS} is the data-MC efficiency ratio of the control sample, δ_r^{CS} its statistical error and α a random variable following a gaussian distribution with mean equal to 0 and width set to 1. Finally in order to propagate the systematic error each event is then reweighted applying an efficiency or an inefficiency weights

$$\begin{aligned} w_{eff.} &= \frac{\epsilon_{data}^{'}}{\epsilon_{MC}}, \\ w_{ineff.} &= \frac{1 - \epsilon_{data}^{'}}{1 - \epsilon_{MC}}. \end{aligned} \tag{6.22}$$

Since each source of detector systematic uncertainties was identified and studied by various T2K collaborators, an overview about the relevant systematics for the CC0π selection is detailed in Appendix C.
A overview of detector uncertainties computed for the FGD2 and the Hybrid FGD1 and different MC (NEUT or GENIE) can be found in Tab. 6.10. The largest systematics is the one due to the out of fiducial volume background, while the systematics on the muon and charge identification in the TPC and on the pion secondary interaction provide also a relevant source of uncertainty for the ratio analysis.

6.4.3 FGD Mass Uncertainty

The oxygen over carbon CC0π ratio cross-section formula (Eq. 6.6) depends on the total number of neutron targets in the FV for oxygen and carbon. The total number

	Category	**FGD2(NEUT)** [%]	**FGD2(GENIE)** [%]	**Hybrid FGD1(NEUT)** [%]
Magnetic Field	variation	0.003	0.002	0.002
Momentum resolution	variation	0.057	0.051	0.064
Momentum Scale	variation	0.007	0.022	0.015
TPC PID	variation	0.311	0.260	0.296
FGD PID	variation	0.035	0.027	0.029
TPC Cluster Eff	weight	$< 10^{-4}$	$< 10^{-4}$	$< 10^{-4}$
TPC Track Eff	weight	0.088	0.075	0.102
FGD Track Eff	weight	0.102	0.130	0.142
Time of Flight	weight	0.098	0.112	0.093
TPC-FGD Match Eff	weight	0.210	0.111	0.218
ChargeID	weight	0.258	0.224	0.302
Michel Electron	weight	0.016	0.020	0.013
OOFV	weight	0.390	0.508	0.384
Pile Up	weight	0.003	0.001	0.004
Pion Secondary Interaction	weight	0.279	0.452	0.326
Total		0.875	1.14	0.938

Table 6.10: List of detector systematic uncertainty contribution used in the FGD2 CC0π oxygen over carbon cross-section ratio analysis.

of neutron targets is extracted using the following formula:

$$T_n^{module} = \sum_i^{elements} f_i \langle N_i \rangle \frac{M_{TOT}}{\sum_i \langle M_A^i \rangle} N_A, \tag{6.23}$$

where $N_A = 6.022 \cdot 10^{23}\ mol^{-1}$ is the Avogadro number, f_i is the fraction of each element in the FV, $\langle N_i \rangle$ and $\langle M_A^i \rangle$ are the number of neutrons and the atomic weight averaged over the natural isotopic abundance and M_{TOT} is the total mass inside the FV. The total mass can be defined as:

$$M_{TOT} = \rho \times V_{FV}, \tag{6.24}$$

where V_{FV} is the volume inside the FV and $\rho = \rho_{areal} \cdot \Delta z$ is the total density averaged over the areal density of each module component in FGD2, as indicated in Tab. 6.11 [83]. The average density is defined as follow:

$$\rho = \frac{\sum_i^{module\ component} \rho_i \cdot \Delta z_i}{\sum_i^{module\ component} \Delta z_i} \tag{6.25}$$

The number of neutron targets in each module type is computed separately, taking into account all the different materials located in the FGD2 FV for the water (T_n^{water}) and scintillator ($T_n^{scint.}$) modules. The FGD2 consists of 7 XY-modules (polystyrene) and 6 carbon-based panels (polycarbonate structure) filled with water. A detailed description of the scintillator and water module elemental composition in terms of areal density (ρ_{areal}) can be found in Ref. [83] and summarized in Tab. 6.12. Hence, Eq. 6.23 can be re-written in terms of areal density as:

$$T_n^{module} = \sum_i^{module\ elements} \frac{N_i}{\sum_i M_A^i} \rho_i^{areal} \times \frac{V_{fid} N_A}{\Delta z_{TOT}}, \tag{6.26}$$

	Components	Δz (mm)	ρ (g/cm^3)
XY-module			
	G10(× 2)	0.232 × 2	1.700
	glue layer 1(× 2)	0.188 × 2	0.920
	glue layer 2	0.19	0.920
	XY-module	9.61 × 2	1.041
	air	2.0	0.00129
	fibers	0.0019	1.050
Water module			
	water + polycarbonate	25.06	1.023
	glue layer 3	0.633 ×2	0.657
	Polypropylene skin	0.804 ×2	0.900
	air	2.062	0.00129

Table 6.11: Thickness and density of each components of the scintillator and water module

mg/cm^2	C	O	H	Ti	Si	N	Total
XY-module	1849.0 ± 9.2	79.4 ± 4.8	157.9 ± 2.1	35.5 ± 5.9	21.8 ± 4.3	3.1 ± 1.2	2147 ± 14.4
mg/cm^2	C	O	H	Mg	Si		Total
Pure water	0	1967.4 ± 3.3	248.0 ± 0.4	0	0		2215.4 ± 3.7
Water module	418.7 ± 7	2063.9 ± 5	292.8 ± 1	7 ± 1	11 ± 1		2793.4 ± 13

Table 6.12: Average areal density of FGD2 for the scintillator and the water modules.

the total uncertainty on the number of neutrons will depend on the uncertainty on ρ_i^{areal} of each element in the FV and on the correlation between them. Correlations for the scintillator and water modules are detailed in Tab. 6.13. Thus, the covariance matrix is built using the correlations between the elements in the same module.
Finally the total number of targets is computed through Eq. 6.26 via 10^4 pseudo-experiments (throws) built varying the density ρ_i^{areal} of each element accordingly to the covariance matrix. The pseudo-experiment distributions for the number of neutron targets for water and scintillator are shown in Fig. 6.28. The number of neutrons targets is the mean of such distribution and the uncertainty is its standard deviation. The resulting number of targets with the relative uncertainty are:

$$\begin{aligned} T_n^{water} &= 1.384 \cdot 10^{29} \pm 0.53\%, \\ T_n^{scint.} &= 1.255 \cdot 10^{29} \pm 0.72\%. \end{aligned} \tag{6.27}$$

The mass uncertainties for the FGD2 composition are evaluated and propagated separately for the water and scintillator module, no correlation is expected between passive and active modules. The total number of targets in Eq. 6.6 accounts for oxygen and carbon contributions in each module type (water, x-layers and y-layers) can be extracted from Eq. 6.27 considering the fractional component of each nucleus (see Tab. 6.12).

XY-module	C	O	H	Ti	Si	N
C	1.000	0.210	0.587	-0.193	-0.161	0.226
O		1.000	0.115	0.830	0.068	-0.033
H			1.000	-0.121	-0.879	0.875
Ti				1.000	0.074	-0.097
Si					1.000	-0.972
N						1.000

Water module	C	O	H	Mg	Si
C	1.000	0.791	0.976	0.748	0.748
O		1.000	0.697	0.988	0.988
H			1.000	0.678	0.678
Mg				1.000	1.000
Si					1.000

Table 6.13: Correlation matrix between elemental composition for the scintillator (top table) and water (bottom table) modules.

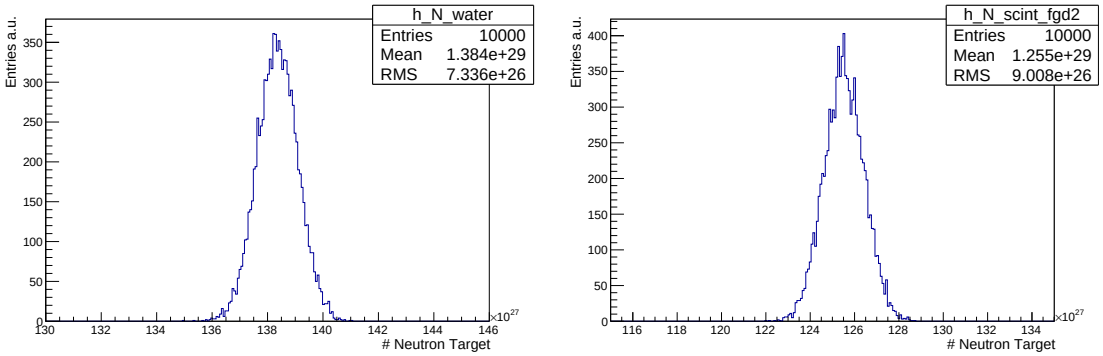

Figure 6.28: Distribution of number of neutrons inside the FDG2 fiducial volume for the water module on the left and scintillator module on the right. The uncertainty on the mass is the RMS of the distribution.

6.4.4 Systematics on vertex migration

As already discussed in the Sec. 6.3.1 the systematic due to backward tracks can be constrained using a Hybrid FGD1 control sample. In particular in Sec. 6.3.1.2, the reweighting study highlights the requirement to have a control sample in which the FGD2 passive/active structure is properly simulated in order to reproduce the same reconstruction effects.
Results in the Hybrid FGD1 (see Sec. 6.16) show that the bias on $R_{C/C}$ due to backward migrations in the data is smaller than 4%. Therefore the knowledge on the backward tracks in the MC is not wrong more than 100%, which corresponds to a total uncertainty of 4.4% in the FGD2, see Tab. 6.8.

6.4.5 Flux systematics

The flux uncertainties are parametrised in bins of true $E_\nu \in [0, 30]$ GeV/c^2 and neutrino flavors $\nu_\mu, \bar{\nu}_\mu, \nu_e, \bar{\nu}_e$. The neutrino flux prediction is affected by uncertainties on kaon and pion production multiplicity, secondary nucleons production, proton beam intensity and profile, off-axis angle, horn absolute current and angular alignment, target alignment. The hadron production uncertainties in the T2K flux are constrained with external data from a dedicated experiment at CERN (NA61/SHINE) [76, 77], as described in Sec. 2.3.1. Figure 6.29 shows the uncertainties on the ν_μ flux sample as a function of the neutrino energy at ND280. The hadron production uncertainties dominate in particular at low and high neutrino energy. Finally, the total covariance matrix in bins of neutrino energy, flavor and detector (ND280 or SK) is obtained by summing all covariance matrices evaluated for each source of uncertainty. It accounts for correlations among flux parameters and it is used to built the pseudo-experiments and propagate the flux uncertainty on the analysis. The systematic uncertainty due to the flux is expected to be canceled out in the oxygen over carbon ratio in FGD2. The provided flux prediction (see Fig. 2.12) distinguishes between different neutrino flavors, however its main contribution comes from ν_μ. Thus taking into account only ν_μ, the integrated total flux can be computed as the sum of the flux of single T2K Runs by using the following formula:

$$\Phi(E_\nu) = \sum_{Run} \sum_{j}^{E_\nu \ bins} \Phi_{j,Run} \mathrm{POT}_{Run}^{DATA} \approx 1.11 \cdot 10^{13} \ \mathrm{cm}^{-2}. \tag{6.28}$$

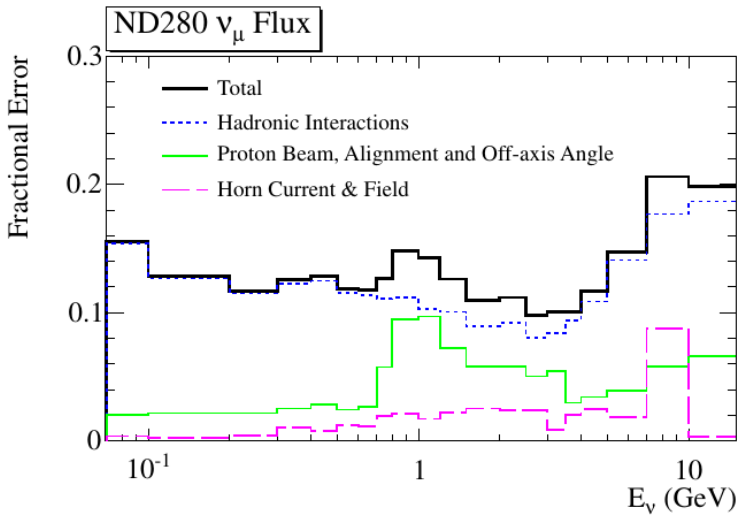

Figure 6.29: Fractional systematic uncertainty on the ν_μ flux prediction at ND280. Figure from [67].

6.4.6 Theoretical systematic

As already mentioned, efficiency, purity and migration corrections are evaluated from MC. Therefore proper uncertainties on signal and background models have to be considered, since signal or background mismodeling could introduce a bias on the extracted ratio. Indeed, dependence on the signal model generally affects the measurements through the signal efficiency, while background mismodeling may affect the purity. Moreover, the most relevant effects may come from different mismodeling between C and O, which may cause a direct bias in the measurement of the ratio.
The systematic uncertainty determination relies on a general-purpose reweighting framework called *T2KReWeight*. It is a package, developed by the T2K collaboration, which includes a set of underlying parameters and can be used to predict the effect of changing one or more of them in the MC model. This means that one nominal MC (i.e. NEUT) can be used to give the predictions for any parameter set, without having to generate MC with several different parameter sets. Thus, *T2KReWeight* generates weights, event by event, by tweaking a given set of parameters to some values different from the nominal in the MC. Correlations between parameters are also taken into account with a covariance matrix across all parameters.
The neutrino interaction model parameters considered for this analysis, can be split into three main categories:

CCQE model: they are the axial mass for quasi-elastic interactions M_A^{QE} which is assumed to be the same for carbon and oxygen, the Fermi momentum p_F, the binding energy E_B and the normalization for 2p2h/MEC processes which are parametrized separately for carbon and oxygen.

Background model: three parameters for single pion production, the axial mass M_A^{RES}, the normalization of the axial form factor $C_5^A(Q^2 = 0)$ and the isospin non-resonant background $I_{1/2}$ based on the Rein-Sehgal predictions (see Sec. 5.4.1). The uncertainty on the multi-pions productions due to DIS are parametrized by *CC Oth shape*. Other parameters account for the neutral current and coherent background. The latter are parametrized separately for carbon and oxygen. The parameter ν_e/ν_μ *CC* takes into account effects on the interactions due to different neutrinos flavor.

Final State Interactions: as explained in Sec. 5.2.5 they affect the intranuclear cascade model used in NEUT. According to the particle momentum threshold, these parameters are split into low ($p_\mu \leq 500$ MeV) and high ($p_\mu > 500$ MeV) energy regions. Six parameters are used: inelastic rescattering probability at low ($\mathrm{FSI}^{\mathrm{INEL.}}_{\mathrm{low}}$) and high ($\mathrm{FSI}^{\mathrm{INEL.}}_{\mathrm{high}}$) energy, charge exchange at low ($\mathrm{FSI}^{\mathrm{EXC.}}_{\mathrm{low}}$) and high ($\mathrm{FSI}^{\mathrm{EXC.}}_{\mathrm{high}}$) energy, pion absorption ($\mathrm{FSI}^{\mathrm{ABS.}}_{\pi}$) and pion production ($\mathrm{FSI}^{\mathrm{PROD.}}_{\pi}$) within the nuclear media.

Table 6.14 presents a list of all the parameters and their uncertainties.

Parameter	Type	Nominal value	Error
M_A^{QE}	CCQE	1.2 GeV/c^2	0.07
MEC ^{12}C	CCQE	100%	100%
p_F ^{12}C	CCQE	217 MeV/c	13
E_B ^{12}C	CCQE	25 Mev	9
MEC ^{16}O	CCQE	100%	100%
p_F ^{16}O	CCQE	225 MeV/c	13
E_B ^{16}O	CCQE	27 Mev	9
M_A^{RES}	Background	0.95 GeV/c^2	0.15
$C_5^A(0)$	Background	1.01	0.12
$I = 1/2$	Background	1.30	0.20
$\nu_e/\nu_\mu CC$	Background	1.0	0.03
CC Oth shape	Background	0.0	0.40
CC Coherent ^{12}C	Background	1.0	1.0
CC Coherent ^{16}O	Background	1.0	1.0
NC Other	Background	1.0	0.30
NC Coherent	Background	1.0	0.30
$\mathrm{FSI}_{\mathrm{low}}^{\mathrm{INEL.}}$	FSI	0.0	0.41
$\mathrm{FSI}_{\mathrm{high}}^{\mathrm{INEL.}}$	FSI	0.0	0.34
$\mathrm{FSI}_{\mathrm{low}}^{\mathrm{EXC.}}$	FSI	0.0	0.57
$\mathrm{FSI}_{\mathrm{high}}^{\mathrm{EXC.}}$	FSI	0.0	0.28
$\mathrm{FSI}_{\pi}^{\mathrm{PROD.}}$	FSI	0.0	0.50
$\mathrm{FSI}_{\pi}^{\mathrm{ABS.}}$	FSI	0.0	0.41

Table 6.14: List of the theoretical parameters with their associated uncertainty.

In order to evaluate the theoretical uncertainties for each parameter a set of 14 variations of the nominal MC is produced by varying the parameter within its validity range. For each tweaked value of each parameter the ratio cross-section is then extracted so as to get a relation between the ratio and the parameter itself, the so called *response function*. Hence, each response function shows how $R_{O/C}$ changes as a function of the parameter. Response functions for the integrated value of the CC0π oxygen over carbon cross-section ratio are shown in Figures 6.31, 6.32 and 6.33 for each group of parameters. Each point gives a value of $R_{O/C}$ associated whit each one of the 14 MC datasets, around the ratio nominal value (8^{th} point). Fully correlated parameters between ^{12}C and ^{16}O gives very small uncertainties on the ratio (i.e. flat response functions).
For the determination of the systematic uncertainties on the ratio measurement a set of 10^5 pseudo-experiments has been performed. In each pseudo-experiment, all the parameters are simultaneously varied taking into account the correlations among them. Figure 6.30 shows the covariances between the parameters. The new set of parameters is obtained via the Cholesky decomposition of the covariance matrix which provides the proper correlations. The CC0π oxygen over carbon cross-section ratio for a fixed set of

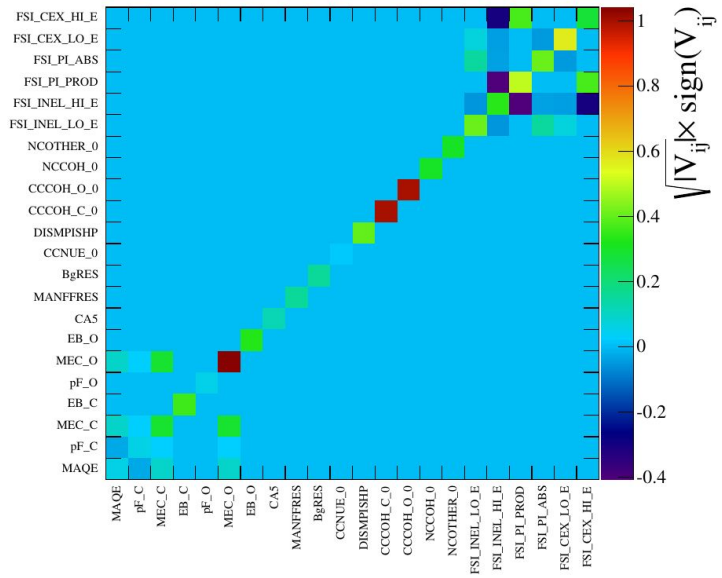

Figure 6.30: Covariance matrix of the parameters describing the theoretical systematic uncertainties. The values are shown as the sign of the element times the square root of the absolute value of the element.

parameters of each pseudo-experiment is given by the formula:

$$R_{O/C} = R_{nom.} \cdot \prod_{i}^{N_{par.}} \frac{R_i}{R_{nom}}. \tag{6.29}$$

Here R_{nom} is the cross-section ratio of the nominal set of parameters while R_i is the ratio associated to each parameter of the pseudo-experiment, evaluated with the corresponding response function. Finally, the total uncertainty in each bin and on the integrated value is evaluated by using the standard deviation of the ratio distribution of Eq. 6.29. For the integrated value it corresponds to 1.5% as shown in Fig. 6.34. Table 6.15 summarizes the ratio uncertainties due to each parameter. The total uncertainty is dominated by the theoretical parameters associated to the signal where ^{12}C and ^{16}O are considered separately. A key role is played by the knowledge of the MEC contributions in the CC0π interactions and their correlation.

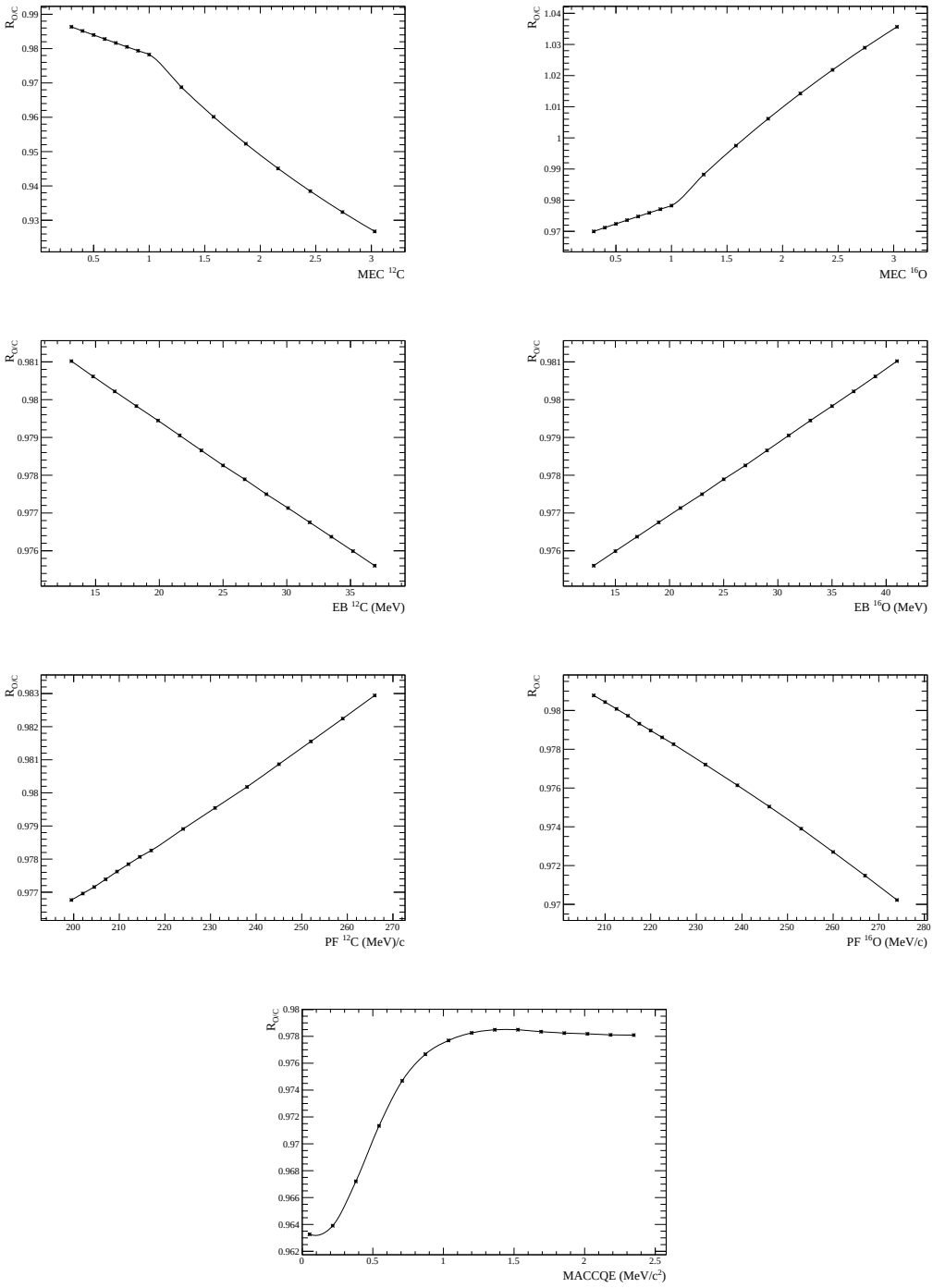

Figure 6.31: Integrated CC0π oxygen over carbon cross-section ratio response functions for CCQE signal parameters.

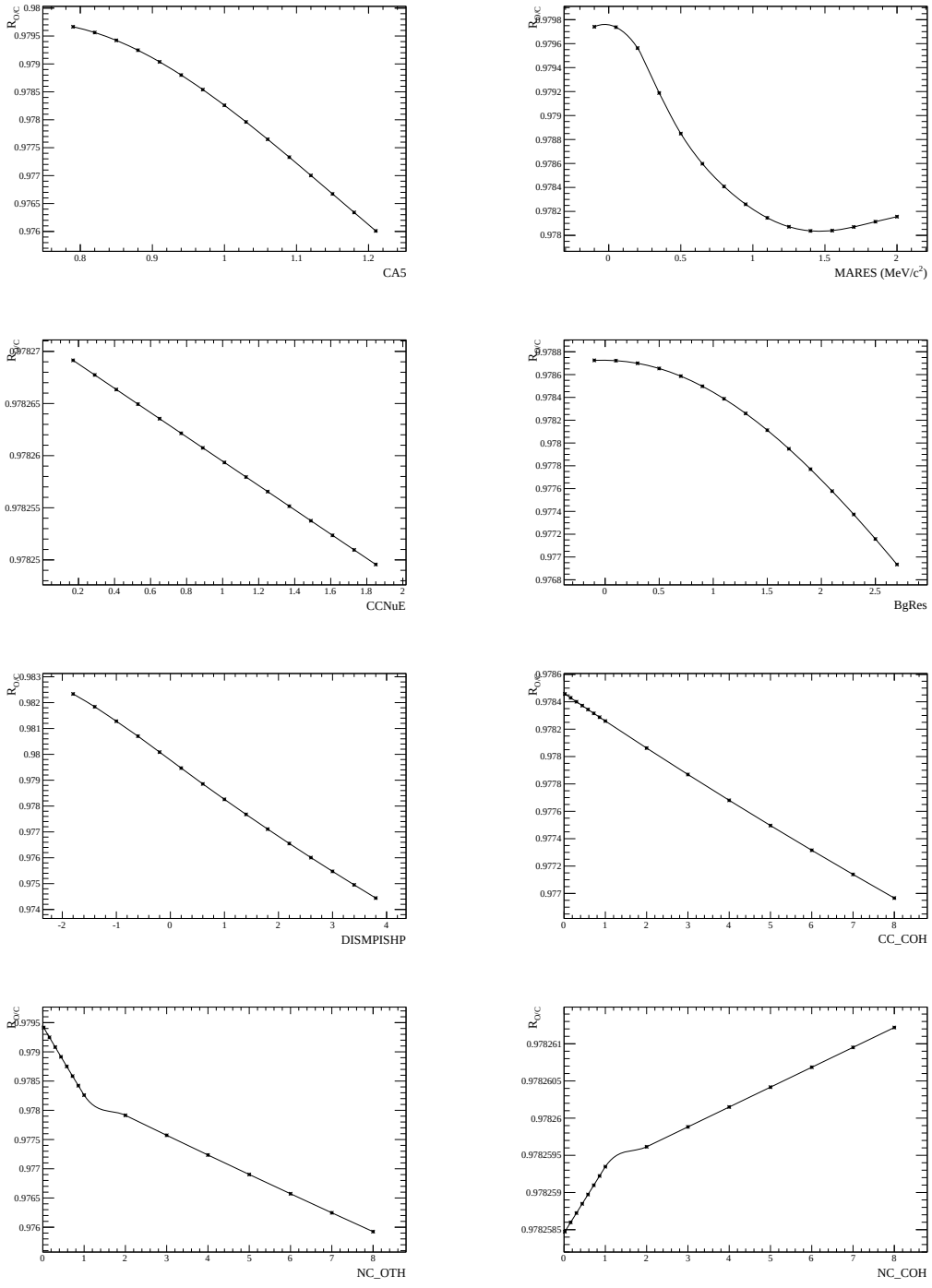

Figure 6.32: Integrated CC0π oxygen over carbon cross-section ratio response functions for the background parameters.

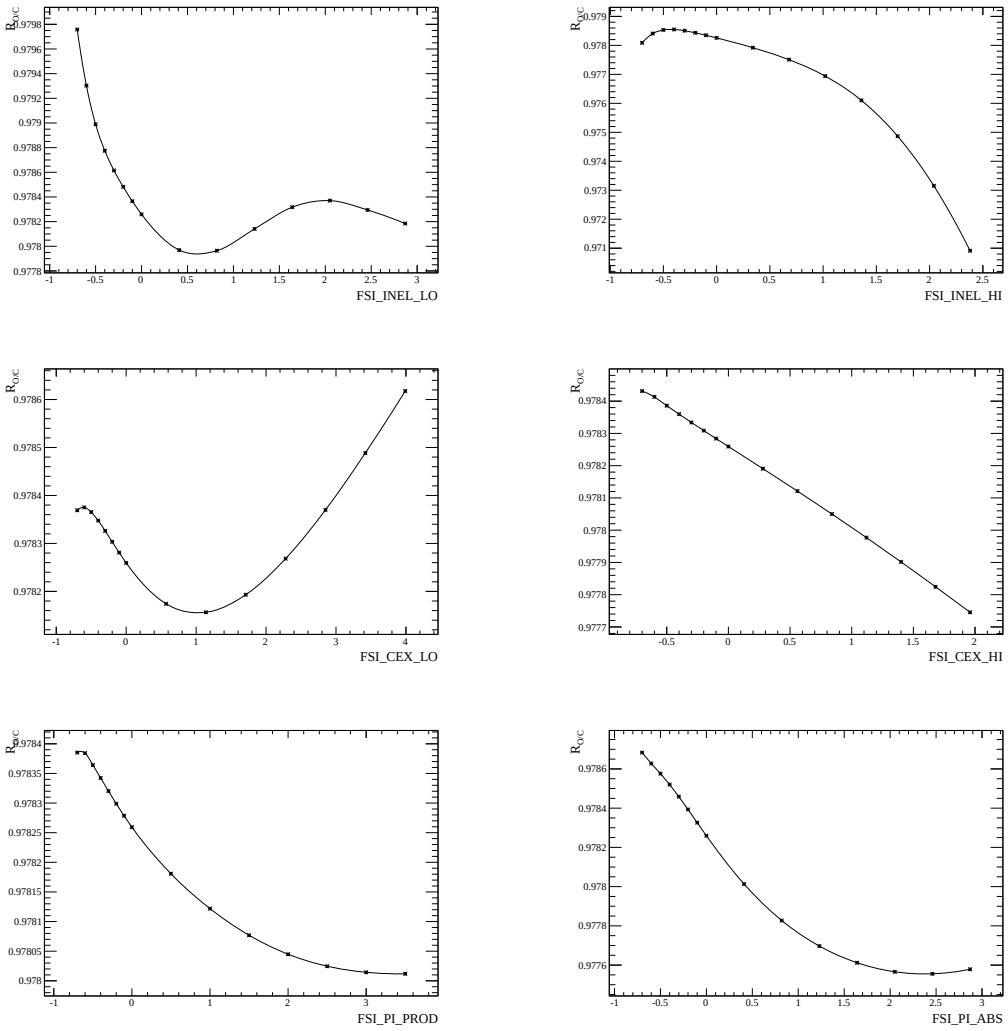

Figure 6.33: Integrated CC0π oxygen over carbon cross-section ratio response functions for the FSI parameters.

Parameter	**Type**	$\sigma_{R_{O/C}}$**(NEUT)** [%]
$MEC\ ^{12}C$	CCQE	1.877
$p_F\ ^{12}C$	CCQE	0.101
$E_B\ ^{12}C$	CCQE	0.165
$MEC\ ^{16}O$	CCQE	2.000
$p_F\ ^{16}O$	CCQE	0.185
$E_B\ ^{16}O$	CCQE	0.141
M_A^{QE}	CCQE	0.018
$C_5^A(0)$	Background	0.112
M_A^{RES}	Background	0.014
$\nu_e/\nu_\mu CC$	Background	$< 10^{-4}$
$I = 1/2$	Background	0.014
CC Oth shp	Background	0.062
CC Coherent	Background	0.016
NC Other	Background	0.024
NC Coherent	Background	$< 10^{-4}$
$\text{FSI}^{\text{INEL.}}_{\text{low}}$	FSI	0.060
$\text{FSI}^{\text{INEL.}}_{\text{high}}$	FSI	0.031
$\text{FSI}^{\text{EXC.}}_{\text{low}}$	FSI	0.007
$\text{FSI}^{\text{EXC.}}_{\text{high}}$	FSI	0.007
$\text{FSI}^{\text{PROD.}}_{\pi}$	FSI	0.008
$\text{FSI}^{\text{ABS.}}_{\pi}$	FSI	0.025
Total	CCQE + Background + FSI	1.463

Table 6.15: List of the sources of the model uncertainty used in the FGD2 CC0π oxygen over carbon cross-section ratio analysis.

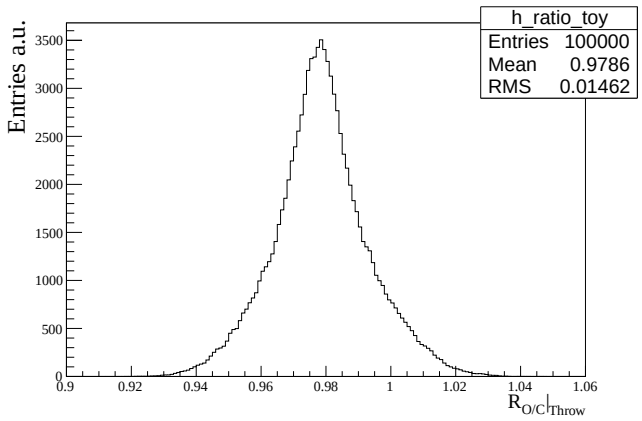

Figure 6.34: Toys distribution of the integrated CC0π oxygen over carbon cross-section ratio for the theoretical uncertainty evaluation. The total uncertainty is the RMS of the distribution.

6.4.7 Summary of the uncertainties

Figure 6.35 shows a summary of the total uncertainty on the cross-section ratio in all the analysis bins for all the systematic sources. The uncertainties have been evaluated calculating the cross-section ratio for each pseudo-experiment as the variance of the ratio distribution obtained by varying each source of uncertainty separately: statistics, detector, FGD2 mass and theory. The detector, as well as the theoretical uncertainties, are grouped all together in these plots although there are several sources of detector systematics, correlated among each others as described in Sec. 6.4.2. Nevertheless, they can be independently propagated to the cross-section result, obtaining a fractional error for each detector source, as listed in Tab.6.10. In the same way also the theoretical systematics can be propagate separately, the single contribution is shown in Tab.6.15. The systematic uncertainty due to the migration of events between water and scintillator modules, has been constrained using a control sample in data. The total uncertainty (statistical + systematic) on the integrated value is of the order of 6.8%, dominated by statistical and migration uncertainties.

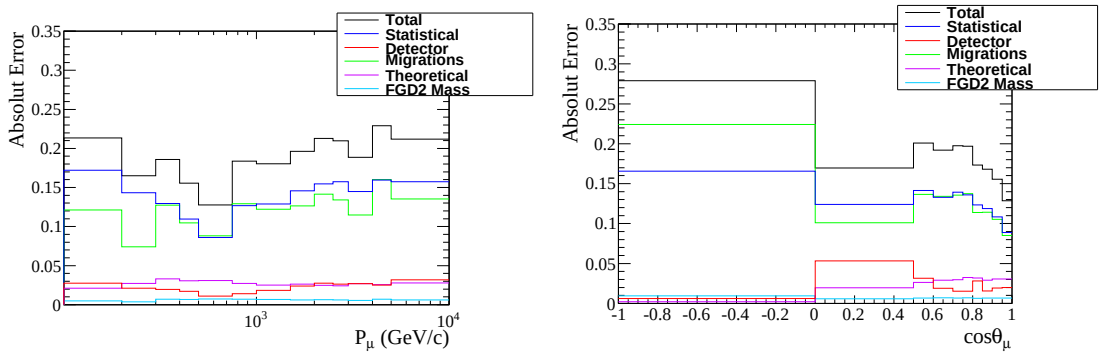

Figure 6.35: All systematic uncertainties in bins of true muon momentum (left) and true angle (right). The blue line shows the statistical uncertainty, in red the detector systematics, green lines for backward tracks uncertainty, in magenta the full set of theoretical systematics and in orange the uncertainty due to the number of targets normalization. The black line is the total error on the ratio obtained summing in quadrature all the sources of uncertainties.

Chapter 7

Cross-section ratio measurement

This Chapter describes the measurement of the ν_μ CC0π oxygen over carbon cross-section ratio using the ND280 detector. In Sec. 7.1 the results of the cross-section analysis are presented using a series of alternative models to check if the strategy is working properly, Sec. 7.2 is focused on the single differential cross-section ratio extraction in terms of the muon momentum or muon direction using the T2K RunII-IV data. Finally Sec. 7.3 presents the results in terms of reconstructed neutrino energy $E_\nu^{CC0\pi}(p_\mu, \cos\theta_\mu)$.

7.1 Fake datasets studies

The ratio analysis was performed keeping blind the data in the signal selection, this means that the method for the measurement was built without looking at the data. Blind analyses are an optimal way to reduce the risk of biasing the final results. Therefore various MC-based pseudo-experiments need to be performed to test the solidity of the analysis. Those pseudo-experiments, commonly called "*fake datasets*", have been built by reweighting the official T2K generator NEUT or exploiting a different generator, like GENIE, as alternative. Thus, different fake datasets can be used to test various aspects of the cross-section extraction, the consistency of the uncertainties and that the eventual bias is small. For all of these tests, the nominal NEUT MC sample is used to generate the prior (transfer matrix, purity, etc..), however the fake data sample is changed each time. The used pseudo-experiments are:

Nominal NEUT: is the distribution of events selected by the signal selection and used to train the procedure. It generates the prior: the transfer matrix, purity, efficiency and migration fractions. Therefore by using it as a fake dataset, it is possible to test the internal consistency and look for pathological problems of the method.

Oxygen reweight: this fake dataset is based on nominal NEUT where the oxygen cross-section is enhanced or reduced. It is used to test the validity of the ratio

formula (Eq. 6.6) in a wide range.

NEUT RFG+RPA: the nominal NEUT is tuned, via event-by-event reweighting to match the RFG + RPA models for CCQE interactions.

GENIE: the event selection is run over the GENIE sample after applying the detector systematic uncertainties. It is used to check if, by training using a model (NEUT), it is possible to recover a different model (GENIE).

2p2h oxygen: it is the nominal NEUT where the 2p2h contribution to oxygen interactions is doubled.

All the fake datasets are scaled to the total data RunII-IV statistics of $5.80 \cdot 10^{20}$ POTs.

7.1.1 Nominal NEUT

In this section the results using the full RunII-IV statistics of the NEUT MC are shown. Predictions are scaled to the data RunII-IV POTs. The CC0π Oxygen/Carbon cross-section ratio ($R_{O/C}^{CC0\pi}$) is extracted using NEUT to compute the prior, the transfer matrix and all the other MC related variables in Eq. 6.6: the CC0π purities in the x(y)-layers $f_{x(y)}^{CC0\pi}$, the migration fractions $f_{x(y,w)}^{x,y}$ of events generated in a module and detected in the x or y-layers and the efficiencies $\epsilon_{water,x-layer,y-layer}^{CC0\pi}$. The differential results as a function of muon kinematic variables with the total uncertainties (statistical + detector + mass + backward + theoretical) are shown in Fig. 7.1.
The obtained total integrated cross-section ratio is:

$$R_{O/C}^{NEUT\ RunII-IV} = 0.978 \pm 0.048(stat.) \pm 0.048(syst.), \tag{7.1}$$

while the prediction from the NEUT truth is $R_{O/C}^{NEUT\ Truth} = 0.991$. The result highlights a bias of the method which underestimates the MC prediction by -1.3%, it comes from all the assumptions made on the purity and background in the determination of the true CC0π sample and in the true vertex of the interaction. However, it is reasonably small compared to the statistical and systematic uncertainties.

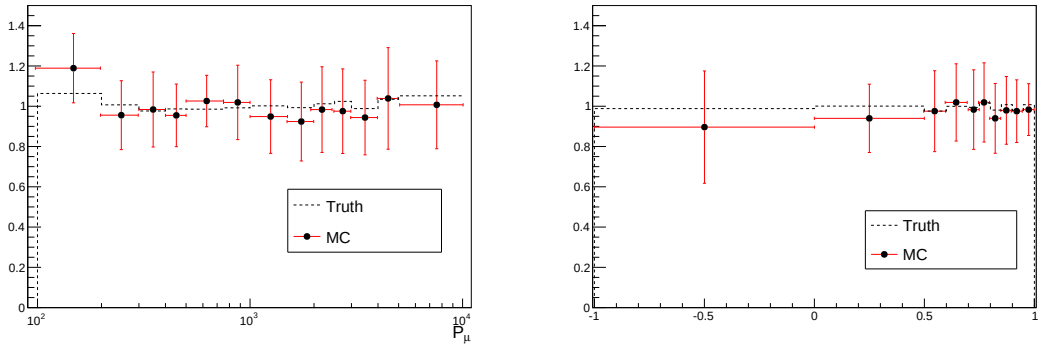

Figure 7.1: CC0π Oxygen/Carbon cross-section ratio versus the muon kinematics: momentum (left) and direction (right) obtained using NEUT.

7.1.2 Oxygen reweight

In order to validate the oxygen over carbon formula in a wide range of the value of the ratio, a reweighting study is performed. The oxygen cross-section is then reweighted in the range $[0, 2] \cdot \sigma_O$ according to different hypotheses. Since the ratio is a linear function of σ_O, a straight line with unitary slope is expected. Figure 7.2 shows the results of this study superimposed with the ideal case (red dashed line). The linearity is satisfied, the formula is sensitive to the cross-section ratio whatever is its value, however it does not perfectly match the ideal case. Therefore this bias needs to be further investigated. Table 7.1 shows the reweighting study results for different oxygen cross-section hypotheses as well as the bias due to the method. However, the bias is of the order of few percents around the nominal NEUT prediction.

Reweight σ_O	True $R_{O/C}$	Meas. $R_{O/C}$	Bias
-100%	0.	0.008 $\pm$ 0.022	0.008 $\pm$ 0.022
-80%	0.194	0.214 $\pm$ 0.028	0.020 $\pm$ 0.028
-50%	0.493	0.502 $\pm$ 0.039	0.009 $\pm$ 0.039
-20%	0.792	0.788 $\pm$ 0.052	-0.004 $\pm$ 0.052
-10%	0.891	0.883 $\pm$ 0.057	-0.008 $\pm$ 0.057
-5%	0.941	0.930 $\pm$ 0.059	-0.010 $\pm$ 0.059
Nominal	0.991	0.978 $\pm$ 0.062	-0.013 $\pm$ 0.062
$+5\%$	1.040	1.025 $\pm$ 0.064	-0.015 $\pm$ 0.064
$+10\%$	1.090	1.072 $\pm$ 0.066	-0.018 $\pm$ 0.066
$+20\%$	1.190	1.167 $\pm$ 0.071	-0.023 $\pm$ 0.071
$+50\%$	1.488	1.449 $\pm$ 0.086	-0.039 $\pm$ 0.086
$+80\%$	1.787	1.730 $\pm$ 0.101	-0.057 $\pm$ 0.101
$+100\%$	1.986	1.917 $\pm$ 0.111	-0.069 $\pm$ 0.111

Table 7.1: True and measured ratio of the oxygen fake datasets and their bias.

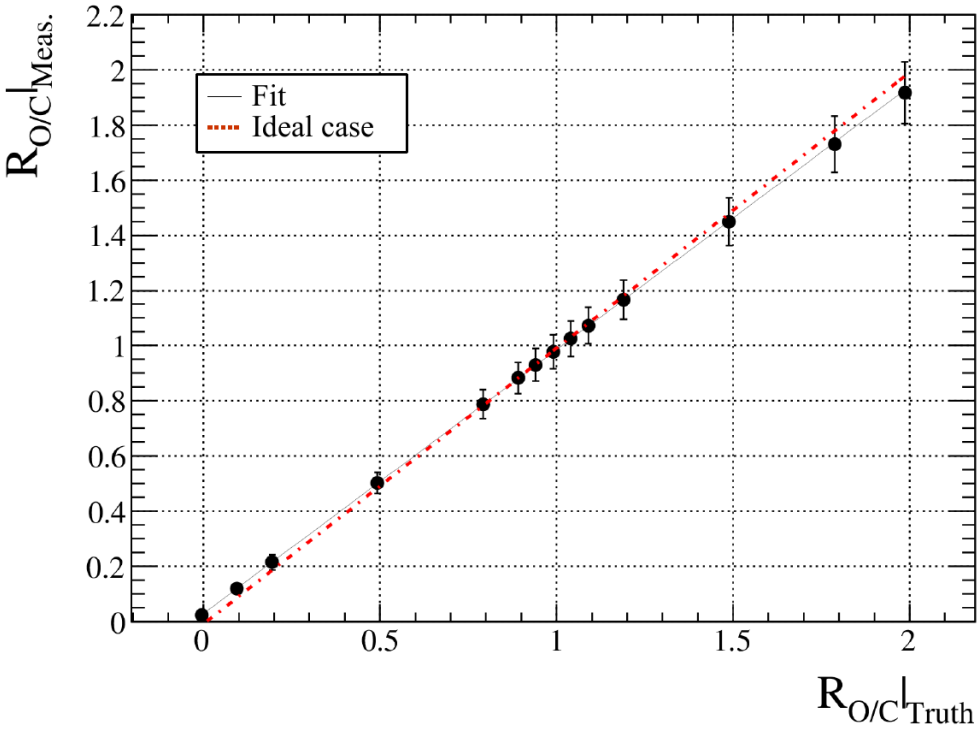

Figure 7.2: Integrated value of measured cross-section ratio as a function of their truth value. The red dashed line represents the ideal linear case.

7.1.3 NEUT RFG + RPA

As described in Sec. 5.4.1, the T2K official generator NEUT comes with two alternative models depending on the nuclear implementation used to describe CCQE interactions on carbon and oxygen. Since the NEUT version 5.3.2 relies on the spectral function (SF) model, this analysis has been first entirely performed with the NEUT SF, then the alternative Relativistic Fermi Gas (RFG) with the inclusion of RPA correction is used as additional cross-check of the method robustness. Although it is currently well known that both SF and RFG+RPA do not reproduce the data, a choice had to be made about the model used to get the prior of the cross-section ratio. The SF model is more accurate than RFG in the representation of nucleon momenta distributions within a nucleus, however no RPA correction is available for SF.
A fit to the external CCQE measurement by MINERνA and MiniBooNE collaborations was performed using different nuclear models implemented in NEUT [156]. The fit shows that none of these models is able to completely describe all of the data which slightly prefer the RFG + RPA implementation. Therefore in an analysis aimed to highlight the difference between carbon and oxygen, a comparison with this alternative nuclear model for the CCQE interactions is needed. The nominal NEUT SF is tuned via T2KReWeight in order to match the results for a MC based on RFG + RPA to test

on eventual bias due to the assumed CCQE model. The resulting cross-section ratio for the NEUT RFG + RPA fake data studies is:

$$R_{O/C}^{RFG+RPA} = 0.984 \pm 0.044(\sim 4.4\%\ stat.) \pm 0.048(\sim 4.8\%\ syst.), \tag{7.2}$$

while the prediction of the reweighted NEUT is $R_{O/C}^{True\ NEUT\ RFG+RPA} = 0.996$.

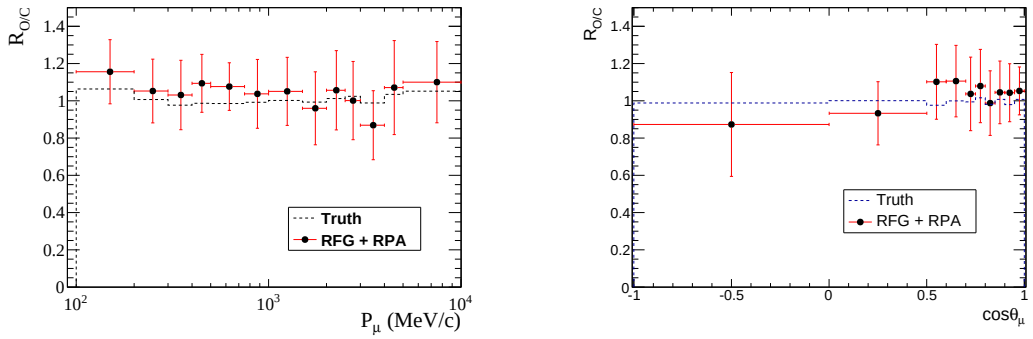

Figure 7.3: NEUT RFG + RPA tuning fake dataset results in the true muon kinematic. Dashed line is the NEUT RFG + RPA truth prediction.

7.1.4 GENIE

In order to check the potential bias given by two different generators, a fake dataset is realized with a combination of NEUT and GENIE. In this case the priors are estimated using NEUT while GENIE is used as fake data. Figure 7.4 shows the single differential results in the muon kinematics, while the total cross-section is:

$$R_{O/C}^{GENIE\ with\ NEUT} = 1.021 \pm 0.046(\sim 4.5\%\ stat.) \pm 0.049(\sim 4.8\%\ syst.). \tag{7.3}$$

GENIE prediction from truth gives a value for the ratio: $R_{O/C}^{True\ GENIE} = 0.996$. The unfolded cross-sectio ratio is compatible with the prediction from the GENIE truth in most of the bins. Furthermore, it can be noticed that even if the differences between NEUT and GENIE are not negligible, they become small in the cross-section ratio.

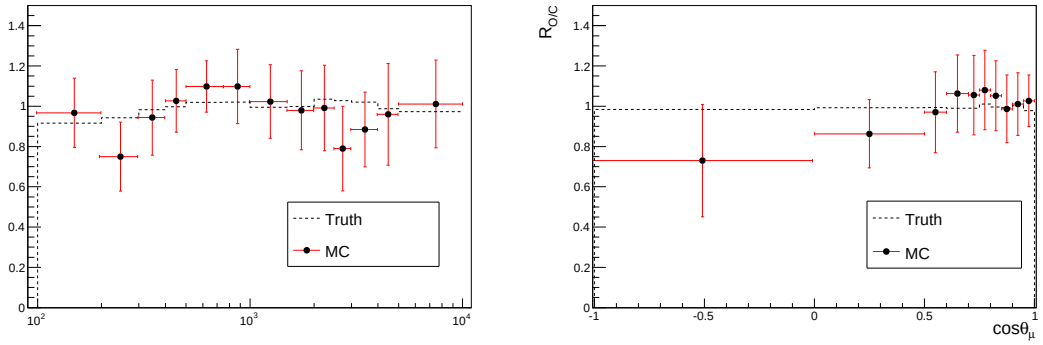

Figure 7.4: Predicted cross-section ratio using the nominal GENIE as data and the nominal NEUT for the training. The dashed line is the GENIE truth.

7.1.5 2p2h Oxygen

Another test of the ability of the method to predict ratio cross-section is shown in Fig. 7.5. The test uses the nominal NEUT as reference to extract the MC related quantities while the fake dataset is built using NEUT where the 2p2h events on oxygen are reweighted by a factor 2 and the pure CCQE interactions, the 2h2p on carbon and all background remain unchanged. This choice has been made because in some kinematic regions the Martini [137] contribution to the neutrino cross-section is twice with respect the Nieves [133] model. The total cross-section obtained is:

$$R_{O/C}^{2p2h} = 1.062 \pm 0.052(\sim 4.9\%\ stat.) \pm 0.048(\sim 4.8\%\ syst.) \tag{7.4}$$

and the prediction from the truth is: $R_{O/C}^{True\ 2p2h} = 1.115$.

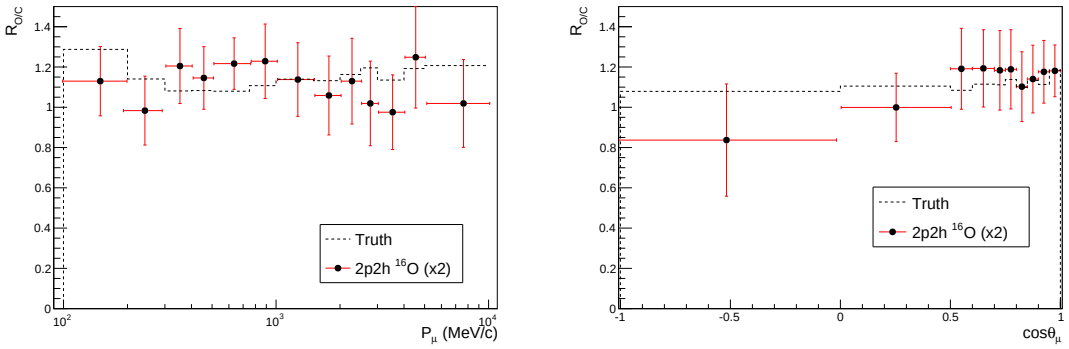

Figure 7.5: Increased 2p2h interactions in the water fake dataset's results in the muon kinematic variables: momentum (left), direction (right).

7.2 Muon kinematics results

This section presents the results obtained using the real data sample RunII-IV (see Tab. 6.1) to evaluate the ratio cross-section between oxygen and carbon. Results are presented as a function of the muon momentum and direction. The total cross-section ratio in FGD2 has been obtained by integrating the variables distribution in one single bin and listed in Tab. 7.2. The NEUT generator results and prediction are also listed for comparison. The difference between the integrated results in momentum and angle is due to the differences in the efficiency and acceptance and to the slightly different phase space: in the muon angle all the phase space is considered while a cut rejecting very low (< 100 MeV/c) and very high (> 10000 MeV/c) momentum muons is applied in the momentum analysis. Distributions of the numbers of selected muon candidates as a function of momentum and direction are also shown in Fig. 7.6 where data (black dots) are overimposed on NEUT MC. The binned results are shown in Fig. 7.7, where the real data (black dots) are compared with the NEUT prediction (black dashed line).

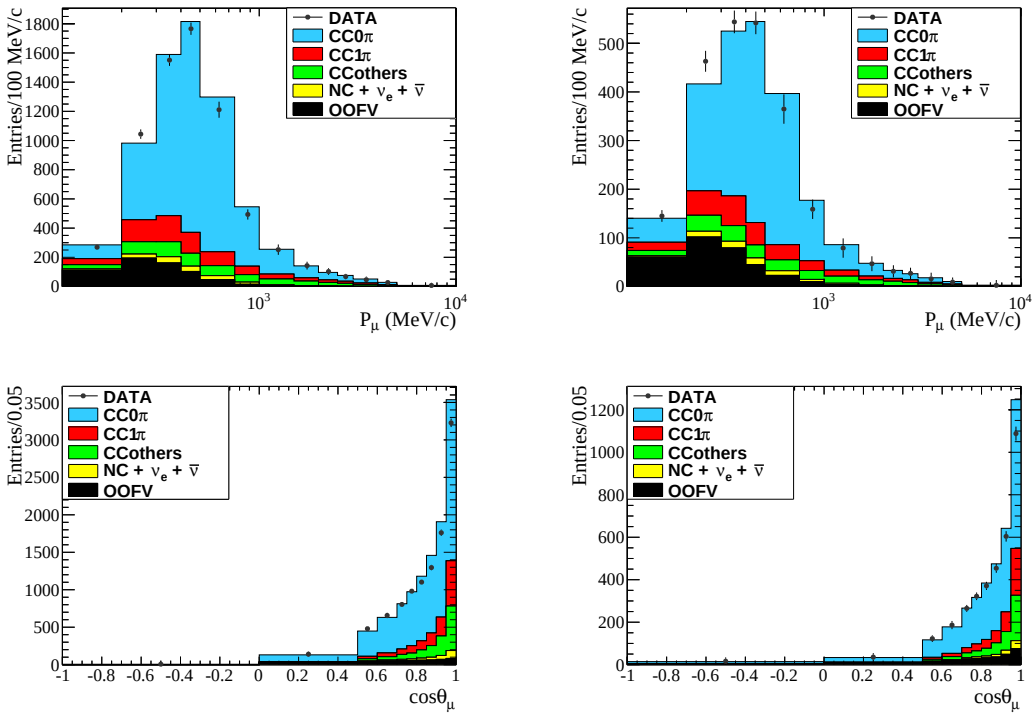

Figure 7.6: CC0π muon candidate in FDG2 as a function of muon reconstructed momentum (top) and angle (bottom) normalized to data POT and divided into the different reaction topologies for the x-layer (left) and y-layer (right). Black dots represent the data before applying the Reco-True transfer matrix.

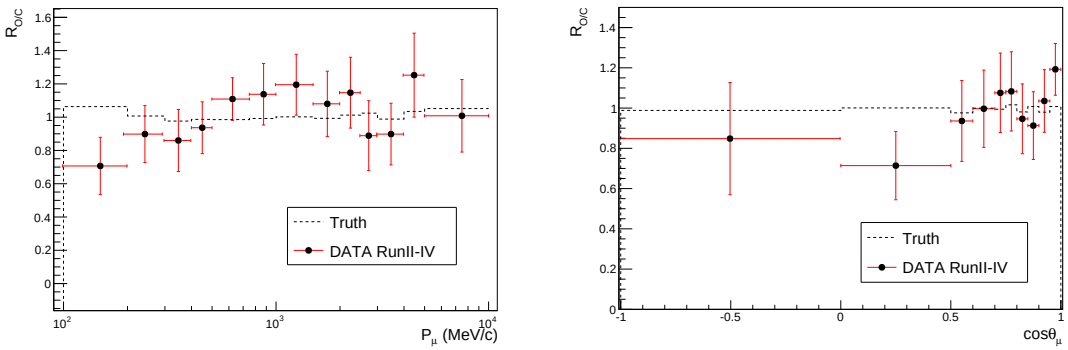

Figure 7.7: Differential ratio cross section obtained as a function of muon momentum (left) and direction (right).

Prediction $R_{O/C}^{NEUT} = 0.991$	P_μ	**cos**θ_μ
T2K RunII-IV	0.930 ± 0.048 (stat.) ± 0.045 (syst.)	0.927 ± 0.048 (stat.) ± 0.045 (syst.)
NEUT	0.978 ± 0.048 (stat.) ± 0.048 (syst.)	0.976 ± 0.048 (stat.) ± 0.048 (syst.)

Table 7.2: Data RunII-IV and MC integrated cross section ratio results with total uncertainty in FGD2.

7.3 Cross-section ratio as a function of the reconstructed neutrino energy

In the previous section the ratio is extracted in bins of muon momentum p_μ and direction $\cos\theta_\mu$, however the reconstructed energy of the incoming neutrino E_ν has a more significant meaning for the oscillation analyses, since at SK they are performed in bins of this same quantity. Unfortunately, the true neutrino energy cannot be reconstructed on a event by event basis, but it can be inferred by using angles and momenta of all the particles produced in the neutrino-nucleon interaction. However those observables are smeared by detector resolution and they can only be measured after they get possibly modified by the FSI. Nevertheless, in a CCQE interaction the only produced particle is a lepton, hence the energy of the incident neutrino can be reconstructed using the 2-body formula in Eq. 5.3. Therefore, for a ν_μ quasi-elastic interaction the neutrino energy can be easily computed as:

$$E_\nu^{CCQE}(p_\mu, \cos\theta_\mu) = \frac{(m_n - E_B)\,E_\mu + \left(2m_n E_B - E_B^2 - m_\mu^2 + m_p^2 - m_n^2\right)}{2\,(m_n - E_B - E_\mu + p_\mu cos\theta_\mu)}. \tag{7.5}$$

ND280 selects CC0π rather than pure CCQE interactions, however in the CC0π selection the CCQE process are dominant, therefore it is possible to extract the cross-section

ratio in terms of reconstructed neutrino energy as well. Equation 7.5 gives a good approximation of the incident neutrino energy of the selected events $E_\nu^{CC0\pi}(p_\mu, \cos\theta_\mu) \simeq E_\nu^{CCQE}(p_\mu, \cos\theta_\mu)$ if the final state of the muon is well reconstructed. This quantity is directly related to the flux shape and more sensitive to any shifts in the MC simulation. In addition oscillation analyses at the far detector are performed in reconstructed neutrino energy, indeed the mass squared difference Δm^2_{23} is sensitive to the position of the maximum of such distribution. While the far detector has a 4π acceptance, the ND280 angular acceptance is limited to the forward region. As shown in Fig. 6.12 the efficiency for forward muons is very good while it is low for high angle and low momentum tracks, for which the reconstruction is also less accurate. Therefore the measurement in terms of reconstructed neutrino energy is performed with a phase space restriction where the reconstruction is reliable and the efficiency is high. Moreover a restricted phase space can be used to compare the measurement with other experiments.
For the $E_\nu^{CC0\pi}(p_\mu, \cos\theta_\mu)$ ratio determination the following phase space cuts are applied:

$$\begin{aligned} \cos\theta_\mu &> 0.5 \\ p_\mu &> 250 \text{ MeV/c}. \end{aligned} \tag{7.6}$$

This allows to have a quite flat distribution of the efficiency as a function of the reconstructed neutrino energy, as shown in Fig. 7.8. The analysis uses the same binning as for the muon momentum case (see Tab. 6.2), in the figure the lowest bins are not displayed since they are empty due to the phase space restriction. After the cut the average efficiencies are: $\epsilon_{water} = 0.811 \pm 0.009$, $\epsilon_{x-layer} = 0.802 \pm 0.009$ and $\epsilon_{y-layer} = 0.754 \pm 0.008$.

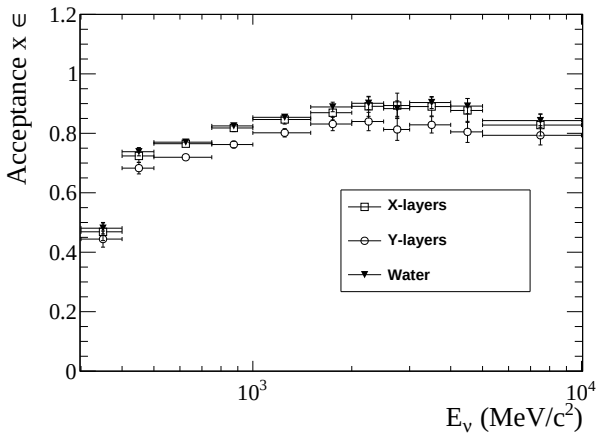

Figure 7.8: Reconstruction efficiencies for the water modules and the scintillator layers as a function of the reconstructed neutrino energy.

Figure 7.9 shows the data-MC comparison for the event distribution of the ν_μ CC0π

selection as a function of the reconstructed neutrino energy after the phase space restriction. The neutrino energy is evaluated with Eq. 7.5 in which $\epsilon_B = 27$ MeV/c^2 is set to the oxygen binding energy. For both x and y-layers the MC prediction agrees quite well with the data. Table 7.3 details the mean value of the distribution as well as the data-MC and the x-y layers comparisons, while the x-layer distribution agree quite well with the prediction, the y-layer mean energy is shifted by ~ 9 MeV/c^2 below with respect to the MC. Given the much lower statistics in that layers this is compatible with statistical fluctuation. Finally, assuming a peak energy of 650 MeV/c^2, the mean reconstructed energy is reproduced by the MC at the level of $(7.14 \pm 5.96)/650$.

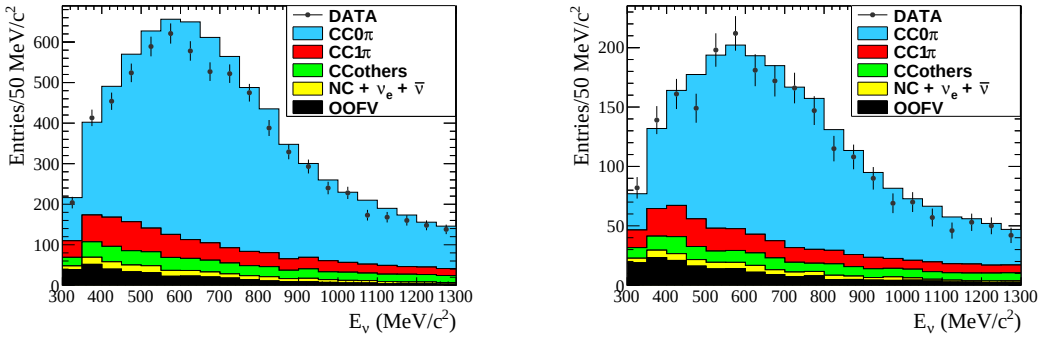

Figure 7.9: Data-Monte Carlo comparison of the reconstructed energy distribution for both the x-layer (left) and the y-layer (right). Black circles (with statistical error bars) represent the data points.

	μ_{DATA}	μ_{MC}	$\mu_{DATA} - \mu_{MC}$
x-layer	705.53 ± 2.85	707.34 ± 0.70	-1.81 ± 2.93
y-layer	697.25 ± 5.04	706.20 ± 1.26	-8.95 ± 5.19
$\mu_{x-layer} - \mu_{y-layer}\vert_{DATA}$	8.28 ± 5.79		
$\mu_{x-layer} - \mu_{y-layer}\vert_{MC}$	1.14 ± 1.44		
DATA - MC	7.14 ± 5.96		

Table 7.3: Mean reconstructed energy of the incident neutrino for CC0π interactions in the x and y-layers of the FGD2. All the energy are in units of MeV/c^2.

The transfer matrices, the selection purity and the migration fractions are summarized in Appendix D. The ratio results using real data and the total uncertainties are shown in Fig. 7.10. The data results are compared with the NEUT prediction. The integrated cross-section ratio is:

$$R_{O/C} = 0.928 \pm 0.049(stat.) \pm 0.044(syst.) \tag{7.7}$$

and the prediction from the truth is: $R_{O/C}^{TrueNEUT} = 0.996$.

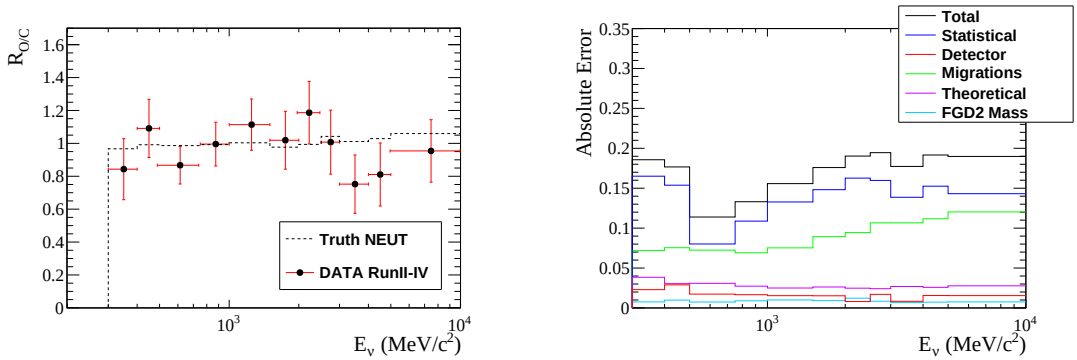

Figure 7.10: **Left:** CC0π cross-section ratio as a function of the reconstructed energy of the incoming neutrino. **Right:** total error sorted by source of uncertainty.

7.4 Results discussion

The ν_μ CC0π selection in the FGD2 subdetector has been used to evaluate the CC0π interaction cross-section ratio between oxygen and carbon. The total cross-section uncertainty is dominated by the data statistical uncertainty, however as more neutrino data will be available in the future (RunVIII see Fig. 2.2) this error will be reduced. The detector and theoretical systematic uncertainties have been evaluated, with the migration systematics being the largest for this analysis. It has been estimated to be of the order of 4%. It could be reduced by increasing the statistics, since it is strictly related with the total uncertainty on the used control sample which is also dominated by the statistical error. An improved knowledge of the FGDs and their responses might reduce even further this systematic, however the 100% is a reasonable value for such uncertainty and in agreement with previous studies performed by other T2K collaborators. Unfortunately, a limit on the achievable uncertainties is represented by the FGD mass, which is the second largest, giving a $\sim 0.9\%$ error on the ratio. It cannot be reduced further since it is computed taking into account the uncertainties on the internal composition as it was built independently for water and scintillator modules. The theoretical uncertainties instead, strongly depend on the 2p2h contributions to the CC0π signal and on the correlation assumed for the oxygen and carbon parameters.
A MC-based method exploiting a transfer matrix is used to measure the cross-section ratio. Results are obtained using the nominal NEUT to set the prior, however several fake datasets has been produced in order to test the consistency of the method. They show a reasonably small bias of the order of few percent and do not show any serious issue. The T2K data from RunII-IV is used to evaluate the total and single differential cross-section ratio in the muon momentum kinematics first: momentum p_μ and direction $\cos\theta_\mu$.

$$\begin{aligned} R_{O/C}^{CC0\pi} &= 0.930 \pm 0.048(stat.) \pm 0.045(syst.) \quad \text{when integrated in } p_\mu \\ R_{O/C}^{CC0\pi} &= 0.927 \pm 0.048(stat.) \pm 0.045(syst.) \quad \text{when integrated in } \cos\theta_\mu \end{aligned} \tag{7.8}$$

The results in Fig. 7.7 may indicate a deficit in the high angles $cos\theta_\mu < 0.7$ and in the momentum 0.2 GeV/c $< P_\mu <$ 1 GeV/c regions compared to the NEUT prediction. The results for the cross-section ratio measurement, integrated in muon momentum and direction are summarized in Eq. 7.8. They slightly differ depending on the observable, however this is expected because of the different efficiency of the various variables and of the different phase space considered in the two analysis. In the muon angle no cut is applied to restrict the phase space, while in the momentum analysis the lowest ($<$ 100 MeV/c) and the highest ($>$ 10000 MeV/c) bins are cut off. Nonetheless the two distributions differ of $\sim$ 300 events, the results are then compatible with each other (within statistical uncertainties), and at 1σ level with the NEUT prediction.
Finally it was argued in Sec. 7.3 the need of a ratio measurement as a function of the incoming neutrino energy. A reasonably flat efficiency as a function of neutrino energy is found selecting the muon candidate in the restricted phase space $\cos\theta_\mu > 0.5$ and $p_\mu >$ 250 MeV/c. The differential result is shown in Fig. 7.10 and as expected the integrated result is consistent with the kinematic ones in Eq. 7.8

$$R_{O/C}^{CC0\pi} = 0.928 \pm 0.049(stat.) \pm 0.044(syst.) \text{ when integrated in } E_\nu^{CC0\pi}(p_\mu, \cos\theta_\mu). \quad (7.9)$$

In the future, this analysis might be improved by increasing the available phase space to higher angles and backwards-going tracks, and in parallel it could be also useful to consider both FGD2 and FGD1 samples simultaneously. In this way the cross-section ratio could be extracted by subtraction without splitting the FGD2 sample in the x-layers and y-layers interactions.

Conclusion

The work presented in this manuscript aims to improve the track reconstruction in the near detector ND280 of the T2K experiment, as well as to measure the cross-section ratio between oxygen (O) and carbon (C) nuclei for the charged current interaction without pions in the final state (CC0π). T2K is a long baseline neutrino oscillation experiment which uses a high purity muon neutrino (ν_μ) beam produced at the J-PARC accelerator complex, to precisely measure the mixing parameters θ_{13}, θ_{23} and Δm^2_{32} and to study CP violation in the leptonic sector. In the oscillation analysis those parameters are measured by comparing the neutrino interaction rate at near and far detectors: ND280 is used to measure and then better constrain the neutrino rate expected at SK. At the same time, it can also provide cross-section measurements that will help understanding the neutrino interaction model. Current oscillation analyses include ND280 results relative to interactions on carbon to normalize the beam flux and to constrain theory cross-section parameters. Indeed, at T2K energies the main process is CC0π which dominates the cross-section. Therefore, measuring the ν_μ oxygen over carbon cross-section ratio is extremely important for the T2K experiment to eliminate the uncertainties arising from the carbon/oxygen difference but also for the neutrino community to prove the validity of the neutrino interaction models.
In this thesis work a full analysis was developed based on neutrino data RunII-IV collected by ND280. The definition of the chosen signal CC0π corresponds to what the detector is able to observe in the final state of the interaction allowing to perform a more model independent measurement. The signal consists mainly of CCQE, but is also sensitive to nuclear (2p-2h) and FSI effects (pion absorption from resonant production), or any interaction resulting in the emission of a muon and one or more protons. The FGD2 subdetector, which consists of plastic scintillators interleaved with passive water modules, is used for the ratio extraction while the FGD1 is used as control sample to constrain the migration uncertainty. The cross-section ratio is measured in the full phase space of muon kinematic (p_μ and cosθ_μ) but also in reconstructed neutrino energy (E_ν) in the reduced phase space $p_\mu > 250$ MeV/c and cos$\theta_\mu > 0.5$. The latter is directly related to the oscillation analyses since they are performed in bins of the same quantity, while the muon kinematics are more associated to the neutrino interaction models. The total cross-sections differ slightly when measured in different variables, but they are all compatible within the error with each other $R_{O/C}(p_\mu) = 0.930 \ \pm 0.048(stat.) \ \pm 0.045(syst.)$ and at 1σ with the NEUT $R^{NEUT}_{O/C} = 0.991$ and

GENIE $R_{O/C}^{GENIE} = 0.996$ generators predictions.
Since the energy of the incoming neutrino can be inferred using the muon kinematics a study to improve the detector performance on the muon momentum measurement in the TPC was also performed. Indeed misalignment between the MicroMegas modules instrumenting the TPCs of the near detector ND280 can deteriorate the resolution of the momentum measurement. A cosmic rays sample collected with magnetic field off has been used for this study, in order to disentangle misalignment effects in the momentum determination from other sources of error and to have straight segments of tracks which are much easier to compare. After this alignment procedure a fit to the residual distribution shows a precision of ~ 0.070 mrad in rotations and of ~ 20 μm and ~ 50 μm in the transverse y and horizontal z directions.

Acknowledgements

Dear reader, thank you for coming to the end of this manuscript, I hope you do not get bored too much. Actually, I would have wished a different cover for this thesis, a cover with the words **DON'T PANIC** inscribed in large friendly letters. The pasts were tough and intense years, such words of comfort together with the inseparable towel would do not be useful to running away from panicking. I guess that without the help and support of the people I care, I never could have done it. I owe them my thanks.
In first place I know for certain that this work would not be possible without the help of my thesis's supervisor Marco. Thank you for the trust, patience and tough discussions that kept me on track. He taught me lots, but more importantly, he also encouraged me to figure out things on my own giving me the independence to develop along the PhD path analysis and personal skills.
I would like to express my infinite gratitude to Sara for all the advises, conversations and motivation in the dark moments during these 3 years. She helped me in every step of research and writing of this thesis since the beginning. Her doors was open anytime to answer to my many questions (even the silly ones) about neutrino physics and T2K. Besides, I will never forget how much you and Andrea helped me at the very beginning. Thank you, I could not have imagined having a better supervisor and friend. These few words are not enough to express my gratitude.
I would also like to thank all the CEA group for the valuable advises in the internal meeting: merci Eddy, Sandrine, Georges.
Certainly, I was lucky enough to have the opportunity to know amazing people in this 3 years long adventure. Amazing like my officemates Mathieu and Ciro, we had endless discussions about neutrino physics and the implementation details in the T2K software. Together we shared not just an office. Thanks for the funny moments that made my stay at CEA more enjoyable.
Moreover fly to Japan 2-3 times per year can be tough sometimes, however it becomes very easy when there is a good fellowship: Alfonso, Davide and Lorenzo I will never forget our favorite restaurant in Ueno and the sauna at the capsula hotel. Thank you to make my stays in Japan unforgettable.
A sincere thanks to the stunning emph Business Class Group: Andrei, Andrea and Daria. I would have never imagined to can bound like that to someone in a such short time before, you are the proof that a true and genuine friendship can be born without prior solid foundations. See you to untap some Sierra Nevada together.

Also I need to mention my family in Paris: Capitani, Robertone, Karo, Massimo and Stefania. When I moved here in Paris I was alone but I was so lucky to find you, thank you for all the sunday meals and the free time spent together (Capitani don't complain as usual I know I can cook just a couple of things).
I have to particularly thank all my friends: Salvatore, Capriotti, Livia, Silvia, Matteo, Fausto. Even if we are spread around Europe feel your friendship and support helped me in more than one situation.
Definitely I owe a special thanks to my brothers Gasta, *Cookie Monster* Peter, Yak and Nello we cannot be related by blood, however you are there no matter what.
Da casa in Abruzzo devo ringraziare tutta la mia famiglia che mi ha sempre sostenuto nelle mie scelte e permesso di arrivare fino a questo traguardo anche se ciò significa essere a 2000 km di distanza, mi mancate molto. A mio nonno Francesco, so che non passa un giorno senza chiedere come sto; a mia nonna Filomena di cui spesso sento la mancanza, è venuta a mancare durante questi anni di dottorato; ai miei genitori Antonina e Alfiero che non importa cosa accada sono sempre lì presenti per me; alle mie sorelle Martina e Cristiana ora ho scalato seppur per un giorno la graduatoria adesso tocca a voi; infine a mia zia Oriana che è sempre stata una mamma per me. Grazie di cuore a tutti voi.
Infine con poche parole (non ne basterebbero milioni) vorrei ringraziare Eleonora, sei la cosa più bella che potesse capitarmi trasferitomi a Parigi. Fin dall'inizio hai condiviso tutto di questo dottorato, sei stata lo scoglio a cui aggrapparmi mentre annegavo nei momenti difficili, mi hai fatto ragionare e spronato ad andare avanti fino a questo traguardo. Grazie per essere cosí, sincera, diretta e premurosa, anche se a volte non lo do a vedere rendi la mia vita ogni giorno migliore e felice. So che adesso ti starai vergognando e appena hai letto il tuo nome sei corsa a nasconderti in camera ma nonostante questo sento di doverti dirti: TI AMO!

Bibliography

[1] "The idea of the neutrino". In: *Physics Today* 31.9 (1978), pp. 23–28. DOI: http://dx.doi.org/10.1063/1.2995181.

[2] J. Chadwick. "Intensitatsverteilung im magnetischen Spektrum der β-Strahlen von Radium B+C". In: *Verhandlungen der Deutschen Physikalischen Gesellschaft* 16 (1914), pp. 383–391.

[3] J. Chadwick. "Possible existence of a neutron". In: *Nature* 129 (1932), p. 312.

[4] E. Fermi. "Versuch einer Theorie der β-Strahlen. I". In: *Zeitschrift für Physik* 88.3 (1934), pp. 161–177. ISSN: 0044-3328. DOI: 10.1007/BF01351864. URL: http://dx.doi.org/10.1007/BF01351864.

[5] C. L. Cowan et al. "Detection of the Free Neutrino: a Confirmation". In: *Science* 124.3212 (1956), pp. 103–104. ISSN: 0036-8075. DOI: 10.1126/science.124.3212.103. eprint: http://science.sciencemag.org/content/124/3212/103.full.pdf. URL: http://science.sciencemag.org/content/124/3212/103.

[6] G. Danby et al. "Observation of High-Energy Neutrino Reactions and the Existence of Two Kinds of Neutrinos". In: *Phys. Rev. Lett.* 9 (1 1962), pp. 36–44. DOI: 10.1103/PhysRevLett.9.36. URL: http://link.aps.org/doi/10.1103/PhysRevLett.9.36.

[7] M. L. Perl et al. "Evidence for Anomalous Lepton Production in $e^+ - e^-$ Annihilation". In: *Phys. Rev. Lett.* 35 (22 1975), pp. 1489–1492. DOI: 10.1103/PhysRevLett.35.1489. URL: http://link.aps.org/doi/10.1103/PhysRevLett.35.1489.

[8] K. Kodama et al. "Observation of tau neutrino interactions". In: *Physics Letters B* 504.3 (2001), pp. 218 –224. ISSN: 0370-2693. DOI: http://dx.doi.org/10.1016/S0370-2693(01)00307-0. URL: http://www.sciencedirect.com/science/article/pii/S0370269301003070.

[9] Peter W. Higgs. "Broken Symmetries and the Masses of Gauge Bosons". In: *Phys. Rev. Lett.* 13 (16 1964), pp. 508–509. DOI: 10.1103/PhysRevLett.13.508. URL: http://link.aps.org/doi/10.1103/PhysRevLett.13.508.

[10] F. Englert and R. Brout. "Broken Symmetry and the Mass of Gauge Vector Mesons". In: *Phys. Rev. Lett.* 13 (9 1964), pp. 321–323. DOI: 10.1103/PhysRevLett.13.321. URL: http://link.aps.org/doi/10.1103/PhysRevLett.13.321.

[11] Andrew Purcell. "Go on a particle quest at the first CERN webfest. Le premier webfest du CERN se lance conqu des particules". In: BUL-NA-2012-269. 35/2012 (2012), p. 10. URL: https://cds.cern.ch/record/1473657.

[12] Steven Weinberg. "A Model of Leptons". In: *Phys. Rev. Lett.* 19 (21 1967), pp. 1264–1266. DOI: 10.1103/PhysRevLett.19.1264. URL: http://link.aps.org/doi/10.1103/PhysRevLett.19.1264.

[13] Abdus Salam and J. C. Ward. "Weak and electromagnetic interactions". In: *Il Nuovo Cimento (1955-1965)* 11.4 (1959), pp. 568–577. ISSN: 1827-6121. DOI: 10.1007/BF02726525. URL: http://dx.doi.org/10.1007/BF02726525.

[14] The ALEPH Collaboration The DELPHI Collaboration The L3 Collaboration The OPAL Collaboration The SLD Collaboration The LEP Electroweak Working Group The SLD Electroweak and Heavy Flavour Groups. "Precision electroweak measurements on the Z resonance". In: *Physics Reports* 427.5?6 (2006), pp. 257 –454. ISSN: 0370-1573. DOI: http://dx.doi.org/10.1016/j.physrep.2005.12.006. URL: http://www.sciencedirect.com/science/article/pii/S0370157305005119.

[15] H. Weyl. "Electron and Gravitation. 1. (In German)". In: *Z. Phys.* 56 (1929). [Surveys High Energ. Phys.5,261(1986)], pp. 330–352. DOI: 10.1007/BF01339504.

[16] B. Pontecorvo. "Mesonium and anti-mesonium". In: *Sov. Phys. JETP* 6 (1957). [Zh. Eksp. Teor. Fiz.33,549(1957)], p. 429.

[17] Ziro Maki, Masami Nakagawa, and Shoichi Sakata. "Remarks on the Unified Model of Elementary Particles". In: *Progress of Theoretical Physics* 28.5 (1962), p. 870. DOI: 10.1143/PTP.28.870. eprint: /oup/backfile/Content_public/Journal/ptp/28/5/10.1143/PTP.28.870/2/28-5-870.pdf. URL: +http://dx.doi.org/10.1143/PTP.28.870.

[18] R. N. Cahn et al. "White Paper: Measuring the Neutrino Mass Hierarchy". In: *Proceedings, 2013 Community Summer Study on the Future of U.S. Particle Physics: Snowmass on the Mississippi (CSS2013): Minneapolis, MN, USA, July 29-August 6, 2013*. 2013. arXiv: 1307.5487 [hep-ex]. URL: https://inspirehep.net/record/1243859/files/arXiv:1307.5487.pdf.

[19] L. Wolfenstein. "Neutrino oscillations in matter". In: *Phys. Rev. D* 17 (9 1978), pp. 2369–2374. DOI: 10.1103/PhysRevD.17.2369. URL: https://link.aps.org/doi/10.1103/PhysRevD.17.2369.

[20] S. P. Mikheev and A. Yu. Smirnov. "Resonance Amplification of Oscillations in Matter and Spectroscopy of Solar Neutrinos". In: *Sov. J. Nucl. Phys.* 42 (1985). [Yad. Fiz.42,1441(1985)], pp. 913–917.

[21] G. Bellini et al. "Neutrinos from the primary proton-proton fusion process in the Sun". In: *Nature* 512.7515 (2014), pp. 383–386. DOI: 10.1038/nature13702.

[22] B. T. Cleveland et al. "Measurement of the solar electron neutrino flux with the Homestake chlorine detector". In: *Astrophys. J.* 496 (1998), pp. 505–526. DOI: 10.1086/305343.

[23] Raymond Davis, Don S. Harmer, and Kenneth C. Hoffman. "Search for Neutrinos from the Sun". In: *Phys. Rev. Lett.* 20 (21 1968), pp. 1205–1209. DOI: 10.1103/PhysRevLett.20.1205. URL: http://link.aps.org/doi/10.1103/PhysRevLett.20.1205.

[24] W. Hampel et al. "GALLEX solar neutrino observations: Results for GALLEX IV". In: *Phys. Lett.* B447 (1999), pp. 127–133. DOI: 10.1016/S0370-2693(98)01579-2.

[25] M. Altmann et al. "Complete results for five years of {GNO} solar neutrino observations". In: *Physics Letters B* 616.3?4 (2005), pp. 174 –190. ISSN: 0370-2693. DOI: http://dx.doi.org/10.1016/j.physletb.2005.04.068. URL: http://www.sciencedirect.com/science/article/pii/S0370269305005149.

[26] J. N. Abdurashitov et al. "Measurement of the solar neutrino capture rate with gallium metal. III: Results for the 2002–2007 data-taking period". In: *Phys. Rev.* C80 (2009), p. 015807. DOI: 10.1103/PhysRevC.80.015807. arXiv: 0901.2200 [nucl-ex].

[27] G. Bellini et al. "Final results of Borexino Phase-I on low energy solar neutrino spectroscopy". In: *Phys. Rev.* D89.11 (2014), p. 112007. DOI: 10.1103/PhysRevD.89.112007. arXiv: 1308.0443 [hep-ex].

[28] K. S. Hirata et al. "Observation of ^{8}B solar neutrinos in the Kamiokande-II detector". In: *Phys. Rev. Lett.* 63 (1 1989), pp. 16–19. DOI: 10.1103/PhysRevLett.63.16. URL: http://link.aps.org/doi/10.1103/PhysRevLett.63.16.

[29] S. Fukuda et al. "Solar ^8B and hep Neutrino Measurements from 1258 Days of Super-Kamiokande Data". In: *Phys. Rev. Lett.* 86 (25 2001), pp. 5651–5655. DOI: 10.1103/PhysRevLett.86.5651. URL: http://link.aps.org/doi/10.1103/PhysRevLett.86.5651.

[30] Q. R. Ahmad et al. "Direct Evidence for Neutrino Flavor Transformation from Neutral-Current Interactions in the Sudbury Neutrino Observatory". In: *Phys. Rev. Lett.* 89 (1 2002), p. 011301. DOI: 10.1103/PhysRevLett.89.011301. URL: https://link.aps.org/doi/10.1103/PhysRevLett.89.011301.

[31] Paul Langacker. "Grand Unified Theories and Proton Decay". In: *Phys. Rept.* 72 (1981), p. 185. DOI: 10.1016/0370-1573(81)90059-4.

[32] Edward Kearns. "Experimental measurements of atmospheric neutrinos". In: *Nucl. Phys. Proc. Suppl.* 70 (1999), pp. 315–323. DOI: 10.1016/S0920-5632(98)00441-1. arXiv: hep-ex/9803007 [hep-ex].

[33] K. S. Hirata et al. "Observation of a small atmospheric muon-neutrino / electron-neutrino ratio in Kamiokande". In: *Phys. Lett.* B280 (1992), pp. 146–152. DOI: 10.1016/0370-2693(92)90788-6.

[34] Y. Fukuda et al. "Evidence for oscillation of atmospheric neutrinos". In: *Phys. Rev. Lett.* 81 (1998), pp. 1562–1567. DOI: 10.1103/PhysRevLett.81.1562. arXiv: hep-ex/9807003 [hep-ex].

[35] K. A. Olive et al. "Review of Particle Physics". In: *Chin. Phys.* C38 (2014), p. 090001. DOI: 10.1088/1674-1137/38/9/090001.

[36] Petr Vogel, Liangjian Wen, and Chao Zhang. "Neutrino Oscillation Studies with Reactors". In: *Nature Commun.* 6 (2015), p. 6935. DOI: 10.1038/ncomms7935. arXiv: 1503.01059 [hep-ex].

[37] K. Eguchi et al. "First Results from KamLAND: Evidence for Reactor Antineutrino Disappearance". In: *Phys. Rev. Lett.* 90 (2 2003), p. 021802. DOI: 10.1103/PhysRevLett.90.021802. URL: http://link.aps.org/doi/10.1103/PhysRevLett.90.021802.

[38] T. Araki et al. "Measurement of Neutrino Oscillation with KamLAND: Evidence of Spectral Distortion". In: *Phys. Rev. Lett.* 94 (8 2005), p. 081801. DOI: 10.1103/PhysRevLett.94.081801. URL: http://link.aps.org/doi/10.1103/PhysRevLett.94.081801.

[39] S. Abe et al. "Precision Measurement of Neutrino Oscillation Parameters with KamLAND". In: *Phys. Rev. Lett.* 100 (22 2008), p. 221803. DOI: 10.1103/PhysRevLett.100.221803. URL: http://link.aps.org/doi/10.1103/PhysRevLett.100.221803.

[40] A. Gando et al. "Reactor on-off antineutrino measurement with KamLAND". In: *Phys. Rev. D* 88 (3 2013), p. 033001. DOI: 10.1103/PhysRevD.88.033001. URL: https://link.aps.org/doi/10.1103/PhysRevD.88.033001.

[41] F. Ardellier et al. "Letter of intent for Double-CHOOZ: A Search for the mixing angle theta(13)". In: (2004). arXiv: hep-ex/0405032 [hep-ex].

[42] F. P. An et al. "New Measurement of Antineutrino Oscillation with the Full Detector Configuration at Daya Bay". In: *Phys. Rev. Lett.* 115 (11 2015), p. 111802. DOI: 10.1103/PhysRevLett.115.111802. URL: http://link.aps.org/doi/10.1103/PhysRevLett.115.111802.

[43] Soo-Bong Kim. "New results from RENO and prospects with RENO-50". In: *Nucl. Part. Phys. Proc.* 265-266 (2015), pp. 93–98. DOI: 10.1016/j.nuclphysbps.2015.06.024. arXiv: 1412.2199 [hep-ex].

[44] Y. Abe et al. "Improved measurements of the neutrino mixing angle θ_{13} with the Double Chooz detector". In: *JHEP* 10 (2014). [Erratum: JHEP02,074(2015)], p. 086. DOI: 10.1007/JHEP02(2015)074,10.1007/JHEP10(2014)086. arXiv: 1406.7763 [hep-ex].

[45] M. H. Ahn et al. "Measurement of neutrino oscillation by the K2K experiment". In: *Phys. Rev. D* 74 (7 2006), p. 072003. DOI: 10.1103/PhysRevD.74.072003. URL: http://link.aps.org/doi/10.1103/PhysRevD.74.072003.

[46] P. Adamson et al. "Measurement of Neutrino and Antineutrino Oscillations Using Beam and Atmospheric Data in MINOS". In: *Phys. Rev. Lett.* 110 (25 2013), p. 251801. DOI: 10.1103/PhysRevLett.110.251801. URL: http://link.aps.org/doi/10.1103/PhysRevLett.110.251801.

[47] P. Adamson et al. "First measurement of electron neutrino appearance in NOvA". In: *Phys. Rev. Lett.* 116.15 (2016), p. 151806. DOI: 10.1103/PhysRevLett.116.151806. arXiv: 1601.05022 [hep-ex].

[48] P. Adamson et al. "Measurement of the neutrino mixing angle θ_{23} in NOvA". In: *Phys. Rev. Lett.* 118.15 (2017), p. 151802. DOI: 10.1103/PhysRevLett.118.151802. arXiv: 1701.05891 [hep-ex].

[49] C. Patrignani et al. "Review of Particle Physics". In: *Chin. Phys.* C40.10 (2016). DOI: 10.1088/1674-1137/40/10/100001.

[50] K. Abe et al. "A Long Baseline Neutrino Oscillation Experiment Using J-PARC Neutrino Beam and Hyper-Kamiokande". In: 2014. arXiv: 1412.4673 [physics.ins-det]. URL: https://inspirehep.net/record/1334360/files/arXiv:1412.4673.pdf.

[51] Maury A Goodman. "The Deep Underground Neutrino Experiment". In: *Advances in High Energy Physics* 2015 (2015), p. 9. DOI: http://dx.doi.org/10.1155/2015/256351. eprint: 10.1155/2015/256351.

[52] Wladyslaw Henryk Trzaska. "LBNO-DEMO (WA 105): a large demonstrator of the Liquid Argon double phase TPC". In: *PoS* PhotoDet2015 (2016), p. 054.

[53] "ProtoDUNE - proposal". In: *CERN-SPSC-2015-020;SPSC-P-351* (2015).

[54] K. Abe et al. "The T2K Experiment". In: *Nucl. Instrum. Meth.* A659 (2011), pp. 106–135. DOI: 10.1016/j.nima.2011.06.067. arXiv: 1106.1238 [physics.ins-det].

[55] T. Ajima et al. "T2K letter of Intent". In: (2006).

[56] "T2K letter of Intent". In: *http://jnusrv01.kek.jp/public/t2k/loi/loi.v2.030528.pdf* ().

[57] K. Abe et al. "Indication of Electron Neutrino Appearance from an Accelerator-produced Off-axis Muon Neutrino Beam". In: *Phys. Rev. Lett.* 107 (2011), p. 041801. DOI: 10.1103/PhysRevLett.107.041801. arXiv: 1106.2822 [hep-ex].

[58] F. P. An et al. "Observation of Electron-Antineutrino Disappearance at Daya Bay". In: *Phys. Rev. Lett.* 108 (17 2012), p. 171803. DOI: 10.1103/PhysRevLett.108.171803. URL: http://link.aps.org/doi/10.1103/PhysRevLett.108.171803.

[59] J. K. Ahn et al. "Observation of Reactor Electron Antineutrinos Disappearance in the RENO Experiment". In: *Phys. Rev. Lett.* 108 (19 2012), p. 191802. DOI: 10.1103/PhysRevLett.108.191802. URL: http://link.aps.org/doi/10.1103/PhysRevLett.108.191802.

[60] Y. Abe et al. "Indication of Reactor $\overline{\nu}_e$ Disappearance in the Double Chooz Experiment". In: *Phys. Rev. Lett.* 108 (13 2012), p. 131801. DOI: 10.1103/PhysRevLett.108.131801. URL: http://link.aps.org/doi/10.1103/PhysRevLett.108.131801.

[61] K. Abe et al. "Observation of Electron Neutrino Appearance in a Muon Neutrino Beam". In: *Phys. Rev. Lett.* 112 (6 2014), p. 061802. DOI: 10.1103/PhysRevLett.112.061802. URL: http://link.aps.org/doi/10.1103/PhysRevLett.112.061802.

[62] K. Abe et al. "Measurement of neutrino and antineutrino oscillations by the T2K experiment including a new additional sample of ν_e interactions at the far detector". In: (2017). arXiv: 1707.01048 [hep-ex].

[63] *Proceedings, 34th International Cosmic Ray Conference (ICRC 2015)*. Vol. ICRC2015. 2015. URL: http://pos.sissa.it/cgi-bin/reader/conf.cgi?confid=236.

[64] M. G. Aartsen et al. "Neutrino oscillation studies with IceCube-DeepCore". In: *Nucl. Phys.* B908 (2016), pp. 161–177. DOI: 10.1016/j.nuclphysb.2016.03.028.

[65] D. Beavis, A. Carroll, and I. Chiang. "Long baseline neutrino oscillation experiment at the AGS". In: (1995).

[66] Kirk T McDonald. "An Off-axis neutrino beam". In: (2001). arXiv: hep-ex/0111033 [hep-ex].

[67] K. Abe et al. "T2K neutrino flux prediction". In: *Phys. Rev. D* 87 (1 2013), p. 012001. DOI: 10.1103/PhysRevD.87.012001. URL: http://link.aps.org/doi/10.1103/PhysRevD.87.012001.

[68] K. Matsuoka et al. "Development and production of the ionization chamber for the T2K muon monitor". In: *Nucl. Instrum. Meth.* A623 (2010), pp. 385–387. DOI: 10.1016/j.nima.2010.03.010.

[69] K. Matsuoka et al. "Design and performance of the muon monitor for the T2K neutrino oscillation experiment". In: *Nucl. Instrum. Meth.* A624 (2010), pp. 591–600. DOI: 10.1016/j.nima.2010.09.074. arXiv: 1008.4077 [physics.ins-det].

[70] R. Brun et al. "GEANT3". In: (1987).

[71] Szymon Pulawski. "Recent results from NA61/SHINE". In: *Acta Phys. Polon.* B46.11 (2015), p. 2381. DOI: 10.5506/APhysPolB.46.2381. arXiv: 1510.07794 [nucl-ex].

[72] Giuseppe Battistoni et al. "The FLUKA code: Description and benchmarking". In: *AIP Conf. Proc.* 896 (2007). [,31(2007)], pp. 31–49. DOI: 10.1063/1.2720455.

[73] Alfredo Ferrari et al. "FLUKA: A multi-particle transport code (Program version 2005)". In: (2005).

[74] In: (). URL: http://www.atlas.uni-wuppertal.de/zeitnitz/gcalor.

[75] N Abgrall et al. "Report from the NA61/SHINE experiment at the CERN SPS." In: ().

[76] N Abgrall et al. "Measurements of Cross Sections and Charged Pion Spectra in Proton-Carbon Interactions at 31 GeV/c". In: *Phys. Rev.* C84 (2011), p. 034604. DOI: 10.1103/PhysRevC.84.034604. arXiv: 1102.0983 [hep-ex].

[77] N. Abgrall et al. "Pion emission from the T2K replica target: method, results and application". In: *Nucl. Instrum. Meth.* A701 (2013), pp. 99–114. DOI: 10.1016/j.nima.2012.10.079. arXiv: 1207.2114 [hep-ex].

[78] A. Vacheret et al. "Characterization and Simulation of the Response of Multi Pixel Photon Counters to Low Light Levels". In: *Nucl. Instrum. Meth.* A656.1 (2011), pp. 69–83. DOI: 10.1016/j.nima.2011.07.022. arXiv: 1101.1996 [physics.ins-det].

[79] D. H. Wilkinson. "The Geiger Discharge". In: *Phys. Rev.* 74 (10 1948), pp. 1417–1429. DOI: 10.1103/PhysRev.74.1417. URL: https://link.aps.org/doi/10.1103/PhysRev.74.1417.

[80] K. Abe et al. "Measurement of the ν_μ charged current quasielastic cross section on carbon with the T2K on-axis neutrino beam". In: *Phys. Rev. D* 91 (11 2015), p. 112002. DOI: 10.1103/PhysRevD.91.112002. URL: http://link.aps.org/doi/10.1103/PhysRevD.91.112002.

[81] G. Arnison et al. "Experimental Observation of Lepton Pairs of Invariant Mass Around 95-GeV/c**2 at the CERN SPS Collider". In: *Phys. Lett.* 126B (1983), pp. 398–410. DOI: 10.1016/0370-2693(83)90188-0.

[82] J. Altegoer et al. "The NOMAD experiment at the CERN SPS". In: *Nucl. Instrum. Meth.* A404 (1998), pp. 96–128. DOI: 10.1016/S0168-9002(97)01079-6.

[83] P. A. Amaudruz et al. "The T2K Fine-Grained Detectors". In: *Nucl. Instrum. Meth.* A696 (2012), pp. 1–31. DOI: 10.1016/j.nima.2012.08.020. arXiv: 1204.3666 [physics.ins-det].

[84] In: *The Theory and Practice of Scintillation Counting*. Ed. by J.B. BIRKS. International Series of Monographs in Electronics and Instrumentation. Pergamon, 1964, pp. iv –. ISBN: 978-0-08-010472-0. DOI: https://doi.org/10.1016/B978-0-08-010472-0.50002-1. URL: http://www.sciencedirect.com/science/article/pii/B9780080104720500021.

[85] Masaya Hasegawa. "Measurement of neutrino oscillation parameters with neutrino-nucleus interaction studies in the K2K experiment". PhD thesis. Kyoto U., 2006. URL: http://inspirehep.net/record/723602/files/masaya_dt.pdf.

[86] T. Suzuki, D. F. Measday, and J. P. Roalsvig. "Total nuclear capture rates for negative muons". In: *Phys. Rev. C* 35 (6 1987), pp. 2212–2224. DOI: 10.1103/PhysRevC.35.2212. URL: https://link.aps.org/doi/10.1103/PhysRevC.35.2212.

[87] Y. Fukuda et al. "The Super-Kamiokande detector". In: *Nucl. Instrum. Meth.* A501 (2003), pp. 418–462. DOI: 10.1016/S0168-9002(03)00425-X.

[88] Y. Fukuda et al. "Evidence for Oscillation of Atmospheric Neutrinos". In: *Phys. Rev. Lett.* 81 (8 1998), pp. 1562–1567. DOI: 10.1103/PhysRevLett.81.1562. URL: http://link.aps.org/doi/10.1103/PhysRevLett.81.1562.

[89] Y. Fukuda et al. "Measurement of the Solar Neutrino Energy Spectrum Using Neutrino-Electron Scattering". In: *Phys. Rev. Lett.* 82 (12 1999), pp. 2430–2434. DOI: 10.1103/PhysRevLett.82.2430. URL: http://link.aps.org/doi/10.1103/PhysRevLett.82.2430.

[90] Y. Ashie et al. "A Measurement of atmospheric neutrino oscillation parameters by SUPER-KAMIOKANDE I". In: *Phys. Rev.* D71 (2005), p. 112005. DOI: 10.1103/PhysRevD.71.112005. arXiv: hep-ex/0501064 [hep-ex].

[91] J. Hosaka et al. "Three flavor neutrino oscillation analysis of atmospheric neutrinos in Super-Kamiokande". In: *Phys. Rev. D* 74 (3 2006), p. 032002. DOI: 10.1103/PhysRevD.74.032002. URL: http://link.aps.org/doi/10.1103/PhysRevD.74.032002.

[92] S. H. Ahn et al. "Detection of accelerator produced neutrinos at a distance of 250-km". In: *Phys. Lett.* B511 (2001), pp. 178–184. DOI: 10.1016/S0370-2693(01)00647-5. arXiv: hep-ex/0103001 [hep-ex].

[93] S. Fukuda et al. "The Super-Kamiokande detector". In: *Nuclear Instruments and Methods in Physics Research Section A: Accelerators, Spectrometers, Detectors and Associated Equipment* 501.2–3 (2003), pp. 418 –462. ISSN: 0168-9002. DOI: http://dx.doi.org/10.1016/S0168-9002(03)00425-X. URL: http://www.sciencedirect.com/science/article/pii/S016890020300425X.

[94] S. Agostinelli et al. "Geant4—a simulation toolkit". In: *Nuclear Instruments and Methods in Physics Research Section A: Accelerators, Spectrometers, Detectors and Associated Equipment* 506.3 (2003), pp. 250 –303. ISSN: 0168-9002. DOI: http://dx.doi.org/10.1016/S0168-9002(03)01368-8. URL: http://www.sciencedirect.com/science/article/pii/S0168900203013688.

[95] N. Abgrall et al. "Time Projection Chambers for the T2K Near Detectors". In: *Nucl. Instrum. Meth.* A637 (2011), pp. 25–46. DOI: 10.1016/j.nima.2011.02.036. arXiv: 1012.0865 [physics.ins-det].

[96] C. Ramsauer and R. Kollath. "er den Wirkungsquerschnitt der Edelgasmolekle gegenber Elektronen unterhalb 1 Volt". In: *Annalen der Physik* 395.4 (1929), pp. 536–564. ISSN: 1521-3889. DOI: 10.1002/andp.19293950405. URL: http://dx.doi.org/10.1002/andp.19293950405.

[97] D.R Nygren and J.N. Marx. "The Time Projection Chamber". In: *Physics Today* 31.10 (1978). DOI: 10.1063/1.2994775. URL: http://dx.doi.org/10.1063/1.2994775.

[98] J. Bouchez et al. "Bulk micromegas detectors for large TPC applications". In: *Nucl. Instrum. Meth.* A574 (2007), pp. 425–432. DOI: 10.1016/j.nima.2007.02.074.

[99] I. Giomataris et al. "Micromegas in a bulk". In: *Nuclear Instruments and Methods in Physics Research Section A: Accelerators, Spectrometers, Detectors and Associated Equipment* 560.2 (2006), pp. 405 –408. ISSN: 0168-9002. DOI: http://dx.doi.org/10.1016/j.nima.2005.12.222. URL: http://www.sciencedirect.com/science/article/pii/S0168900205026501.

[100] A. Cervera-Villanueva, J.J. Gómez-Cadenas, and J.A. Hernando. ""RecPack" a reconstruction toolkit". In: *Nuclear Instruments and Methods in Physics Research Section A: Accelerators, Spectrometers, Detectors and Associated Equipment* 534.1–2 (2004). Proceedings of the {IXth} International Workshop on Advanced Computing and Analysis Techniques in Physics Research, pp. 180 –183. ISSN: 0168-9002. DOI: http://dx.doi.org/10.1016/j.nima.2004.07.074. URL: http://www.sciencedirect.com/science/article/pii/S0168900204015220.

[101] Claudio Giganti. "Particle Identification in the T2K TPCs and study of the electron neutrino component in the T2K neutrino beam". PhD thesis. IRFU, Saclay, 2010. URL: http://irfu.cea.fr/Documentation/Theses/recherche_theses.php.

[102] R.L. Gluckstern. "Uncertainties in track momentum and direction, due to multiple scattering and measurement errors". In: *Nuclear Instruments and Methods* 24 (1963), pp. 381 –389. ISSN: 0029-554X. DOI: http://dx.doi.org/10.1016/0029-554X(63)90347-1. URL: http://www.sciencedirect.com/science/article/pii/0029554X63903471.

[103] E Frank et al. "A dedicated device for measuring the magnetic field of the ND280 magnet in the T2K experiment". In: *Journal of Instrumentation* 7.01 (2012), P01018. URL: http://stacks.iop.org/1748-0221/7/i=01/a=P01018.

[104] D. Karlen. *Internal Surveys of the T2K TPCs at JPARC, T2K Internal Note-11.*

[105] F. James. URL: https://seal.web.cern.ch/seal/snapshot/work-packages/mathlibs/minuit/.

[106] S. Agostinelli et al. "GEANT4: A Simulation toolkit". In: *Nucl. Instrum. Meth.* A506 (2003), pp. 250–303. DOI: 10.1016/S0168-9002(03)01368-8.

[107] R. Brun and F. Rademakers. "ROOT: An object oriented data analysis framework". In: *Nucl. Instrum. Meth.* A389 (1997), pp. 81–86. DOI: 10.1016/S0168-9002(97)00048-X.

[108] K. Abe et al. "Combined Analysis of Neutrino and Antineutrino Oscillations at T2K". In: *Phys. Rev. Lett.* 118 (15 2017), p. 151801. DOI: 10.1103/PhysRevLett.118.151801. URL: https://link.aps.org/doi/10.1103/PhysRevLett.118.151801.

[109] J. A. Formaggio and G. P. Zeller. "From eV to EeV: Neutrino cross sections across energy scales". In: *Rev. Mod. Phys.* 84 (3 2012), pp. 1307–1341. DOI: 10.1103/RevModPhys.84.1307. URL: https://link.aps.org/doi/10.1103/RevModPhys.84.1307.

[110] C. H. Llewellyn Smith. "Neutrino Reactions at Accelerator Energies". In: *Phys. Rept.* 3 (1972), pp. 261–379. DOI: 10.1016/0370-1573(72)90010-5.

[111] M. L. Goldberger and S. B. Treiman. "Decay of the Pi Meson". In: *Phys. Rev.* 110 (5 1958), pp. 1178–1184. DOI: 10.1103/PhysRev.110.1178. URL: https://link.aps.org/doi/10.1103/PhysRev.110.1178.

[112] Veronique Bernard, Latifa Elouadrhiri, and Ulf-G. Meissner. "Axial structure of the nucleon: Topical Review". In: *J. Phys.* G28 (2002), R1–R35. DOI: 10.1088/0954-3899/28/1/201. arXiv: hep-ph/0107088 [hep-ph].

[113] Ko Abe et al. "Measurement of double-differential muon neutrino charged-current interactions on C_8H_8 without pions in the final state using the T2K off-axis beam". In: *Phys. Rev.* D93.11 (2016), p. 112012. DOI: 10.1103/PhysRevD.93.112012. arXiv: 1602.03652 [hep-ex].

[114] V Lyubushkin et al. "A Study of quasi-elastic muon neutrino and antineutrino scattering in the NOMAD experiment". In: *Eur. Phys. J.* C63 (2009), pp. 355–381. DOI: 10.1140/epjc/s10052-009-1113-0. arXiv: 0812.4543 [hep-ex].

[115] A. A. Aguilar-Arevalo et al. "First measurement of the muon neutrino charged current quasielastic double differential cross section". In: *Phys. Rev. D* 81 (9 2010), p. 092005. DOI: 10.1103/PhysRevD.81.092005. URL: https://link.aps.org/doi/10.1103/PhysRevD.81.092005.

[116] G. A. Fiorentini et al. "Measurement of Muon Neutrino Quasielastic Scattering on a Hydrocarbon Target at $E_\nu \sim 3.5$?GeV". In: *Phys. Rev. Lett.* 111 (2013), p. 022502. DOI: 10.1103/PhysRevLett.111.022502. arXiv: 1305.2243 [hep-ex].

[117] L. Fields et al. "Measurement of Muon Antineutrino Quasielastic Scattering on a Hydrocarbon Target at $E_\nu \sim 3.5$ GeV". In: *Phys. Rev. Lett.* 111.2 (2013), p. 022501. DOI: 10.1103/PhysRevLett.111.022501. arXiv: 1305.2234 [hep-ex].

[118] T. Walton et al. "Measurement of muon plus proton final states in ν_μ interactions on hydrocarbon at $< E_\nu >= 4.2$ GeV". In: *Phys. Rev.* D91.7 (2015), p. 071301. DOI: 10.1103/PhysRevD.91.071301. arXiv: 1409.4497 [hep-ex].

[119] Dieter Rein and Lalit M. Sehgal. "Neutrino Excitation of Baryon Resonances and Single Pion Production". In: *Annals Phys.* 133 (1981), pp. 79–153. DOI: 10.1016/0003-4916(81)90242-6.

[120] C. L. McGivern et al. "Cross sections for ν_μ and $\bar{\nu}_\mu$ induced pion production on hydrocarbon in the few-GeV region using MINERvA". In: *Phys. Rev.* D94.5 (2016), p. 052005. DOI: 10.1103/PhysRevD.94.052005. arXiv: 1606.07127 [hep-ex].

[121] K. Abe et al. "First measurement of the muon neutrino charged current single pion production cross section on water with the T2K near detector". In: *Phys. Rev. D* 95 (1 2017), p. 012010. DOI: 10.1103/PhysRevD.95.012010. URL: https://link.aps.org/doi/10.1103/PhysRevD.95.012010.

[122] D. Rein and L. M. Sehgal. "Coherent π ^{0} production in neutrino reactions". In: *Nuclear Physics B* 223 (Aug. 1983), pp. 29–44. DOI: 10.1016/0550-3213(83)90090-1.

[123] Stephen L. Adler. "Tests of the Conserved Vector Current and Partially Conserved Axial-Vector Current Hypotheses in High-Energy Neutrino Reactions". In: *Phys. Rev.* 135 (4B 1964), B963–B966. DOI: 10.1103/PhysRev.135.B963. URL: https://link.aps.org/doi/10.1103/PhysRev.135.B963.

[124] A. Higuera et al. "Measurement of Coherent Production of $\pi^{\pm}$ in Neutrino and Antineutrino Beams on Carbon from E_{ν} of 1.5 to 20 GeV". In: *Phys. Rev. Lett.* 113.26 (2014), p. 261802. DOI: 10.1103/PhysRevLett.113.261802. arXiv: 1409.3835 [hep-ex].

[125] Ch. Berger and L. M. Sehgal. "PCAC and coherent pion production by low energy neutrinos". In: *Phys. Rev.* D79 (2009), p. 053003. DOI: 10.1103/PhysRevD.79.053003. arXiv: 0812.2653 [hep-ph].

[126] E. Stein W. Greiner S. Schramm. *Quantum Chromodynamics*. Springer Berlin Heidelberg New York. ISBN: 103-540-48534-1,

[127] J. D. Bjorken and E. A. Paschos. "Inelastic Electron-Proton and γ-Proton Scattering and the Structure of the Nucleon". In: *Phys. Rev.* 185 (5 1969), pp. 1975–1982. DOI: 10.1103/PhysRev.185.1975. URL: https://link.aps.org/doi/10.1103/PhysRev.185.1975.

[128] R. A. Smith and E. J. Moniz. "NEUTRINO REACTIONS ON NUCLEAR TARGETS". In: *Nucl. Phys.* B43 (1972). [Erratum: Nucl. Phys.B101,547(1975)], p. 605. DOI: 10.1016/0550-3213(75)90612-4, 10.1016/0550-3213(72)90040-5.

[129] K. Rith C. Scholz B. Povh M. Lavelle and F. Zetsche. "Particles and Nuclei: An Introduction to the Physical Concepts". In: *Springer Berlin Heidelberg* (2013). DOI: 10.1007/978-3-662-05432-1.

[130] L. Alvarez-Ruso, Y. Hayato, and J. Nieves. "Progress and open questions in the physics of neutrino cross sections at intermediate energies". In: *New J. Phys.* 16 (2014), p. 075015. DOI: 10.1088/1367-2630/16/7/075015. arXiv: 1403.2673 [hep-ph].

[131] O. Benhar et al. "Spectral function of finite nuclei and scattering of GeV electrons". In: *Nucl. Phys.* A579 (1994), pp. 493–517. DOI: 10.1016/0375-9474(94)90920-2.

[132] J. Nieves, I. Ruiz Simo, and M. J. Vicente Vacas. "Inclusive charged-current neutrino-nucleus reactions". In: *Phys. Rev. C* 83 (4 2011), p. 045501. DOI: 10.1103/PhysRevC.83.045501. URL: https://link.aps.org/doi/10.1103/PhysRevC.83.045501.

[133] J. Nieves, J. E. Amaro, and M. Valverde. "Inclusive quasielastic charged-current neutrino-nucleus reactions". In: *Phys. Rev. C* 70 (5 2004), p. 055503. DOI: 10.1103/PhysRevC.70.055503. URL: https://link.aps.org/doi/10.1103/PhysRevC.70.055503.

[134] M. Martini et al. "A Unified approach for nucleon knock-out, coherent and incoherent pion production in neutrino interactions with nuclei". In: *Phys. Rev.* C80 (2009), p. 065501. DOI: 10.1103/PhysRevC.80.065501. arXiv: 0910.2622 [nucl-th].

[135] I. Ruiz Simo et al. "Relativistic model of 2p-2h meson exchange currents in (anti)neutrino scattering". In: *J. Phys.* G44.6 (2017), p. 065105. DOI: 10.1088/1361-6471/aa6a06. arXiv: 1604.08423 [nucl-th].

[136] A. A. Aguilar-Arevalo et al. "First Measurement of the Muon Neutrino Charged Current Quasielastic Double Differential Cross Section". In: *Phys. Rev.* D81 (2010), p. 092005. DOI: 10.1103/PhysRevD.81.092005. arXiv: 1002.2680 [hep-ex].

[137] M. Martini, M. Ericson, and G. Chanfray. "Neutrino quasielastic interaction and nuclear dynamics". In: *Phys. Rev. C* 84 (5 2011), p. 055502. DOI: 10.1103/PhysRevC.84.055502. URL: https://link.aps.org/doi/10.1103/PhysRevC.84.055502.

[138] T.G. O'Neill et al. "A-dependence of nuclear transparency in quasielastic A(e, ef'p) at high Q2". In: *Physics Letters B* 351.1 (1995), pp. 87 –92. ISSN: 0370-2693. DOI: http://dx.doi.org/10.1016/0370-2693(95)00362-O. URL: http://www.sciencedirect.com/science/article/pii/037026939500362O.

[139] Artur M Ankowski and Camillo Mariani. "Systematic uncertainties in long-baseline neutrino-oscillation experiments". In: *Journal of Physics G: Nuclear and Particle Physics* 44.5 (2017), p. 054001. URL: http://stacks.iop.org/0954-3899/44/i=5/a=054001.

[140] M. V. Ivanov et al. "Charged-current inclusive neutrino cross sections in the SuperScaling model including quasielastic, pion production and meson-exchange contributions". In: *J. Phys.* G43.4 (2016), p. 045101. DOI: 10.1088/0954-3899/43/4/045101. arXiv: 1506.00801 [nucl-th].

[141] J. E. Amaro et al. "Density dependence of 2p-2h meson-exchange currents". In: *Phys. Rev.* C95.6 (2017), p. 065502. DOI: 10.1103/PhysRevC.95.065502. arXiv: 1704.01539 [nucl-th].

[142] Yoshinari Hayato. "A neutrino interaction simulation program library NEUT". In: *Acta Phys. Polon.* B40 (2009), pp. 2477–2489.

[143] C. Andreopoulos et al. "The GENIE Neutrino Monte Carlo Generator". In: *Nucl. Instrum. Meth.* A614 (2010), pp. 87–104. DOI: 10.1016/j.nima.2009.12.009. arXiv: 0905.2517 [hep-ph].

[144] R. Bradford et al. "A New parameterization of the nucleon elastic form-factors". In: *Nucl. Phys. Proc. Suppl.* 159 (2006). [,127(2006)], pp. 127–132. DOI: 10.1016/j.nuclphysbps.2006.08.028. arXiv: hep-ex/0602017 [hep-ex].

[145] Krzysztof M. Graczyk and Jan T. Sobczyk. "Form factors in the quark resonance model". In: *Phys. Rev. D* 77 (5 2008), p. 053001. DOI: 10.1103/PhysRevD.77.053001. URL: https://link.aps.org/doi/10.1103/PhysRevD.77.053001.

[146] G. M. Radecky et al. "Study of single-pion production by weak charged currents in low-energy νd interactions". In: *Phys. Rev. D* 25 (5 1982), pp. 1161–1173. DOI: 10.1103/PhysRevD.25.1161. URL: https://link.aps.org/doi/10.1103/PhysRevD.25.1161.

[147] T. Kitagaki et al. "Charged Current Exclusive Pion Production in Neutrino Deuterium Interactions". In: *Phys. Rev.* D34 (1986), pp. 2554–2565. DOI: 10.1103/PhysRevD.34.2554.

[148] A. Bodek and U. K. Yang. "Modeling neutrino and electron scattering inelastic cross- sections in the few GeV region with effective LO PDFs TV Leading Order". In: *2nd International Workshop on Neutrino-Nucleus Interactions in the Few GeV Region (NuInt 02) Irvine, California, December 12-15, 2002*. 2003. arXiv: hep-ex/0308007 [hep-ex].

[149] E. Glück M.and Reya and A. Vogt. "Dynamical parton distributions revisited". In: *The European Physical Journal C - Particles and Fields* 5.3 (1998), pp. 461–470. ISSN: 1434-6052. DOI: 10.1007/s100529800978. URL: http://dx.doi.org/10.1007/s100529800978.

[150] Torbjorn Sjostrand et al. "High-energy physics event generation with PYTHIA 6.1". In: *Comput. Phys. Commun.* 135 (2001), pp. 238–259. DOI: 10.1016/S0010-4655(00)00236-8. arXiv: hep-ph/0010017 [hep-ph].

[151] Roger D. Woods and David S. Saxon. "Diffuse Surface Optical Model for Nucleon-Nuclei Scattering". In: *Phys. Rev.* 95 (2 1954), pp. 577–578. DOI: 10.1103/PhysRev.95.577. URL: https://link.aps.org/doi/10.1103/PhysRev.95.577.

[152] A. Bodek and J. L. Ritchie. "Fermi-motion effects in deep-inelastic lepton scattering from nuclear targets". In: *Phys. Rev. D* 23 (5 1981), pp. 1070–1091. DOI: 10.1103/PhysRevD.23.1070. URL: https://link.aps.org/doi/10.1103/PhysRevD.23.1070.

[153] T. Yang et al. "A Hadronization Model for Few-GeV Neutrino Interactions". In: *Eur. Phys. J.* C63 (2009), pp. 1–10. DOI: 10.1140/epjc/s10052-009-1094-z. arXiv: 0904.4043 [hep-ph].

[154] K. Abe et al. "Measurements of neutrino oscillation in appearance and disappearance channels by the T2K experiment with 6.60^{20} protons on target". In: *Phys. Rev.* D91.7 (2015), p. 072010. DOI: 10.1103/PhysRevD.91.072010. arXiv: 1502.01550 [hep-ex].

[155] Particle Data Group. *Atomic and nuclear properties of materials*. URL: http://pdg.lbl.gov/2016/AtomicNuclearProperties/.

[156] "NEUT development for T2K and relevance of updated 2p2h models, Proceedings, 16th International Workshop on Neutrino Factories and Future Neutrino Beam Facilities (NUFACT 2014)". In: vol. NUFACT2014. SISSA. SISSA, 2015. URL: http://pos.sissa.it/cgi-bin/reader/conf.cgi?confid=226.

Appendix A

Data residual distributions

The distributions of all the residuals (Δy and $\Delta\phi$) for each MM pair are shown in this appendix. Residuals are extracted using a cosmic rays sample collected with magnetic field off in RunII-IV. First and second rows show the MMs pair in the EP0: the MM0-MM6 pair corresponds to the first plot while the couple MM6-MM11 is the third plot of the second row. The distributions for the EP1 are shown in the third and fourth row, as in the previous case the first plot of the third row represents the MM0-MM6 pairs while the third in the fourth row corresponds to the MM6-MM11. The residual Δy is shown in Fig. A.1, A.2 and A.3, while $\Delta\phi$ in Fig. A.4, A.5 and A.6.

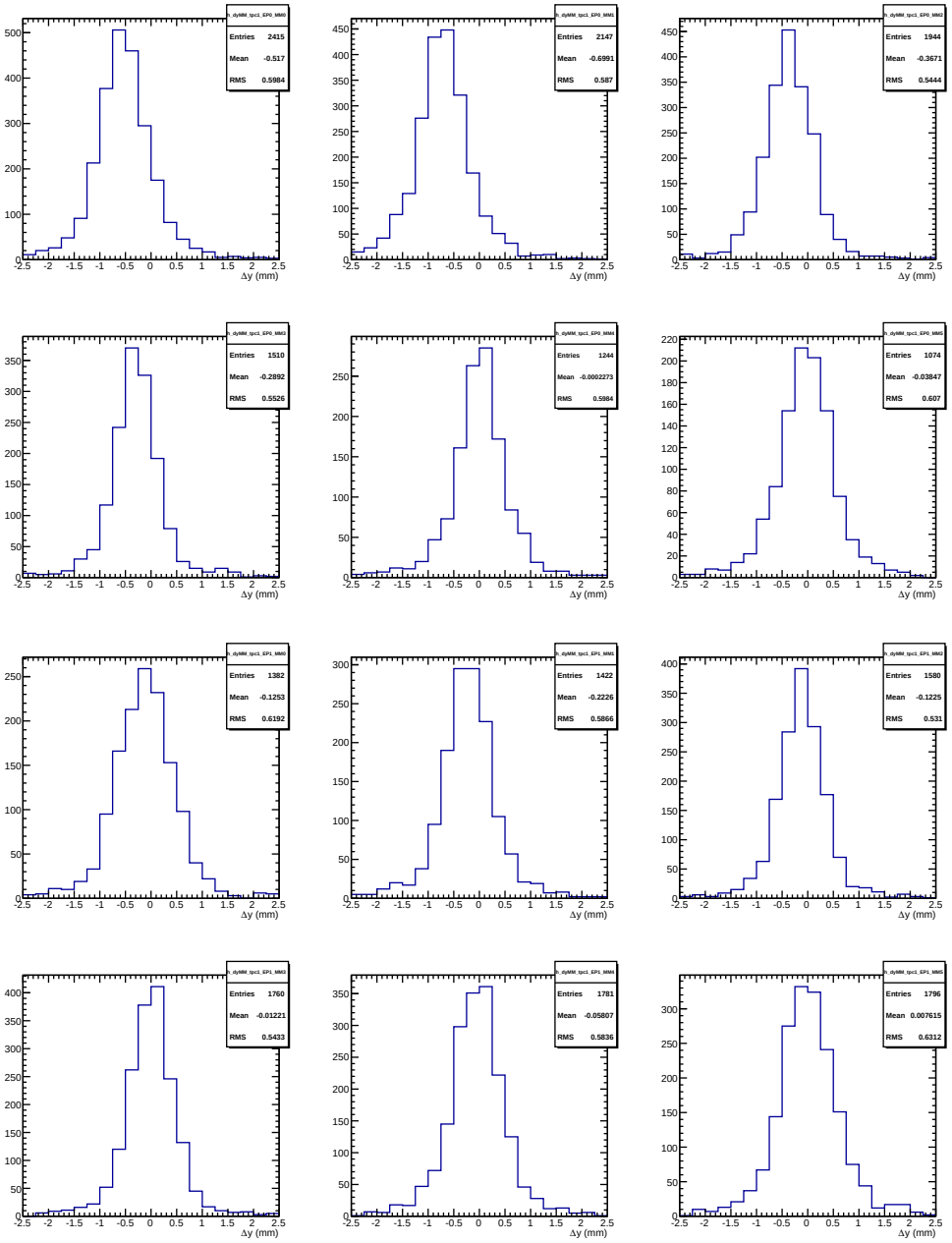

Figure A.1: Δy residuals distribution for all the MM pairs in the TPC1 EPs. The EP0 in the first two rows and EP1 in the last two rows.

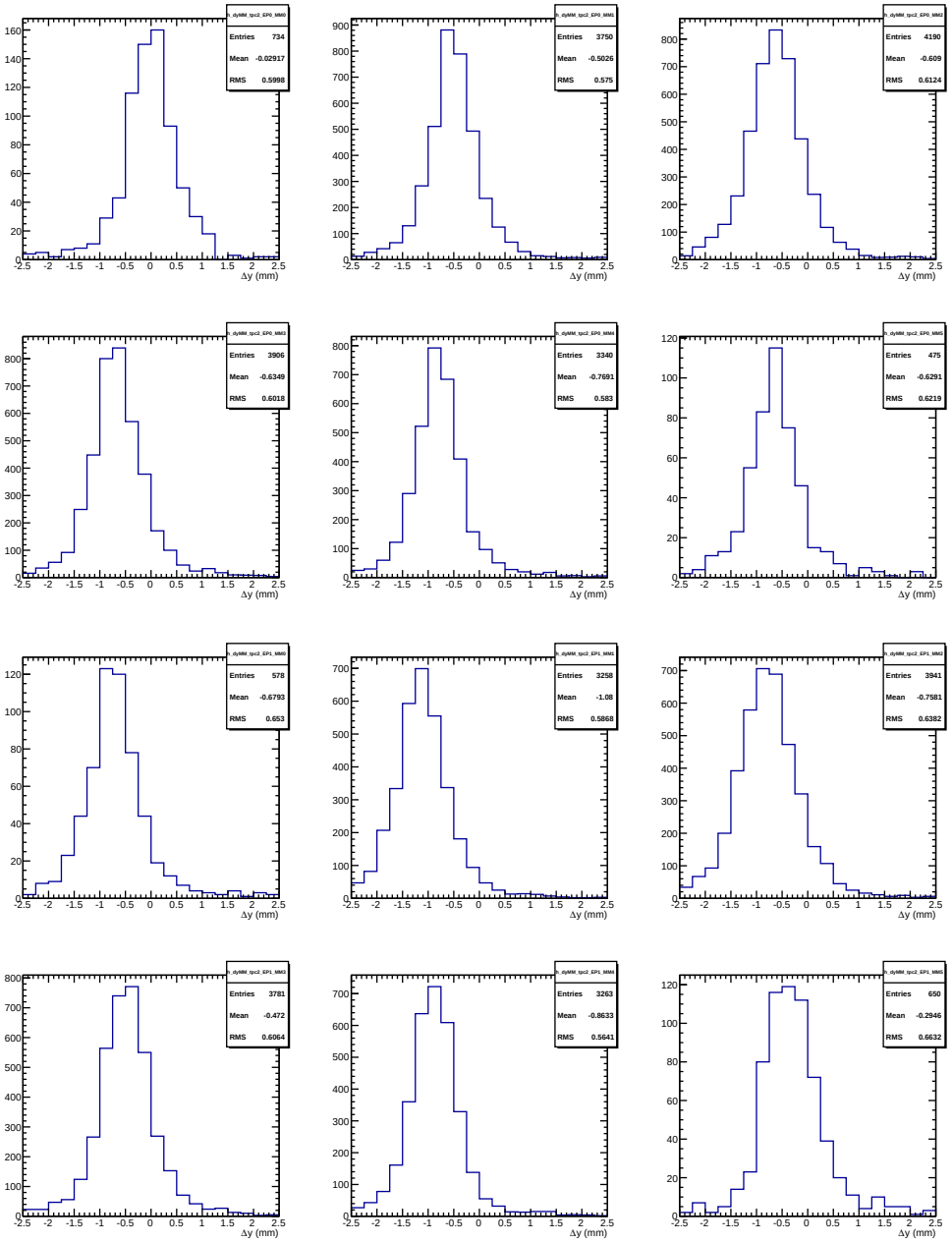

Figure A.2: Δy residuals distribution for all the MM pairs in the TPC2 EPs. The EP0 in the first two rows and EP1 in the last two rows.

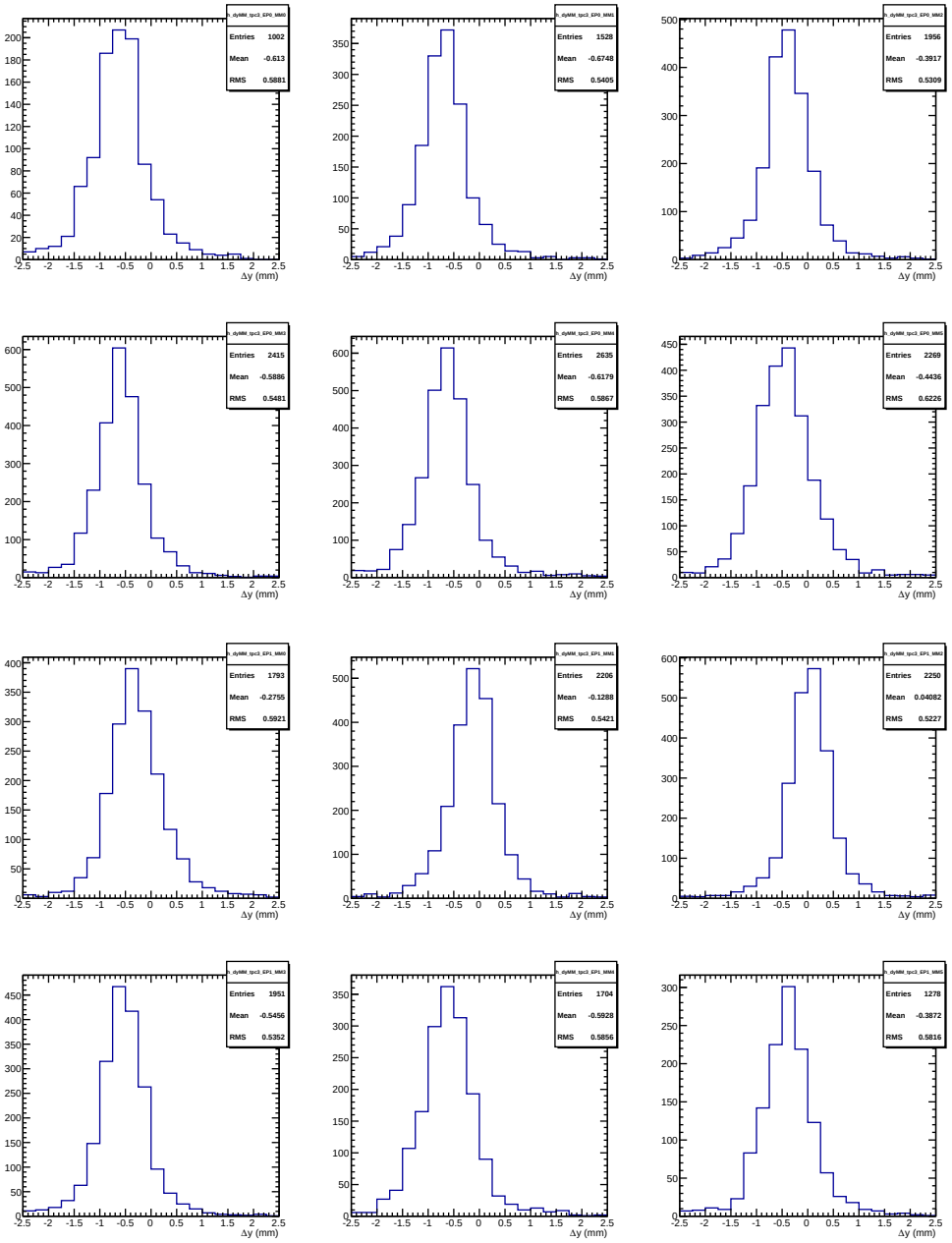

Figure A.3: Δy residuals distribution for all the MM pairs in the TPC3 EPs. The EP0 in the first two rows and EP1 in the last two rows.

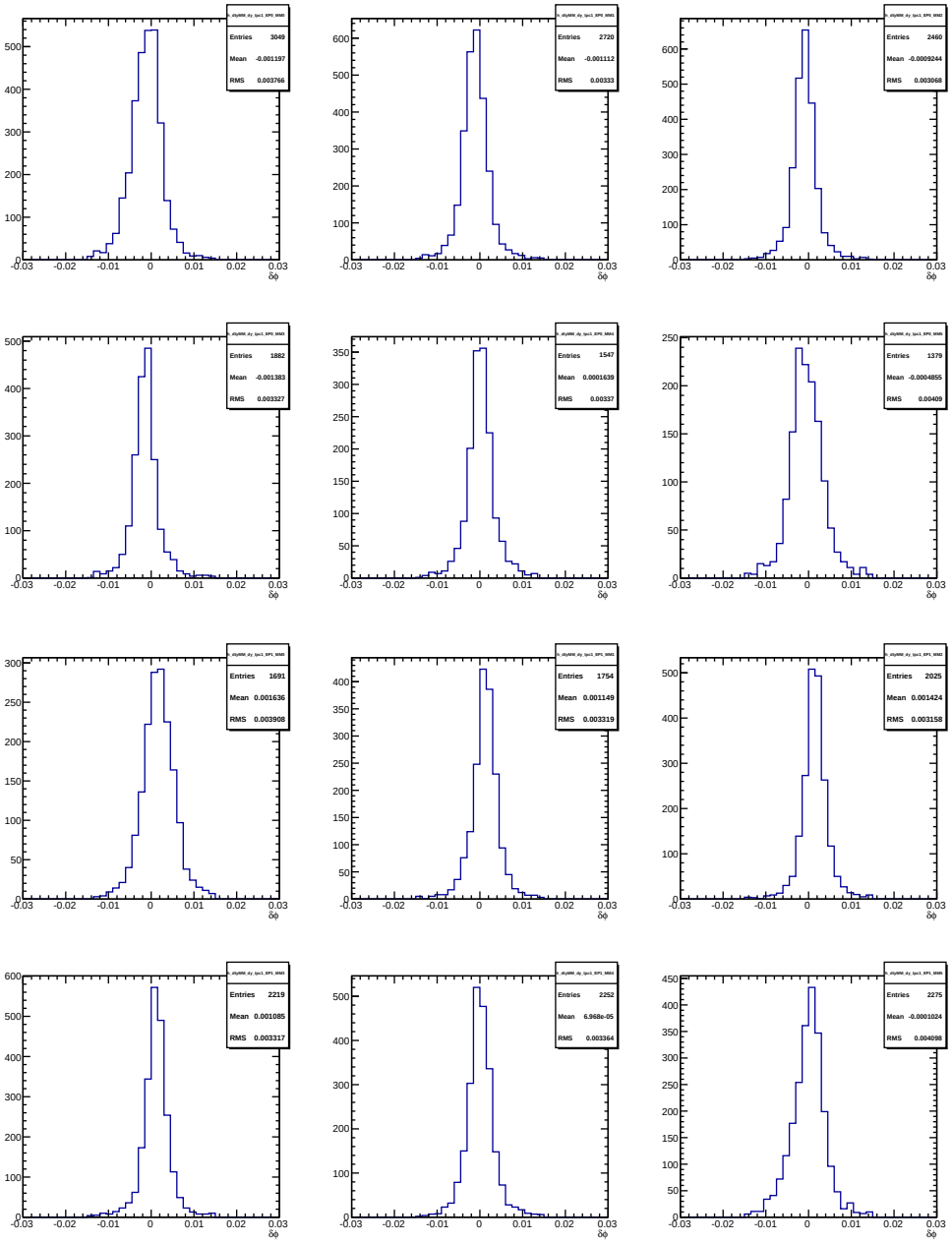

Figure A.4: $\Delta\phi$ residuals distribution for all the MM pairs in the TPC1 EPs. The EP0 in the first two rows and EP1 in the last two rows.

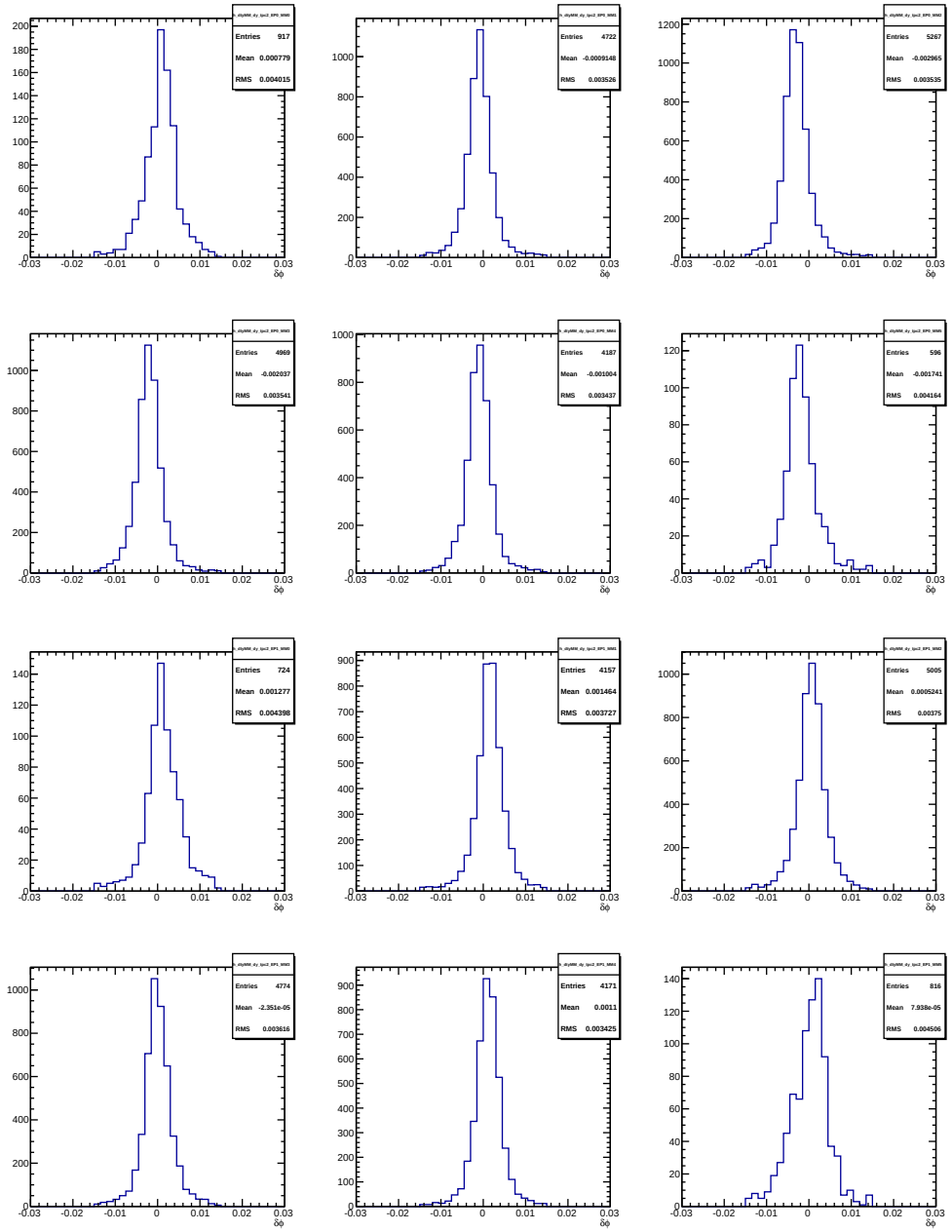

Figure A.5: $\Delta\phi$ residuals distribution for all the MM pairs in the TPC2 EPs. The EP0 in the first two rows and EP1 in the last two rows.

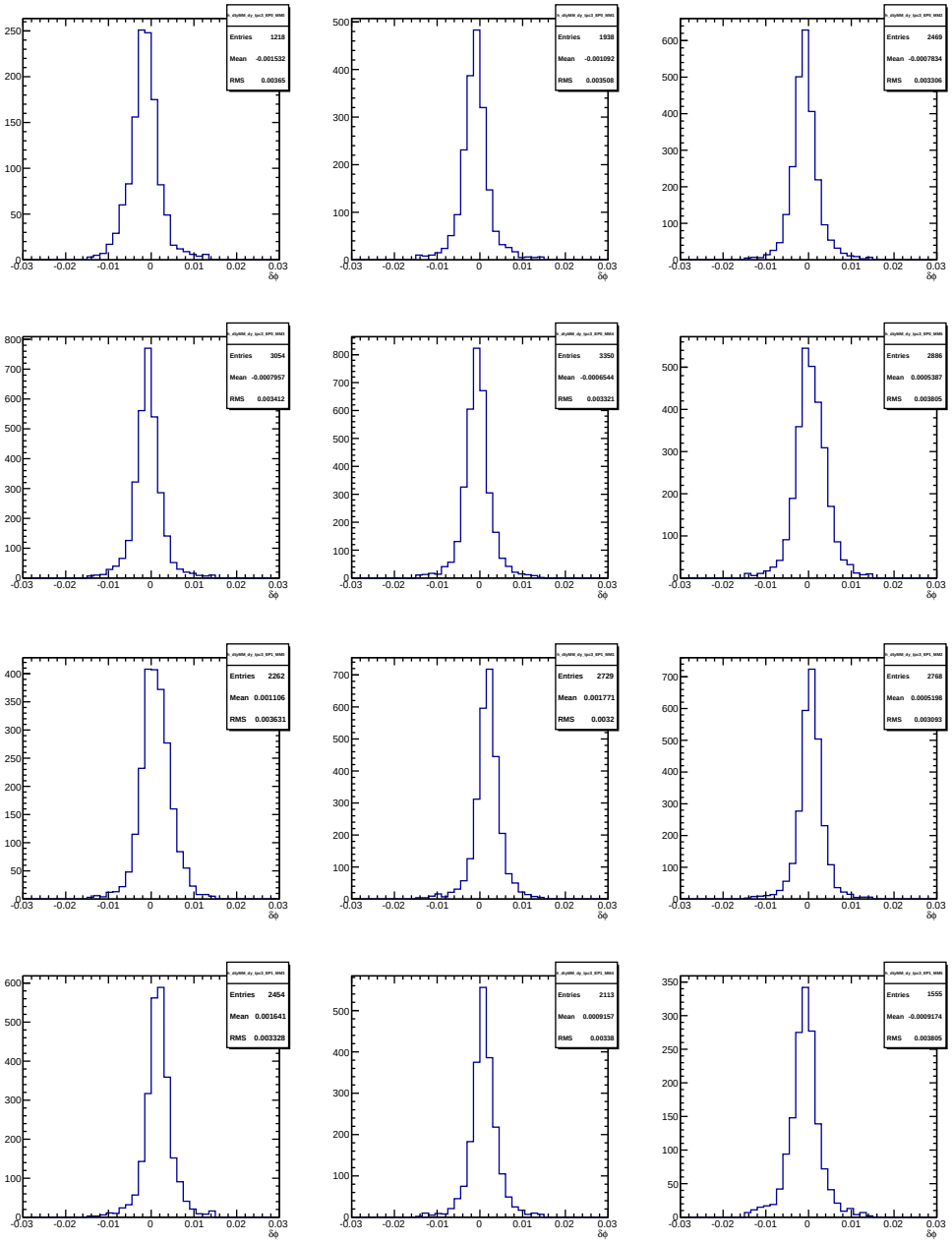

Figure A.6: $\Delta\phi$ residuals distribution for all the MM pairs in the TPC3 EPs. The EP0 in the first two rows and EP1 in the last two rows.

Appendix B

The MINUIT Fit

In this appendix a look up to the fit alignment procedure used to extrapolate MM correction constants is given. The alignment foresees a χ^2 minimization of the residuals via a two step procedure. The χ^2_Δ is defined as:

$$\chi^2_\Delta = \chi^2_{\Delta y} + \chi^2_{\Delta\phi}; \tag{B.1}$$

$$\chi^2_\Delta = \sum^{n_{tracks}} \left(\frac{\Delta + f_\Delta}{\sigma_\Delta} \right)^2. \tag{B.2}$$

It dependes from:

- track residual $\Delta \; = \; \Delta y, \; \Delta\phi$
- σ_Δ MM resolution extracted from bi-gaussian fit to residual distribution
- correction formulas $f_\delta \; = traslation \; + \; rotation$

$$f_{\delta\phi} = \phi_{MM_i} - \phi_{MM_j}, \tag{B.3}$$

$$\begin{aligned} f_{\delta y}\left(y_{MM_i}, y_{MM_j}, z_{MM_i}, z_{MM_j}, \phi_{MM_i}, \phi_{MM_j}\right) = \left(y_{MM_i} - y_{MM_j}\right) - \left(z_{MM_i} - z_{MM_j}\right) tan\left(\phi'_{MM}\right) \\ - \left(\phi_{MM_i} - \phi_{MM_j}\right) \left(\frac{d+L}{2} - y_{MM_i} tan\left(\phi'_{MM}\right) \right), \end{aligned} \tag{B.4}$$

  where $tan\left(\phi'_{MM}\right) = tan\left(\phi - \left(\phi_{MM_i} - \phi_{MM_j}\right)\right)$ and ϕ is the track angle
- $L =$ MM length
- $d =$ MM center distance from middle plane (MP)

Rotational term (3rd)

$$\left(\phi_{MM_i} - \phi_{MM_j}\right)\left(\frac{d+L}{2} - y_{MM_i} tan\left(\phi'_{MM}\right)\right). \tag{B.5}$$

Assuming a rotation $\Delta\phi$ between a MM pair, if the magnetic field is off is possible to parametrize a muon track with a first order function, calling:

- The reconstructed track

$$y = ztan\phi + b; \tag{B.6}$$

- The true track

$$y' = z'tan\phi' + b', \tag{B.7}$$

where the true track is the track we would have if the MM couple would be perfectly aligned ($\Delta\phi = 0$ mrad). It is possible to move from one reference system to the other thanks to a rotation of $\Delta\phi$

$$\begin{cases} z' = zcos\Delta\phi + ysin\Delta\phi \\ y' = -zsin\Delta\phi + ycos\Delta\phi \end{cases} \tag{B.8}$$

replacing true quantities with reconstructed ones in track's parametrization

$$y\left[cos\Delta\phi - sin\Delta\phi tan\left(\phi - \Delta\phi\right)\right] = z\left[sin\Delta\phi + cos\Delta\phi tan\left(\phi - \Delta\phi\right)\right] + b', \tag{B.9}$$

under the assumption of relative small displacements (order of milliradiands) $\Delta\phi \sim 0$ at the first order:

$$\begin{array}{l} cos\Delta\phi \sim 1; \\ sin\Delta\phi \sim \Delta\phi; \\ \frac{1}{1-\Delta\phi tan(\phi-\Delta\phi)} \sim 1 + \Delta\phi tan\left(\phi - \Delta\phi\right). \end{array} \tag{B.10}$$

In order to have a terse notation the term $tan\left(\phi - \Delta\phi\right)$ is not developed for the moment. After the expansion the true track will parametrize by the expression:

$$y = z\left[1 + tan\left(\phi - \Delta\phi\right) + \Delta\phi tan^2\left(\phi - \Delta\phi\right)\right] + b'\left[1 + \Delta\phi tan\left(\phi - \Delta\phi\right)\right]. \tag{B.11}$$

Considering the middle plane between two MMs placed at $z = -\frac{L+d}{2}$ (the origin is the center of MM in the 2nd column), thanks to Eq. B.7 and B.11 it is possible to parametrize the true (y_{true}) and the reco (y_{reco}) position in the y direction as:

$$\begin{cases} y_{true} = -\frac{L+d}{2} tan\left(\phi - \Delta\phi\right) + b' \\ y_{reco} = -\frac{L+d}{2}\left[1 + tan\left(\phi - \Delta\phi\right) + \Delta\phi tan^2\left(\phi - \Delta\phi\right)\right]. + b'\left[1 + \Delta\phi tan\left(\phi - \Delta\phi\right)\right] \end{cases} \tag{B.12}$$

The difference along y when the MM is rotated will be:

$$\Delta y_\phi = y_{reco} - y_{true} = \Delta\phi \left[\frac{d+L}{2} \left(tan^2\phi + 1 \right) - b' tan\phi \right]. \tag{B.13}$$

Thanks to goniometric relation and taylor expansion at the first order:

$$tan\left(\phi - \Delta\phi\right) = \frac{tan\phi - tan\Delta\phi}{1 + tan\phi tan\Delta\phi} \simeq tan\phi - tan\Delta\phi, \tag{B.14}$$

however $\Delta\phi \to 0$ then at the first order $tan\Delta\phi \sim \Delta\phi$.
The b coefficient is the last one to compute. Considering a point A placed in the middle plane, its coordinates are $A\ (\frac{d+L}{2}, y_A)$; a second point B along the y-axis will be $B\ (0, b)$. The slope $tan\phi$ is the incremental ratio between the two points A and B (see Fig. B.1), for this reason the b coefficient is:

$$b = \frac{d+L}{2} tan\phi + y \tag{B.15}$$

where y is the y coordinate of the track in the MP. Finally, considering relations B.13 and B.15, the correction to Δy residual due to a mutual rotation between the MM pair is:

$$\Delta y_\phi = \Delta\phi \left[\frac{d+L}{2} - y_{MP} tan\left(\phi - \Delta\phi\right) \right] \tag{B.16}$$

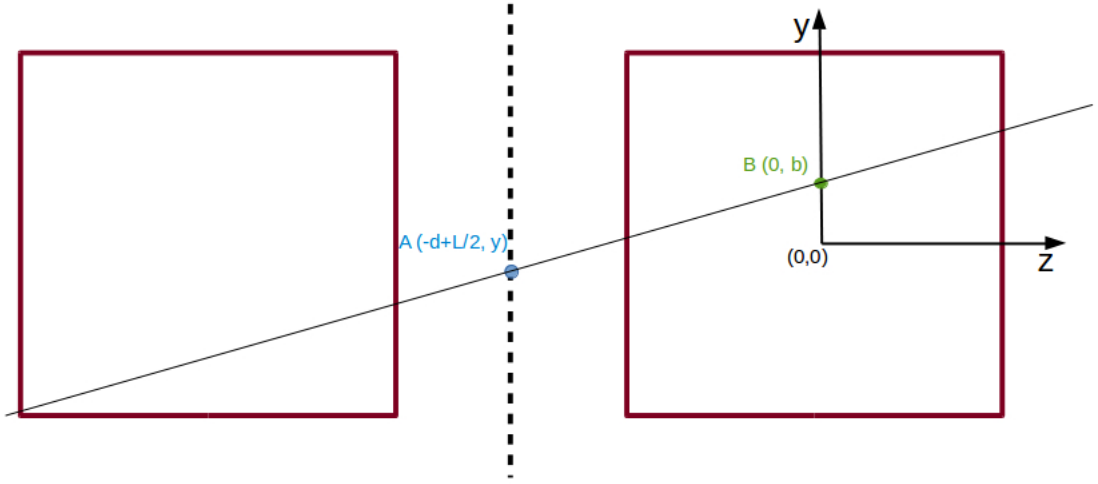

Figure B.1: Schematic view of the b coefficient extrapolation.

Appendix C

Detector systematics

Magnetic Field distortion: as previously stated in Sec. 3.5.4 the magnetic field inside the magnet were measured with Hall probes prior detectors installation [103]. This magnetic field mapping (B Field map, see Fig. 3.12) is then used during the reconstruction to account for field distortions, as the field is not constant throughout the magnet volume. The systematic uncertainty is evaluated by looking at the difference in y and z position of each cluster evaluated drifting back them to the ionization point. Therefore the propagation of such difference in the reconstructed momentum of each track, turning on/off the magnetic field corrections, gives an estimation of the systematic.

TPC Momentum Resolution: it is studied using the same approach introduced in Sec. 4.8.2 which compares the difference between the inverse of the reconstructed momentum of the two TPC segment of a track crossing multiple TPCs. Figure 4.38 shows that the MC has better TPC performance than data, a smearing is then applied to the MC in order to match the data distribution. Such smearing (Eq. 4.15) accounts for the momentum resolution in bin of x position (the drift direction) using the fractional difference between data and MC.

TPC Momentum Scaling: it strictly depends on the magnetic field strength and its distortions [103]. The momentum scale uncertainty has been estimated as 0.57%.

TPC Particle IDentification: as described in Sec. 3.5.3 the TPC particle ID is calculated starting from the truncated mean of the energy deposit in the TPC. It is evaluated using high purity sample of muon, electron and proton and binned in particle momentum. The data-MC difference in the pull means (Eq. 3.11) gives an estimation of the systematic bias while their ratio is used to estimate the smearing which needs to be applied.

TPC Cluster Efficiency: it describes the efficiency in reconstructing a cluster in the TPC where one is expected. It is evaluated looking at the data-MC difference in reconstruction efficiency since it affects the number of events passing the TPC

track quality cut (tracks with at least 18 clusters). The ratio between the two efficiencies is found to be 0.9989 ± 0.0002, in case of vertical clusters.

TPC Track Reconstruction: it describes the efficiency for successfully reconstructing tracks originated from particles that crossed the TPCs. It accounts potential lack due to the likelihood fit (see Sec. 3.5.1) which can lead to the wrong classification of a neutrino event topology. The systematic uncertainty is evaluated comparing data and MC for the reconstruction efficiency of tracks with at least 16 cluster for all angles, momenta and track lengths. The overall efficiency is calculated separately for the three TPCS and summarized in Tab. C.1

	TPC1	TPC2	TPC3
Data efficiency	$99.9^{+0.1}_{-0.1}\%$	$99.7^{+0.2}_{-0.7}\%$	$99.3^{+0.5}_{-0.2}\%$
MC efficiency	$99.6^{+0.2}_{-0.3}\%$	$99.5^{+0.3}_{-0.4}\%$	$99.8^{+0.1}_{-0.2}\%$

Table C.1: Data and MC TPC track reconstruction efficiencies for the three TPCs.

Charge ID: in the ν_μ CC selection crucial is the determination of a negative charged particle as muon candidate. The charge is assigned by comparing the charge determination in each TPC (local fit) with the charge assignment from the global track reconstruction. A control sample of tracks starting in the PØD and crossing at least one TPC segment are used in order to compute the probability between the local and global fit of swapping the charge of the track. The uncertainty on the mis-identification of the charge is found to be $1 \pm 0.2\%$ for track momentum between 500 MeV and 5 GeV and increase up to few percent in the low and high momentum regions since for that tracks the curvature in the magnetic field can be quite small.

FGD Particle IDentification: it is applied when a particle does not reach the TPC and stops inside the FGD (FGD-only track). As in the TPC case, the FGD PID is determined using the energy deposit measured along the FGD-only tracks, therefore pulls can be used for particle determination. The same TPC approach is used and the systematic error is estimated looking at the difference and ratio between the mean value of pulls for data and MC.

FGD Hybrid Track Reconstruction: it is defined as the efficiency of reconstructing a fully contained track in FGD in presence of a long TPC-FGD matched track. Since the FGD PID is applied to FGD-only tracks, the knowledge of the reconstruction efficiency of these tracks is necessary for propagation of systematic error. The used sample consists of selected muon candidate long tracks for which a FGD-only simulated track (either pion or proton) is isotropically generated in the same vertex using a particle gun in GEANT4 [106]. The efficiency is calculated for both data and MC as a function of the angle between the tracks and

is defined as the ratio of the number of events with at least one reconstructed FGD-only track over the total number of selected events. The overall systematic uncertainties on the track efficiency is found to be $< 8\%$ in each bin for both proton and pion.

Particle Time of Flight: it is used to determine the track direction. As explained in Sec. 2.6.4 a track that crosses both FGDs is reconstructed as backwards-going when the average time difference of the FGD hits is greater than $\Delta t_{21} > 3$ ns. For its determination a sample of muon candidate tracks passing through both FGD1 and FGD2 is used. The difference between the mean value and the resolution of the time of flight distribution for both data and MC is used to compute this uncertainty which is estimated to be $\Delta t_{21} = 0.78$ ns.

TPC-FGD Matching Efficiency: is mostly due to tracks generated close to the edge of the FGD2 and it is related to the efficiency of connecting the FGD hits to the reconstructed TPC track. It is evaluated using a muon track sample passing through TPC2 and TPC3 which assures that the track has crossed the FGD2 as well. The systematics studies find that the probability of matching TPC tracks with momentum greater than 200 MeV with the FGD segment is approximately 100% for both data and MC.

Michel Electron Detection: it is associated to Michel electron detection efficiency and purity. Michel electrons are used to tag charged pions from neutrino interactions and sort them into topologies. An event is considered to have a Michel electron if it has at least one delayed out-of-bunch timebin with more than 5 hits in the FGD2. The efficiency of reconstruct the electron from a pion decay, is studied using a sample of cosmic muon decaying in the FGD2 (stopping muons) in order to compare data and MC reconstruction efficiency and use their difference to assign a systematic error. A good data-MC agreement is found, leading to an uncertainty of $\approx 2\%$ for the rate at which Michel electron events are tagged.

Out Of Fiducial Volume Events: parts of the background come from particles originated outside the FGD2 but reconstructed in its FV. In order to evaluate this contribution these events are separated into categories according to the true interaction vertex and particle type: neutral particles (π^0 and γ) entering the FGD2, charged particles originating outside the tracker, and charged particles originating inside the tracker. At each category two uncertainties are assigned, one related to the interaction rate and a reconstruction uncertainty which is mainly due to TPC-FGD matching failure. The rate uncertainty is 0 for particles originating inside the ND280 Tracker and 20% for particles originating outside. Instead, the reconstruction uncertainty has been estimated to be below 40% for almost all categories except for the high-angle tracks for a 150% is assigned because of the matching that sometimes fails to include some hits that are outside the FGD FV.

Event Pile-Up: it occurs when a ν_μ interaction happens at the same time of an OOFV event leading the external veto cut (see Sec. 6.1.2) to remove such event. Since this uncertainty depends on the beam intensity it is computed separately for each T2K run period.

Pion Secondary Interaction: pions produced from neutrino interactions escaping the nucleus, can undergo hadronic secondary interactions (SI) in the detector, resulting in detection inefficiencies in FGD2. These interactions (absorption, elastic scattering, etc...) are modelled in the GEANT4 simulation of ND280. In order to propagate this uncertainty in FGD2 the pion path is broken into steps of 1 mm, in each step an interaction probability is calculated under different cross-section assumptions. The event weight is calculated as a product of such probabilities.

Appendix D

Reconstructed neutrino energy

In this section the detector response and the transfer matrices as a function of the neutrino reconstructed energy are shown in Fig. D.1. The muon reconstruction efficiencies after the phase space resctriction are shown in Fig. D.2

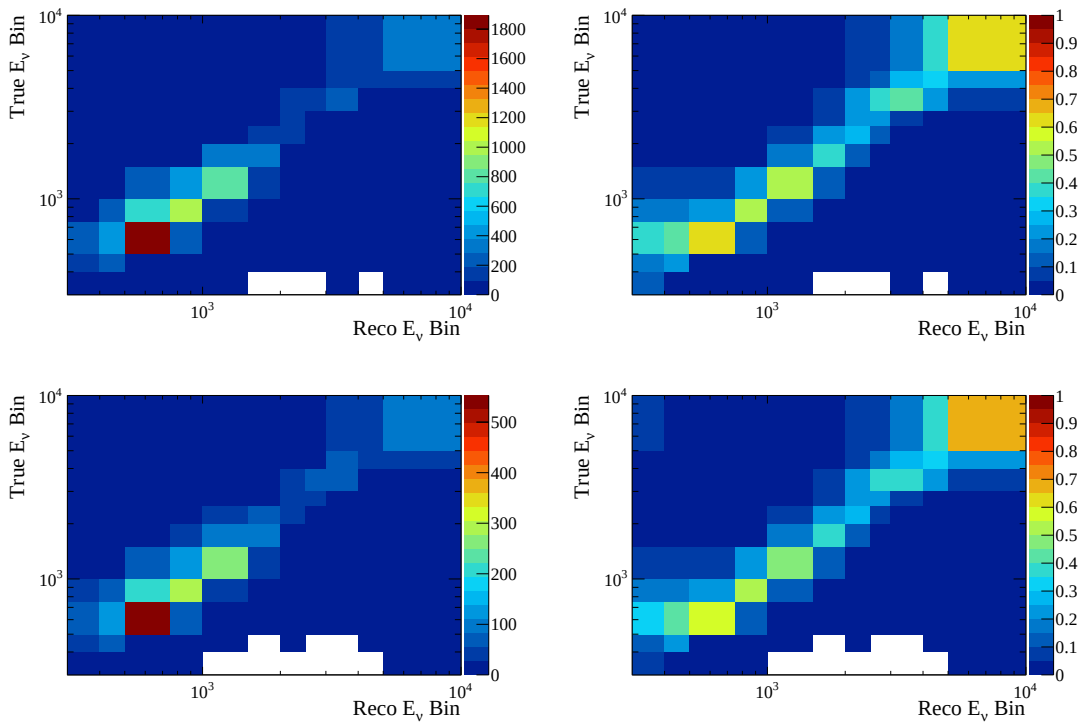

Figure D.1: Detector response and trasfer matrix for the neutrino energy of the selected CC0π interactions in the x-layer (top) and y-layer (bottom).

The event distributions in the chosen binning breakdown by reaction topology and interaction vertex are shown in Fig. D.3 for the x-layers (top) and y-layers (bottom).

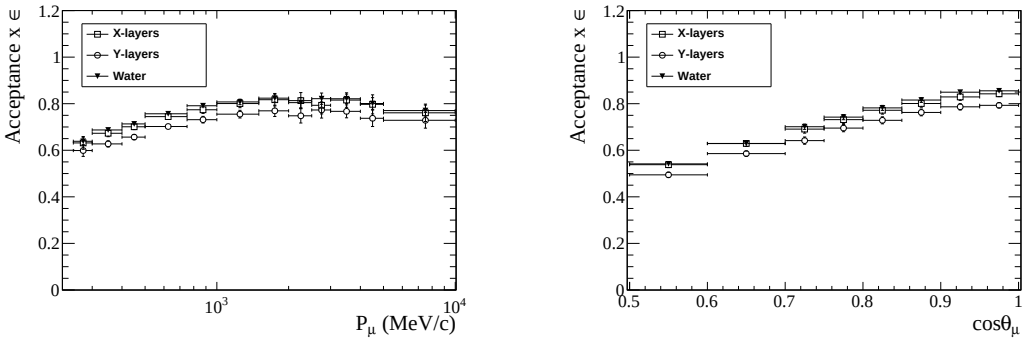

Figure D.2: Detector efficiencies as a function of the muon momentum (left) and direction (right) after the phase space restriction.

Figure D.4 shows the migration fractions in FGD2 as a function of reconstructed neutrino energy. The integrated values of the migration fraction and of the selection purity are summarized in Tab. D.1

Purity	$f_x^{CC0\pi} = 0.709 \pm 0.008$	$f_y^{CC0\pi} = 0.664 \pm 0.008$
Migration $j \to i$		
$f_{x\to x} = 0.902 \pm 0.009$	$f_{x\to y(fwd)} = 0.082 \pm 0.002$	$f_{x\to y(bkw)} = 0.016 \pm 0.001$
$f_{y\to y} = 0.726 \pm 0.008$	$f_{y\to x(fwd)} = 0.107 \pm 0.002$	$f_{y\to x(bkw)} = 0.167 \pm 0.003$
$f_{w\to x} = 0.925 \pm 0.009$	$f_{w\to y} = 0.075 \pm 0.002$	

Table D.1: List of purity of the sample and of the migration fractions. The first index represent the true interaction module, the second one the reconstructed vertex.

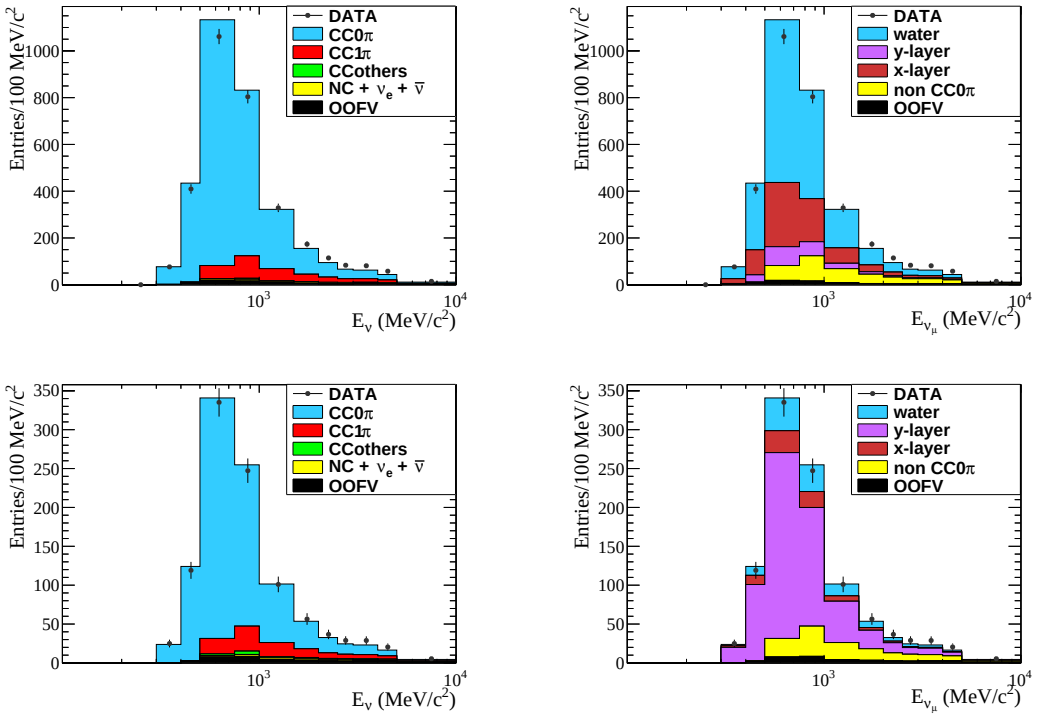

Figure D.3: CC0π selected events as a function of the incoming neutrino reconstructed energy and normalized to data POT and sorted into the different reaction (left) and vertex (right) topologies for the x-layer (top) and y-layer (bottom). Black dots represent the data before applying the Reco-True transfer matrix.

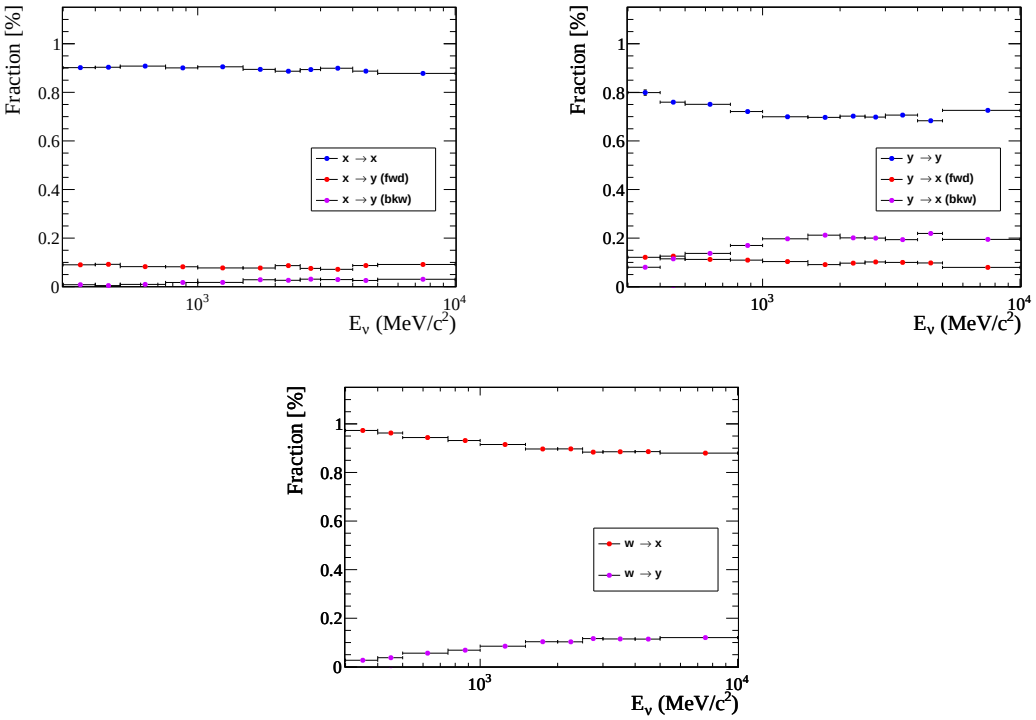

Figure D.4: Migration fractions in FGD2 as a function of reconstructed neutrino energy.

École Doctorale
PHENIICS
Doctoral School

Titre : Mesure du rapport des sections efficaces d'interaction des neutrinos sur les noyaux d'oxygène et de carbone, à partir des données du détecteur proche ND280 de l'expérience T2K

Mots-clés : *neutrinos, expérience T2K, oxygène, section efficace, interaction par courant chargé quasi-elastique, Chambres à Projections Temporelles*

Résumé : Le Modèle Standard de la physique des particules décrit les interactions des particules sub-atomiques à travers les interactions fortes, faibles et électromagnétiques. Toutefois, il est clair que cette théorie ne constitue pas une description complète de la Nature. Mais le fait expérimental que les neutrinos changent de saveur au cours de leur propagation (oscillation des neutrinos) implique qu'ils ont une masse non nulle. Le travail de cette thèse se concentre sur l'expérience d'oscillation T2K : une expérience à longue ligne de base installée au Japon qui est détaillés dans le Chapitre 2. Pour la première fois T2K a pu observer l'apparition de neutrinos de saveur électronique dans le faisceau principalement composé de neutrinos muoniques et obtenir les premières contraintes sur la violation de la symétrie Charge-Parité. Il permet également de mesurer précisément les paramètres d'oscillations θ_{13}, θ_{23} et Δm^2_{23}. Cela nécessite une excellente compréhension du détecteur et des modèles d'interactions des neutrinos. Cette thèse se concentre sur ces deux objectifs : réduire les systématiques liées au détecteur et approfondir nos connaissances sur l'interaction des neutrinos avec la matière. Le groupe CEA, dans lequel je suis impliqué, est responsable de la maintenance et de l'opération des Chambres à Projections Temporelles (TPC) du détecteur proche (ND280). Elles permettent l'identification des particules chargées produites par l'interaction des neutrinos dans le detecteur et la mesure de leur impulsion. Une partie de mon travail a consisté en l'étude des TPCs et en particulier de l'alignement des modules MicroMegas installés sur les plans de lecture. En effet tout défaut d'alignement entre différents modules peut causer un biais sur la mesure de l'impulsion des particules traversant la TPC. Les neutrinos sont étudiés grâce à l'observation de l'état final de leur interaction avec la matière. Les modèles d'interactions doivent alors être parfaitement bien compris, car les expériences d'oscillation présentes et futures approchent d'une phase où notre connnaissance des interactions des neutrinos devient un facteur limitant pour la détermination des paramètres d'oscillations. L'interaction quasi élastique par courant chargé (CCQE) est le processus dominant pour T2K. Ce manuscrit décrit la mesure du rapport des sections efficaces d'interaction des neutrinos sur les noyaux de Carbone et d'Oxygène. Cette mesure contribue à la réduction des incertitudes pour l'analyse d'oscillation, liées à l'utilisation d'une différente cible pour le détecteur proche et le détecteur lointain.

Title: Oxygen/Carbon cross-section ratio for neutrino-nucleus interactions using the ND280 near detector of the T2K experiment

Keywords: *neutrinos, T2K experiment, oxygen, cross-section, charge current quasi-elastic interaction, Time Projection Chambers*

Abstract: The Standard Model of particle physics describes the interactions of subatomic particles through the strong, weak and electromagnetic interactions. However, it is known that this theory is not a complete description of the nature. Indeed the observation that neutrinos can change their flavor along their propagation path (neutrino oscillation) proves that they actually have a mass. The work of this thesis has been performed in the T2K oscillation experiment: a long baseline experiment located in Japan detailed in Chapter 2. Using the data collected so far, T2K has been able to observe for the first time the $\nu_\mu \rightarrow \nu_e$ appearance and to give first results on the Charge-Parity simmetry in neutrino oscillation. It provides also precise measurements of the oscillation parameters θ_{13}, θ_{23}, Δm^2_{23}. The precise measurement of oscillation parameters requires a good understanding of the detector and of the neutrino interaction model. This thesis is thus focused on both these aspects: reduce the detector uncertainties and improve our knowledge of neutrino interactions with matter. The CEA Saclay group where I am involved, is in charge of the maintenance and operation of the Time Projection Chambers (TPCs) of the T2K near detector (ND280) which are used to identify and measure the kinematics of the charged particles produced in neutrino interactions. Part of my work was focused on the study of the TPC and in particular on the alignment of the MicroMegas modules instrumenting their readout planes. Indeed, misalignments between modules may cause a bias on the momentum measurement of the particles crossing the TPC. Neutrinos are studied through the observation of the final state of their interactions with matter. Therefore, the interaction models need to be extremely well understood to infer the neutrino properties correctly. Indeed current and next future oscillation experiments are approaching the phase of precise measurements of the mixing parameters becoming limited by our knowledge of neutrino interactions. The charged current quasi-elastic (CCQE) interaction is the most relevant process at T2K. This manuscript describes the measurement of CCQE cross-section ratio between oxygen and carbon nuclei. It can contribute to reduce the uncertainties on the oscillation analysis arising from the different target between the near and far detector.

1. **Université Paris-Saclay**
Espace Technologique / Immeuble Discovery
Route de l'Orme aux Merisiers RD 128 / 91190, Saint-Aubin, France